



**Computational fluid dynamics modelling of biomass
slow pyrolysis in screw reactors for the production
of biochar and charcoal**

Xiaogang Shi

May, 2017

Promoters

Prof. dr. ir. Jan Pieters

Department of Biosystems Engineering, Faculty of Bioscience Engineering, Ghent University, Ghent, Belgium

Prof. dr. ir. Frederik Ronsse

Department of Biosystems Engineering, Faculty of Bioscience Engineering, Ghent University, Ghent, Belgium

Members of the Examination Committee

Prof. dr. ir. Pascal Boeckx (Chairman)

Faculty of Bioscience Engineering, Ghent University

Prof. dr. ir. Tom Desmet (Secretary)

Faculty of Bioscience Engineering, Ghent University

Prof. dr. ir. Robert Carleer

Faculty of Science, Hasselt University

Prof. dr. ir. Ondrej Masek

School of GeoSciences, University of Edinburgh

Prof. dr. ir. Geraldine Heynderickx

Faculty of Engineering and Architecture, Ghent University

Dean

Prof. dr. ir. Marc Van Meirvenne

Rector

Prof. dr. Anne De Paepe

**Computational fluid dynamics modelling of biomass slow
pyrolysis in screw reactors for the production of biochar
and charcoal**

DOCTORAL DISSERTATION

Thesis submitted in fulfillment of the requirements for the degree of

Doctor (Ph.D.) of Applied Biological Sciences:

Chemistry and Bioprocess Technology

by

Xiaogang Shi

Ghent University

Ghent, Belgium

Cover illustration by Xiaogang Shi

This work was supported by China Scholarship Council (CSC) and by Special Research Fund of Ghent University.

For citation:

Xiaogang Shi (2017). *Computational fluid dynamics modelling of biomass slow pyrolysis in screw reactors for the production of biochar and charcoal* (doctoral dissertation). Ghent University, Ghent, Belgium

ISBN: 978-90-5989-995-7

All rights reserved. No part of this document may be reproduced or transmitted in any form or by any means, electronic, mechanical, photocopying, scanning, recording, or otherwise, without prior written permission of the author and/or dissertation promoter(s). A written permission of the author is also required to use the methods, products, schematics and programs described in this work for industrial or commercial use, and for submitting any part of this dissertation in scientific contests. Every other use is subjected to the copyright laws.

Contents

	Nomenclature	i
	Abstract	vii
	Samenvatting	xiii
Chapter 1	Introduction	1
Chapter 2	Modeling of pyrolysis of a biomass particle with a general kinetic scheme	51
Chapter 3	Modeling of pyrolysis of a biomass particle with a comprehensive kinetic scheme	99
Chapter 4	Space-time integral method for simplifying the modeling of pyrolysis of a biomass particle	131
Chapter 5	3D Eulerian-Eulerian simulations of solids flow dynamics and back-mixing in a screw reactor	171
Chapter 6	Numerical study of biomass slow pyrolysis for char production in a screw reactor	205
	Main conclusions and future perspectives	235
	Appendix A	243
	Appendix B	247
	Appendix C	249
	Reference	253
	Acknowledgements	271
	Curriculum Vitae	273



NOMENCLATURE

Symbols

B	$[m^2]$	Effective permeability
Bi	$[-]$	Biot number
c_p	$[J/(kg \cdot K)]$	Specific heat capacity
C_d	$[-]$	Drag coefficient
D	$[m^2/s]$	Diffusivity
d	$[m]$	Diameter
e	$[-]$	Emissivity
\dot{E}	$[W/m]$	Energy rate
EF	$[-]$	Enhancement factor
e_{ss}	$[-]$	Particle-particle restitution coefficient
$E(t), E(\theta)$	$[-]$	RTD function
$F(t), F(\theta)$	$[-]$	Cumulative RTD function
g	$[m/s^2]$	Gravity constant
$g_{0,ss}$	$[-]$	Radial distribution function
h	$[W/(m^2 \cdot K)]$	Heat transfer coefficient
HHV	$[MJ/kg]$	Higher heating value
$\bar{\mathbf{i}}$	$[-]$	Unit tensor
I_{2D}	$[-]$	Second invariant of the deviatoric stress tensor
k	$[1/s]$	Reaction rate
L	$[m]$	Characteristic length
M	$[wt. \%]$	Moisture content

Nomenclature

MD		Mean deviation
MW	[kg/mol]	Molecular weight
n	[-]	Number of variables
P	[Pa]	Pressure
Py/Py'	[-]	Internal/external pyrolysis number
q	[W/m ³]	Net heat flux at particle surface
Q	[W/m ³]	Heat source
r	[m]	Radius
\dot{r}	[kg/(m ³ ·s)]	Pyrolysis rate
R	[kg/(m ³ ·s)]	Interphase mass transfer term due to interfacial reactions or moisture evaporation
R ²	[-]	Coefficient of determination
R _{cons}	[8.314 J/(mol·K)]	Universal gas constant
Re	[-]	Relative Reynolds number
S	[kg/(m ³ ·s)]	Net formation rate of a species
t	[s]	Time
T	[K]	Temperature
u	[m/s]	Velocity
V	[m ³]	Volume
w	[-]	Weight fraction
X	[-]	Variable
Y	[-]	Mass concentration or mass yield
z	[-]	Axial position

Greek letters

β	[kg/(m ³ ·s)]	Interphase momentum exchange coefficient
---------	--------------------------	--

Nomenclature

σ^2	[-]	Variance of RTD
σ_θ^2	[-]	Dimensionless variance of RTD
θ	[-]	Dimensionless variable
Θ_s	[m ² /s ²]	Granular temperature
ε	[-]	Porosity or volume fraction
ρ	[kg/m ³]	Density
λ	[W/(m·K)]	Effective conductivity
λ	[Pa·s]	Bulk viscosity
μ	[kg/(m·s)]	Dynamic or shear viscosity
σ	[W/(m ² ·K ⁴)]	Stefan–Boltzmann constant
ΔH	[kJ/kg]	Heat of reaction
\sum_v	[-]	Sum of the atomic volumes
η	[-]	Yield
τ	[Pa]	Stress tensor
γ_{Θ_s}	[kg/(m ³ ·s)]	Collisional dissipation of the fluctuating kinetic energy
φ	[°]	Angle of internal friction
φ_{sg} or φ_{gs}	[kg/(m ² ·s ²)]	Interphase momentum exchange due to interphase reaction or moisture evaporation
k_{Θ_s}	[kg/(m·s)]	Diffusion coefficient
ϕ_{gs}	[-]	Interphase fluctuating energy exchange coefficient
ν	[Hz]	Screw rotating frequency

Subscripts

0	Initial condition
2	The second heating stage

Nomenclature

c or char	Char
c1	Primary char
c2	Secondary char
clearance	Clearance between the flight and the shell
collision	Collisional term
convective	Convective heat transfer
direction	Parallel to and across grain direction of the biomass particle
eff	Effective parameter
energy	Energy
exp	Experimental data
external	External of the particle
f	At the end of the pyrolysis or torrefaction
feedstock	Raw biomass, dry basis
flight	Flight of the reactor
friction	Frictional term
g	Gas phase
g1	Primary non-condensable gases
g2	Secondary non-condensable gases
i,j	Species i or j
in	Energy flowing into
inert	Inert gas (N ₂)
is	Intermediate solid product
kinetic	Kinetic term
m	Mean
max	Maximum
mixture	Gas mixture

Nomenclature

mod	Model results
n	Species n
out	Energy flowing out
p	Particle
pitch	Pitch of the reactor
radiative	Radiative heat transfer
reactor	Pyrolysis reactor
residual	Solid residual
s	Solid phase or particle surface
screw	Rotating screw of the reactor
shaft	Shaft of the reactor
shell	Shell of the reactor
shrink	Particle shrinkage
solid charry product	Solid product from biomass pyrolysis
t	Tarry product
w	Virgin biomass
wall	At the shell of the screw reactor
water	Water
wave	Thermal wave

Abbreviation

BET	Brunauer–Emmett–Teller
CFD	Computational fluid dynamics
CPM	Comprehensive particle model
DEM	Discrete element method
FC	Fixed carbon

Nomenclature

FEM	Finite element method
GPC	Gel permeation chromatography
HHV	Higher heating value
ODE	ordinary differential equations
PDE	Partial differential equations
RTD	Residence time distribution
SPM	Simplified particle model
TGA	Thermal gravimetric analysis
UCM	Uniform conversion model
USCM	Unreacted-shrinking-core model
VM	Volatile matter
3D	Three-dimensional

ABSTRACT

Biomass as a renewable energy source can be converted into gas, liquid and char through pyrolysis. Char (biochar or charcoal) produced from biomass pyrolysis (particularly slow pyrolysis) has gained increasing interest for its potential applications in combustion, as soil amendment and in preparing functional carbon materials. Char production from biomass pyrolysis involves complex physical and chemical phenomena occurring at different scales (particle and reactor scale) and in multiple phases (non-condensable gases, condensable tarry vapors and solids). Computational modeling is a useful tool for simulating these complex physical and chemical phenomena. In this thesis, a multiscale modeling study was performed to investigate the coupled transport phenomena and pyrolysis reactions in producing char (and non-condensable gases as well as condensable tarry vapors at the same time) at both particle scale and reactor scale.

At the particle scale, a general kinetic scheme without considering biomass composition and a comprehensive kinetic scheme considering biomass composition (cellulose, hemicellulose and lignin) were both coupled to the transport phenomena, and three-dimensional (3D) comprehensive particle models (CPMs) were then established. While the CPM with the general kinetic scheme can describe the intraparticle transport phenomena and the production of primary and secondary char, the CPM with the comprehensive kinetic scheme considering on biomass composition can further describe the char production from the pyrolysis of different biomass species/types (e.g. hardwood and softwood). Simulation results from these CPMs were extensively compared to experimental data available in the literature, and mean deviations (MDs) between modeling results and experimental data were

31 K with respect to the intraparticle temperature, 6.0 wt.% with respect to the residual solid mass fraction, and 3.6 wt.% with respect to the final char yield, at operating temperatures ranging from 623 K to 773 K for a cylindrical wood particle with a diameter of 2 cm and a length of 10 cm. Modeling results with respect to the intraparticle conversion of tarry vapors (1.8 wt.%, 4.9 wt.% and 6.7 wt.%, feedstock dry-based) were comparable to the experimental data (4.6 wt.%, 5.3 wt.% and 7.2 wt.%, feedstock dry-based) for three wood cylinders with 8 mm in diameter and with lengths of 2 mm, 5 mm and 9 mm, respectively, at a heating rate of 30 K/min to a temperature of 873 K. These comparisons between the modeling results and experimental data demonstrated the accuracy of the models. The models were further applied to study the importance of the intraparticle secondary charring reactions due to the conversion of the primary volatiles when they are flowing out of the biomass particle. Results showed that the secondary char can account for up to 26 wt.% of the total char for wood cylinders with a diameter of 2 cm and a length of 10 cm in slow pyrolysis at atmospheric pressure. The effects of parameters, including physical properties of the biomass particle (particle size and particle shape), and process conditions (heating rate, peak temperature, pressure, and external particle concentration of reactive volatiles) on the char production, particularly on the secondary char production, were studied with the particle model. Particularly, at thermally thin pyrolysis regime (at a heating rate of 30 K/min), a critical particle size of 2.5 mm, at which the intraparticle secondary charring reactions start to be relevant, was determined with the present models.

The 3D CPM was further simplified for reducing computational time by only considering the dominant intraparticle physical and chemical phenomena in a 1D model. A space-time integral method was used in simplifying the 3D CPM, which

resulted into a simplified particle model (SPM). In this SPM, the intraparticle heat transfer was described by a group of linearized equations, which substantially reduces the model complexity compared to the partial differential equations (PDEs) in the CPM. The SPM was applied to describe the slow pyrolysis (at torrefaction conditions) of biomass. The capability of the SPM in predicting the time evolution of the residual solid mass fraction (and hence char production) was demonstrated by comparing the modeling results with the experimental data (MD of less than 3.0 wt.%, feedstock dry basis) for the pyrolysis of a cylindrical biomass particle with a diameter of 2.54 cm and a length of 15.24 cm at operating temperatures ranging from 513 K to 553 K. In addition, the SPM was found to run over 100 times faster compared to the CPM. The applicability of the SPM was further studied to address the limitations of this model. Results showed that the SPM can be applied to predict the biomass pyrolysis (at torrefaction conditions) for a centimeter-sized or larger cylindrical biomass particle with an aspect ratio larger than 3 within the temperature range of 473~573 K.

At the reactor scale, a computational fluid dynamics (CFD) model was developed based on the Eulerian-Eulerian method for a screw reactor aimed at conducting biomass pyrolysis to produce char. A comprehensive kinetic scheme considering the biomass composition (cellulose, hemicellulose and lignin) was incorporated into the CFD model. The model was validated against experimental data from literature (of a 2 kg/hr torrefaction screw reactor unit) with respect to the total solids mass holdup in the screw reactor (modeling results of 86.1 g, 65.2 g and 49.4 g versus experimental data of 109.9 g, 69.5 g and 51.4 g), the degree of fullness (modeling results of 0.20, 0.12, and 0.09 versus experimental data of 0.18, 0.13 and 0.10) and the mean solids residence time (152.4 s, 112.8 s and 84.6 s versus

experimental data of 166.7 s, 100.5 s and 77.0 s) at steady-state inside the reactor at three corresponding screw rotating frequencies of 0.243 Hz, 0.364 Hz and 0.486 Hz. Modeling results were also validated against the experimental data with respect to the steady-state axial temperature distribution in the screw reactor (MD of 12.6 K) at the operating temperature of 598 K, and the products mass yields (MDs of 7.7 wt.%, 6.2 wt.% and 1.7 wt.% for the mass yields of solid char, liquid product, and gas product, respectively) at three operating temperatures of 598 K, 623 K and 648 K. With the CFD model, the flow dynamics, residence time distribution (RTD) and back-mixing of the solid phase inside the screw reactor were further analyzed. Potential mechanisms of solids back-mixing were proposed. Simulation results showed that solids back-mixing occurred in two different ways. The first way is solids back-leakage, which is defined as particles near the bottom shell tending to leak behind the main solids stream and underneath the screw, since the solids forward transportation velocity in close proximity of the bottom shell is lower than that in the bulk of the solids. The second way is solids back-flow, which is defined as particles being flung over the shaft and falling down toward the succeeding pitch.

The CFD model was used to predict the elemental composition (C, H and O) of the solid char, which was compared against the experimental data with MDs of 1.6 wt.%, 0.9 wt.% and 2.5 wt.% for the mass fractions of C, H and O, respectively. The predicted elemental information was then used to predict the energy density (higher heating value, HHV) and the energy yield of the solid char, which was also compared against the experimental data with MDs of lower than 1.0 MJ/kg for the HHV and of lower than 9.4% for the energy yield. Simulation results indicate that the CFD-based reactor model was capable of predicting the flow dynamics of biomass particles, and

the yields (mass and energy) and the quality (in terms of HHV) of the resulting solid char in the screw reactor.

The multiscale modeling study in this thesis investigated some critical physical and chemical phenomena (e.g. quantification of intraparticle secondary charring reactions, simplification of particle model, prediction of product quality based on CFD simulation in a pyrolysis reactor) for char production during biomass pyrolysis at particle and reactor scales. The contents addressed in the thesis provide a multiscale modeling view for producing char through biomass (slow) pyrolysis. The thesis also concludes with directions for future modeling works, which should focus on the implementation of more comprehensive and accurate pyrolysis kinetic schemes provided that the detailed secondary reaction kinetics can be well established for *individual components* (hydroxyacetaldehyde, glyoxal, etc.) in the condensable pyrolysis volatiles. In the long term, the CFD-based reactor model could finally be used to guide the design, operation and scale-up of pyrolysis reactors for optimizing the production of tailor-made (i.e. with specific quality traits) chars.

SAMENVATTING

Biomassa, als een hernieuwbare bron van energie en materialen, kan omgezet worden in een gas, een vloeistof en een vast verkoolde product door middel van pyrolyse. Kool (zowel 'biochar' als houtskool) vervaardigd via pyrolyse van biomassa (voornamelijk trage pyrolyse) heeft aan belang gewonnen omwille van de mogelijke toepassingen in verbranding, als een grondverbeteraar en in de aanmaak van gefunctionaliseerde koolstofhoudende materialen. De aanmaak van kool in de pyrolyse van biomassa houdt complexe fysische en chemische fenomenen in, dewelke tegelijkertijd optreden op verschillende schaalgroottes (in de individuele biomassadeeltjes en op het niveau van de reactor) en in verschillende aggregatietoestanden (gas, vloeistof en vast). Numerieke modellen zijn een bruikbaar instrument om deze complexe fysische en chemische verschijnselen te simuleren. In deze thesis wordt een multischaal modelstudie uitgevoerd om de gekoppelde massa- en warmteoverdrachtsverschijnselen en, pyrolyse reacties tijdens de productie van kool (en niet-condenseerbare gassen alsook de condenseerbare, teerachtige dampen) te bestuderen, zowel op deeltjes- als op reactorniveau.

Met betrekking tot het deeltjesniveau, werden twee schema's voor de kinetiek van de pyrolyse reacties (één algemeen schema waarbij biomassa als een homogene component werd beschouwd, zonder verder rekening te houden met de samenstelling; en een tweede, uitgebreid schema waarbij biomassa werd opgedeeld in lignine, cellulose en hemicellulose en de afzonderlijke deelreacties van deze componenten in beschouwing werden genomen) gekoppeld aan de warmte- en massa-overdrachtsverschijnselen in een driedimensionaal (3D) uitgebreid deeltjesmodel (*complex particle model*, CPM). Hoewel het CPM met algemeen

reactieschema de overdrachtsverschijnselen in één enkel deeltje alsook de vorming van primaire en secundaire kool kon voorspellen, kon het CPM met uitgebreid reactieschema rekening houden met verschillen in samenstelling van de biomassa-bron en de koolvorming voorspellen in de pyrolyse van verschillende biomassasoorten (b.v. hard- en zachthout).

Simulatieresultaten van beide CPM's werden uitgebreid vergeleken met experimentele data die beschikbaar is in de literatuur, en de gemiddelde afwijking (*mean deviation*, MD) tussen model en experiment bedroeg 31 K voor wat de tijdsafhankelijke inwendige deeltjestemperatuur betreft, 6.0 gew.% met betrekking tot de tijdsafhankelijke residuele vaste fractie, en 3.6 gew.% voor wat de finale koolopbrengst betreft en dit binnen verwerkingstemperaturen van 623 tot 773 K. Modelresultaten voor de omzetting van teerachtige dampen binnen het één enkele deeltje (respectievelijk 1.8 gew.%; 4.9 gew.% en 6.7 gew.% - op basis van drooggewicht) waren vergelijkbaar met de experimentele data (respectievelijk 4.6 gew.%; 5.3 gew.% en 7.2 gew.% - op basis van drooggewicht) voor de trage pyrolyse van drie houten cilinders met een gelijke diameter van 8 mm maar met verschillende lengtes, van respectievelijk 2, 5 en 9 mm – en dit bij een verhittingssnelheid van 30 K/min tot een maximale verwerkingstemperatuur van 873 K.

Deze vergelijking tussen de bekomen modelresultaten en de beschikbare experimentele data toont de accuraatheid van de modellen aan. De numerieke modellen werden vervolgens aangewend om het belang van de secundaire koolvormingsreacties door de omzetting van de uit het deeltje stromende primaire pyrolysedampen, aan te tonen. Uit de resultaten bleek dat de secundaire kool tot 26 gew.% deel uitmaakt van de totale kool gevormd uit houten cilindrische deeltjes met

een diameter van 2 cm en een lengte van 10 cm in de trage pyrolyse onder atmosferische druk. De invloed van parameters, met inbegrip van de fysische eigenschappen van het biomassadeeltje (vorm en grootte) en procesomstandigheden (verhittingssnelheid, maximale verwerkingstemperatuur, druk en de externe concentratie aan reactieve pyrolysedampen) op de vorming van kool, meer specifiek op de vorming van secundaire kool, werden met het huidige 3D model bestudeerd. Specifiek kon met het model, in een regime waar de interne warmteverstand in het vaste deeltje te verwaarlozen valt, aangetoond worden dat de bijdrage van secundaire koolvormingsreacties niet langer te verwaarlozen valt vanaf een kritische partikeldiameter van 2.5 mm.

Het driedimensionale CPM model werd vervolgens vereenvoudigd met als doel de rekentijd te beperken. De vereenvoudiging werd gerealiseerd door enkel de relevante fysische en chemische verschijnselen op te nemen in het eendimensionaal model. De ruimte-tijd-integraal methode werd gebruikt om dit vereenvoudigd deeltjesmodel (*simplified particle model*, SPM) op te stellen. In dit SPM, werd de inwendige warmteoverdracht beschreven door een set van gelineariseerde vergelijkingen, dewelke het model aanzienlijk vereenvoudigen in vergelijking tot het gebruik van partiële differentiaalvergelijkingen in het CPM. Het SPM werd toegepast om trage pyrolyse van biomassa (milde condities, zoals deze in torrefactie) te beschrijven. Het vermogen van het SPM om accuraat de tijdsafhankelijke evolutie van de residuele vaste massafractie (en dus de koolfractie) te beschrijven werd getoetst aan de hand van beschikbare experimentele gegevens (met een MD van minder dan 3.0 gew.% op droge basis) van de pyrolyse van een cilindrisch biomassadeeltje met een diameter van 2.54 cm en een lengte van 15.24 cm bij verwerkingstemperaturen van 513 tot 553 K. Naast de modelaccuraatheid van het

SPM, vergde dit een rekestijd tot 100x korter dan het CPM model. De toepasbaarheid van het SPM werd eveneens bestudeerd. Resultaten toonden aan dat het SPM biomassapyrolyse van centimeter-grote of grotere biomassadeeltjes met een vormfactor gelijk aan of groter dan 3 en in een temperatuurbereik van 473 tot 573 K nauwkeurig kon voorspellen.

Op het niveau van de reactor, werd vervolgens een numeriek stromingsmodel (CFD) op basis van de Euler-Euler methode ontwikkeld voor een schroefreactor waarin biomassapyrolyse wordt uitgevoerd voor de productie van kool. Een uitgebreid reactieschema, dewelke rekening hield met de samenstelling van de biomassa (op basis van cellulose, hemicellulose en lignine) werd geïntegreerd in het CFD-model. Het model werd gevalideerd aan de hand van experimentele data uit de literatuur (specifiek van een 2 kg/u torrefactie eenheid op basis van schroefreactortechnologie). Met aanvaardbare accuraatheid voorspelde het model de vaste stofinhoud in de reactor (86.1 g, 65.2 g en 49.4 g voorspeld versus respectievelijk 109.9 g, 69.5 g en 51.4 g gemeten), de vullingsgraad van de schroef (0.20, 0.12 en 0.09 voorspeld versus respectievelijk 0.18, 0.13 en 0.10 gemeten), de gemiddelde verblijftijd van de partikels in de reactor (152.4 s, 112.8 s en 84.6 s voorspeld versus respectievelijk 166.7 s, 100.5 s en 77.0 s gemeten) bij *steady-state* omstandigheden en bij schroefsnelheden van respectievelijk 0.243 Hz, 0.364 Hz en 0.486 Hz. Model-voorspelde resultaten werden ook vergeleken met experimentele data met betrekking tot de *steady-state* axiale temperatuurverdeling (MD van 12.6 K) bij een verwerkingstemperatuur van 598 K, de koolopbrengst (MD's van 7.7 gew.%, 6.2 gew.% en 1.7 gew.% voor respectievelijk kool, vloeistof en gas) en dit bij drie verwerkingstemperaturen van 598, 623 en 648 K. Met behulp van het CFD model werd de stromingsdynamica, de verblijftijdsverdeling en terugvloei van de vaste fase

in de schroefreactor verder geanalyseerd. Kandidaat mechanismen, met inbegrip van terugvloeï van vaste deeltjes door het bewegen van deeltjes over de schroefas en het terug lekken van deeltjes met een lage transportsnelheid doorheen de ruimte tussen de onderkant van de (horizontale) schroef en de reactorwand, werden geïdentificeerd als zijnde invloed hebbende op de axiale menging en verblijftijd.

Het CFD model werd eveneens gebruikt om de elementaire samenstelling (C, H en O) van de kool te voorspellen, dewelke werd vergeleken met experimentele data. De MD's bedroegen 1.6 gew.%, 0.9 gew.% en 2.5 gew.% voor de massafracties van respectievelijk C, H en O. De model-voorspelde samenstelling werd vervolgens aangewend om de bovenste verbrandingswaarde van de kool te berekenen alsook de energieopbrengst in de kool. De MD's lagen lager dan 1.0 MJ/kg voor de bovenste verbrandingswaarde van de kool en lager dan 9.4 % voor de energieopbrengst. De modelresultaten bewijzen dat het model met voldoende accuraatheid de deeltjesstroming, pyrolyse, massa- en energieopbrengsten en, koolkwaliteit (bovenste verbrandingswaarde) kan voorspellen in schroefreactoren.

De multischaal modelering toegepast in deze thesis bestudeerde een aantal cruciale thema's (o.a. kwantificering van de secundaire koolvormingsreacties, modelvereenvoudiging, voorspelling productkwaliteit) met betrekking tot koolproductie. Daarnaast sluit de thesis af met een aantal aanbevelingen voor toekomstig modelgebaseerd onderzoek, met name de implementatie van meer uitgebreide reactieschema's in de modellen alsook het verder experimenteel afleiden van dergelijke reactieschema's, zeker met betrekking tot de secundaire reacties van individuele dampfase componenten (hydroxyacetaldehyde, glyoxal, enz...). Het ultieme doel is het komen tot betrouwbare CFD-modellen welke gebruikt kunnen worden in het ontwerp, de opschaling en het bedrijven van pyrolysereactoren voor de

productie van op maat gemaakte (tz. voldoende aan specifiek vereiste eigenschappen) kool.

CHAPTER 1

Introduction

In this chapter, a general overview on the world's energy supply will be given first. Problems related to conventional fossil energy and the advantage of biomass as a renewable energy resource will be discussed. Current utilization technologies for biomass will be reviewed. The application of pyrolysis in producing biochar and charcoal will then be discussed. Experimental and modeling studies for biomass pyrolysis aiming to produce char at biomass particle scale and at pyrolysis reactor scale will be reviewed. Finally the outline of the thesis will be given.

1. Biomass as renewable energy source

1.1 Introduction to energy

Energy is one of the most basic needs of human life and is extremely crucial in driving human development. Human civilization is largely dependent on the increasingly efficient and extensive utilization of various types of energy to extend human capabilities and ingenuity. It is always essential to provide adequate and affordable energy for improving human living standards. The growth of the world population (United Nations estimates that the world population will increase by 50 % from 7.4 billion in the year 2016 to 11.2 billion in the year 2100) has continuously driven us to develop methods of generating and utilizing energy while protecting the planet.

Various forms of energy have been employed worldwide to meet human energy needs. Conventionally, fossil fuels, including coal, crude oil and natural gas, have been the main energy resources for human requirements, and it was estimated in 2002 that 80 % of the world primary energy demand was met by fossil fuels.[1] Although fossil fuels have greatly promoted world economic development in the past two centuries, they have brought several concerns. One concern is that the world's reserves in fossil fuels are limited. By taking crude oil as an example, it is estimated that about 1000 billion barrels of oil have already been consumed and only 1000 billion barrels of proven oil reserves are left in the world.[2] Another concern is the close relationship between energy utilization and the environment. It is believed that fossil fuels have been the major source of anthropogenic CO₂ emissions, which are responsible for global warming. Coal for power generation and liquid oil products for transportation are largely responsible for severe air pollution (e.g. smog), for instance in the northern part of China.[3] In addition, fossil fuels are non-uniformly distributed

in the world, and it is estimated that about 70 % of the world's proven oil and gas reserves are concentrated in the “energy strategic ellipse”, an area stretching from the Arabian Peninsula to Western Siberia as shown in Fig. 1.1.[4] The non-uniform distribution of fossil fuels has increased concerns about energy security.



Figure 1.1 The so-called “energy strategic ellipse” for proven oil and reserves[4]

These concerns about fossil energy have driven the development of alternative or renewable energy sources that are collected from renewable resources, that are low in emissions of both greenhouse gas and air pollutants, and that are abundant and available worldwide. Renewable energy refers to the energy resources that can regenerate and can replenish themselves indefinitely. The five renewable energy sources used most often are biomass, wind, solar, hydro and geothermal. Among these renewable energy sources, biomass, including wood and woody, herbaceous, agricultural, aquatic biomass, etc. is so far the only alternative source for renewable carbon.[5] More and more research is driven towards the utilization of CO₂ in chemical reactions, which may constitute a way of generating carbon-containing compounds using energy sources other than biomass. The net CO₂ emissions from

the utilization (e.g. biofuel) of biomass are considered zero since the released CO₂ during biomass utilization can be captured during photosynthesis.[6] In addition, since most biomass has a low content of Sulphur, the combustion of biofuels has lower emissions of air pollutants (e.g. SO₂) than most fossil fuels.[7] Furthermore, biomass is abundant and widespread on the planet. Energy from biomass captured by land plants each year is estimated to be 3-4 times greater than human energy demands. The potential energy from biomass that is accessible to humans is estimated to be 1.9×10^{20} J per year, which is 35 % of the current global energy demand.[8] Consequently, increasing interest has been gained to convert biomass into renewable fuels and other value-added renewable products.[9]

1.2 Biomass utilization

Biomass can be converted into renewable fuels and products through either biochemical processes or thermochemical processes, as shown in Fig. 1.2.

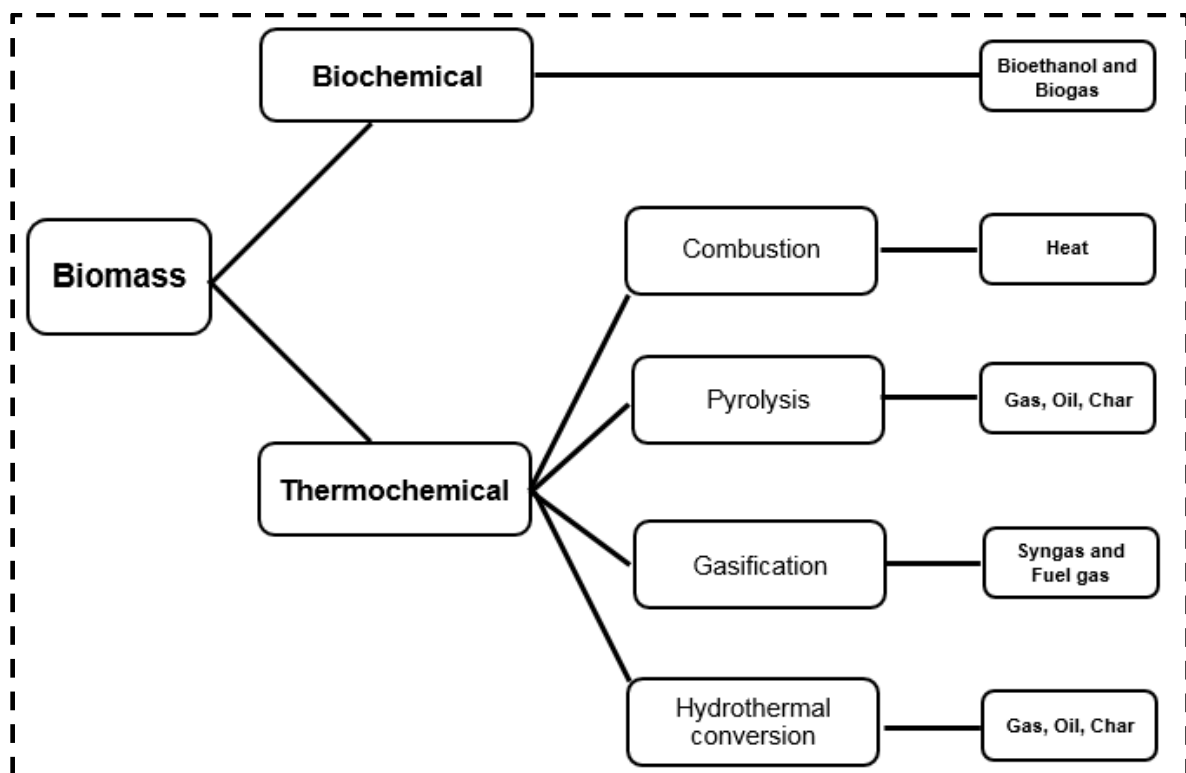


Figure 1.2 Biomass utilization through biochemical and thermochemical processes

1.2.1 Biochemical processes

Biochemical processes apply micro-organisms (yeasts, bacteria,...) or enzymes to produce – amongst others – bioethanol and biogas (for further providing energy and chemical products).[10] One benefit of biochemical processes is that they require limited input of external energy. However, biochemical conversion of biomass is a slow process. In addition, biochemical processes require hydrolytic pretreatment (thermal, acidic, alkaline or enzymatic) to separate cellulose, hemicellulose and lignin (macromolecular components of the biomass, which will be discussed later), and efforts are required for overcoming the natural resistance of plant cell walls to enzymatic and microbial deconstruction, which inevitably increases the cost of the biochemical processes.[11, 12]

1.2.2 Thermochemical processes

In contrast, thermochemical processes are usually operated at high temperatures and consequently these processes can convert biomass in a fast way at the input of external energy. Thermochemical processes include, as shown in Fig. 1.2, combustion, pyrolysis, gasification, and hydrothermal conversion (liquefaction, carbonization and gasification).

1.2.2.1 Pyrolysis versus combustion, gasification and hydrothermal conversion

Combustion is the complete oxidation process of biomass in the presence of excess oxygen to provide heat for domestic or industrial applications.[13, 14] Biomass pyrolysis is the thermal degradation of biomass in the absence or with limited supply of an oxidizing agent at temperatures ranging from 470 K to 1020 K to produce permanent gas, condensable volatiles (liquid/tar/bio-oil) and char (biochar/charcoal).[15-17] Catalytic pyrolysis of biomass[18] is also an important field

of biomass pyrolysis, but is beyond the scope of the present work and thus not discussed. Gasification of biomass is the thermal conversion of biomass in the limited presence of an external supply of an oxidizing agent, including pure oxygen, carbon dioxide, air and/or steam, to produce fuel gas and syngas (i.e. mixture of CO and H₂).[19, 20] Biomass hydrothermal conversion refers to the conversion of biomass in the liquid phase (e.g. water) aimed either to produce liquid/oil products (named hydrothermal liquefaction, at temperatures of 520~670 K and pressures of up to 20 MPa), or to produce char (named hydrothermal carbonization, at temperatures of 450~520 K and saturated pressure), or to produce gas products (named supercritical water gasification, at temperatures of about 670 K and at the critical pressure of water).[21-25]

Among these thermochemical processes, combustion is the most commonly employed technology. However, combustion of biomass can only provide heat. Gasification of biomass requires to be operated at high temperatures (around 1070 K or higher). Hydrothermal conversion of biomass requires to be operated at high pressures, as discussed above. The harsh operating conditions used for gasification and hydrothermal conversion bring challenges for the reactor design. In contrast, pyrolysis of biomass can be operated in a wide medium temperature range (from 470 K to 1020 K) usually around atmospheric pressure.[5, 15-17, 26-30] Pyrolysis of biomass can provide both energy, fuels and chemical products (gas, liquid/tar/oil, and char), and the formation of each of these products can be optimized depending on the operating conditions, which can extend the application of pyrolysis and which makes pyrolysis one of the promising thermochemical technologies to process biomass.[5, 15-17, 26-30] In addition, pyrolysis itself is also an important sub-process in other thermochemical processes (gasification and combustion).[9] The pyrolysis

products (i.e. biochar, as discussed later) can also be used for carbon sequestration and act as a sink for atmospheric CO₂, as shown in Fig. 1.3, which makes pyrolysis a potential, so-called carbon-negative technology.[31]

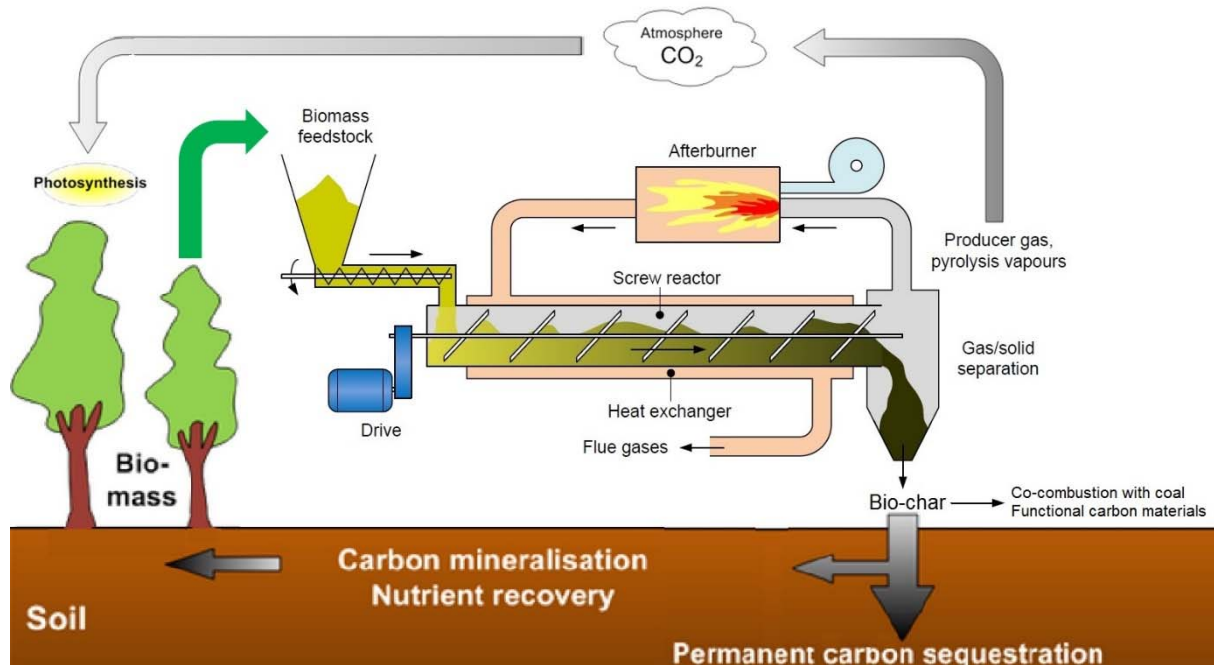


Figure 1.3 Carbon cycle in biomass pyrolysis products when combining energy production with biochar production[5]

1.2.2.2 Pyrolysis: fast pyrolysis versus slow pyrolysis

Depending on the operating conditions, distinction can be made between fast and slow pyrolysis. It should be mentioned that the terms ‘fast pyrolysis’ and ‘slow pyrolysis’ are somewhat arbitrary and the literature does not provide a universal reaction time and heating rate for each of these terms.

Fast pyrolysis is particularly designated for maximizing the yield of bio-oil (condensable volatile products) usually at a temperature of 670~870 K with a heating rate of 10³–10⁴ K/s and whereby the vapors are quenched into bio-oil within 1 to 2 seconds after their formation. [15, 30, 32] Bio-oil can be further upgraded physically, chemically and/or catalytically for downstream applications (e.g. as substitution to

fossil fuels).[15, 26] Most researches about biomass pyrolysis were focused on fast pyrolysis and bio-oil applications.[15, 26]

In contrast, slow pyrolysis is a technology targeting the production of char at a temperature of 470~1020 K with a heating rate of around or lower than 80 K/min. [5, 16, 17, 27-30] The increasingly extended applications of the char (its potential applications as solid fuels in providing heat through co-combustion with coal, as soil amendment, and in preparing functional carbon materials,[33-40] which will be discussed later) have facilitated slow pyrolysis being a promising technology for biomass conversion. Slow pyrolysis covers both carbonization or conventional slow pyrolysis and torrefaction,[5] and the typical operating conditions and product mass yields of these two slow pyrolysis processes are shown in Table 1.1.

Table 1.1 Typical operating conditions and product mass yields obtained from different types of slow pyrolysis processes. Data is based from Refs.[5, 15, 17, 41, 42]

Parameter	Carbonization	Torrefaction
Temperature	>670 K	<570 K
Heating rate	<80 K/min	~10 K/min
Reaction time	Hours ~ days	<2 h
Pressure	Atmospheric or elevated up to 1 MPa	Atmospheric
Reaction medium	Oxygen-free or oxygen limited	Oxygen-free
Liquid	30 wt.%	5 wt.%
Gas	35 wt.%	15 wt.%
Char	35 wt.%	80 wt.%

Carbonization refers to the conventional slow pyrolysis of biomass aiming to produce a highly carbonaceous, charcoal-like material. Carbonization has been applied to produce charcoal from woody biomass since long in history.[5]

In contrast, torrefaction, also named mild pyrolysis, is a thermal pretreatment method of biomass for the purpose of upgrading biomass.[17, 41] Torrefaction of biomass aims to produce a char (also named torrefied biomass) that has a number of advantages over its parent biomass, e.g. lower moisture content, higher energy density (as measured by lower, or higher heating value, LHV or HHV), and improved grindability (as measured by the grinding energy per unit heating value).[17, 41]

2. Biochar and charcoal

2.1 Definition

In this work, the char is a general term describing any solid product obtained from the thermochemical conversion of biomass. Both biochar and charcoal are the solid products from the thermochemical conversion of biomass. The terms “biochar” and “charcoal” are used only to distinguish among the intended applications of the char. The term “biochar” is used when the char is used as a soil amendment while the term “charcoal” is applied when the char is meant to be a solid fuel or as a reductant in metallurgical smelting applications.[5] The char for other applications, which will be described later, may have specific names in the literature. In general, the term biochar is used to designate any char made for an application in which the carbon in the char is not (rapidly) oxidized. All types of char, regardless of their different applications, are produced in a similar way, and they have some common properties, which will be described later. To avoid confusion, a universal term “char” will be used in this thesis to describe the solid product from the thermochemical conversion of biomass.

2.2 Applications

Traditionally, the char from biomass has been used as solid fuel (hence called charcoal) for a long time in human history. Even today, it is still an important smokeless solid fuel in developing countries. It is estimated that 30 million metric tons of charcoal are produced each year in African countries.[43] In addition, it is still frequently used as a valuable reductant for smelting and sintering processes in metallurgical industries.[5]

In addition to its conventional applications as solid fuel and reductant, the char from biomass has found its potential applications in a broader range (soil amendment, functional carbon material, catalysis, etc.) with the development of human technology. For instance, the char from biomass has received increasing attention for its potential application as soil amendment (hence called biochar) that can mitigate greenhouse gas emissions and improve soil health.[33] The idea of adding the char from biomass to soil for improving soil fertility was inspired by the ancient agricultural activities that created *terra preta* soils (black soil).[44] These soils occupy up to 10 % of Amazonia[45] and are characterized by higher levels of soil fertility than other soils without the historic addition of biochar.[44] Furthermore, biochar can increase the capacity of soil in retaining water, which makes biochar promising in dealing with climate uncertainty.[44]

Other applications of char from biomass are briefly described here. The char with high electrical conductivity, porosity and stability has been proposed as a sustainable electrode material in microbial fuel cells.[46] The char with high content of structural bound oxygen groups can be used as fuels for the direct carbon fuel cell.[47] Materials prepared from the char have been proposed for environmental protection and energy storage.[48] By tuning the surface functionalities of the char through oxidation, sulfonation, amination, and recombination, valuable functional

carbon materials can be produced.[38] In addition, the char can be applied as catalyst for removing the detrimental tarry vapors during biomass gasification.[49]

2.3 Physicochemical properties

Char from biomass can be characterized both by its physical properties and by its chemical properties. Physical properties include specific surface area, morphology, etc.. Chemical properties mainly refer to proximate (moisture, ash, volatile matter and fixed carbon) and ultimate analyses (elemental composition including C, H, O, N and S), and energy density (higher heating value, HHV).[17, 33]

Experimental techniques based on Brunauer–Emmett–Teller (BET) theory are usually applied to measure the specific surface area of the char. It was reported that the char from woody biomass pyrolysis at a reaction temperature ranging from 470 to 970 K had corresponding BET surface areas ranging from 10 to 500 m²/g,[50] which requires to be increased through an activation step to allow for certain of its further applications (i.e. as activated carbon).[5] Other experimental techniques to characterize the char include Fourier transform infrared (FT-IR), Raman spectroscopy, etc., which are beyond the scope of this work.

As a renewable solid fuel, the char is largely different from its parent biomass with respect to contents of ash, volatile matter (VM) and fixed carbon (FC), energy density (HHV), and elemental composition (mainly C, H and O). Table 1.2 compares some chemical properties of biomass, char and coal. This table shows that the char has reduced volatile matter content, increased fixed carbon content and increased energy density compared to the raw parent biomass. In addition, this table shows that the energy density of the char is comparable to coal, which makes the char a promising solid fuel in replacing coal. With the increase of the reaction severity (e.g.

longer pyrolysis time and/or higher pyrolysis temperature) during biomass conversion, higher contents of fixed carbon and lower contents of volatile matter can be expected in the char, as shown in Fig. 1.4. However, these compositional changes under more severe reaction conditions are also met by lower char yields.

Table 1.2 Volatile matter (VM), fixed carbon (FC), and higher heating value (HHV) of raw biomass, char from biomass and coal[17]

Material	VM (wt.%)	FC (wt.%)	HHV (MJ/kg)
Raw biomass	67-88	0.5-20	15-20
Char from biomass pyrolysis	34-55	13-45	16-29
Coal	0.5-50	46-92	25-35

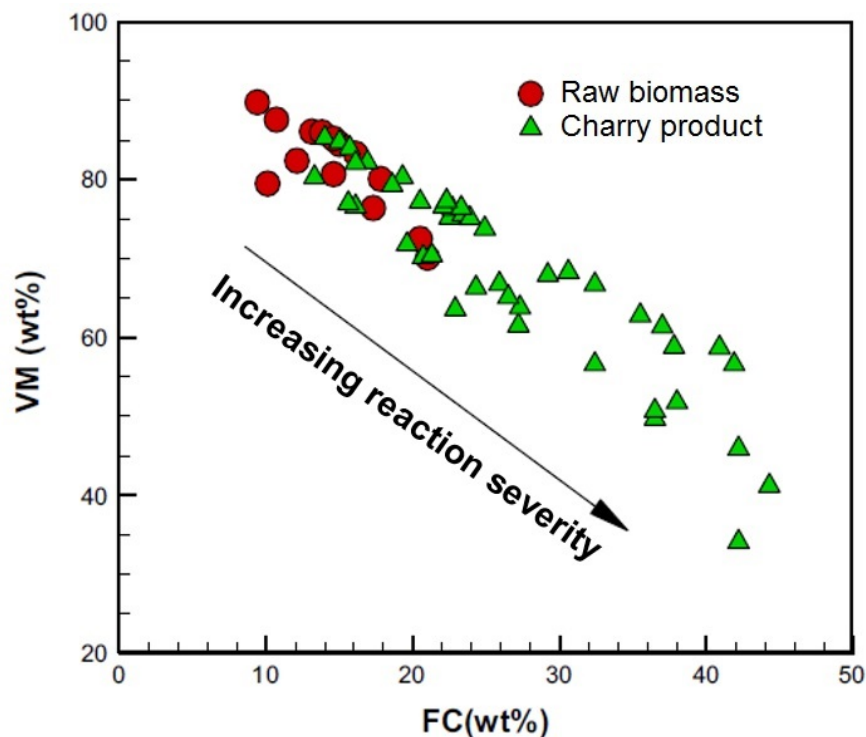


Figure 1.4 Fixed carbon (FC) versus volatile matter (VM) in chars under varying reaction severity, adapted from Chen et al.[17]

Ultimate analysis quantifies the elemental composition in both the raw biomass and the char. Biomass mainly contains C, O and H in decreasing order of abundance

(weight fraction) and other elements in much lower amounts (N, S, Ca, K, Si, etc.).[7] Biomass feedstock (dry basis) has an atomic O/C ratio of 0.4-0.8, and an atomic H/C ratio of 1.2-2.0, as shown in Fig. 1.5. During pyrolysis, with the devolatilization of biomass, carbon tends to concentrate into the char while hydrogen and oxygen tend to evolve into gas and liquid product. As a result, the char has a higher carbon content. Fig. 1.5 shows the relationship between the atomic ratio of O/C and the atomic ratio of H/C, in the so-called “van Krevelen” diagram, for various carbon-containing materials. This figure shows that the char (charcoal) has lower atomic ratios of H/C and O/C than the raw biomass, indicating that the char has a higher carbon-content than the raw biomass. The enrichment of carbon in the char can substantially increase the energy density of the char compared to its parent biomass.[34] The close relationship between the elemental composition and the energy density (HHV) of the char also indicates that the accurate prediction of the elemental composition (mainly C, H and O) would allow for the prediction of the energy density of the char.

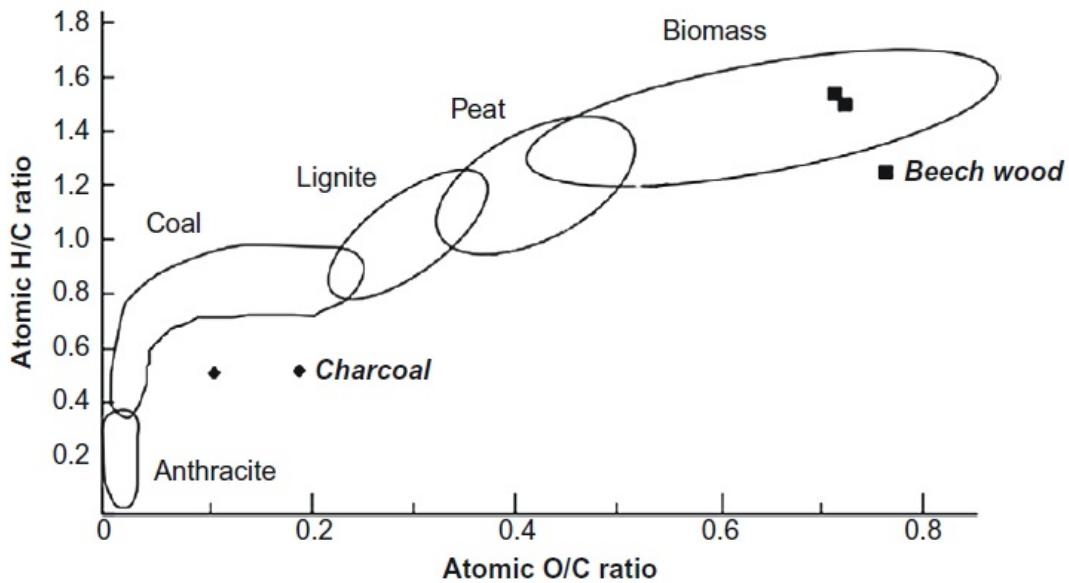


Figure 1.5 The van Krevelen diagram for various materials, adapted from van der Stelt et al. (2011).[41]

2.4 Production

All thermochemical conversion processes of biomass, except combustion can produce char. Table 1.3 lists some of the typical thermochemical processes and their char yields. Among these thermochemical processes, slow pyrolysis (covering carbonization and torrefaction, as discussed in Section 1.2.2.2) is characterized by lower heating rates (up to, but often much lower than 100 °C/min) that incur maximum yields in char, and therefore it is a suitable technology for char production.[5, 29]

Table 1.3 Typical reaction conditions and char yields for various thermochemical processes of biomass

Thermochemical process	Temperature (K)	Residence time, (s/min/h/days)	Yield of char (wt.%)	References
Slow pyrolysis	470~1020	Min to days	20~80	[5, 15, 17, 28-30, 41, 42]
Fast pyrolysis	670~870	Few seconds	10~20	[15, 30, 32]
Gasification	1070~1270	5~20 s	10	[51, 52]
Hydrothermal carbonization	450~520	1~12 h	30~60	[21, 22, 53]

2.5 Physical and chemical phenomena occurring during biomass pyrolysis for char production

The production of char from slow pyrolysis involves multiscale/level multiphase phenomena.[9] From a broad point of view, the multiscale/level phenomena include the atomic and molecular level of intrinsic chemical pyrolysis reactions, the particle level with the influence of intraparticle transport phenomena, the reactor level with the influence of hydrodynamics and mass and heat transfer, the industrial plant level with the effect of upstream and downstream operations, and the ecological system with the effect of ecological conditions. “Multiphase” refers to the gas phase (inert gas being N₂ and non-condensable gas product), the liquid phase (condensable liquid/tar/bio-oil product) and the solid phase (virgin biomass and char) simultaneously present in the system. The in-depth understanding of these multiscale and multiphase phenomena is critical in optimizing the production of char.

Specifically, the following will briefly introduce the char production from biomass slow pyrolysis covering the particle and the reactor scale (phenomena at other scales, e.g. atomic and molecular scale, industrial plant scale, and ecological system scale, as discussed above, are beyond the scope of this thesis).

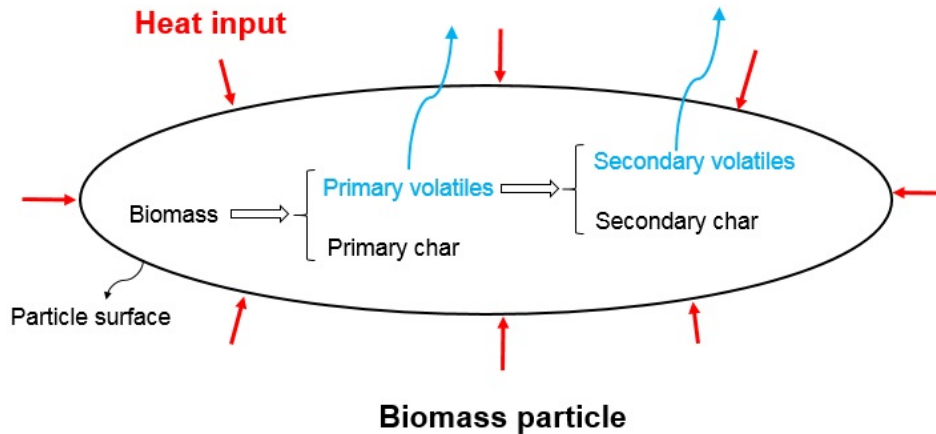


Figure 1.6 Physical and chemical phenomena occurring during biomass pyrolysis at the particle scale

At the particle scale, physical and chemical phenomena occur in the following sequences driven by the heat input at the particle surface, as shown in Fig. 1.6. First, heat is transferred into the particle from the particle surface, as a result of which the particle (from external part to internal part) is heated, which drives the evaporation of moisture (for wet biomass particle). The dried biomass particle finally heats up to the temperature at which pyrolysis reactions occur to form primary char and primary volatiles. While the primary char is left inside the particle, the primary volatiles flow out of the particle. During the outflow, the primary volatiles (usually the reactive components in primary volatiles) can undergo secondary reactions through homogeneous cracking (usually at temperatures higher than 870 K [20, 54]) and heterogeneous reactions (by interacting with the mixture of solid biomass and char at relatively lower temperatures of around 670 K [55]), which produce secondary char and secondary volatiles. At the reactor scale, the coupled transport phenomena and pyrolysis reactions occur in a much more complex way and are influenced by many factors, which will be described later. In the reactor, the long reaction process for slow pyrolysis will provide enough opportunity for the primary volatiles to interact with

the solid mixture of biomass and char, which promotes the production of secondary char. Therefore, at both particle scale and reactor scale, the char during the slow pyrolysis is a mixture of primary and secondary char. It should be mentioned that the production of secondary char through the homogeneous and heterogeneous conversions of the primary volatiles (named secondary charring reactions) is dependent on the biomass species, physical properties of the biomass particle (e.g. size and shape) and the operating conditions (e.g. heating rate, temperature, pressure and vapor residence time), which will be discussed later.

3. Pyrolysis kinetics

Mathematical description of the pyrolysis kinetics coupled with the transport phenomena at particle scale and at reactor scale results into advanced computational models for predicting biomass pyrolysis at particle scale and at reactor scale. The pyrolysis reaction kinetics were proposed by researchers to describe the mass loss process of the virgin biomass and to describe the formation process of char and volatiles. In this part, the properties of the feedstock (biomass) will be first discussed, and then various kinetic schemes proposed in previous literature reports will be dealt with.

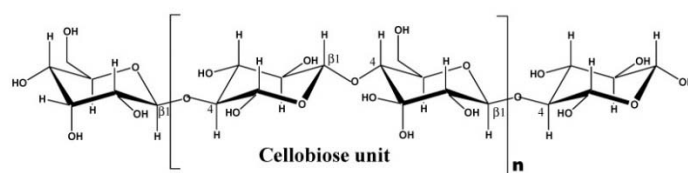
3.1 Feedstock characterization

Lignocellulosic biomass, regardless of its origin, is generally a complex mixture of organic matter and, in lower amounts, inorganic matter (salts or minerals) and water (bound or hygroscopic water and free or capillary water).[7] In biomass, the organic matter refers to the macromolecular substances, including cellulose, hemicellulose, lignin and, to a lesser extent, extractives, with cellulose accounting for

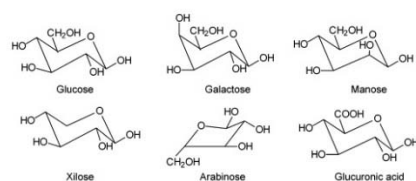
40-44 wt.%, hemicellulose for 25-30 wt.%, and lignin for 18-35 wt.% depending on the type (hardwood or softwood) of the dry biomass.[56]

The typical chemical structures of cellulose, hemicellulose and lignin are shown in Fig. 1.7. As shown in this figure, cellulose is composed of a long (degree of polymerization, DP, up to 10000), linear polymer of glucose. On the other hand, hemicellulose is a mixture of various polymerized monosaccharides (glucose, mannose, galactose, xylose, arabinose, etc.), exhibits a low degree of polymerization (DP ~ 200) and is a branched polymer. Finally, lignin is a complex polymer made of aromatic (phenolic) structures.

(1) Cellulose



(2) Hemicellulose



(3) Lignin

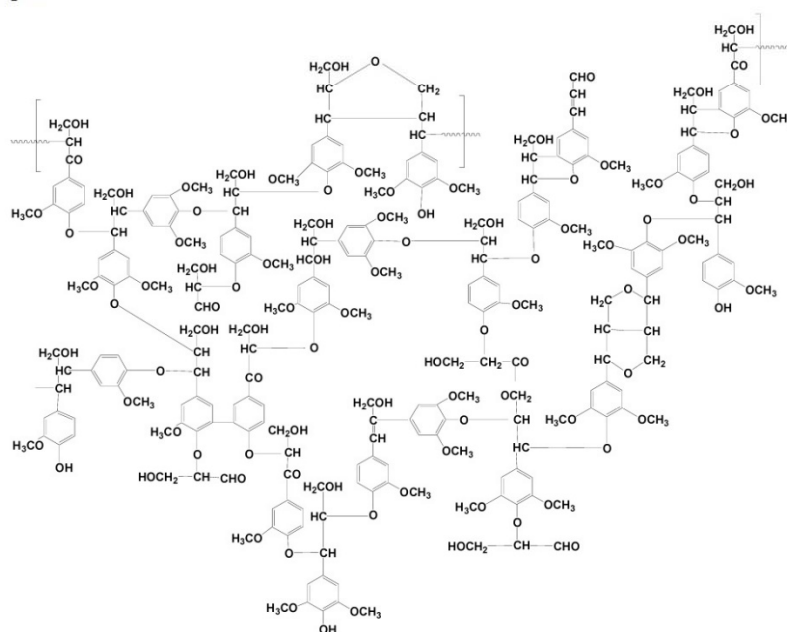


Figure 1.7 *Chemical structures of cellulose, hemicellulose and lignin*[16]

The pyrolysis of biomass mainly refers to the thermal conversion of cellulose, hemicellulose, and lignin. Therefore, chars as well as volatile products are a complex mixture of primary char and volatiles, respectively, from the individual conversions of these macromolecular components and secondary char and volatiles (respectively) from the homogeneous and heterogeneous conversions of the primary volatiles.[9, 16]

The pyrolysis of hemicellulose and cellulose is faster with lower yields of char compared to the pyrolysis of lignin.[57] At atmospheric pressure, hemicellulose mainly decomposes at temperatures of 490~590 K with char yields ranging from 15 wt.% to about 40 wt.%, while cellulose pyrolysis occurs at 590~670 K with char yields of 3.3-11.3 wt.% depending on the crystallinity of the cellulose.[36, 58-63] The pyrolysis of lignin at atmospheric pressure occurs at a wide temperature range of 430~1170 K with a higher char yield (~40 wt.%) compared to the pyrolysis of cellulose and hemicellulose.[57] The higher char yield from lignin is mainly due to the fact that lignin is full of aromatic structures, as shown in Fig. 1.7, which can be easily to repolymerize into char. In addition, lignin already has a higher carbon fraction compared to cellulose and hemicellulose. The mass fraction of carbon in lignin is over 60 wt.% (e.g. one typical composition of lignin $C_{15}H_{14}O_4$ with a carbon content of 70 wt.%), while in cellulose it is about 44 wt.% ($C_6H_{10}O_5$) and in hemicellulose it is about 45 wt.% (e.g. $C_5H_8O_4$). Therefore, biomass with higher content of lignin normally results in higher char yields during pyrolysis.

3.2 Reaction kinetics

Pyrolysis kinetics for biomass have been extensively investigated, and various kinetic models/schemes have been proposed.[9, 64-66] The names of these models vary in literature. However, these kinetic models have the similar objective to describe the evolution of the residual solid mass and the product distribution during biomass pyrolysis.

3.2.1 Global kinetic model

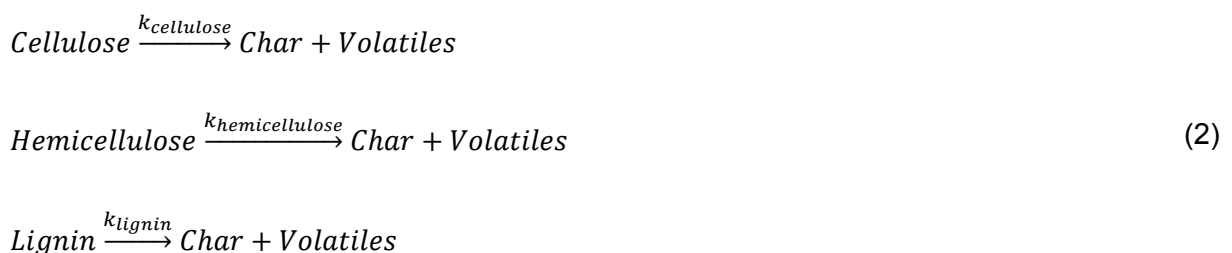
The simplest kinetic model for describing biomass pyrolysis is the global kinetic model, as shown in Eq. 1.



Where $k_{biomass}$ (s^{-1}) is the reaction rate constant.

In this kinetic model, the formation rates of char and volatiles are assumed to be the same. It was reported that the activation energy for this kinetic model ranges from 88 to 174 kJ/mol depending on the operating conditions, the experimental techniques, and the mathematical calculation methods used in processing the experimental data.[17]

By neglecting the interactions among the components of biomass (cellulose, hemicellulose and lignin), the mass loss process of biomass can also be predicted by the sum of the mass losses of the individual components using the component-based global kinetic, as described in Eq. (2).



Where $k_{cellulose}$, $k_{hemicellulose}$, k_{lignin} are the corresponding reaction rate constants for the global conversion of individual components.

The benefit of the global kinetic model is that it is simple to use in predicting the mass loss process of biomass during pyrolysis. However, as this model assumes the same formation rates for char and for volatiles, it cannot predict the different product distributions for individual biomass components at different heating conditions (e.g. lower char yields at higher temperatures).

3.2.2 One-component competitive model

In this model, biomass feedstock is regarded as a single component while products from biomass pyrolysis are lumped into gas, tar and char. These products are formed through competitive reactions with formation rates depending on their corresponding kinetic parameters. Secondary reactions of tar are usually considered in this kinetic model. Fig. 1.8 shows a typical one-component competitive kinetic model considering secondary reactions for pyrolysis of dry biomass.

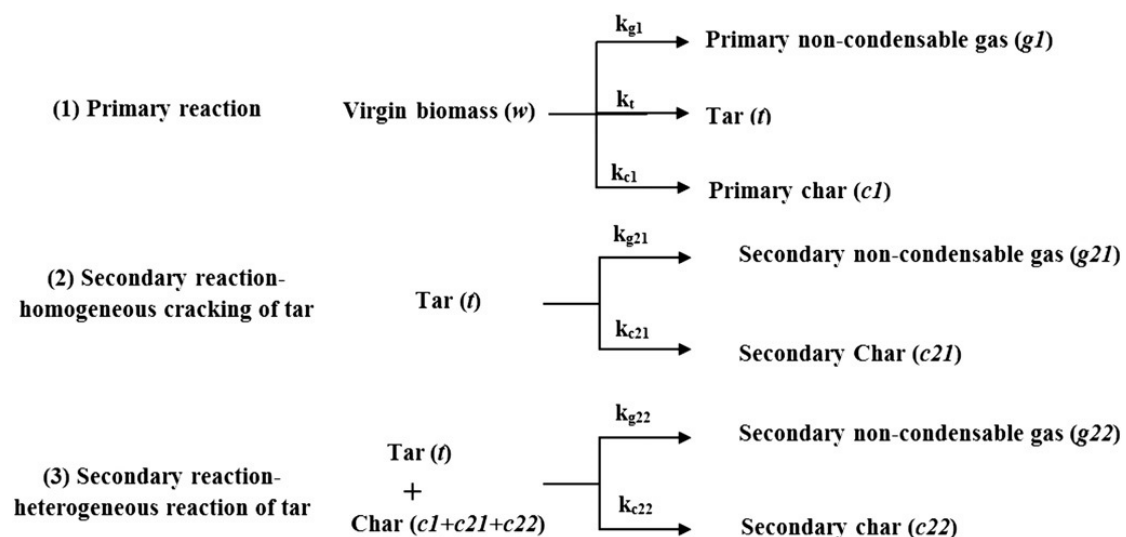


Figure 1.8 One-component competitive kinetic model considering secondary reactions for biomass pyrolysis [67]

The benefit of this model is that it allows to predict product distributions at different operating conditions (temperature, heating rate, residence time, pressure, etc.).[67] The limitation of this model is that it does not distinguish between the different components of biomass (cellulose, hemicellulose and lignin) and therefore it cannot account for changes in biomass composition. However, it is possible to apply this kinetic model to describe the pyrolysis of different biomass species (e.g. hardwood and softwood, as described in Section 3.1) on the condition that the kinetic parameters of this kinetic model have been correspondingly fitted for a specific biomass species. In other words, this kinetic model would have different kinetic parameters for describing the pyrolysis of different biomass species, and the kinetic parameters resulting from a fit to this kinetic model are only valid for the specific biomass species that these kinetic parameters have been tested with.

3.2.3 Multi-component competitive model

This model describes the detailed reactions of individual biomass components usually by assuming that the interactions in the decomposition of cellulose, hemicellulose and lignin are negligible. The detailed mechanistic pyrolysis scheme based on biomass pseudo-components (cellulose, hemicellulose, carbon-rich lignin, oxygen-rich lignin and hydrogen-rich lignin) originally proposed by Ranzi et al.[68] is considered to be one of the most promising kinetic schemes. In this kinetic scheme, as shown in Table 1.4, the overall conversion in biomass pyrolysis is regarded as the sum of the individual contributions of these biomass pseudo-components. Table 1.5 shows the detailed information about the components in Table 1.4.

This reaction scheme uses representative species to describe the composition of char and volatiles. Debiagi et al.,[69] Calonaci et al.,[70] and Corbetta et al.,[71] performed further adaptation of the original scheme of Ranzi et al.[68] The adaptation

of this scheme proposed by Anca-Couce et al.[72, 73] further considered the secondary charring reaction.

Although complex, the multi-component competitive scheme originally proposed by Ranzi et al.[68] and its adaptations[69-73] include elemental information (C, H and O), which allows to predict the elemental composition of the char and to estimate the quality (e.g. higher heating value, or HHV) of the char based on some appropriate correlations (e.g. the HHV correlation as a function of the product elemental composition from Sheng and Azevedo[74]). In addition, this multi-component competitive kinetic model can also be used to describe the different pyrolysis behaviors for different biomass species (e.g. hardwood and softwood),[72, 73] which extends this model to broader applications than the global kinetic model and the one-component competitive kinetic model.

Table 1.4 Detailed multi-component competitive model for pyrolysis of individual biomass components from Ranzi et al.[68]

Reaction number	Reaction	Kinetic constant [1/s] (Activation energy in J/mol)
R1	CELL→CELLA	$8 \times 10^{13} \exp(-192000/RT)$
R2	CELLA→0.95HAA+0.25GLYOX+0.2CH ₃ CHO+0.2C ₃ H ₆ O+0.25HMFU+0.2CO ₂ +0.15CO+0.1CH ₄ +0.9H ₂ O+0.65Char	$1 \times 10^{10} \exp(-126000/RT)$
R3	CELLA→LVG	$4 \times T \exp(-41800/RT)$
R4	CELL→5H ₂ O+6Char	$8 \times 10^7 \exp(-134000/RT)$
R5	HCE→0.4HCE1+0.6HCE2	$1 \times 10^{10} \exp(-130000/RT)$
R6	HCE1→2.5 H ₂ +0.125H ₂ O+CO+ CO ₂ +0.5CH ₂ O+0.25CH ₃ OH+0.125ETOH+2Char	$3 \times 10^9 \exp(-113000/RT)$
R7	HCE1→XYL	$3 \times T \exp(-46000/RT)$
R8	HCE2→1.5H ₂ +0.125H ₂ O+0.2CO ₂ +0.7CH ₂ O+0.25C ₃ H ₇ OH+0.125ETOH+0.8 G[CO ₂]+ 0.8 [COH ₂] +2Char	$1 \times 10^{10} \exp(-138000/RT)$
R9	LIGC→0.35LIGCC+0.1pCOUMARYL+0.08PHENOL+1.49H ₂ +H ₂ O+1.32G[COH ₂]+7.05Char	$4 \times 10^{15} \exp(-203000/RT)$
R10	LIGH→LIGOH+C ₃ H ₆ O	$2 \times 10^{13} \exp(-157000/RT)$
R11	LIGO→LIGOH+ CO ₂	$1 \times 10^9 \exp(-107000/RT)$

R12	LIGCC→0.3pCOUMARYL+0.2PHENOL+0.35 C ₃ H ₄ O ₂ +1.2 H ₂ +0.7H ₂ O+0.25CH ₄ +0.25C ₂ H ₄ +1.3G[COH ₂]+0.5G[CO]+7.5Char	5×10 ⁶ exp(-132000/RT)
R13	LIGOH→LIG+0.5H ₂ +H ₂ O+CH ₃ OH+1.0G[CO] +1.5G[COH ₂]+5Char	1×10 ¹³ exp(-207000/RT)
R14	LIG→FE2MACR	8×10 ¹ ×T exp(-50000/RT)
R15	LIG→0.7 H ₂ +H ₂ O+0.2CH ₂ O+0.5CO+0.4 CH ₃ OH+0.2 CH ₃ CHO +0.2 C ₃ H ₆ O ₂ +0.4 CH ₄ +0.5C ₂ H ₄ +G{CO}+0.5G[COH ₂]+6Char	1.2 ×10 ⁹ exp(-126000/RT)
R16	G[CO ₂]→CO ₂	1×10 ⁵ exp(-100000/RT)
R17	G[CO]→CO	1×10 ¹³ exp(-209000/RT)
R18	G[COH ₂]→CO+H ₂	5×10 ¹¹ exp(-272000/RT)

Table 1.5 The list of components in the kinetic scheme (Table 1.4) from Ranzi et al. [68])

Abbreviation	Molecular name	Atomic composition
Reactant		
CELL	Cellulose	C ₆ H ₁₀ O ₅
HCE	Hemicellulose	C ₅ H ₈ O ₄
LIG-C	Carbon-rich lignin	C ₁₅ H ₁₄ O ₄
LIG-H	Hydrogen-rich lignin	C ₂₂ H ₂₈ O ₉
LIG-O	Oxygen-rich lignin	C ₂₀ H ₂₂ O ₁₀
Solid product		
CELLA	Activated cellulose	C ₆ H ₁₀ O ₅
HCE1	Activated hemicellulose 1	C ₅ H ₈ O ₄
HCE2	Activated hemicellulose 2	C ₅ H ₈ O ₄
LIGCC	Carbon-rich lignin 2	C ₁₅ H ₁₄ O ₄
LIG	Lignin	C ₁₁ H ₁₂ O ₄
LIGOH	OH-rich lignin	C ₁₉ H ₂₂ O ₈
G[CO ₂]	Trapped CO ₂	CO ₂
G[CO]	Trapped CO	CO
G[COH ₂]	Trapped COH ₂	CH ₂ O
Char	Char	C
Volatile products		
<i>Condensable volatiles</i>		
HAA	Hydroxyacetaldehyde	C ₂ H ₄ O ₂
GLYOX	Glyoxal	C ₂ H ₂ O ₂
C ₃ H ₆ O	Propanal (acetone)	C ₃ H ₆ O
C ₃ H ₄ O ₂	Propanedial	C ₃ H ₄ O ₂
HMFU	5-Hydroxymethylfurfural	C ₆ H ₆ O ₃
LVG	Levogluconan	C ₆ H ₁₀ O ₅
XYL	Xylose monomer	C ₅ H ₈ O ₄
pCOUMARYL	Paracoumaryl alcohol	C ₉ H ₁₀ O ₂
PHENOL	Phenol	C ₆ H ₆ O
FE2MACR	Sinapaldehyde	C ₁₁ H ₁₂ O ₄
CH ₂ O	Formaldehyde	CH ₂ O
CH ₃ OH	Methanol	CH ₄ O
CH ₃ CHO	Acetaldehyde	C ₂ H ₄ O
ETOH	Ethanol	C ₂ H ₆ O
H ₂ O	Water vapor	H ₂ O
<i>Non-condensable volatiles</i>		
H ₂	Hydrogen	H ₂
CO	Carbon monoxide	CO

CO ₂	Carbon dioxide	CO ₂
CH ₄	Methane	CH ₄
C ₂ H ₄	Ethylene	C ₂ H ₄

3.2.4 Other kinetic models

There are also other kinetic models, including the distributed activation energy (DAE) model, the chemical percolation devolatilization (CPD) model, etc.[64, 75]

In the DAE model, biomass pyrolysis is described by a large number of independent parallel reactions (assumed to be first-order or n^{th} -order). These reactions are assumed to have different activation energies that can be represented by a continuous distribution function (e.g. Gaussian distribution function) to reflect variations in the bond strengths of species.[75]

The CPD model, which was originally proposed to describe coal pyrolysis,[76] has been extended to describe biomass pyrolysis.[77] In this model, parallel and competitive reactions are assumed to happen considering a chain structure for the biomass.[77]

Both DAE model and CPD models can be used to describe the evolution of the residual solid mass fraction during biomass pyrolysis and to predict product yields. However, it is difficult to use these two models to predict the detailed elemental composition (C, H and O) of the pyrolysis products.

4. Experimental study of biomass pyrolysis for char production

As discussed in Section 2.4, char production from biomass pyrolysis involves coupled multiscale and multiphase transport phenomena and chemical reactions. Plenty of experimental studies have been performed to understand the transport phenomena and chemical reactions of biomass pyrolysis occurring at particle scale and reactor scale. In this part, the particle scale and reactor scale experimental

studies are first discussed, and then the experimental results with respect to parameters that can affect char production in biomass pyrolysis will follow.

4.1 Particle scale experiments

As discussed in Section 2.4, the char from biomass pyrolysis is potentially a mixture of primary and secondary char at the particle scale. The importance of secondary char production through intraparticle homogeneous and heterogeneous conversion of primary volatiles (named intraparticle secondary charring reactions), despite being known for long, has not been well understood.[9]

Particle scale experimental studies indicated that the intraparticle secondary charring reactions can influence both the product yields and the reaction enthalpy. [55, 78-80]

Zobel and Anca-Couce[78] conducted experiments for the slow pyrolysis of dry spherical beech wood particles with a diameter of 25 mm at a heating rate of 18 K/min to a temperature of 770 K. They found that the intraparticle secondary reactions can promote the production of char and are responsible for the exothermic global heat of reaction.

Pattanotai et al.[55] experimentally compared the pyrolysis of wood sawdust (particle size < 1 mm) and wood cylinders (8 mm in diameter and 9 mm in length) at a heating rate of 30 K/min. They found that the char yield was higher and the tar yield was lower for the wood cylinder compared to the wood sawdust (Fig. 1.9), which, as they concluded, was due to the intraparticle heterogeneous conversion of tarry vapors (or intraparticle secondary charring reactions) at temperatures ranging from 670 to 770 K.

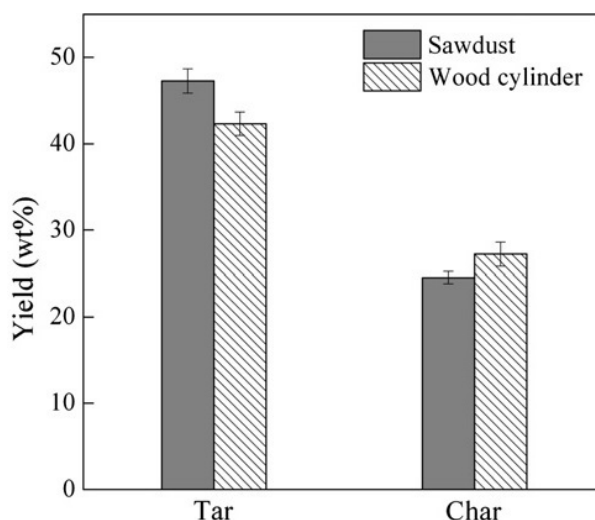


Figure 1.9 Total tar and char yields for the pyrolysis of sawdust (particle size < 1 mm) and wood cylinders (8 mm in diameter and 9 mm in length) at a heating rate of 30 K/min to a temperature of 873 K. [55]

Depending on the operating conditions and the types of raw biomass, some experimental studies reported that char could be exclusively a secondary product resulting from the conversion of tarry vapors for the pyrolysis of pure cellulose particles (one macromolecular component of biomass).[79]

Sadhukhan et al.[81] performed experiments to study the pyrolysis of a spherical wood particle (with a diameter of 20 mm) and a cylindrical wood particle (with a diameter of 20 mm and length of 100 mm) at the reaction/operating temperature of 593 K. They observed a temperature peak (higher than the reaction/operating temperature), as shown in Fig. 1.10, at the center of these two particles during their pyrolysis, which was due to exothermic intraparticle secondary charring reactions, as they concluded. Similar findings with respect to the exothermicity of the intraparticle secondary charring reactions were also reported by Ahuja et al.[80] and by Koufopoulos et al.[82] The extent to which the exothermicity of the secondary charring reactions can influence the overall reaction enthalpy, resulting from both

primary pyrolysis reactions and secondary charring reactions, is dependent on operating conditions and biomass properties (e.g. biomass species, particle size, etc.).[81, 83]

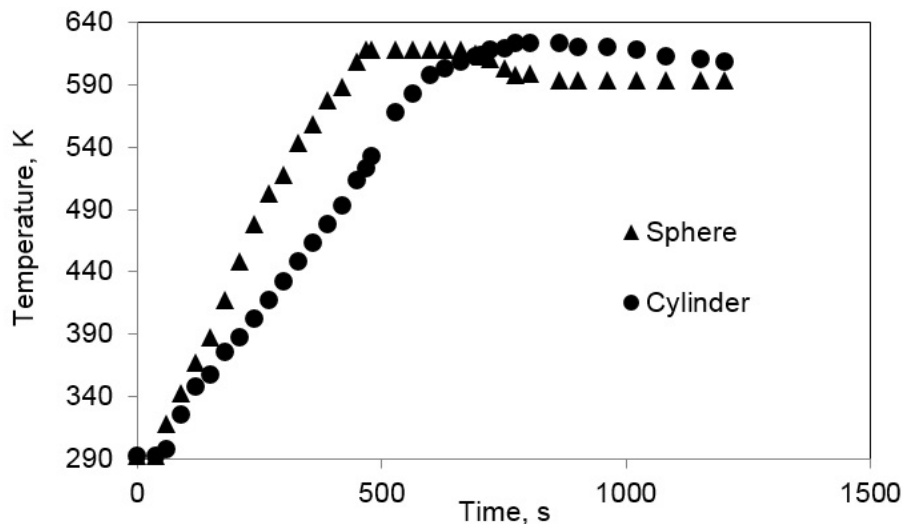


Figure 1.10 Temperature at the center of a spherical wood particle (with a diameter of 20 mm) and a cylindrical wood particle (with a diameter of 20 mm and length of 100 mm) during their pyrolysis at the reaction/operating temperature of 593 K, adapted from Sadhukhan et al.[80]

4.2 Reactor scale experiments

Various reactors, including batch reactors (traditional pit and mound kilns, steel and brick kilns, and retorts) and continuous reactors (multiple-hearth kilns, rotary kilns and screw reactors), have been used for char production.[5] The screw reactor, which is shown in Fig. 1.3, is one of the promising reactors that can continuously produce char from slow pyrolysis of biomass. In the screw reactor, biomass is transported through a heated zone by means of either a single rotating screw or two counter-rotating screws or multiple rotating screws. Driven by mechanical force, the screw reactor is advantageous in processing biomass particles with various shapes, sizes and morphological characteristics (e.g. from fine sawdust, to lumpy, sticky and

fibrous biomass particles).[5] The screw reactor for char production also has its limitations. It was reported that a single screw reactor is only limited to a processing capacity of a few tons per hour, beyond which the screw reactor may be too large to withstand the high temperatures without considerable deformation.[84]

Some studies have focused on the volumetric throughput in a screw reactor. It was reported that the volumetric throughput is theoretically influenced by the reactor geometry, the rotating speed and the filling degree (the bulk volume fraction of solids inside the screw reactor), as shown in the following theoretical equation,[85, 86]

$$G = \alpha \frac{\pi}{4} ((D_{screw} + 2L_{clearance})^2 - D_{shaft}^2) (L_{pitch} - L_{flight}) n \times 60 \quad (3)$$

Where G is the volumetric throughput (m^3/h), α is the filling degree, D_{screw} is the screw diameter (m), $L_{clearance}$ is the clearance between the screw and the shell (m), D_{shaft} is the shaft diameter (m), L_{pitch} is the screw pitch length (m), L_{flight} is the flight thickness (m), and n is the screw rotational speed (rpm). A typical geometry and the dimensions of the screw reactor is shown in Fig. 5.1 in Chapter 5.

As can be seen from Eq. (3), for a certain geometry at a constant filling degree, the volumetric throughput of the screw reactor increases with the increase of the screw rotational speed. However, the filling degree is actually influenced by both the material properties and the screw rotational speed. For the case in which the feed rate at the inlet of the screw reactor cannot match the potential conveying capacity, a reduction of filling degree occurs. The net result would be that the volumetric throughput of the screw reactor reaches a limiting value, as illustrated in Fig. 1.11.

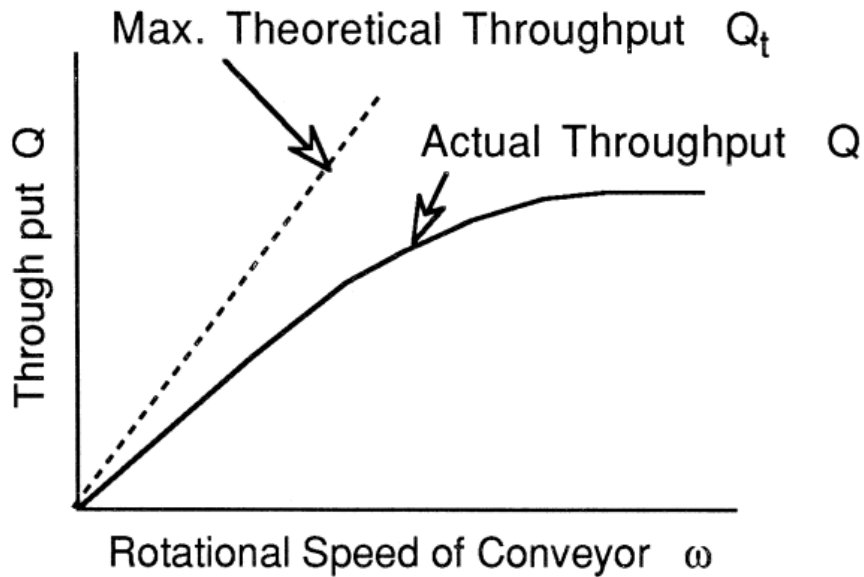


Figure 1.11 Volumetric throughput of a screw reactor.[85]

Considering that the materials morphological properties may vary greatly from fine powders to larger (regular and irregularly shaped) particles, the volumetric throughput is more difficult to estimate. Nachenius et al.[87] reported that larger biomass particles were affected more dramatically by the geometric limitations, resulting into lower volumetric throughput for larger biomass particles.

Researchers have studied the residence time distribution of biomass particles and the slow pyrolysis (torrefaction) of biomass inside the screw reactor.[87, 88] Fig. 1.12 shows the mean residence time of biomass particles in a screw reactor with a length of 1.64 m at different screw rotating frequencies and different feeding rates.[87] This figure shows that the residence time of biomass decreases with the increase of the screw rotating frequency, while it is influenced in only a limited way by the rate of biomass feeding into the screw reactor.

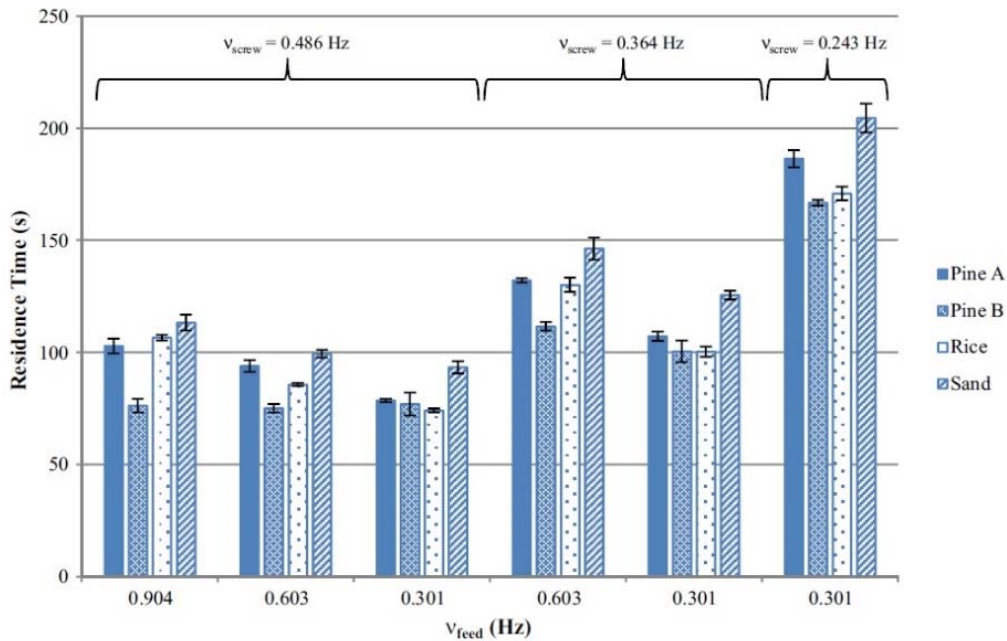


Figure 1.12 Comparison of mean residence times for different particles (Pine A, Pine B, Rice and Sand) inside a screw reactor at different combinations of feed screw (v_{feed}) and screw conveyor rotational frequencies (v_{screw}) [87]

Experimental studies found that the quality (i.e. energy density) of the char was influenced by both the operating temperature and the residence time of the biomass particles inside the screw reactor.[88] Longer residence time and higher operating temperature for the slow pyrolysis of biomass in the screw reactor can increase the energy density of the char, which is desired considering that the char can be used as a solid fuel. However, at longer residence times and higher operating temperatures the char yield will diminish.[88] Therefore, experiments and models are needed to find the optimized operating conditions, which should be a result of the compromise between the quality (energy density) and the yield of the char.

4.3 Factors influencing char production

Through particle scale and reactor scale experimental studies, various parameters that can affect char production have been recognized. As discussed in

Section 2.4, char production from biomass pyrolysis involves multiscale and multiphase phenomena. Any parameter related to these multiscale and multiphase phenomena can affect the char production. These parameters mainly include: (1) biomass species/type, (2) physical properties of the biomass particle (particle size, particle shape, grain orientation inside particle) and (3) operating conditions (temperature, heating rate, residence time, pressure).

4.3.1 Biomass species

Different biomass species (e.g. hardwood and softwood) usually have different amounts of macromolecular components (cellulose, hemicellulose, and lignin). For instance, hemicellulose usually accounts for 28 wt.% of the dry mass in softwood, and 35 wt.% of the dry mass in hardwood on average, and lignin can account for 23-33 wt.% of the dry mass in softwood and 16-25 wt.% of the dry mass in hardwood.[16]

As discussed in Section 3.1, different macromolecular components exhibit different pyrolysis behavior and produce different amounts of primary char. It was reported that higher amounts of lignin in biomass will lead to higher primary char yields.[57] Therefore, the type of biomass species can affect the production of primary char during biomass pyrolysis.

In addition, the primary volatiles from cellulose, hemicellulose and lignin have different properties (e.g. content of reactive components[89]), and the secondary reactions of the primary volatiles from cellulose, hemicellulose and lignin are different. It was reported that the primary volatiles from lignin are more aromatic and are more prone to produce secondary char compared to the primary volatiles from cellulose and hemicellulose.[89] Therefore, different amounts of cellulose, hemicellulose and lignin in different biomass species will affect the production of secondary char.

Therefore, different contents of macromolecular components in different biomass species affect the production and yields of both primary and secondary char.

4.3.2 Physical properties of the biomass particle

(1) Particle size

Pyrolysis can process biomass particles with a wide size range from micrometers to centimeters.[16, 17, 71] The residence time of volatiles inside larger particles can be expected to be longer, which is beneficial for secondary char production.[51, 90]

Larger particles tend to result into larger temperature gradients inside the particle (i.e. temperature at the internal of the particle is lower than that at the external of the particle), indicating that more (primary) pyrolysis reactions at the internal of the particle occur at temperatures lower than the operating temperature. Since the primary char production is favored at lower temperatures (as will be described later in Section 4.3.3), the pyrolysis of larger biomass particles tends to have higher yields of primary char. However, this conclusion is valid on the condition that the overall (global) pyrolysis reactions are endothermic or neutral in reaction heat. When the overall pyrolysis reactions are exothermic (e.g. when more exothermic secondary charring reactions occur,[81, 83] as discussed in Section 4.1), the influence of the particle size on the production of primary char would be complex, which requires further study.

(2) Particle shape

In reality, biomass particles commonly have irregular shapes with typical aspect ratios (ratio of the longest dimension to the smallest dimension of the biomass particle) ranging from 2 to 15.[91] For the same biomass species/types at the same

particle mass/volume, spherical particles have the lowest external surface area to volume ratio compared to other particle shapes (cylindrical, cubic and other irregular shapes). As the external surface area to volume ratio determines the available area per unit mass for heat exchange of the particle with the surroundings,[92] spherical biomass particles tend to exhibit lower conversion rates and higher char yields compared to particles with other shapes, which was also addressed by Lu et al. [91] The difference between the pyrolysis of spherical particles and the pyrolysis of particles with other shapes was observed to increase with increasing particle size.[91] In addition, the shape of the particle is closely related to the vapor residence time inside the particle (intraparticle mass transfer), which can affect the conversion of the tarry vapors in producing secondary char inside the particle.[67]

(3) Grain orientation

Raw biomass particles are physically anisotropic. The permeability (determining the outflow of volatiles inside the particle) parallel to the grain is almost 10^3 times larger than across the grain, and the thermal conductivity parallel to the grain is about 2.5 times the one across the grain.[93] The different permeability and thermal conductivity indicate that the pyrolysis reactions parallel to and across the grain orientation proceed at different rates.[94]

4.3.3 Operating conditions

(1) Temperature

As a thermochemical conversion process, biomass pyrolysis is significantly influenced by the operating temperature.[17, 33, 34] The basic role of a high temperature is to provide heat for the decomposition of macromolecular biomass components. Temperature can influence both the char yield and the elemental

composition and hence the quality (e.g. energy density) of the char.[17] Lower temperature favors char production but usually at the expense of longer processing duration. The atomic ratios of O/C and H/C decrease with the increase of temperature. With the increase of temperature, char will lose the hydroxyl more easily, which means that the char loses hydrogen and oxygen preferentially through dehydration with the temperature increases. As a result, the char produced at higher operating temperatures is more carbon-concentrated and hence higher in energy density.[17] However, higher temperature at the same duration (reaction time) also leads to lower energy yield or more energy loss for the char.[17, 88] Therefore, optimized pyrolysis temperature should be searched for in order to maximize the social and economic advantage of char production from biomass pyrolysis at the compromise between the quality and the energy yield of the char.

(2) Heating rate

Heating rate is an important factor determining the decomposition of biomass. Faster heating rate can cause quick fragmentation of biomass, thus can enhance the volatiles formation.[95] Therefore, lower heating rates are preferred for increasing the production of char. [90] However, lower heating rates also imply that the process lasts for a longer time. Therefore, it is simply not practical to apply very low heating rates.

(3) Residence time

Char is usually a mixture of primary char from the devolatilization of biomass and secondary char from the homogeneous and heterogeneous conversion of primary volatiles.[9, 67, 90] It was reported that the secondary char can be as reactive (e.g. during gasification with carbon dioxide and steam) as the primary char.[96] The

production of primary char is related to the particle/solid residence time inside the reactor, while the production of secondary char is influenced by both the particle/solid residence time and the volatiles residence time inside the particle/reactor.[90] Longer particle/solid residence time, indicating stronger reaction severity, will lead to more extensive devolatilization, and thus will reduce the yield of the residual solid (considered as primary char).[88]

Fig. 1.13 shows the effect of gas flow (thus volatiles residence time) at various operating pressures on the yield of the total char during pyrolysis of cellulose,[90, 97] one of the macromolecular components in biomass.

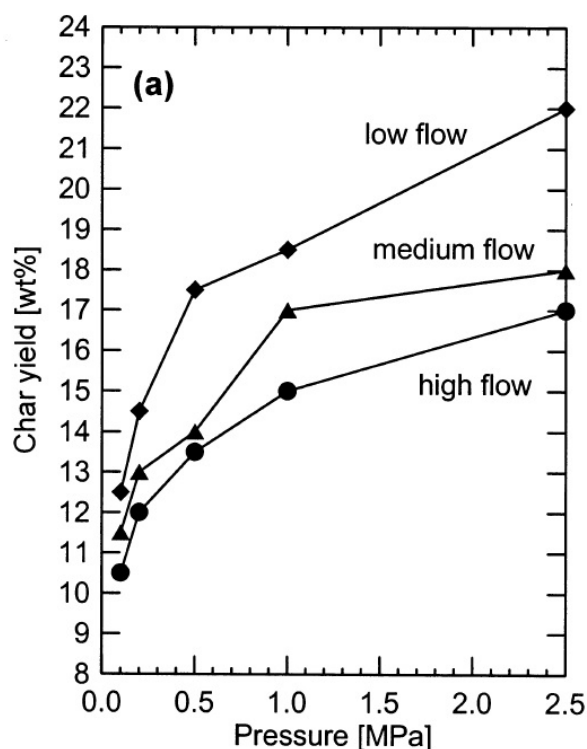


Figure 1.13 Effect of gas flow rates (and hence gas residence time) on the yield of char at different pressures [90, 97]

As can be seen from this figure, lower gas flow rates, thus longer residence times of volatiles, lead to higher char yields. Longer residence time for volatiles will provide more opportunity for the reactive volatiles (e.g. tarry vapors from pyrolysis of

lignin[89]) to interact with the solid residue from biomass pyrolysis, which can enhance the production of secondary char and hence can improve the total char yield. Due to the different effects of residence time on the production of primary and secondary char, the residence time of particles inside the pyrolysis reactor and the residence time of volatiles inside the particle should be separately optimized to maximize the production of char.

(4) Pressure

Pressure is an important factor influencing the production of char from biomass pyrolysis by affecting the conversion of volatiles to produce secondary char. Antal and his collaborators have contributed leading researches in this area.[90, 98] Generally, elevated pressure can enhance the production of char from biomass pyrolysis. From the view of particle scale phenomena, more char production at higher pressures is mainly due to the increased significance of the conversion of the reactive volatiles within the biomass particle at higher pressures. At higher pressure, the mass concentration of reactive volatiles will be higher and the specific volume of the volatiles will be lower, which results into a lower velocity for the volatiles to flow out of the biomass particle. Therefore, reactive volatiles will have longer residence times to produce secondary char inside the biomass particle at higher pressures. The combination of higher mass concentration and longer residence time for the reactive volatiles within the biomass particle at higher pressures will further enhance the conversion of the reactive volatiles to produce secondary char and hence increase the total char yield.[67] At the reactor scale, higher pressures can increase the concentration (partial pressure) of the reactive volatiles, and therefore can increase the conversion rate of reactive volatiles to form secondary char.[99] However, the current understanding about the pressure effect on the char production through

conversion of reactive volatiles is largely qualitative, and to the best of our knowledge, no kinetic models that combine the complex effects of operating pressure and residence time of reactive volatiles have been reported in the literature. Quantitative and mechanistic researches are still required to reveal the role of the homogeneous and heterogeneous conversion of reactive volatiles on the secondary char and hence the total char production during biomass pyrolysis.[9, 51, 90]

4.4 Benefits and limitations of experimental studies

Experimental studies have obtained valuable information on the char production through biomass pyrolysis at both particle scale and reactor scale. Factors influencing the char production in biomass pyrolysis have been recognized through experiments. The intraparticle physical (e.g. intraparticle heat transfer) and chemical (e.g. primary and secondary reactions) phenomena, particularly the intraparticle secondary charring reactions, have been revealed by experiments at the particle scale. Reactor scale experiments have provided valuable data for designing, operating and optimizing the performance of pyrolysis reactors for producing char. In addition, experimental studies have provided plenty of useful data that are necessary for validating computational models at both particle scale and reactor scale. However, experimental studies also have limitations.

Experimental studies are expensive considering the materials and equipment that are employed. The volatile products from biomass pyrolysis contain harmful components (e.g. aromatics), and their potential leakage during experiments can be dangerous. In addition, experimental studies can only provide limited information on the complex and transient coupled transport phenomena and chemical reactions at particle scale and reactor scale, which brings challenges in designing, operating and optimizing the performance of the pyrolysis reactors for char production.

Specifically, at the particle scale, the study of the coupled physical and chemical phenomena related to the intraparticle secondary charring reactions, which are essential for understanding the transient processes occurring inside the biomass particle, is beyond the capability of experimental techniques.

At the reactor scale, the transient particle flow dynamics inside the reactor (e.g. screw reactor), of which the knowledge thereof is essential for optimizing the performance of the screw reactor, has seldom been reported in experimental works. In addition, previous experimental studies were mainly focused on the characterization (yield, elemental composition, energy density, etc.) of the products (char and volatiles).[88] Little was known about the complex coupled physical and chemical phenomena occurring inside the reactor, which is usually beyond the capability of the current experimental techniques.

5. Modeling study of biomass pyrolysis for char production

With the development of computational sciences, computational (or numerical) models have been applied to study the coupled transport phenomena and pyrolysis reactions for biomass pyrolysis at particle scale and at reactor scale.[9] Compared to the experiments, modeling studies are safe (e.g. without worry about leakage of harmful gases). In addition, modeling studies are able to obtain in-depth knowledge about the transient and complex flow dynamics, heat transfer, mass transfer and chemical reactions occurring at particle scale and at reactor scale, which is essential for designing and optimizing the pyrolysis reactor for char production. It should be stressed that experimental data should be applied to validate the computational models. The following will discuss some previous particle scale and reactor scale modeling studies.

5.1 Particle scale modeling

The computational model can be used to give mathematical descriptions for the coupled transport phenomena and chemical reactions during the pyrolysis of a single biomass particle. The complexity of the computational model at the particle scale (named particle model) depends on the possible physical and chemical phenomena that the particle model can include (or neglect). The most complex particle model should consider (1) the realistic boundary conditions including the real geometry of the particle (typically far from spherical or cylindrical), the shrinkage or fragmentation and the realistic instantaneous temperature and volatiles distribution at the particle surface, (2) the pore structure and the anisotropic characteristics inside the particle, (3) the residual solid mass loss kinetics and the secondary conversion kinetics of reactive volatiles, (4) the heats of reaction, (5) the pressure build-up due to volatiles formation within the particle, (6) the outflow of volatiles. However, the most complex particle model also indicates that all physical and chemical information, some of which may be unnecessary for practical applications, would also be predicted. Practically, assumptions will first be made before performing the particle modeling, and such model assumptions should guarantee that the particle model can describe the dominant intraparticle physical and chemical phenomena. Usually, these dominant phenomena can be preliminarily estimated from the analysis of non-dimensional numbers, e.g. Biot number, pyrolysis number, etc.[9] While some works have tried to describe the realistic geometry of the biomass particle in particle modeling,[92, 100] most modeling works (three-dimensional, two-dimensional and one-dimensional models) assume a spherical, cylindrical or cubic geometry for the biomass particle and the ensuing modeling results are still within acceptable errors.[71, 81, 83, 91, 94, 101-112] Although plenty of modeling works have been

performed at the particle scale, most of these works have mainly focused on the accurate prediction of product yields and the temperature evolution inside the particle. [71, 81, 83, 91, 94, 101-112] Only very limited modeling works have considered and validated the potential homogeneous and heterogeneous conversion of reactive volatiles inside the particle, [67, 81] which makes the role of the secondary char in the total char largely unknown. In addition to model accuracy, another research direction of previous modeling studies at particle scale is to save computational time by deriving simplified particle models for biomass pyrolysis. The ultimate aim of these so-called simplified particle models is to be integrated into complete reactor models. In the literature, some simplified particle models have been developed, e.g. uniform conversion model (UCM), unreacted-shrinking-core model (USCM) and others. [65, 107, 113, 114] However, these simplified particle models usually follow two extreme assumptions of either homogeneous heating and reactions across the whole particle or an infinitely thin moving reaction front separating the pyrolyzing particle into one layer of virgin biomass and another layer of hot char. [115-122] The actual pyrolysis conditions that are far from these two extreme conditions (for instance, biomass slow pyrolysis in this thesis) may introduce more errors when predicting the char production compared to the actual pyrolysis of a biomass particle. Therefore, a simplified particle model that is suitable for describing the slow pyrolysis of biomass in producing char remains to be developed.

5.2 Reactor scale modeling

As discussed above, biomass pyrolysis involves both solids (biomass particles) and gas phases (inert gas and volatile products). In a pyrolysis reactor (e.g. screw reactor), it is important to understand the complex coupled physical (gas-solids flow dynamics including gas-solids, solids-solids and solids-wall interactions, and heat

and mass transfer) and chemical (pyrolysis reactions) phenomena. With the development of computer science, the computational fluid dynamics (CFD) method has been widely applied to study such kind of multiphase systems involving chemical reactions. Both Eulerian-Lagrangian modeling method and Eulerian-Eulerian modeling method have been applied to perform CFD simulations for such kind of multiphase systems.

5.2.1 Eulerian-Lagrangian modeling method

The combined computational fluid dynamics and discrete element model (CFD-DEM) is a typical Eulerian-Lagrangian modeling method. In CFD-DEM, the gas phase is treated as a continuum described by the local averaged Navier–Stokes equations, and the particles are tracked individually by solving Newtonian equations of the motion. The motions of gas and particles are coupled through an interphase interaction term. The DEM model can accurately predict the exchange of mass, momentum and energy at the intra- and interparticle level, and between gas phase and particles in the pyrolysis reactor. Therefore, trajectories, temperature, chemical composition (pyrolysis reaction rates) and any other additional phenomena on an individual particle level can be obtained with this Eulerian-Lagrangian modeling method. The Eulerian–Lagrangian modeling method has clearer physical meanings by considering the particle-scale physical and chemical phenomena in a discrete manner which is different than in an Eulerian–Eulerian model in which the particle phase is assumed as a continuous medium (described later in detail). The information on the particle level from the Eulerian–Lagrangian modeling method is essential to study effects like pyrolysis reactions, particle shrinkage, particle breakage, particle segregation, mixing and entrainment.

Orefice and Khinast[123] studied the volume flow rate of particles in a horizontal screw system with DEM simulations, and they found that the volumetric flow rate of particles increased with the increase of the screw rotating speed (or rotating frequency). Owen and Cleary[124] performed DEM simulations for a screw reactor, and they systematically studied particle flow dynamics inside a screw reactor with different screw inclinations, rotating speeds and filling levels. Hou et al.[125] studied the flow of cohesive particles in screw systems with DEM simulations, and they addressed the importance of the cohesive interactions among particles on the performance of screw systems. From these modeling studies, it can be seen that DEM based on the Eulerian-Lagrangian approach can obtain valuable information on the particle flow dynamics inside the screw reactor (or screw systems). Detailed information on the particle's trajectory inside the reactor, which is currently extremely difficult, if not impossible, to obtain with experimental measurements[126], can be solved with Eulerian-Lagrangian approaches.

However, current CFD-DEM models based on Eulerian-Lagrangian approach are normally limited to small numbers of particles due to computational limitations,[127] which restrict their application in simulating full-scale pyrolysis reactors (e.g. screw reactors) containing millions or billions of biomass particles.

5.2.2 Eulerian- Eulerian modeling method

CFD models based on the Eulerian-Eulerian approach (two-fluid model, or TFM) assume gas and solid phases to be interpenetrating continua. The TFM has its limitations. Since Eulerian formulations are based on spatial averaging techniques with strong simplifications made on the particle kinematics and chemical reactions, information about the phenomena on an individual particle scale is less reliably and less naturally included in the Eulerian-Eulerian modeling method compared to the

Eulerian-Lagrangian modeling method. Furthermore, no information can be obtained from TFM about the residence time of an individual reacting particle, which is highly important for assessing the overall pyrolysis process in a pyrolysis reactor. However, the Eulerian-Eulerian based CFD models are computationally efficient and are capable of handling multiphase systems (e.g. screw reactors) containing large numbers of particles. [128] Some Eulerian-Eulerian simulation works have been reported for the screw reactor. Aramideh et al.[129] applied the Eulerian-Eulerian method to study a screw reactor at conditions of fast pyrolysis for maximizing the production of liquid/oil product. Further works (e.g. particle flow dynamics, residence time distribution, particle back-mixing, product distributions, and quality and energy yield of the char) about biomass pyrolysis inside the screw reactor still remain to be studied based on CFD simulations using the Eulerian-Eulerian approach.

6. Thesis objective and outline

6.1 Thesis objective

6.1.1 Summary of problems to be solved

Pyrolysis is one of the promising thermochemical technologies for biomass conversion. Char, as one of the pyrolysis products, gains increasing attention for its potential applications in energy, fuels and functional carbon materials. The production of char from slow pyrolysis of biomass involves complex physical and chemical phenomena occurring at different scales (multiscale) and phases (multiphase). Char is usually a mixture of primary char from biomass devolatilization and secondary char from the conversion of reactive volatiles. Any factors from the multiscale and the multiphase can have potential influences on the biomass pyrolysis and hence the primary and secondary char production. Computational modeling is an

important approach to study the coupled physical and chemical phenomena during biomass pyrolysis at multiscale and in multiphase, which is essential in designing and optimizing pyrolysis reactors for char production.

While other researchers have performed extensive experimental and modeling works for biomass pyrolysis at both particle scale and reactor scale, many problems still remain to be solved for char production. The following questions are still largely to be answered.

At the particle scale:

(1) To what extent the primary volatiles can be converted into secondary char and secondary volatiles inside a single biomass particle?

(2) What is the critical particle size above which secondary char production starts to be relevant?

(3) How to develop a simplified particle model that can describe the dominating physical and chemical phenomena during biomass slow pyrolysis (including torrefaction) for saving computational time?

At the (screw) reactor scale:

(4) How are the particle flow dynamics and back-mixing behavior in a screw reactor?

(5) How to develop a CFD model including chemical reaction kinetics in order to characterize the performance of a screw reactor in producing char (mass yield, elemental composition, quality and energy yield) through biomass pyrolysis?

6.1.2 Thesis objective

The objective of the present thesis is to study the char production during biomass pyrolysis with a methodology of multiscale modeling (particle scale and reactor scale with multiphase phenomena involved). The research questions listed above will be dealt with in this thesis.

6.2 Thesis outline

The thesis outline is shown in Fig. 1.14.

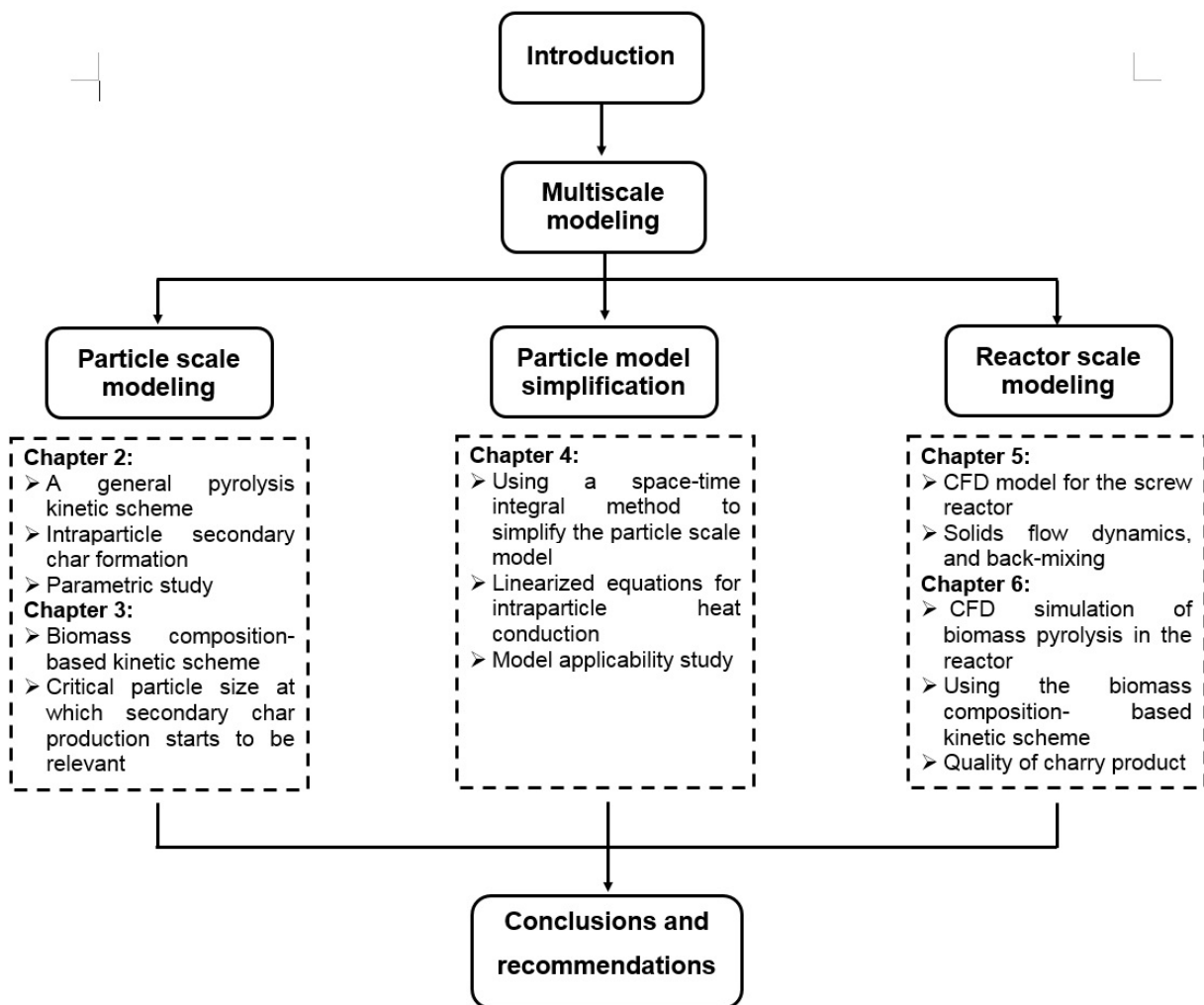


Figure 1.14 Thesis outline

Chapter 2 deals with the modeling of char production at the biomass particle scale. In this chapter, a finite element comprehensive particle model will be

developed for the pyrolysis of a three-dimensional biomass particle. The model will consider the relevant physical and chemical phenomena, including intraparticle conductive, convective and radiative heat transfer, intraparticle volatiles flow, intraparticle mass transfer of different volatile components (inert gas of N₂, gaseous and tarry products), the pyrolysis reactions, and the anisotropic characteristics of the biomass particle. A general kinetic scheme (one-component competitive kinetic scheme) without considering the biomass composition will be incorporated into the model. The kinetic scheme considers both the primary char formation from biomass devolatilization and the secondary char production from the homogeneous and heterogeneous conversion of primary volatiles (tarry vapors). The model will be validated against experimental data from literature. Parameters, including physical properties of the biomass particle (particle shape, size shrinkage and particle fragmentation), operating conditions (temperature, heating rate, pressure) and the extra-particle concentration of tarry vapors will be studied using the model, and with respect to their effects on the production of char (primary and secondary char).

In **Chapter 3**, a comprehensive pyrolysis kinetic scheme, which considers the primary pyrolysis of biomass pseudo-components (cellulose, hemicellulose, and lignin) and the secondary charring reactions due to the heterogeneous conversion of the primary volatiles, will further be incorporated into the comprehensive particle model that is developed in Chapter 2. This comprehensive pyrolysis kinetic scheme is able to deal with differences in biomass composition (e.g. dealing with both softwood and hardwood), and therefore can be expected to be more applicable than the general kinetic scheme in Chapter 2 that does not consider the biomass composition. In this chapter, the model will be validated against available experimental data. The importance of the intraparticle secondary char production at

different particle sizes will be addressed. A critical particle size, at which the intraparticle secondary charring reactions start to be relevant, will be determined for the pyrolysis of a cylindrical biomass particle.

For saving computational time, the comprehensive particle models that are developed in Chapter 2 and Chapter 3 will be further simplified in **Chapter 4**. In this chapter, a space-time integral method will be applied to linearize the partial differential equations (PDEs) in the comprehensive particle models in describing the intraparticle heat transfer, which will result into a simplified particle model. This simplified particle model will be applied to study the slow pyrolysis of a biomass particle at torrefaction conditions. The accuracy of the model will be discussed by comparing with either the experimental data or the comprehensive particle model (Chapter 2 and Chapter 3) whenever the experimental data is not available. The applicability of the simplified particle model will be further examined to determine the limitations of this simplified particle model.

In **Chapter 5**, a CFD cold flow model based on the Eulerian-Eulerian method will be developed for a screw reactor for processing biomass particles. The flow dynamics, residence time distribution (RTD) and back-mixing behavior of the solid phase (biomass) inside the screw reactor will be studied with this CFD model. The model results will be compared to the experimental data with respect to the solid mass flow rate at the reactor outlet, the total solid mass inside the reactor at steady flow conditions, the degree of fullness of the solid phase inside the reactor, and the mean solid residence time inside the reactor. Mechanisms leading to solids back-mixing inside the screw reactor will be discussed.

Chapter 6 further incorporates the biomass composition-based (cellulose, hemicellulose, and lignin) pyrolysis kinetic scheme (multi-component competitive

kinetic scheme), which considers the detailed elemental composition of both biomass and its pyrolysis products, into the CFD cold model developed in Chapter 5. Model results, with respect to the temperature distribution inside the reactor, the product yields and the elemental composition of the products (gas, liquid/oil and char) will be compared to the experimental data. The energy density (higher heating value, or HHV) and the energy yield of the char will then be calculated with the predicted elemental composition. The capability of the CFD-based reactor model in predicting the quality (e.g. energy density) of the product will be addressed in this chapter.

The thesis ends with a summary of the main conclusions and some recommendations for future works.

CHAPTER 2

Modeling of pyrolysis of a biomass particle with a general kinetic scheme

In this chapter, a three-dimensional (3D) comprehensive particle model (CPM) will be developed for the pyrolysis of a centimeter-sized biomass particle based on finite element method. A general kinetic scheme, without considering biomass composition, will be incorporated into the CPM to describe the primary biomass devolatilization and the intraparticle secondary charry reactions (secondary reactions of tarry vapors to produce secondary char). The model will be validated against experimental data from literature. Effects of process conditions (heating rate, peak temperature, pressure of the gas phase surrounding the particle and extra-particle concentration of the tarry vapors) and particle properties (particle shape, particle shrinkage and particle attrition or splitting) on pyrolysis of a single biomass particle will be discussed.

This chapter was published in a modified form as:

Xiaogang Shi, Frederik Ronsse, Jan G. Pieters. Finite element modeling of intraparticle heterogeneous tar conversion during pyrolysis of woody biomass particles. *Fuel Processing Technology*, 2016, 148: 302–316.

1. Introduction

The formation of char is generally believed to be the result of both the primary pyrolysis of the feedstock biomass (hence labeled as primary char) and the secondary charry reactions (secondary char resulting from the secondary conversion of the tarry vapors).[35, 51, 90, 130] Secondary char formation can be achieved both by homogeneous tar cracking and by heterogeneous interactions between the tarry vapors and the hot char.[54, 89, 131-133] The char formation from homogeneous tar cracking is found to be limited even at high temperatures ranging from 770 to 1070 K.[54] On the contrary, the heterogeneous conversion of the tarry vapors induced by contact with primary char can occur at lower temperatures and plays a key role in the formation of the secondary char.[55, 80, 90] Mok and Antal[79] concluded that the secondary heterogeneous reactions of the tarry vapors are effectively the only source of char in the pyrolysis of pure cellulose. Qualitative studies of the heterogeneous reactions of the tarry vapors suggest that high concentration and prolonged vapor-phase residence time of the tarry vapors in the reaction zone as well as high temperatures are beneficial to the secondary char formation.[51] However, the quantitative understanding of the secondary heterogeneous reactions of the tarry vapors (reactions outside and inside the biomass particle) is still limited.[51, 66, 90, 134] Boroson et al.[89] experimentally studied the heterogeneous tar reaction over fresh wood char surfaces (tar conversion outside the biomass particle) and found that $14\pm 7\%$ of the tarry vapors undergo heterogeneous conversion. Anca-Couce et al.[72, 73] considered the secondary heterogeneous reactions of the tarry vapors in a comprehensive pyrolysis reaction scheme for mechanistic description of biomass pyrolysis, and promising results have been obtained. The tarry vapors primarily produced inside the biomass particle can also experience heterogeneous reactions

as the vapors pass the decomposing biomass.[51, 55, 80, 135] It is generally believed that larger biomass size is favorable to the heterogeneous conversion of the tarry vapors due to the prolonged residence time of the tarry vapors in large-sized particles.[51, 55, 80, 82, 90, 136, 137] Pattanotai et al.[55] found that about 5% of the tarry vapors undergo heterogeneous secondary conversion in a centimeter-sized wood particle. Due to the limitations of experimental set-ups, current experimental studies of the pyrolysis of centimeter-sized biomass particles mainly provide the product distributions and the intraparticle temperature histories [55, 110, 136-138] without any information on the transient reaction and transport behavior of the tarry vapors inside the biomass particle, although this kind of information is critical in characterizing the intraparticle heterogeneous tar conversion.[51] A modeling study by coupling the pyrolysis kinetics and transport phenomena can provide detailed information on the pyrolysis process of a centimeter-sized biomass particle and hence the intraparticle conversion of the tarry vapors for producing secondary char.[65] However, only limited modeling studies have focused on the intraparticle heterogeneous conversion of the tarry vapors. Koufopoulos et al.[82] developed a model for the pyrolysis of centimeter-sized biomass particles by coupling the heat transfer and pyrolysis kinetics. Their kinetic scheme considered the heterogeneous tar reaction. A parameter, coefficient of deposition, was introduced to account for the residence time of the volatiles inside the biomass particle. Ahuja et al.[80] also considered the intraparticle heterogeneous volatiles conversion. Babu and Chaurasia[139-143] used the kinetic scheme of Koufopoulos et al.[82] to simulate the pyrolysis of a biomass particle and they further studied the particle shrinkage effects, the sensitivity analysis, and the optimum parameters for the pyrolysis. Sadhukhan et al.[81, 144] modeled the pyrolysis of large spherical and cylindrical wood particles

with a similar kinetic scheme as Koufopoulos et al.[82] Basu et al.[145] simulated the torrefaction of a large wet wood particle by assuming that part of the primary volatiles were deposited on the char surface and experienced secondary reaction. In reviewing these previous modeling efforts, comprehensive results for the pyrolysis of single large biomass particles have been found. However, to our knowledge, few models have considered the factors influencing the heterogeneous conversion rate of the tarry vapors when contacting the hot char fraction. For a three-dimensional biomass particle, little is known when the model accounts for the diffusive/convective mass transport and conductive/convective heat transport. In addition, the biomass particle was usually regarded as an isotropic particle in previous modeling works, which could not describe the actual anisotropic characteristics occurring during the pyrolysis of the biomass particle.[136, 137] Moreover, efforts are still needed to study the extent to which the process conditions (peak temperature, heating rate, pressure of the gas phase surrounding the biomass particle and extra-particle tarry vapor concentration), particle shape and particle size reduction (particle shrinkage and particle splitting) can affect the production of the primary and secondary char.

In this chapter, a three-dimensional comprehensive particle model (3D CPM) that couples pyrolysis reactions and transport processes is developed. The pyrolysis reactions are described with a general kinetic scheme, which considers the primary conversion of virgin biomass into char, tarry vapors and non-condensable gases and the formation of the secondary char resulting from the secondary reaction of the tarry vapors. A characteristic time scale analysis is first performed to identify the dominant physical and chemical phenomena occurring during pyrolysis of a single particle. Then the mathematical formulation of the 3D CPM is presented. Finally, the CPM is used to examine the effects of process conditions (peak temperature, heating rate,

pressure of the gas phase surrounding the biomass particle and extra-particle tarry vapor concentration), particle shape and particle size reductions (shrinkage and splitting).

2. Methods

2.1. Theoretical background

2.1.1. Characteristic time analysis

Complex physical and chemical phenomena occur during the pyrolysis of a single biomass particle. The particle (e.g. dry biomass particle) absorbs heat from the hot surroundings, which evokes pyrolysis reactions to produce char in solid phase and volatiles in gas phase. While the char is left inside the particle, the volatiles will flow out of the particle driven by the pressure difference between the interior and the exterior of the particle, which arises from the production and accumulation of volatiles within the biomass particle during pyrolysis.

It is important to judiciously consider the most relevant physical and chemical processes to formulate the representative model. The analysis of the characteristic time can aid in the understanding of the dominating and rate-controlling processes during biomass pyrolysis.[9, 83, 106, 112, 146] The characteristic times of five major different physical and chemical phenomena occurring during the pyrolysis process were calculated for a centimeter-sized particle (with a length scale of 10^{-2} m) and a fine particle (with a length scale of 10^{-3} m), separately: (1) mass transfer rate by molecular diffusion in the gas phase, (2) mass transfer rate by intraparticle fluid flow (due to the outflow of volatiles formed inside the particle), (3) internal conductive heat transfer rate, (4) external convective heat transfer rate, and (5) apparent pyrolysis reaction rate. Temperatures range from 500 to 900 K with a heating rate of 10~30

K/min,[27] which characterizes slow pyrolysis. The calculated results of these characteristic times and the related parameters are listed in Table 2.1.

In this calculation, the value of the effective diffusivity (D_{eff}) was estimated using the correlation described in Section 2.2.2 by choosing phenol as a typical and representative component of the intraparticle tarry products. The pressure gradient ($\Delta p/\Delta x$) in the biomass, i.e. pine wood, was estimated to be about 300 Pa/cm.[147] The permeabilities (B) along and across the wood's grain direction and the dynamic viscosity of the gas mixture (μ) were taken from Di Blasi.[93] The biomass density was taken from the experimental work of Pattanotai et al.[55] based on which the present model was developed. The thermal conductivities along and across the grain direction of the biomass were estimated with the correlation described in Section 2.2.2. The specific heat capacities for the virgin biomass, char, gas and tar (c_p) were obtained from Grønli and Melaaen.[148]

Table 2.1 Calculated characteristic times for the physical and chemical processes during slow pyrolysis

<i>Parameters</i>	Characteristic times (s) in slow pyrolysis, (heating rate ≤ 30 K/min, temperature range is 500~900 K)	
	Centimeter-sized particles, $L = 10^{-2}$ m	Fine particles, $L = 10^{-3}$ m
Diffusion, L^2/D_{eff}	10^1	10^{-1}
Intraparticle fluid flow, $\mu L^2/(\Delta P \cdot B)$	10^0 (along the grain direction) 10^3 (across the grain direction)	10^{-1} (along the grain direction) 10^2 (across the grain direction)
Conductive heat transfer, $(\rho c_p)_s L^2/\lambda$	10^2 (along the grain direction) 10^3 (across the grain direction)	10^0 (along the grain direction) 10^1 (across the grain direction)
External heat transfer, $(\rho c_p)_s L/h_{ext}$	10^2 (at 500 K) \sim 10^1 (at 900 K)	10^1 (at 500 K) \sim 10^0 (at 900 K)
Apparent pyrolysis mass loss kinetics, $1/k_{apparent}$	10^5 (at 500 K) \sim 10^{-2} (at 900 K)	10^5 (at 500 K) \sim 10^{-2} (at 900 K)

Calculated using following assumptions,

$D_{\text{eff}} \approx 10^{-5} \text{ m}^2/\text{s}$	$\mu \approx 10^{-5} \text{ kg}/(\text{m}\cdot\text{s})$
$\Delta p \approx 10^2 \text{ Pa}$ (for $L = 10^{-2} \text{ m}$), 10^1 Pa (for $L = 10^{-3} \text{ m}$),	$B \approx 10^{-11} \text{ m}^2$ (along the grain direction), 10^{-14} m^2 (across the grain direction)
$(\rho c_p)_s \approx 10^6 \text{ J}/(\text{m}^3\cdot\text{K})$	$h_{\text{ext}} \approx 5 \times 10^1 \text{ W}/(\text{m}^2\cdot\text{K})$ (500K), $2 \times 10^2 \text{ W}/(\text{m}^2\cdot\text{K})$ (900K)
$(\rho c_p)_g \approx 10^3 \text{ J}/(\text{m}^3\cdot\text{K})$	$\lambda \approx 0.3 \text{ W}/(\text{m}\cdot\text{K})$ (along the grain direction), $0.1 \text{ W}/(\text{m}\cdot\text{K})$ (across the grain direction)

The calculated values for specific heats of char and pyrolysis vapors were close to $0.02 \text{ kJ mol}^{-1}\text{K}^{-1}$ (on a carbon mole basis) as reported by Yang et al.[149] The density of the gas mixture was estimated using the ideal gas law. The biomass apparent pyrolysis rates (k_{apparent}) were estimated with the kinetics from Park et al.[110] The external heat transfer coefficient (h_{ext}), including both convection and radiation, was calculated with the correlation,[65]

$$h_{\text{ext}} = h_{\text{convective}} + 4\sigma\epsilon_s T^3 \quad (1)$$

The calculated characteristic times for the centimeter-sized and fine particles, as shown in Table 2.1, show that the characteristic time of the mass transfer via diffusion is comparable to that via the intraparticle fluid flow along the grain direction of the biomass, indicating that the mass transfer along the grain direction is contributed both by diffusion and by convective intraparticle fluid flow. Across the grain direction of the biomass, however, the intraparticle fluid flow takes more time than the diffusion process, indicating that the mass transfer across the grain happens mainly by diffusion. It should be mentioned that the role of the diffusion may be reduced considering that the concentration of vapor species outside the particle is not zero. Since slow pyrolysis occurs at low temperature and low heating rate, the pressure drop/gradient across the centimeter-sized particle was low, which indicates that the intraparticle fluid flow process took longer time. Therefore, the intraparticle

diffusive mass transfer is comparable to (or dominate over) the convective mass transfer in magnitude, and this was consistent with the work of Grønli,[150] who described that the diffusive mass transfer played an important role during biomass pyrolysis at low heat fluxes and low temperatures.

Besides, the conductive heat transfer along the grain direction is faster than that across the grain direction of the biomass particle. The distinct transport phenomena along and across the grain direction of the biomass indicate that the modeling of the biomass particle pyrolysis process should consider the anisotropic characteristics of the particle. For a centimeter-sized particle, the characteristic time of the external heat transfer is slightly shorter than that of the internal conductive heat transfer, which indicates that a mild temperature gradient will be built inside this particle. For the fine particle, a negligible temperature gradient will be present inside the particle as indicated in Table 2.1.

2.1.2. Model assumptions

The formulation of the pyrolysis model on the particle scale is based on the following assumptions:

(1) The particle is a homogeneous porous matrix with a continuous gas phase inside the particle pores. Biomass is composed of macromolecular compounds (cellulose, hemicellulose and lignin) and smaller amounts of low molecular weight organic components (extractives) and inorganics (salts or minerals). Biomass consists of cells and has a porous structure. In a typical lignified cell, the cellulose is the important structural element, which is surrounded by other compounds functioning as the matrix (hemicellulose) and the encrusting (lignin) material.[150, 151] Since the exact porous structure of the biomass is very difficult to establish in a

numerical model, the biomass particle is usually modeled as a homogeneous porous matrix.[93, 150]

(2) The biomass particle initially contains inert gas (N_2) in its pores;

(3) The extra-particle concentrations of non-condensable gases and tarry vapors are both substantially lower than the concentration of the extra-particle inert gas (N_2);

(4) Local thermal equilibria exist between the gas mixture (containing inert gas N_2 , non-condensable gases and tarry vapors) and the solids (virgin biomass and char);

(5) The gas mixture behaves as an ideal gas;

(6) The biomass particle is anisotropic and the geometry of the biomass is three-dimensional.

2.2 Model development

2.2.1 Kinetic model

During the pyrolysis of large biomass particles, it is generally difficult to experimentally measure the yields of primary and secondary products separately. In experimental work, the secondary conversion of the tarry vapors inside large particles (centimeter-sized or larger) is often indirectly indicated by comparing the products distributions between fine and large biomass particles since fine particles are generally believed to only experience primary reactions.[65, 136, 137] In the modeling study, however, the primary and secondary products from the pyrolysis of large biomass particles can be calculated separately.

A general kinetic scheme was used to study the intraparticle secondary tar conversion for a centimeter-sized biomass particle. This general kinetic scheme

consists of primary reactions (virgin biomass to primary char and volatiles which consist of tar and non-condensable gases) and secondary conversion of the tar homogeneously (in the vapor phase) and heterogeneously (vapors reacting onto the primary char) yielding secondary non-condensable gases and secondary char, as shown in Fig. 2.1. Each reaction rate was described by a first order Arrhenius function.

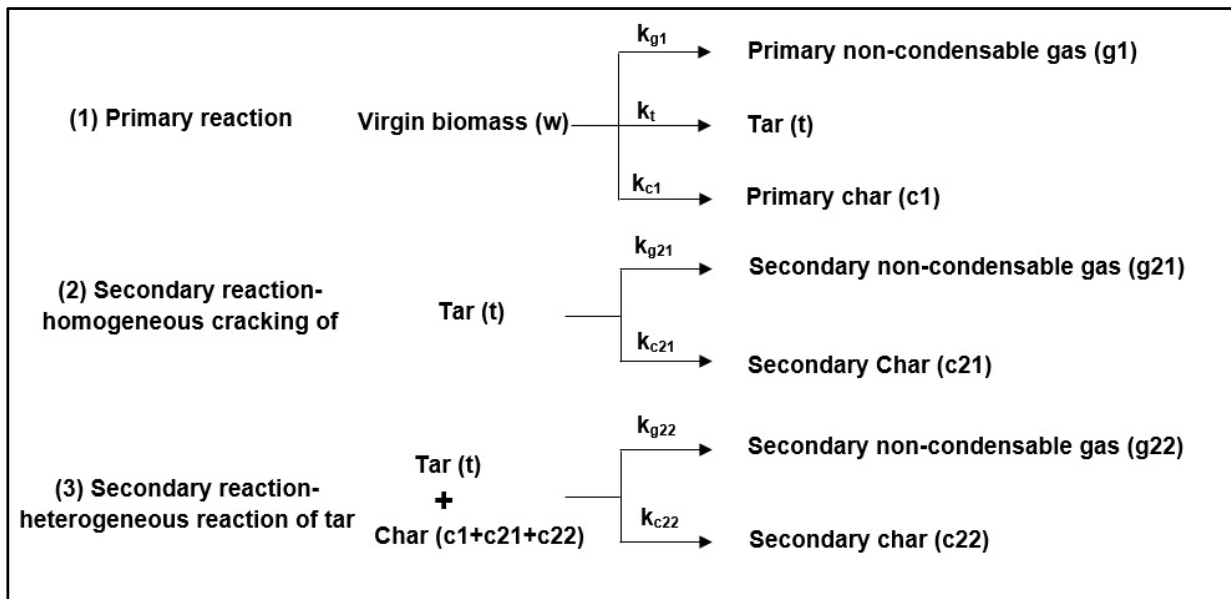


Fig. 2.1 General kinetic scheme of biomass pyrolysis.

(1) Kinetics for primary reaction

The kinetic constants from Di Blasi and Branca[152] were adopted in describing the formation of volatiles (consisting of tar and primary non-condensable gases) and primary char. The volatiles are assumed to consist of 62.6 wt.% of tar and 37.4 wt.% of non-condensable gases. This composition of volatiles primarily produced from biomass pyrolysis is in accordance with the experimental work of Pattanotai et al.,[55] who measured the product distribution in the pyrolysis of biomass sawdust (fine particles with size <1mm) at a low heating rate of 30 K/min.

(2) Kinetics for secondary reaction

For the secondary homogeneous tar reactions, the kinetic constants describing the homogeneous tar cracking are from Liden et al.[153] (for the conversion of tar to secondary non-condensable gases) and Di Blasi[154] (for the conversion of tar to secondary char).

Although previous experimental works have quantitatively analyzed the heterogeneous conversion of tarry vapors,[89, 133] so far and to our knowledge, little to nothing has been experimentally reported on the kinetic constants in describing the heterogeneous tar conversion. The extent of the heterogeneous tar conversion within the biomass particle depends on the heterogeneous reaction kinetics and the residence time of the tarry vapors within the particle.[89] The kinetic constants for the heterogeneous tar conversion were obtained by calibrating the model with the experimental data from Pattanotai et al.,[55] who found that about 5% of the tarry vapors primarily produced within a wood cylinder (8 mm in diameter and 9 mm in length) are converted into secondary char (54 wt.% on tar mass basis, indicating that 54 wt.% of the tarry vapors was heterogeneously converted into secondary char) and secondary non-condensable gases (46 wt.% on tar mass basis, indicating that 46 wt.% of the tarry vapors was heterogeneously converted into secondary non-condensable gases) at a heating rate of 30 K/min and to a final temperature of 873 K. In the review work from Mohan et al.,[16] the elemental composition of the tarry vapors (or bio-oil) was presented for typical biomass. It indicated that the carbon content of the tarry vapors ranged from 48 to over 70 wt.% depending on the type of raw biomass and pyrolysis conditions. The hydrogen content of the tarry vapors was around 7 wt.% while the remaining (ranging from 45 to 23 wt.%) can be regarded as the oxygen content. As such, pyrolysis vapors range in composition from $\text{CH}_{1.75}\text{O}_{0.70}$ to $\text{CH}_{1.20}\text{O}_{0.25}$. Assuming that only CO is coproduced as non-condensable gas together

with the formation of solid C (char) in the secondary reaction, then the maximum (calculated) yield of secondary char – based on stoichiometry – ranges from 14.4 to 52.3 wt.% (on a primary volatile weight basis). Assuming a coproduction of CO₂ instead of CO alters the maximum yield of secondary char to a range from 31.2 to 61.0 wt.%. However, as shown by Crombie and Masek,[155] the CO₂-to-CO ratio from pine chip slow pyrolysis can range from about 1.8 to 2.8 depending on the temperature and, considering that part of the oxygen bound to the primary volatiles will get removed through dehydration rather than decarbonylation/decarboxylation type reactions, it is reasonable to assume a secondary char yield of 54 wt.%, calculated as an upper average. One drawback with assigning a secondary char yield resulting from heterogeneous conversion of the primary vapors in the current model is that the primary vapors are considered as a single species. The model does not discern between tar species originating from different biomass constituents and the differences in secondary char yield amongst them. For instance, primary volatiles from cellulose mostly consist of anhydrosugars, like levoglucosan (C₆H₁₀O₅),[131] which can have a maximum theoretical secondary char yield of 44 wt% (assuming dehydration yielding pure carbon only) whereas pinewood lignin tar (CH_{1.22}O_{0.29} [156]) could potentially yield 67 wt% of secondary char.

The calibration was performed by simulating the pyrolysis of a wood cylinder with the same properties (particle size and density) and at the same pyrolysis conditions (heating rate and final temperature) as in the work of Pattanotai et al.[55] To simplify the calibration process, it was assumed that the heterogeneous formation of secondary char and secondary non-condensable gases within the cylinder are sharing the same activation energy but with different pre-exponential factors. A value of 92.4 KJ/mol was adopted for the activation energy, and this value was from the

work of Sadhukhan et al.,[81, 144] who obtained this value in characterizing the interaction between volatiles and char by fitting a kinetic model to experimental data obtained from pyrolysis of a large biomass particle. The kinetic parameters from the literature and from the calibration are summarized in Table 2.2.

Table 2.2 Kinetic constants for the primary and secondary pyrolysis reactions

Reactions	Frequency factor, s ⁻¹	Activation energy, kJ/mol
Primary reactions		
Biomass → Volatiles*	1.45 × 10 ¹⁰ ^a	148.6 ^a
Biomass → Primary char	4.40 × 10 ⁶ ^a	111.7 ^a
Homogeneous secondary reactions		
Tar → Secondary non-condensable gases	4.28 × 10 ⁶ ^b	108 ^b
Tar → Secondary char	1.00 × 10 ⁵ ^c	108 ^c
Heterogeneous secondary reactions		
Tar → Secondary non-condensable gases	46 % × 4.14 × 10 ⁸ ^e	92.4 ^d
Tar → Secondary char	54 % × 4.14 × 10 ⁸ ^e	

^a Di Blasi and Branca[152]

^b Liden et al.[153]

^c Di Blasi[154]

^d Sadhukhan et al.[81, 144]

^e Through calibration with the experimental data of Pattanotai et al.[55]

* The volatiles primarily produced from biomass are consisting of 62.6 wt.% of tar and 37.4 wt.% of non-condensable gases, which is in accordance with the experimental work of Pattanotai et al.[55]

2.2.2. Particle model description

The mass balances were developed first. The instantaneous concentration of the virgin biomass was expressed by ρ_w (kg/m³, density of biomass calculated with the mass of the particle and its volume), the primary char by ρ_{c1} , the secondary char by ρ_{c2} , the gas mixture by $\rho_{mixture}$, the inert gas by ρ_{inert} , the tar by ρ_t , and the primary and secondary non-condensable gases by ρ_{g1} and ρ_{g2} , respectively. The secondary char

concentration (ρ_{c2}) is the sum of the concentration of secondary char formed by homogenous tar conversion (ρ_{c21}) and by heterogeneous tar cracking (ρ_{c22}).

The mass balances for the solid phase are,

$$\text{Virgin biomass:} \quad \frac{\partial \rho_w}{\partial t} = -(k_t + k_{g1} + k_{c1})\rho_w \quad (2)$$

$$\text{Primary char:} \quad \frac{\partial \rho_{c1}}{\partial t} = k_{c1}\rho_w \quad (3)$$

$$\text{Secondary char:} \quad \frac{\partial \rho_{c2}}{\partial t} = k_{c21}\varepsilon\rho_t + \theta k_{c22}\varepsilon\rho_t \quad (4)$$

It was assumed that the reaction rate for the heterogeneous tar reaction is proportional to the mass fraction of char in the solid phase and the mass concentration (density) of the tarry vapors inside the particle. In Eq. (4) ε is the particle's porosity (see further) and θ is the mass fraction of char and is expressed as:

$$\theta = \frac{\rho_{c1} + \rho_{c2}}{\rho_w + \rho_{c1} + \rho_{c2}} \quad (5)$$

The mass balances for the gas mixture (including the tarry vapor, the non-condensable gases and the inert gas) are,

$$\underbrace{\frac{\partial(\varepsilon\rho_{\text{mixture}})}{\partial t}}_{\text{accumulation term}} + \underbrace{\nabla \cdot (\rho_{\text{mixture}} \mathbf{u}_{\text{mixture}})}_{\text{convective term}} = \underbrace{(k_t + k_g)\rho_w - k_{c21}\varepsilon\rho_t - \theta k_{c22}\varepsilon\rho_t}_{\text{source term}} \quad (6)$$

The transport equations for the tarry vapors and non-condensable gases inside the particle pores are,

$$\underbrace{\frac{\partial(\varepsilon\rho_t)}{\partial t}}_{\text{accumulation term}} + \underbrace{\nabla \cdot (\rho_t \mathbf{u}_{\text{mixture}})}_{\text{convective term}} = \underbrace{\nabla \cdot (D_{\text{eff},t} \nabla \rho_t)}_{\text{diffusive term}} + \underbrace{\left(k_t \rho_w - (k_{c21} + k_{g21}) \varepsilon \rho_t - \theta (k_{c22} + k_{g22}) \varepsilon \rho_t \right)}_{\text{source term}} \quad (7)$$

$$\underbrace{\frac{\partial(\varepsilon\rho_g)}{\partial t}}_{\text{accumulation term}} + \underbrace{\nabla \cdot (\rho_g \mathbf{u}_{\text{mixture}})}_{\text{convective term}} = \underbrace{\nabla \cdot (D_{\text{eff},g} \nabla \rho_g)}_{\text{diffusive term}} + \underbrace{\left(k_g \rho_w + k_{g21} \varepsilon \rho_t + \theta k_{g22} \varepsilon \rho_t \right)}_{\text{source term}} \quad (8)$$

Where $D_{\text{eff},i}$ ($i = t, g$) (m^2/s) is the effective diffusivity of tar and non-condensable gases in the particle pores, and $D_{\text{eff},i}$ ($i = t, g$) is expressed in Eq. (9) according to the theory of Millington and Quirk,[157]

$$D_{\text{eff},i} = \frac{4}{3} \varepsilon D_{\text{inert},i} \quad (i = t, g) \quad (9)$$

where $D_{\text{inert},i}$ ($i = t, g$) is the diffusivity of tar and non-condensable gases in the inert gas (N_2). Due to the complexity of the components in tar and non-condensable gases, model compounds were chosen as being representative of both the tar and the non-condensable gas fraction and whose diffusivity in inert gas was calculated. The diffusion coefficients of CO_2 (model compound representative of the non-condensable gases) and phenol (model compound representative of the tar) in N_2 were separately calculated according to the following correlation:[158]

$$D_{\text{inert},i} = 10^{-4} \frac{0.00143T^{1.75}}{PM_{\text{inert},i}^{0.5} \left[\left(\sum_v \right)_{\text{inert}}^{1/3} + \left(\sum_v \right)_i^{1/3} \right]^2} \quad (i = \text{phenol}, \text{CO}_2) \quad (10)$$

where T is the temperature (K), P is the absolute pressure (bar), $M_{\text{inert},i} = 2(1/M_{\text{inert}} + 1/M_i)^{-1}$ is the mean molecular weight (g/mol) of inert gas (N_2) and tar (phenol) or non-condensable gases (CO_2), and \sum_v is calculated for each component by summing atomic diffusion volumes, which can be found in Table 11-1

in the work of Poling et al.[158] This correlation is valid at lower and moderate pressure (up to 5 ~ 6 MPa). Even though the pyrolysis vapors are complex mixtures and contain many compounds (beyond phenol as model component), assuming an average chemical composition of the pyrolysis vapors of $\text{CH}_{1.4}\text{O}_{0.6}$ and with a mean molecular weight of ~100 amu (based on GC-MS) or a mean molecular weight of ~350 amu (based on GPC, including heavier tars)[159] and recalculating the diffusion coefficients (Eq. (10)), the order of magnitude of the characteristic times (i.e. for the intraparticle diffusion process, $10^{-5} \text{ m}^2 \cdot \text{s}^{-1}$) remained unaffected compared with using phenol as model compound to represent the pyrolysis vapors.

ε is the porosity,

$$\varepsilon = 1 - \frac{\rho_w + \rho_{c1} + \rho_{c2}}{\rho_{w0}} (1 - \varepsilon_{w0}) \quad (11)$$

Darcy's Law was used to describe the momentum transfer of the gas mixture in porous media. The superficial velocity of the gas mixture is defined as,

$$u_{\text{mixture}} = - \frac{B_{\text{eff}}}{\mu} \nabla P \quad (12)$$

where B_{eff} is the effective permeability (m^2) defined by the internal resistance of the particle to the bulk flow of the gas mixture, μ is the dynamic viscosity ($\text{kg}/(\text{m} \cdot \text{s})$) and P is the pressure (Pa). The effective permeability B_{eff} results from contributions by three parts: virgin biomass, primary char and secondary char. Due to the anisotropic properties of the particle, the effective permeability across and parallel to the grain direction was expressed as,

$$B_{\text{eff},j} = \frac{\rho_w B_{w,j} + (\rho_{c1} + \rho_{c2}) B_{c,j}}{\rho_w + \rho_{c1} + \rho_{c2}} \quad (j = \text{cross, parallel}) \quad (13)$$

The state equation was applied to describe the ideal behavior of the gas mixture,

$$P = \frac{\rho_{\text{mixture}} R_{\text{cons}} T}{MW_{\text{mixture}}} \quad (14)$$

The energy conservation equation incorporates the production/consumption of thermal energy due to exo/endergonic reactions. The energy conservation equation in Eq. (15) includes the accumulation of energy (the first term on the left of Eq. (15)), the convective heat transfer due to the bulk flow of the gas mixture inside the particle pore (the second term on the left of Eq. (15)), the conductive heat transfer in the particle (the first term on the right of Eq. (15)) and the heat source (the second term on the right of Eq. (15)).

$$\underbrace{\left(c_{p,w} \rho_w + c_{p,c} (\rho_{c1} + \rho_{c2}) + \varepsilon c_{p,t} \rho_t + \varepsilon c_{p,g} \rho_g + \varepsilon c_{p,\text{inert}} \rho_{\text{inert}} \right)}_{\text{accumulation term}} \frac{\partial T}{\partial t} + \underbrace{\left(c_{p,t} \rho_t + c_{p,g} \rho_g + c_{p,\text{inert}} \rho_{\text{inert}} \right) \mathbf{u}_{\text{mixture}} \cdot \nabla T}_{\text{convective term}} = \underbrace{\nabla \cdot (\lambda_{\text{eff}} \nabla T)}_{\text{conductive term}} + \underbrace{\underline{\underline{Q}}}_{\text{source term}} \quad (15)$$

where the heat source term, Q (W/m^3), is composed of the enthalpies of the primary and secondary reactions as shown in Fig. 2.1:

$$Q = -\rho_w (k_t \Delta H_t + k_{g1} \Delta H_{g1} + k_{c1} \Delta H_{c1}) - k_{c21} \varepsilon \rho_t \Delta H_{c21} - k_{g21} \varepsilon \rho_t \Delta H_{g21} - \theta k_{c22} \varepsilon \rho_t \Delta H_{c22} - \theta k_{g22} \varepsilon \rho_t \Delta H_{g22} \quad (16)$$

In the energy conservation equation, λ_{eff} is the effective thermal conductivity ($\text{W}/(\text{m}\cdot\text{K})$), which was calculated at any instant as the weighted sum of the thermal conductivities of virgin biomass, char (an average of primary and secondary char)

and gas mixture and also accounting for the radiative heat transfer through the pores:[94]

$$\lambda_{\text{eff},i} = \underbrace{\frac{\rho_w \lambda_{w,j} + (\rho_{c1} + \rho_{c2}) \lambda_{c,j}}{\rho_w + \rho_{c1} + \rho_{c2}}}_{\text{due to solid phase}} + \underbrace{\varepsilon \lambda_{\text{mixture}}}_{\text{due to mixture gas}} + \underbrace{\frac{13.5 \sigma T^3 d_{\text{eff}}}{e}}_{\text{due to radiation}} \quad (j = \text{cross, parallel}) \quad (17)$$

For the virgin biomass, the thermal conductivity across the grain was calculated according to,[160]

$$\lambda_{w,\text{cross}} = G(0.1941 + 0.004064 \cdot M + 0.01864) \quad (18)$$

where $G(= \rho_{w0}/\rho_{\text{water}})$ is the specific gravity based on the oven dry weight and volume at a given moisture content M (wt.%) (for the pyrolysis of a dry particle, the moisture content is zero). The thermal conductivity of virgin biomass parallel to the grain was assumed to be equal to 2.8 times of that across the grain ($\lambda_{w,\text{parallel}} = 2.8 \cdot \lambda_{w,\text{cross}}$).

The last term in Eq. (17) represents the radiative component and d_{eff} in this term is the effective pore diameter (m), which is calculated as,

$$d_{\text{eff}} = \frac{\rho_w d_w + (\rho_{c1} + \rho_{c2}) d_c}{\rho_w + \rho_{c1} + \rho_{c2}} \quad (19)$$

2.2.3. Initial and boundary conditions

Initially, the virgin biomass had a density of ρ_{w0} , and the densities of the products (char, tar, and non-condensable gases) were zero. The pores of the biomass particle was filled with inert gas with a density of $\rho_{\text{inert}0}$. The particle had an initial temperature of T_0 , and was exposed to the ambient pressure (P_0). Initially, the velocity of the gas mixture inside the particle pores was zero. The initial conditions are as follows,

$$\rho_w = \rho_{w0}, \rho_c = \rho_t = \rho_g = 0; \rho_{\text{inert}} = \rho_{\text{inert}0}; \rho_{\text{mixture}} = \rho_{\text{inert}0}; \quad (20)$$

$$T = T_0; u_{\text{mixture}} = 0 \text{ m/s}; P = P_0$$

The boundary conditions at the particle surface were defined by external conditions of pressure, constant mass concentration for the gas mixture and heat flux (convective and radiative heat flux), and they are expressed as follows:

$$\begin{aligned} P(t, r = r_p) &= P_0 \\ \rho_g(t, r = r_p) &= \rho_{g\text{-extraparticle}} \\ \rho_t(t, r = r_p) &= \rho_{t\text{-extraparticle}} \\ \rho_{\text{inert}}(t, r = r_p) &= \frac{P_0 MW_{\text{inert}}}{R_{\text{cons}} T_s} \\ -\mathbf{n} \cdot (-\lambda_{\text{eff}} \nabla T) &= h_{\text{convective}} (T_{\text{reactor}} - T_s) + \sigma e_s (T_{\text{reactor}}^4 - T_s^4) \end{aligned} \quad (21)$$

where $h_{\text{convective}}$ is the external convective heat transfer coefficient ($\text{W} \cdot \text{m}^{-2} \text{K}^{-1}$), T_{reactor} is the reactor temperature (K) and T_s is the surface temperature of the particle (K). $\rho_{g\text{-extraparticle}}$ and $\rho_{t\text{-extraparticle}}$ are the extra-particle concentrations ($\text{kg} \cdot \text{m}^{-3}$) of non-condensable gases and tarry vapor, respectively. Parameters in the model are listed in Table 2.3.

Table 2.3 Material properties for the model

Property	Value	Unit	Source
$C_{p,w}$	$1500 + 1.0 T$	$\text{J}/(\text{kg} \cdot \text{K})$	Gronli and Melaaen [148]
$C_{p,c}$	$420 + 2.09 T + 6.85 \times 10^{-4} T^2$	$\text{J}/(\text{kg} \cdot \text{K})$	Gronli and Melaaen [148]
$C_{p,t}$	$-100 + 4.4 T - 1.57 \times 10^{-3} T^2$	$\text{J}/(\text{kg} \cdot \text{K})$	Gronli and Melaaen [148]
$C_{p,g}$	$770 + 0.629 T - 1.91 \times 10^{-4} T^2$	$\text{J}/(\text{kg} \cdot \text{K})$	Gronli and Melaaen [148]
$C_{p,\text{inert}}$	$950 + 0.188 T$	$\text{J}/(\text{kg} \cdot \text{K})$	Gronli and Melaaen [148]
d_w	4×10^{-5}	m	Di Blasi [161]
d_c	4×10^{-4}	m	Di Blasi [161]
e	1	-	Park et al. [110]
e_s	0.95	-	Bates and Ghoniem [83]
λ_c	0.105 (along grain), 0.071	$\text{W}/(\text{m} \cdot \text{K})$	Di Blasi [93]

	(across grain)		
λ_{mixture}	0.0258	W/(m·K)	Gronli and Melaaen [148]
σ	5.67×10^{-8}	W/(m ² ·K ⁴)	Gronli and Melaaen [148]
B_w	1×10^{-11} (along grain), 1×10^{-14} (across grain)	m ²	Di Blasi [93]
B_c	5×10^{-11} (along grain), 5×10^{-12} (across grain)	m ²	Di Blasi [93]
μ	3×10^{-5}	kg/(m·s)	Di Blasi [93]
M_{inert}	0.028	kg/mol	
M_g	0.038	kg/mol	Gronli and Melaaen [148]
M_t	0.11	kg/mol	Gronli and Melaaen [148]
M_{phenol}	0.094	kg/mol	
M_{CO_2}	0.044	kg/mol	
$h_{\text{convective}}$	5	W/(m ² ·K)	Gronli and Melaaen [148]
R_{cons}	8.314	J/(mol·K)	
ϵ_0	0.4	-	Park et al. [110]
ρ_{water}	1000	kg/m ³	
$\rho_{\text{inert}0}$	$P_0 M W_{\text{inert}} / (R_{\text{cons}} T_0)$	kg/m ³	
ρ_{w0}	398	kg/m ³	Pattanotai et al.[55, 136]
	650	kg/m ³	Koufopoulos et al.[82]
T_0	383.15	K	Pattanotai et al.[55, 136]
	293.15	K	Koufopoulos et al.[82]
$\left(\sum \nu\right)_{\text{inert}}$	18.50	-	Poling et al. [158]
$\left(\sum \nu\right)_{\text{phenc}}$	97.07	-	Poling et al. [158]
$\left(\sum \nu\right)_{\text{CO}_2}$	26.90	-	Poling et al. [158]

2.3. Model implementation

The models for the chemical and physical processes during particle pyrolysis were implemented into the commercial software of COMSOL Multiphysics® 5.0, which is a finite element analysis software package. This software was used to solve the ordinary differential equations (ODEs) and partial differential equations (PDEs) involved in the kinetic and particle models. Considering the anisotropic structure of the wood biomass, the geometry of the particle was represented as a three-dimensional object in COMSOL Multiphysics®. The size of the three-dimensional object in the simulation was the same as the biomass particle size in the experimental work against which the model was validated. The unstructured grid was

adopted for the three-dimensional biomass particle, as shown in Fig. 2.2 for a cylindrical particle with a diameter of 8 mm and a length of 9 mm (grids for other particles are similar). Mesh details are summarized in Table 2.4

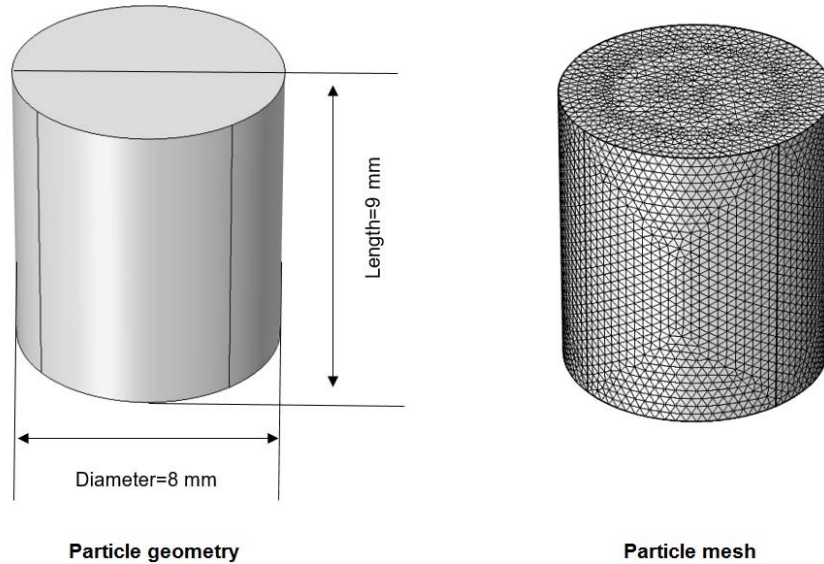


Fig. 2.2 Geometry and mesh for a cylindrical particle with a diameter of 8 mm and a length of 9 mm

Since the particle was assumed as a continuum porous matrix, porosity was used to describe the effect of internal structure on the intraparticle transport of gas mixtures. For simulating particle shrinkage as described in Section 2.5.2 and Section 3.4, the method of Deformed Geometry in COMSOL Multiphysics® was used. With the method of Deformed Geometry, the geometry of the biomass particle shrinks with a radial (diameter)/axial (length) size reduction rate proportional to the conversion process of the virgin biomass, as described in Section 2.5.2.

Table 2.4 Mesh details for simulating the pyrolysis of a biomass particle

Cylinder dimensions, d × L	For validation against Pattanotai et al. [55, 136]				For validation against Koufopoulos et al. [82]	
	Fine spherical particle with 1mm in diameter	8mm × 2mm	8mm × 5mm	8mm × 9mm	Fine spherical particle with 0.3mm in diameter	20mm × 100mm
Number of domain elements	8311	76479	194666	247289	8349	530769
Number of boundary elements	840	5410	7732	8500	840	16364
Number of edge elements	96	212	256	276	96	528
Minimum element size, m	1.80×10^{-5}	1.20×10^{-5}	1.20×10^{-5}	1.35×10^{-5}	5.40×10^{-6}	1.00×10^{-4}
Maximum element size, m	1.00×10^{-4}	2.80×10^{-4}	2.80×10^{-4}	3.15×10^{-4}	3.00×10^{-5}	1.00×10^{-3}
Maximum element growth rate	1.50	1.35	1.35	1.35	1.50	1.35

2.4. Model validation

2.4.1. Comparison with Pattanotai et al.[55, 136]

To validate the primary reaction kinetics, the char yield from the pyrolysis of dry Japanese cypress sawdust (fine particles with size <1 mm) in the experimental work of Pattanotai et al.[55] was compared with the modeling results. The heating rate was 30 K/min and the final temperature was 873 K. The cypress sawdust particles were modeled as spherical particles with a diameter of 1 mm in the model, which coupled the primary reaction kinetics (Section 2.2.1) and the particle model (Section 2.2.2).

To validate the simultaneous reaction kinetics and the particle model for centimeter-sized particles, the experimental results from different works of Pattanotai et al.[136] were used. Pattanotai et al.[136] performed pyrolysis on dry Japanese cypress sawdust (with particle size <1 mm) and dry Japanese cypress wood

cylinders with a diameter of 8mm and lengths of 2, 5, and 9 mm at the same heating rate of 60 K/min and to the same final temperature of 1173 K. The differences of the product yields (mainly tar yield and char yield) between the sawdust and the wood cylinders at this low heating rate were believed to be due to the conversion of the tarry vapors within the wood cylinder.[136] Therefore, the observed amount of tar experiencing secondary conversion and the amount of secondary char formed within these cylinders were adopted for validating the model, which couples the primary and secondary reaction kinetics (Section 2.2.1) and the particle model (Section 2.2.2).

In the simulation, the reaction heat was assumed to be endothermic for the primary reactions ($\Delta H_t = \Delta H_{g1} = \Delta H_{c1} = 68 \text{ KJ}\cdot\text{kg}^{-1}$ [110]) and exothermic for the secondary reactions. More specifically, the reaction heat for the homogeneous tar cracking was equal to $\Delta H_{c21} = \Delta H_{g21} = -42 \text{ KJ}\cdot\text{kg}^{-1}$, [110] and for the heterogeneous tar conversion, it was equal to $\Delta H_{c22} = \Delta H_{g22} = -245 \text{ KJ}\cdot\text{kg}^{-1}$ [144]).

2.4.2. Comparison with Koufopoulos et al.[82]

The pyrolysis of both fine (0.30~0.85 mm in diameter) and centimeter-sized (cylindrical particle with a diameter of 2 cm and a length of 10 cm) wood particles was conducted in the experimental work of Koufopoulos et al.[82] In order to examine the ability of the model in predicting the primary product (mainly char) yields, the experimental results of the isothermal pyrolysis of dry fine wood particles at operating temperatures of 623, 673 and 873 K were used for comparison. The fine particle was assumed as a spherical particle with a diameter of 0.30 mm in the model, in which the primary reaction kinetics (Section 2.2.1) and the particle model (Section 2.2.2) were coupled. The predicted char yields were also compared with the experimental data for the isothermal pyrolysis of centimeter-sized wood cylinders at 623 and 773 K, respectively. The model for the centimeter-sized wood cylinder coupled the primary

and secondary reaction kinetics (Section 2.2.1) and the particle model (Section 2.2.2). Besides, the experimental temperature profiles at the center (for the case at the operating temperature of 623 and 773 K) and at a distance of $r_p/2$ (for the case at the operating temperature of 673 K) of these centimeter-sized particles were also compared using the model.

In order to capture the temperature profile inside the centimeter-sized cylindrical particles, both the primary reactions and the secondary tar conversion were assumed to be exothermic with a reaction heat for the primary reactions being equal to $\Delta H_t = \Delta H_{g1} = \Delta H_{c1} = -100 \text{ kJ}\cdot\text{kg}^{-1}$. The latter value was obtained through calibration of the model. For the secondary reaction, the reaction heats were equal to $\Delta H_{c1} = \Delta H_{g21} = -42 \text{ kJ}\cdot\text{kg}^{-1}$ [110] for the homogeneous tar cracking, and $\Delta H_{c22} = \Delta H_{g22} = -245 \text{ kJ}\cdot\text{kg}^{-1}$ [144] for the heterogeneous tar conversion. The remaining model parameters were the same as those in modeling the case of Pattanotai et al.[55] The heat of reaction in Koufopoulos et al.[82] was different from that of Pattanotai et al.[55, 136] Generally, the heat of reaction is difficult to assess, and it is usually regarded as an adjustable parameter by calibrating the simulation results with the experimental data.[162] The heat of reaction depends on the experimental setup and the heating conditions.[110, 147] Since the experimental conditions in Koufopoulos et al.[82] were quite different from the work of Pattanotai et al.,[55, 136] the model used different heats of reaction for comparing with the experimental data from these two different research groups. Additionally, a factor contributing to the variability in the reaction heats after calibrating to different experimental datasets is that the current model treats both the biomass as well as the ensuing primary volatiles as two single species. However, the individual heats of reaction for the decomposition of the biomass constituents (cellulose, hemicellulose and lignin) as well as for the secondary reactions involving

the resulting volatiles are different.[78, 163] Consequently, differences in biomass feedstock composition result in variability of the overall heats of reaction for which the current model can only calibrate rather than relying upon underlying (i.e. more detailed) reaction kinetics.

2.4.3. Model error quantification

For each validation, the performance of the model was determined by calculating the mean deviation (MD) by using Eq. (22) for time-dependent variables such as mass and temperature, and using Eq. (23) for variables which are only quantified upon termination of the pyrolysis reaction such as char yield and fraction of tar converted.

$$MD = \frac{1}{n} \sum_{i=1}^n |X_{\text{exp}}(t_i) - X_{\text{mod}}(t_i)| \quad (22)$$

$$MD = |X_{\text{exp}}(t_n) - X_{\text{mod}}(t_n)| \quad (23)$$

In Eqs. (22) and (23) $X_{\text{mod}}(t)$ is the model-predicted variable, $X_{\text{exp}}(t)$ is the experimental variable and n is the number of times at which an observation or model-prediction has been made.

2.5. Model adaptations

2.5.1. Sensitivity analysis

The sensitivity analysis was performed to study the effects of various process conditions, including heating rate, peak temperature, the gas phase pressure surrounding the particle and the extra-particle concentration of the tarry vapor, on the pyrolysis of the wood cylinder with a similar configuration as used in Pattanotai et al.[55] Peak temperature refers to the highest reactor temperature reached during the

pyrolysis of the wood cylinder (also called highest treatment temperature). The studied peak temperatures ranged from 573 to 873K (at a heating rate of 30 K/min) and the studied heating rates ranged from 3 to 30 K/min (with a peak temperature of 873K). At each peak temperature, the effects of pressure (absolute pressure of 1, 2, 5, 10, and 25 atm) for the gas phase surrounding the wood cylinder were compared by particularly focusing on the secondary heterogeneous reactions of the tarry vapors inside the wood cylinder.

Practically, the gas phase surrounding the biomass particle is a mixture of non-condensable gases, tarry vapors and inert gas, among which the tarry vapors are reactive. The extra-particle concentration of the tarry vapors can affect the product yields by influencing the diffusion of the tarry vapors depending on their concentration difference between the internal and the external of the particle. At atmospheric pressure with a heating rate of 30K/min and a peak temperature of 873K, the effect of the extra-particle concentration of the tarry vapors (the extra-particle concentration of the non-condensable gases in Eq. (21) is always assumed to be zero since this parameter exerts negligible influence on the pyrolysis process) was studied by changing the value from 0 to 0.9 mol/m³, which implies that in the latter case, the extra-particle volume fraction of the tarry vapors is about 1 % of the gas mixture (inert gas and tarry vapor) surrounding the particle according to the ideal gas law.

2.5.2. Study of particle shape and size reduction

Since pyrolysis units often treat biomass particles with various geometries and shapes, a parameter, aspect ratio (for a cylinder, the aspect ratio is defined as the ratio of length to diameter), is often introduced to characterize the effect of particle geometry.[91, 136, 137] Biomass particles have typical aspect ratios between 2 and

15.[91] Aspect ratios ranging from 0.1 (flake-like) to 14 (needle-like) were studied (at atmospheric pressure with a heating rate of 30 K/min and a peak temperature of 873K) and particles with different aspect ratios share the same volume and mass as the wood cylinders used in the experimental work of Pattanotai et al.[55]

It is frequently reported that size reduction of biomass particles happens during the thermochemical conversion, which is mainly due to particle shrinkage and particle attrition, splitting or fragmentation.[110, 136, 161, 164, 165] It is also reported that biomass particles suffer size shrinkage during the pyrolysis process with a size reduction of 20~30% .[161] In another work of Pattanotai et al.,[136] they found that the diameter and the length of the wood cylinder shrunk about 40% and 30%, respectively, during the pyrolysis process at a relatively low heating rate. The effect of particle shrinkage (with diameter shrinking 40% and length shrinking 30% during the pyrolysis process) was studied at various pressures (absolute pressure of 1, 2, 5, 10, and 25 atm) with a heating rate of 30 K/min and a peak temperature of 873 K. It was assumed that the wood cylinder from Pattanotai et al.[55] shrinks with a radial (diameter)/axial (length) size reduction rate proportional to the conversion process of the virgin biomass,

$$u_{\text{shrink,radial}} = \frac{f_{\text{radial}} d_{p0}}{\rho_{w0}} \frac{\int \frac{\partial \rho_w}{\partial t} dV}{\int dV} \quad \text{and} \quad u_{\text{shrink,axial}} = \frac{f_{\text{axial}} l_{p0}}{\rho_{w0}} \frac{\int \frac{\partial \rho_w}{\partial t} dV}{\int dV} \quad (1)$$

Where f_{radial} is the radial shrinking percentage ($f_{\text{radial}} = 0.4$), f_{axial} is the axial shrinking percentage ($f_{\text{axial}} = 0.3$). Furthermore, d_{p0} and l_{p0} are the initial values of the diameter (0.008m) and length (0.009m) respectively. The term of $\frac{\int \frac{\partial \rho_w}{\partial t} dV}{\int dV}$ equals

the volume-averaged conversion rate of the virgin biomass.

With respect to particle splitting, it was believed that the biomass particle retains its original morphology during pyrolysis conditions, and the biomass particle can break into a number of fragments with a broad range of sizes.[166] It is still unclear to what extent the particle splitting will affect the biomass pyrolysis process, especially under different heating conditions. A spherical biomass particle with an initial diameter of 1cm and a density of 398 kg/m³ was simulated under two different reactor temperatures ($T_{\text{reactor}} = 573 \text{ K}$ and 873 K) in order to investigate the effect of particle splitting. Normally, the biomass particle would break into a smaller fragment and a larger fragment. While the smaller fragment can be quickly converted, the larger one needs more time to be fully converted, and the conversion process of the larger fragment contributes more to the final residual mass fraction (char yield) and the conversion time due to its larger weight than the smaller fragment. As a special case, the biomass particle may break into two equal parts. It was assumed that the spherical particle breaks into two equal parts (two half-spherical daughter particles). Even though the particle may not exactly break into two equal parts as described earlier, this assumption allows for a relatively simple and concise analysis of the splitting effect. Since the time at which the particle splitting (indicated as 'splitting-time') happens is uncertain, two cases were compared: one case without particle splitting, and another case with particle splitting at two different splitting-times (one at the beginning of the pyrolysis and one at the time at which the total solid mass fraction is 0.80). In COMSOL Multiphysics®, the particle splitting can be achieved by regarding the particle's instantaneous parameters at the time when the particle splitting happens as the initial conditions for the subsequent numerical study of the daughter particles after the splitting.

In order to simulate the particle splitting occurring at the beginning of the pyrolysis, the spherical biomass particle was assumed to be cut into two equal half-spherical parts, and only one half-spherical part was further simulated. The half-spherical biomass particle was initially exposed to the given heating conditions, and the pyrolysis process was simulated until the virgin biomass was completely converted. For the case with particle splitting occurring at the time when the total solid mass fraction was 0.80, the whole spherical biomass particle was simulated to undergo pyrolysis at given initial and boundary conditions before the particle splitting happened. Once the total solid mass fraction reached the value of 0.80, the spherical particle was assumed to be cut into two equal half-spherical parts, and only one half-spherical particle was simulated to undergo further pyrolysis. In COMSOL Multiphysics®, when the particle splitting happens, the boundary conditions including the instantaneous parameters (spatial distributions of temperature, virgin biomass fraction, primary and secondary char fraction, and all other pyrolysis parameters) recorded in the whole spherical particle simulation were copied to the initial conditions of a new simulation case (i.e. of the half-spherical particle).

3. Results and discussion

3.1. Model validation

3.1.1. Comparison with Pattanotai et al. [55, 136]

The predicted char yield for the pyrolysis of Japanese cypress sawdust (at a heating rate of 30 K/min and a final temperature of 873 K) was 0.25, which is close to the experimental value of 0.245 in the work of Pattanotai et al., [55] demonstrating the reliability of the kinetics for the primary pyrolysis reaction.

Table 2.5 summarizes the comparison between the modeling results and the experimental data of the amount of tar experiencing secondary conversion and secondary char formed within the cylinder from another work of Pattanotai et al.[136]

Table 2.5 Comparison between the model prediction and the experimental data from Pattanotai et al. [136] for tar conversion and secondary char formation in wood cylinders; results expressed as percentage relative to dry feedstock weight.

Cylinder dimensions, d × L	Tar conversion			Secondary char yield		
	8mm × 2mm	8mm × 5mm	8mm × 9mm	8mm × 2mm	8mm × 5mm	8mm × 9mm
Experimental data, wt. %	4.6 ± 2.7	5.3 ± 2.5	7.2 ± 2.4	0.6 ± 0.6	1.5 ± 0.5	2.0 ± 0.5
Model prediction, wt. %	1.8	4.9	6.7	1.0	2.7	3.7

Table 2.5 indicates that the predicted values were in good agreement with the experimental data. The mean deviation (MD) between experiment and model for the secondary tar conversion was 1.2 wt.% and for the secondary char yield 1.1 wt.%. The heterogeneous reaction rate of the tarry vapors was found to be significantly faster than the homogeneous reaction rate, and most of the tarry vapors experienced heterogeneous conversion within the particle. The modeling results show that more tar is converted within the particle as the length of the biomass cylinder increases (at the same diameter), which was also observed in the experiments described by Pattanotai et al.[136] The predicted amount of secondary char formed within the biomass cylinder was over-predicted slightly compared to the experimental results. One possible explanation can be the omission of particle shrinkage in the model as in the experiments[136] shrinkage of the biomass particle was indeed observed. The

exclusion of particle shrinkage in the model tended to over-predict the conversion of the tarry vapors within the particle (hence higher amount of secondary char), which has also been addressed in the literature[161] and will be further discussed in Section 3.4.

3.1.2. Comparison with Koufopoulos et al. [82]

Table 2.6 shows the comparison between the modeling results and the experimental data for the pyrolysis of fine wood particles at various operating temperatures. Table 2.6 indicates that the present model can reasonably predict the char (primary char) yield at different temperatures with a MD of 3 wt.%. Furthermore, it was predicted that char yield for the wood sawdust decreases when the operating temperature increases. This trend is in accordance with previous experimental results.[34, 90] Table 2.6 indicates that the model can predict to an acceptable extent the qualitative trends with respect to the char yield, despite that some quantitative differences were present.

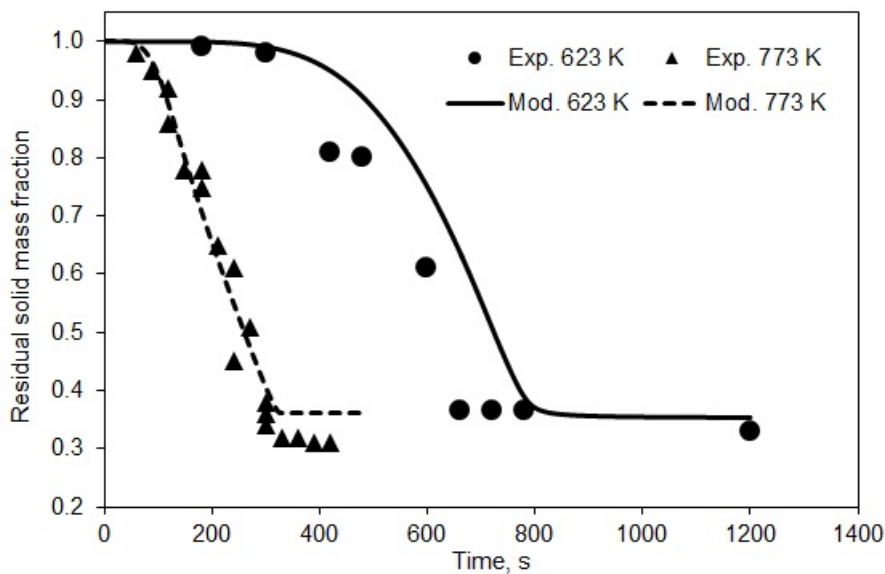
Table 2.6 Comparison between the model predicted and experimental char yield of fine wood particles, results expressed in weight percentage (on feedstock dry basis).

Experimental data from Koufopoulos et al. [82]

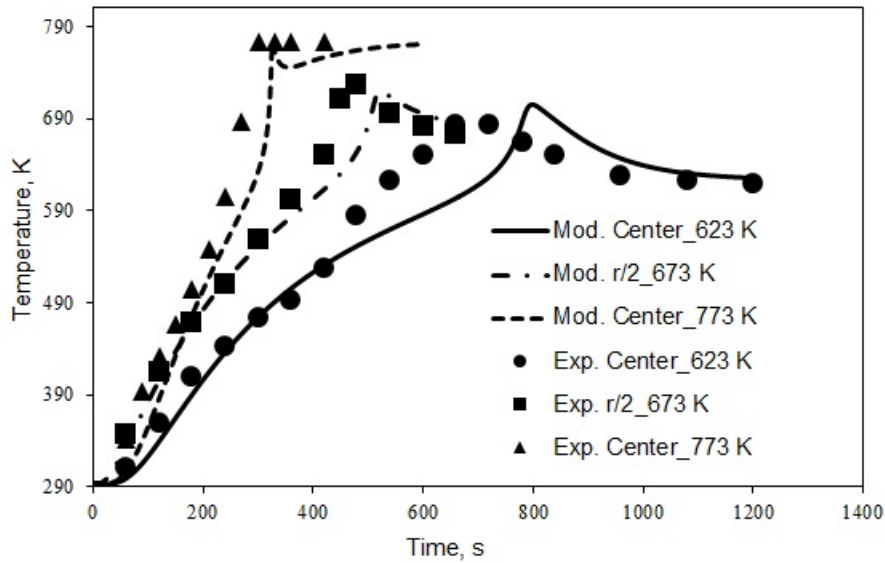
Pyrolysis temperature, K	623	673	873
Experimental char yield, wt%	20	20	14
Model predicted char yield, wt%	28	20	13

Fig. 2.3(a) and Fig. 2.3(b) further compare the predicted solid mass and temperature profiles with the experimental data for the pyrolysis of centimeter-sized cylindrical particles. Fig. 2.3(a) shows that the predicted evolution of solids mass matched well with the experimental data. The MD of the dynamic solid mass

throughout the pyrolysis process was 6.0 wt.% (with the MD on final char mass yield being 3.6 wt%). Fig. 2.3(b) shows that the present model could capture the main characteristics of the temperature profile inside the cylindrical particle, with a mean deviation (MD) between model and experiment of 30.6 K, with the largest discrepancies found when nearing the peak temperature in biomass pyrolysis. The model predicts that the peak temperature inside the particle surpasses the operating temperature at the final stage of the pyrolysis, which is due to the strong exothermic primary and secondary reactions, and this temperature behavior was also observed in the experiments, albeit with a minor misalignment of the process time at which this peak temperature occurs in the case of pyrolysis at 623 K.



(a)



(b)

Fig. 2.3 Comparison of residual solid mass fraction at 623 and 773 K (a) and temperature profiles at centre and half-centre position at 623, 673 and 773 K (b) between the model results and the experimental data of Koufopoulos et al.[82] (atmospheric pressure,

$$\rho_{g\text{-extraparticle}} = \rho_{t\text{-extraparticle}} = 0 \text{ kg/m}^3).$$

3.2. Instantaneous pyrolysis behavior of a wood cylinder

Fig. 2.4(a) shows the model-predicted evolution of solid mass including its fraction in primary and secondary char in a wood cylinder undergoing pyrolysis at 873 K. Fig. 2.4(a) to Fig. 2.4(h) show the pyrolysis behavior along the radial and axial directions of a wood cylinder at a simulated time of 640s. Fig. 2.4(b) shows that the temperature (at $t = 640$ s specifically) at the center of the cylinder is 5 to 10 K lower than the temperature near the surface, due to which the decomposition of the virgin biomass and the formation of the primary char are relatively lower at the particle center, resulting in higher content of virgin biomass and a lower content of primary char at the particle center, as shown in Fig. 2.4(c) and Fig. 2.4(d), respectively. Fig. 2.4(e) shows that the content of the secondary char is higher near the particle center.

As expressed in Eq. (4), the formation of secondary char is a function of temperature, residence time and concentration of the tarry vapors and the mass fraction of char in the solid phase. Longer residence time and higher concentration of the tarry vapors near the center of the wood cylinder are responsible of the formation of the secondary char, which is in accordance with previous statements.[51, 65] As the volatiles (tarry vapors and non-condensable gases) form within the wood cylinder, the concentration of the volatiles is higher at the particle center, building a higher pressure (Fig. 2.4(f)), which pushes the volatiles to flow out of the particle with a velocity as shown in Fig. 2.4(g). Fig. 2.4(g) shows that the volatiles find their way to leave the particle with a velocity much higher along the axial direction than along the radial direction of the cylinder, which is due to the higher permeability of the virgin biomass and the char along the axial direction. Pattanotai et al.[137] in their experimental work also indicated that the volatiles tend to be transported predominantly along the axial direction. Besides, part of the volatiles move to the particle surface due to diffusion (Fig. 2.4(h)). As the tarry vapors are transported towards the particle surface, they will contact the hot char, inducing the heterogeneous conversion of the tarry vapor, which produces secondary non-condensable gases and secondary char. The tarry vapors near the particle center experience longer residence times within the particle than those near the particle surface, which contributes to the higher secondary char yield at the inner part of the particle, as shown in Fig. 2.4(e).

The simulations assumed zero concentration for non-condensable gases and tarry vapors outside the biomass particle, which could potentially overestimate the diffusive flux as in practice, the concentrations of non-condensable gases and tarry vapors outside the biomass particle are not zero (which depends on the pyrolysis

reactor type used, whether an inert sweep gas is used to remove volatiles, etc.). The accuracy of the simulation results of an actual pyrolysis process may be improved if the transient concentration distributions of species including non-condensable gases and tarry vapors outside the biomass particle were implemented into the particle model, which was beyond the scope of the present study.

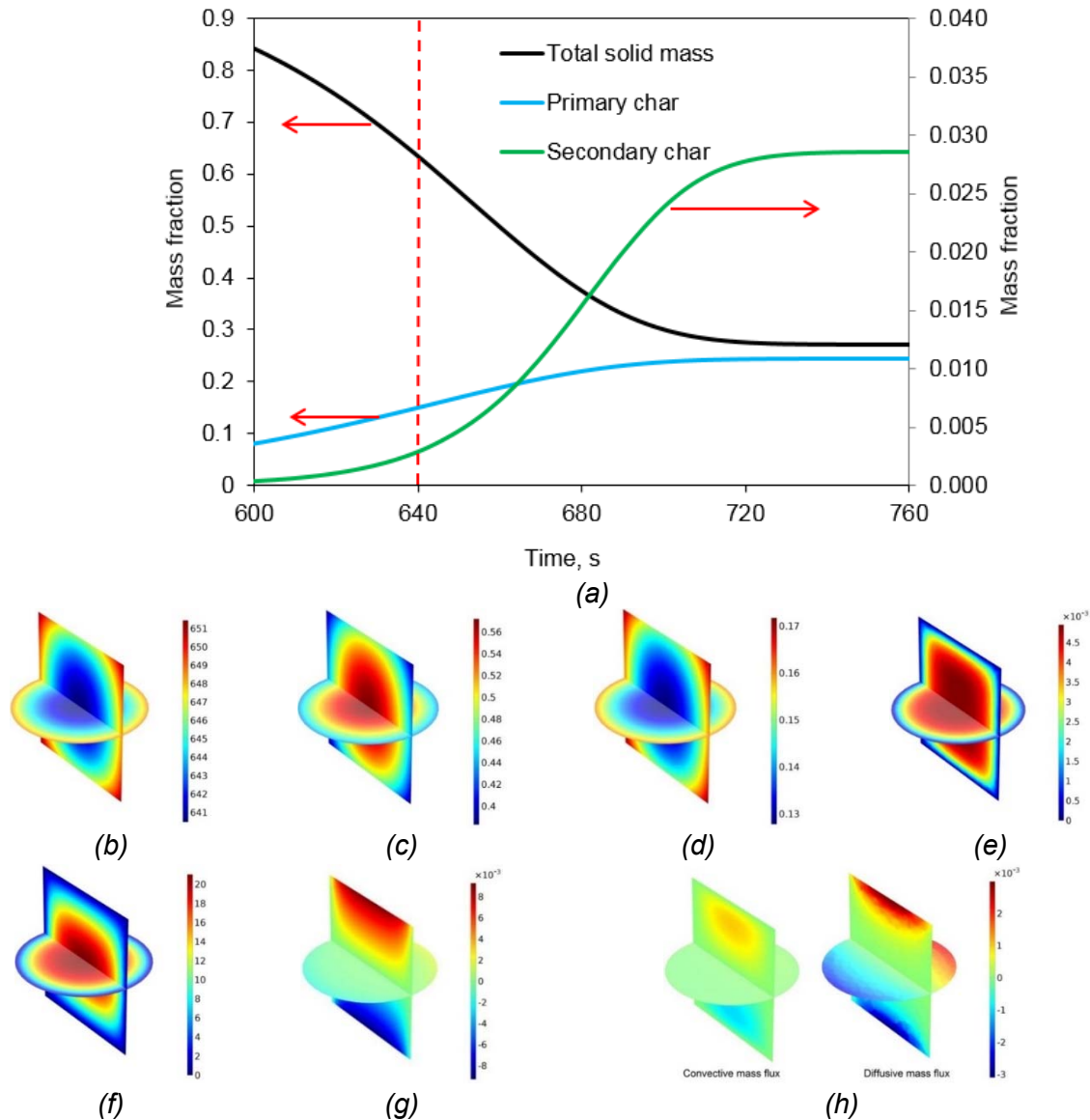


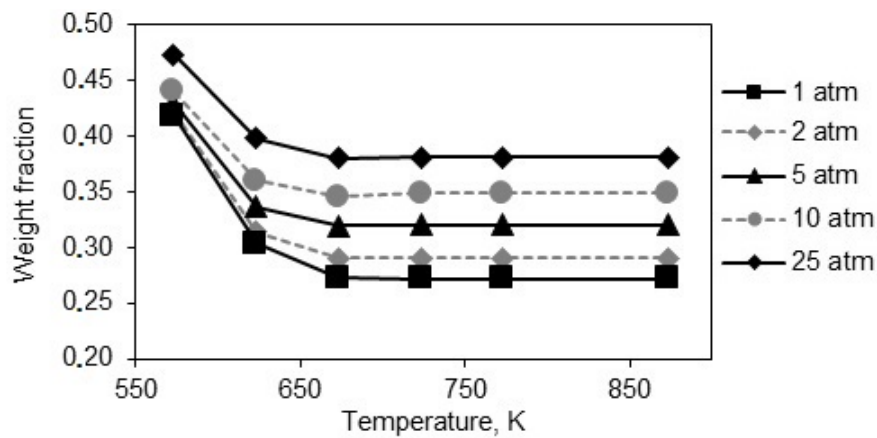
Fig. 2.4 Model-predicted evolution of solid mass (including primary and secondary char) (a) and instantaneous spatial distributions of temperature, K (b), virgin biomass mass fraction (c), primary (d) and secondary char mass fraction (e), gauge pressure, Pa (f), velocity field, m/s (g) and mass flux of the tarry vapors, kg/(m²s) (h) during the pyrolysis of the wood

cylinder at the simulated time of 640s (heating rate = 30 K/min, peak temperature = 873 K,

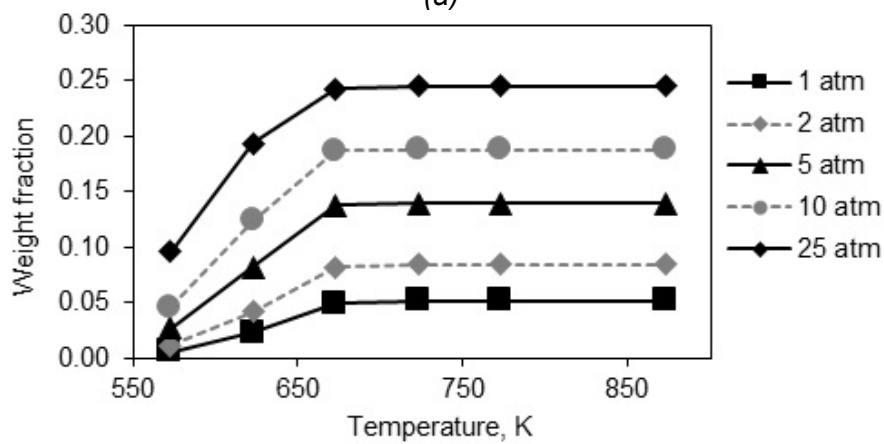
atmospheric pressure, $\rho_{g\text{-extraparticle}} = \rho_{t\text{-extraparticle}} = 0 \text{ kg/m}^3$).

3.3. Effect of process conditions

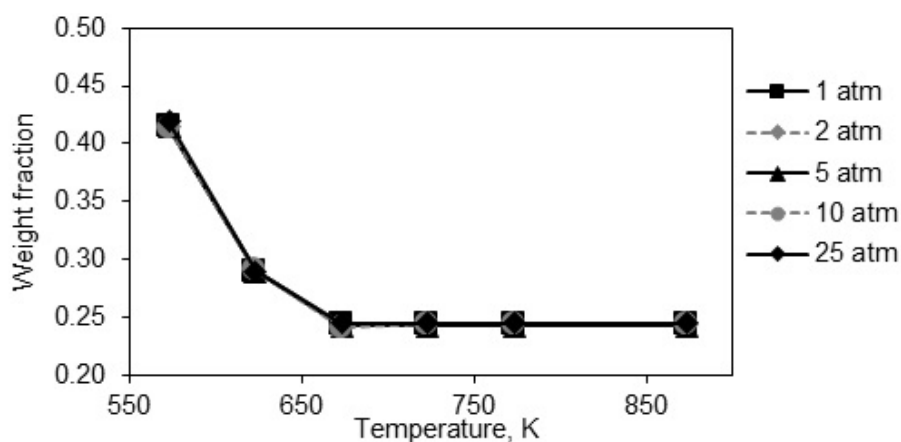
Fig. 2.5 shows the effects of pyrolysis peak temperature and pressure on the pyrolysis of the wood cylinder.



(a)



(b)



(c)

Fig. 2.5 Model results of the effect of peak temperature at various pressures on total char yield (a), heterogeneous tar conversion (b) and primary char yield (c) (heating rate = 30 K/min, $\rho_{g\text{-extraparticle}} = \rho_{t\text{-extraparticle}} = 0 \text{ kg/m}^3$).

Fig. 2.5(a) shows that with the decrease of peak temperature and the increase of pressure, the total char yield increases. This trend is in qualitative agreement with the previous experimental observations.[34, 90] The increased total char yield is mainly due to the increased yield of the primary char when peak temperature decreases (Fig. 2.5(c)). Under atmospheric pressure (0.1MPa), the predicted total char yield changes from 42 to 27 wt.% as the peak temperature increases from 573 to 723 K. Above 723 K, the predicted char yield is constant, which was due to the fact that the pyrolysis process has already been finished under the slow heating rate of 30K min^{-1} when temperature is higher than 700K. Ronsse et al.[34] experimentally studied the slow pyrolysis of several types of biomass with sizes of several millimeters, and they also observed that the char yield reduced from about 40 to around 30 wt.% as the peak temperature increased from 573 to 723 K, above which the char yield almost remained unchanged with increasing peak temperature.

When the pressure increased from 0.1 to 2.5 MPa, Fig. 2.5(a) shows that the total model-predicted char yield increased by about 5 wt.% at 573 K while at 873 K, it

increased by about 11 wt.%, which indicates that the pressure effect is more important at higher peak temperature since the heterogeneous conversion of the tarry vapors is favored at higher peak temperatures, as shown in Fig. 2.5(b). The higher total char yield at higher pressure is due to the significant heterogeneous conversion of the tarry vapors within the particle, as shown in Fig. 2.5(b). Under higher pressure, the mass concentration of the tarry vapors is higher and the specific volume of the volatiles (tar and non-condensable gases) is lower, building a lower pressure difference between the core and the outer area of the particle, which creates a lower velocity for the volatiles moving out of the particle resulting in longer residence times. The diffusivity of the tarry vapors is also lower at higher pressure according to Eq. (10). Both the decreased volatile velocity and tarry vapors diffusivity prolong the residence time of the tarry vapors within the particle. The combined results of longer residence time and higher mass concentration of the tarry vapors within the biomass particle at higher pressure contribute to the heterogeneous conversion of the tarry vapors to form secondary char (and secondary non-condensable gases).

Fig. 2.6 compares the effects of heating rate on the pyrolysis of the wood cylinder. It can be observed that the total char yield increases as the heating rate decreases, which is mainly due to the increased yield of primary char, as shown in this figure. This trend was also found in previous works.[90] It was also predicted that the production of secondary char increased with the increase of the heating rate.

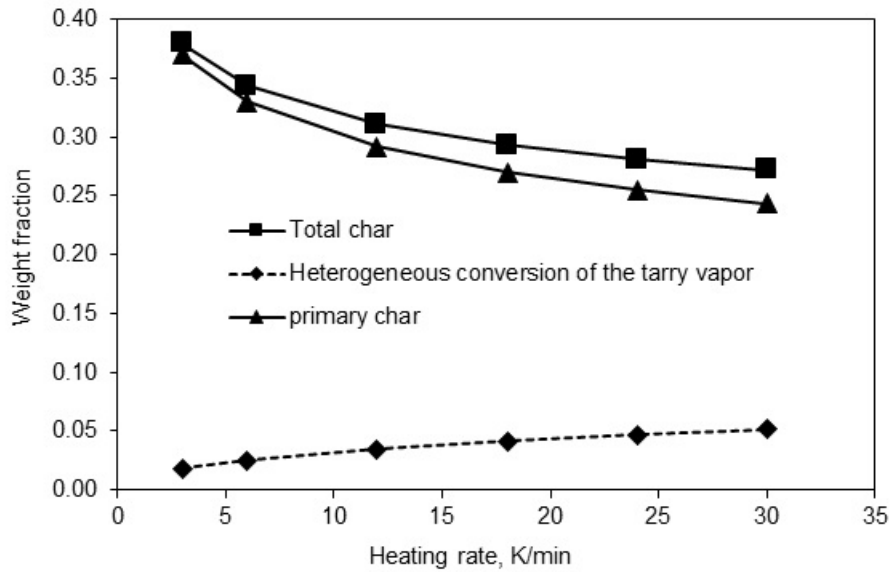


Fig. 2.6 Model results of the effect of heating rate on total char yield, heterogeneous tar conversion and primary char yield (peak temperature = 873 K, atmospheric pressure,

$$\rho_{g\text{-extraparticle}} = \rho_{t\text{-extraparticle}} = 0 \text{ kg/m}^3).$$

As for the effect of the extra-particle concentration of the tarry vapors, Fig. 2.7 indicates that the secondary char yield proportionally increases as the extra-particle tarry vapor concentration increases. At a higher extra-particle tarry vapor concentration, the concentration difference of the tarry vapors between the internal and the external of the particle becomes smaller, resulting in a lower driving force for the tarry vapors produced inside the particle to diffuse outward, which increases the residence time of the tarry vapors inside the particle, promoting their heterogeneous reaction with the hot char. Besides, the tarry vapors outside the particle can diffuse into the particle at the initial and final stage of the pyrolysis process when the concentration of the tarry vapors produced inside the particle is lower than the extra-particle concentration, which indicates that the concentration of the tarry vapors inside the particle will increase with the extra-particle concentration, and this can also facilitate the heterogeneous conversion of the tarry vapors inside the particle.

Modeling results are qualitatively consistent with previous conclusions that high concentration and prolonged vapor-phase residence time of the tarry vapors in the reaction zone favor the secondary char formation.[51]

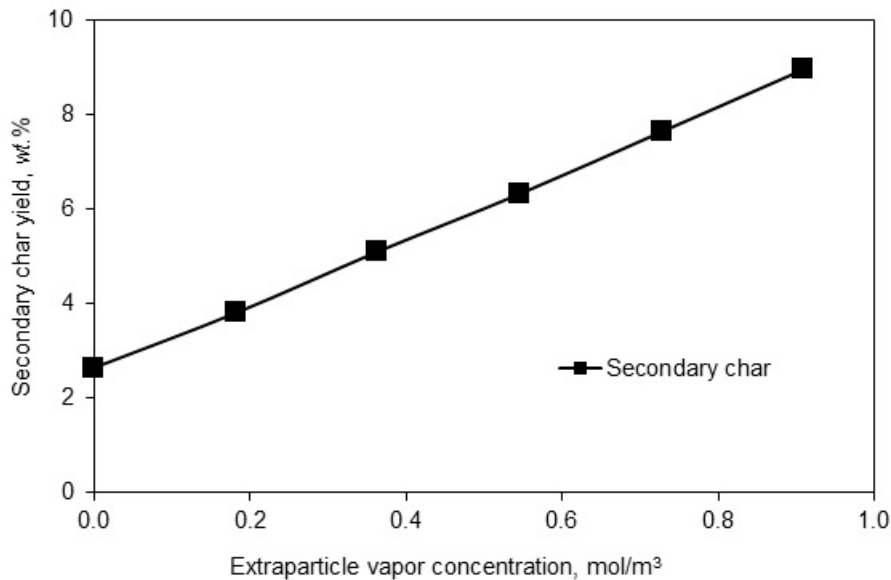


Fig. 2.7 Model results of the effect of the extra-particle tarry vapor concentration on secondary char yield (heating rate = 30 K/min, peak temperature = 873 K, atmospheric pressure, $\rho_{g\text{-extraparticle}} = 0 \text{ kg/m}^3$).

3.4. Effect of particle shape and particle size reduction

Fig. 2.8 shows the effects of aspect ratio on the pyrolysis of wood cylinders that share the same initial volume and mass. The model-predicted results show that the primary char yield is not affected by the aspect ratio, which is due to the similar uniform temperature distribution inside particles with different aspect ratios at the slow heating rate used (30 K/min). However, Fig. 2.8 indicates that the aspect ratio influences the heterogeneous conversion of the tarry vapors and hence the production of the secondary char, which further alters the total char yield.

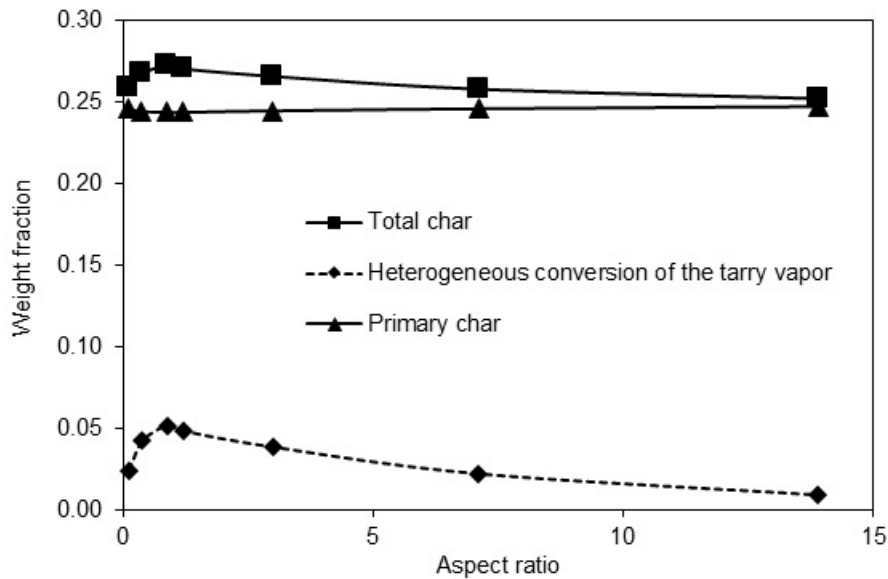


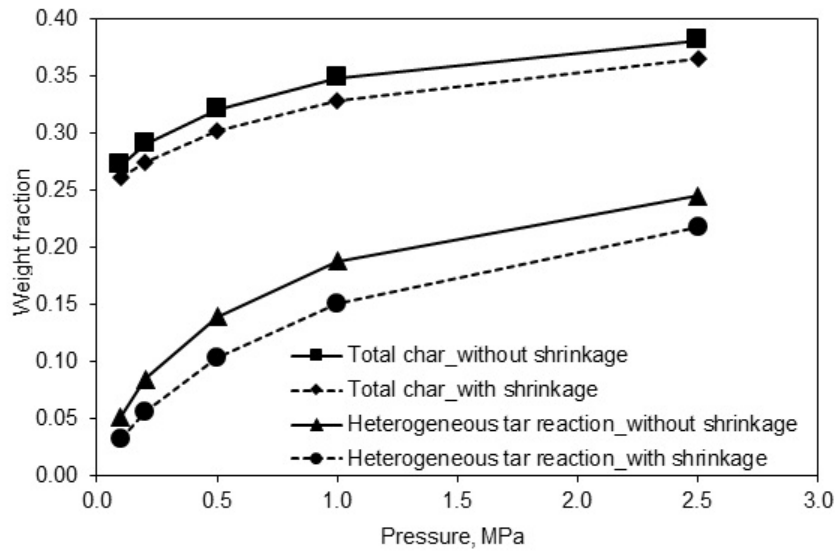
Fig. 2.8 Model results of the effect of particle aspect ratio on total char yield, heterogeneous tar conversion and primary char yield (heating rate = 30 K/min, peak temperature = 873 K, atmospheric pressure, $\rho_{g\text{-extraparticle}} = \rho_{t\text{-extraparticle}} = 0 \text{ kg/m}^3$).

Fig. 2.8 also shows that as the aspect ratio increases from about 0.1 to 0.9, the amount of tarry vapors that experience heterogeneous conversion increase slightly. Since the detailed porous structure inside the particle was unknown, it had been assumed (Section 2.1.2) that the porous structure was homogeneously distributed across the whole particle. However, to describe the anisotropic characteristics of the particle, different physical properties (permeability and thermal conductivity) were assumed along (or parallel to) and across the grain of the particle. It has been experimentally reported that the gas mixture flows out of the particle preferentially along the grain of the biomass particle.[137] As shown in Eq. (12), the outflow velocity of the gas mixture inside the particle was proportional to the permeability. To describe the preferential flow of gas mixture along the grain of the particle, the permeability (Table 2.3) along (or parallel to) the grain direction was set to be higher than that across the grain direction. As a result, prolonged residence time for the

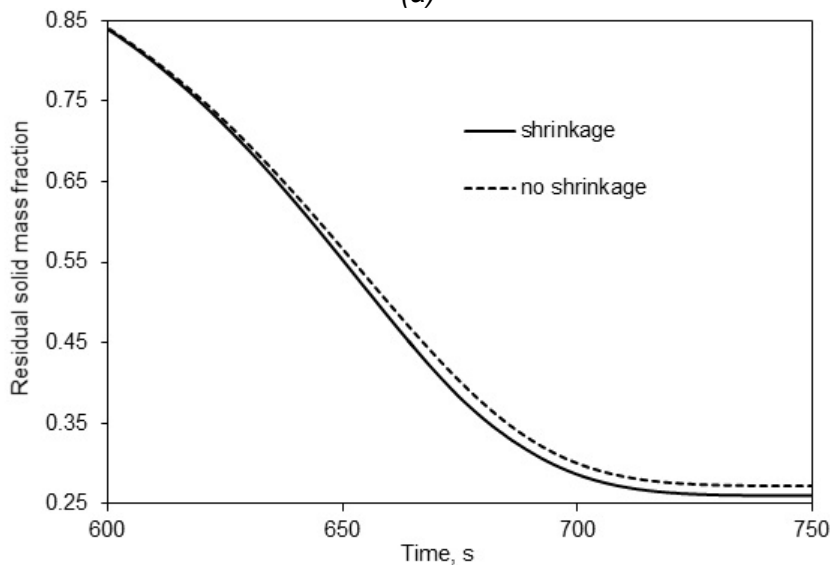
tarry vapors at higher aspect ratio was predicted since the convective transport of the tarry vapors occurs mainly along the axial direction (along the grain) of the wood cylinder. These simulation results were in qualitative accordance with the previous experimental results of Pattanotai et al.,[137] who found increased secondary tar conversion when the particle aspect ratio increased. It was found that, at a much higher (higher than 0.9) aspect ratio, the diffusive transport of the tarry vapors along the radial (across the grain) direction becomes the dominant transport mechanism. As the transport of the tarry vapors at the radial direction is predominantly by diffusion as discussed in Section 2.1.1, and the distance over which the vapors need to diffuse is reduced at higher aspect ratios (> 0.9), the residence time of the tarry vapors is reduced, hindering their heterogeneous conversion within the particle. Therefore, an aspect ratio of 0.9 tends to be an optimal value for the char formation at the current condition (atmospheric pressure with a heating rate of 30 K/min and a peak temperature of 873 K). It should be mentioned that zero concentration for the tarry vapors outside the particle was assumed, which could affect the optimal value found for the aspect ratio (i.e. the optimal value found here is not universally applicable).

Fig. 2.9 compares the model results with and without the consideration of particle shrinkage during the biomass pyrolysis process. Fig. 2.9(a) shows that the incorporation of particle shrinkage in the model led to a lower predicted total char yield due to the hindered heterogeneous conversion of the tarry vapors within the particle. As the particle shrinks, the residence time of the tarry vapors is shorter than in the particle without shrinkage since the particle with shrinkage provides a shorter distance for the tarry vapors to travel, which results in a lower heterogeneous conversion of the tarry vapors within the particle.[161] Fig. 2.9(b) indicates that

particle shrinkage exerts a consistent effect in terms of lower solid residue yield during the pyrolysis process which becomes more observable near the end of the pyrolysis process.

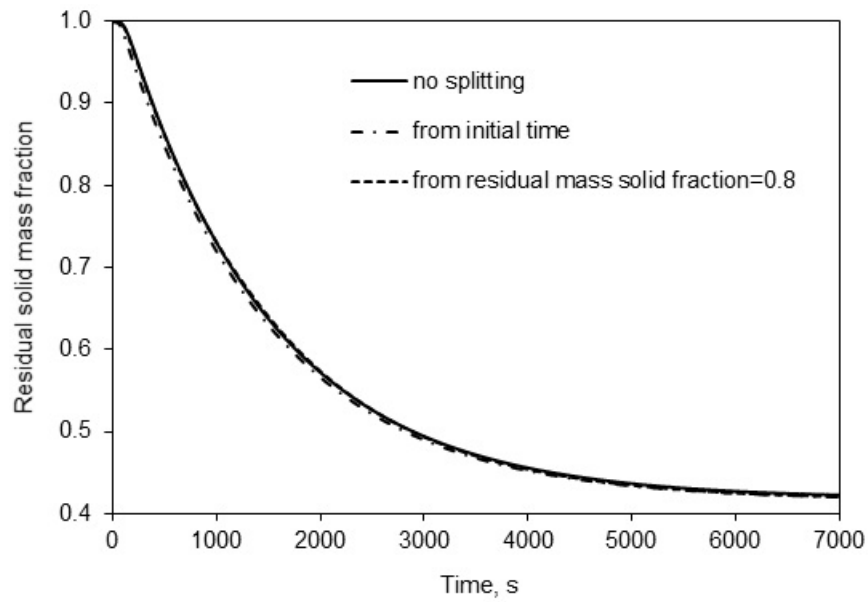


(a)

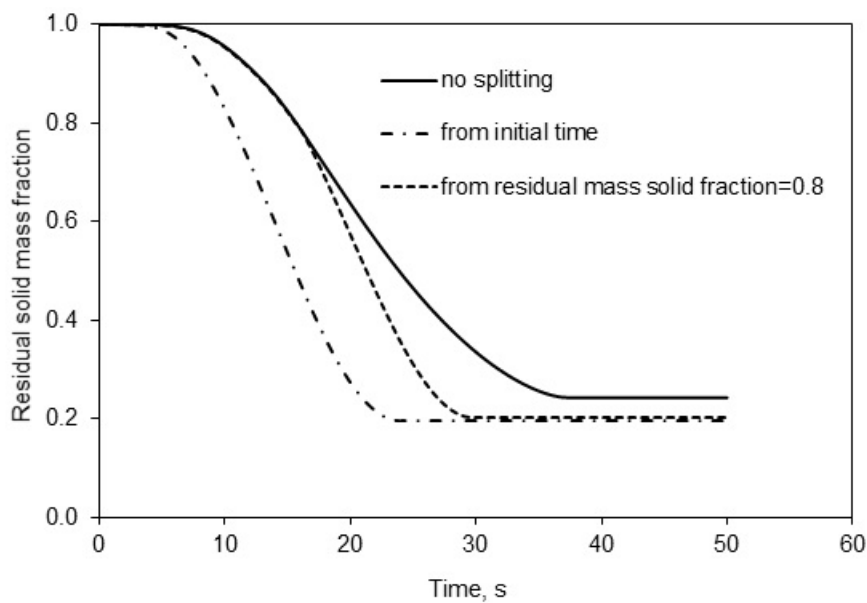


(b)

Fig. 2.9 Comparison of the model results with and without the consideration of particle shrinkage: (a) effect on secondary char yield and heterogeneous tar conversion at various pressures, (b) effect on residual solid mass fraction at atmospheric pressure, (heating rate = 30 K/min, peak temperature = 873 K, $\rho_{g\text{-extraparticle}} = \rho_{t\text{-extraparticle}} = 0 \text{ kg/m}^3$).



(a)



(b)

Fig. 2.10 Simulated particle splitting effect on the evolution of the residual solid mass fraction under different reactor temperatures: (a) $T_{\text{reactor}} = 573 \text{ K}$, (b) $T_{\text{reactor}} = 873 \text{ K}$

(atmospheric pressure, $\rho_{\text{g-extraparticle}} = \rho_{\text{t-extraparticle}} = 0 \text{ kg/m}^3$).

Fig. 2.10 compares two cases with particle splitting and the case without particle splitting at two different reactor temperatures. According to the model results, particle

splitting exerts limited effects on the pyrolysis process at lower temperature and significant effects at higher temperature. At lower reactor temperature, the temperature gradient inside the particle is lower for both the spherical particle and the split half-spherical particles, and the biomass conversion tends to be controlled by the reaction kinetics, indicating that the particle conversion processes for different particle sizes are similar provided they are at the same lower reactor temperature. At higher temperature, Fig. 2.10(b) shows that the particle splitting at the beginning of the process reduced the conversion time (at which the biomass is fully converted) by about 40% and the char yield by about 20% compared with the case without particle splitting. Fig. 2.10(b) also shows that the particle splitting at the moment when the total residual solid mass fraction equals 0.80 reduced the conversion time by about 20% and the char yield by about 17% compared with the case without particle splitting. It can be seen that the particle splitting-time exerts more important effects on conversion time than on char yield. Besides, due to particle splitting, the tarry vapors will experience decreased residence time within the particle, which will reduce the heterogeneous conversion of the tarry vapors inside the particle. Fig. 2.10 also shows that the later the particle splitting happens, the smaller the effect on the pyrolysis process will be. Practically, the particle splitting can occur at any time throughout the pyrolysis process and the particle can break into a larger number (i.e. >2) of fragments depending on the particle properties and the operating conditions. Since the particle splitting significantly influences the conversion time and the char yield, it was indicated that the particle splitting can add uncertainty when experimentally measuring the conversion time and char yield of biomass pyrolysis. This can be a reasonable explanation for the wide ranges of conversion times and char yields reported in the literature even under similar heating conditions.[27]

The modeling results demonstrate that fragmentation of particles during pyrolysis could negatively impact the char yield. In slow pyrolysis systems, purposefully-built to have a high yield of char (i.e. for use as charcoal or biochar), this may be a significant phenomenon if the particles are subjected to a high degree of attrition. Reactor types which use mechanical energy for particle transport and mixing, such as the rotating drum and rotating screw retorts fall under this category, whereas in fixed-bed pyrolysis retorts or kilns, mechanically induced attrition and wear is nearly absent. The impact of particle fragmentation on char yield will furthermore be determined by factors such as the onset of fragmentation, as virgin biomass particles are less likely to break down considering their tensile strength as opposed to brittle near or fully pyrolyzed particles. Also fragmentation patterns other than splitting, such as the continuous removal of the outer surface (chipping) and the fragmentation into multiple, unequally sized daughter particles are more likely to occur.

4. Conclusions

A three-dimensional comprehensive particle model (3D CPM) was developed for the pyrolysis of a biomass particle by coupling the three-dimensional transport phenomena and a general kinetic scheme considering the primary pyrolysis of virgin biomass and the intraparticle secondary charry reactions (i.e. homogeneous and heterogeneous reactions of the tarry vapors). The characteristic time scale analysis was performed to identify the dominant processes for consideration in the model. The model results were compared to the experimental data in literature from two different research groups. The comparison shows that the model can well predict the trends with respect to the evolutions of temperature (MD of 31 K) and mass loss (MD of 6.0 wt%; MD on final char mass yield of 3.6 wt%) as well as with respect to the heterogeneous secondary tar conversion (MD of 1.2 wt%).

Further analyses of the effects of the process conditions (heating rate, peak temperature, pressure of the gas phase surrounding the particle and extra-particle concentration of the tarry vapors) indicate that lower heating rate, lower peak temperature, and higher pressure are favorable for the production of total char, while higher pressure and higher extra-particle concentration of the tarry vapors are particularly beneficial to the formation of secondary char. It was found that the particle shape (aspect ratio) highly affects the secondary char formation. In addition, the size reduction phenomena (particle shrinkage and particle splitting) during pyrolysis of biomass particles significantly affect the particle's conversion process. It was found that the particle shrinkage exerts consistent char yield reducing effects on the biomass pyrolysis during the whole pyrolysis process and that the inclusion of the particle shrinkage in the model decreased the predicted total char yield due to the lower amount of secondary char produced from the heterogeneous conversion of the tarry vapors within the particle. With the model, it was also indicated that the particle splitting highly influences conversion time, char yield and conversion process of the tarry vapors inside the particle. The time at which the particle splitting occurs also affects the conversion process to a large extent. As such, particle splitting can add uncertainty when experimentally measuring the conversion time and char yield during the biomass pyrolysis process.

CHAPTER 3

Modeling of pyrolysis of a biomass particle with a comprehensive kinetic scheme

In the previous chapter (Chapter 2), the pyrolysis of a single biomass particle was studied by incorporating a general kinetic scheme, which did not consider biomass composition (cellulose, hemicellulose, and lignin), into a comprehensive particle model (CPM). In this chapter 3, a comprehensive kinetic scheme, which will consider biomass composition, will be incorporated into the CPM to study the pyrolysis of a single biomass particle. This comprehensive kinetic scheme describes the primary pyrolysis of biomass pseudo-components (cellulose, hemicellulose, and lignin) and the secondary charring reactions due to the heterogeneous conversion of the primary volatiles. The model results will be compared against experimental data. With this model, the effects of particle size on the intraparticle secondary charring reactions will be quantified and a critical particle size, at which the intraparticle secondary charring reactions start to be relevant, will be determined at thermally thin pyrolysis regime.

This chapter was redrafted after:

Xiaogang Shi, Frederik Ronsse, Andrés Anca-Couce, Zuoyi Yan, Jan G. Pieters. Simulation of intraparticle secondary charring reactions during biomass pyrolysis by considering biomass composition. To be submitted to Energy & Fuels.

1. Introduction

Industrial production of char through biomass pyrolysis usually handles woodchips and pellets with a large size in the range of several centimeters.[167] During slow pyrolysis or carbonization of biomass, char is usually regarded as a primary product along with the competitive formation of volatiles.[65, 148] Recent evidence indicate that secondary charring reactions can occur through heterogeneous volatile-char interactions when volatiles, which were primarily formed inside the biomass particle during its pyrolysis, are diffusing/flowing out of the porous biomass particle.[9, 35, 54, 72, 73, 89, 90, 130-133, 168] The homogeneous thermal cracking of volatiles in the gas phase can also produce secondary char. However, the secondary char produced from this thermal cracking of volatiles is very limited even at its favorable temperatures higher than 870 K.[54, 169] Therefore, this study will not consider the secondary char produced from the homogeneous conversion of volatiles. The production of secondary char from the heterogeneous conversion of volatiles can occur at relatively lower temperatures (around 670 K or lower).[55, 89] Several research groups have addressed the heterogeneous conversion of volatile compounds as an important source of char formation during biomass pyrolysis.[55, 79, 80, 90] Therefore, the char is a mixture of primary and (heterogeneous) secondary char from biomass pyrolysis. Knowledge about the individual contribution of primary and secondary char formation to the total char yield is important in optimizing the production of char through biomass pyrolysis.

Extensive research has been performed to characterize the primary char formation with thermal gravimetric analysis (TGA), fixed bed reactors and other types of reactors.[65, 90] It is generally accepted that lower heating rates and lower temperatures are in favor of primary char production.[34, 65] In addition, the biomass

composition (cellulose, hemicellulose and lignin) can also influence the production of primary char. Biomass feedstocks with higher lignin content will offer higher primary char yields.[72, 90]

Compared to the already comprehensive results about the production of primary char from biomass pyrolysis, knowledge about the secondary charring reactions due to the heterogeneous conversion of volatiles within large biomass particles (i.e. centimeter-sized or larger particle) is still limited.[9, 51, 78, 90, 170] This is mainly due to the difficulty in characterizing the complex coupled physical and chemical phenomena inside the biomass particle, including the intraparticle heat transfer, the intraparticle diffusion and flow of volatiles and the intraparticle secondary charring reactions.[51, 67] Some researchers[78, 170] have identified the secondary charring reactions in slow pyrolysis of biomass at low temperatures and they explored the effect of intraparticle secondary charring reactions on the heat of reaction during biomass pyrolysis. Other researchers have identified the factors (including particle size, reactor temperature, operating pressure, biomass composition, etc.) that can affect the intraparticle physical and chemical phenomena and hence the intraparticle secondary charring reactions.[9, 51, 55, 65, 67, 72, 73, 79, 89, 168, 171-176] In these previous works, the final solid product (char) was usually a mixture of primary and secondary char, and the amount of secondary char in the total char mixture was seldom quantified. Anca-Couce *et al.*[72, 73] tried to quantify the intraparticle secondary charring reactions with a comprehensive pyrolysis reaction scheme. Pattanotai *et al.*[55] experimentally studied the pyrolysis of a centimeter-sized wood particle and determined the amount of secondary char. However, the intraparticle physical and chemical phenomena during biomass pyrolysis remain largely unknown. These phenomena are critical to provide fundamental information in characterizing

the secondary charring reactions.[51] With the development of computational science, mathematical simulation has become an efficient and reliable tool in studying coupled transport phenomena and chemical reactions involved in energy conversion processes including biomass pyrolysis.[65, 67, 71, 83, 103, 128, 145, 161, 177-180] Some researchers have used advanced models coupling the transport phenomena and chemical reactions to study the intraparticle conversion of volatiles.[81, 82, 139-144, 181] However, these modeling studies seldom report on the amount of secondary char that was produced from the heterogeneous conversion of volatiles. The individual contributions of primary char and secondary char to the total char remains largely unknown. Besides, the industrial production of char from pyrolysis of biomass is usually at slow heating rates[90], which tend to give rise to the thermally thin pyrolysis regime. The thermally thin pyrolysis regime refers to the regime that the internal heat transfer in the particle and chemical reactions are faster than the external heat transfer to the particle, and, therefore, external heat transfer controls the process, but no intra-particle gradients are present. At this thermally thin pyrolysis regime, the effect of particle size on the intraparticle secondary charring reactions is, however, still unknown.

The objective of this chapter is to study the pyrolysis of a single biomass particle by incorporating a comprehensive kinetic scheme, which considers biomass composition (cellulose, hemicellulose and lignin), into the three-dimensional comprehensive particle model (3D CPM) that has been developed in Chapter 2. With the model in this chapter, the intraparticle secondary charring reactions are quantified. The particle size effect on the secondary charring reactions is quantified and in addition, the particle size, at which the influence of the secondary charring reactions

start to be relevant, is determined for the pyrolysis of cylindrical biomass particles at the thermally thin regime.

2. Methods

2.1 Reaction kinetics

The primary pyrolysis of biomass produces primary volatiles and primary char, and the subsequent secondary charring reactions produce secondary char and lighter gases (CO_2 , H_2 , water vapor[73, 171, 182]) through heterogeneous conversion of primary volatiles when they are flowing out of the hot and porous biomass particle. Since the primary char and the secondary char (as well as the primary volatiles and the secondary lighter gases) usually mix together within the centimeter-sized particle, it is difficult in experiments to discern between the primary products and the secondary products. It is usually accepted that only primary pyrolysis occurs (to produce primary char and volatiles) in a fine biomass particle (with a size of one millimeter or smaller) and that the primary volatiles do not experience further conversion due to the limited residence time of volatiles inside this small biomass particle. Previous experiments usually addressed the conversion of the primary volatiles within a large (i.e. centimeter-sized) biomass particle by comparing the product yields between the small particle (assuming no conversion of primary volatiles) and the centimeter-sized particles (with conversion of primary volatiles).[65, 136, 137] In contrast, a coupled physical-chemical model can obtain detailed information about the primary and secondary products during the pyrolysis of a centimeter-sized biomass particle.[67]

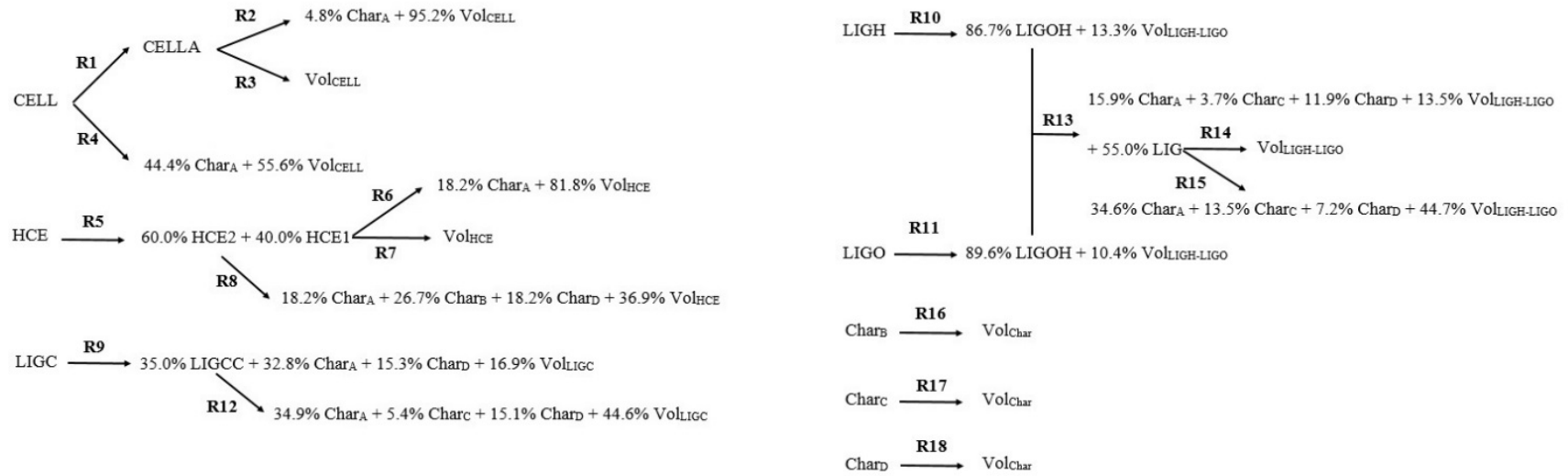
2.1.1 Primary pyrolysis kinetics

To describe the primary pyrolysis of biomass, several authors have proposed various kinetic schemes,[9, 65] among which the detailed mechanistic reaction scheme of the biomass pseudo-components (cellulose, hemicellulose, carbon-rich lignin, oxygen-rich lignin and hydrogen-rich lignin) originally proposed by Ranzi *et al.*[68] is considered to be one of the most promising. In this reaction scheme, the overall progression of the biomass pyrolysis process is the sum of the reactions involving individual biomass components. This reaction scheme considers representative species to describe the composition of char and volatiles. The research group of Ranzi[69-71, 183] and other research groups[72, 73] have extended the application of this original kinetic scheme from Ranzi *et al.*[68]. The kinetic scheme of Ranzi *et al.*[68] was also applied in this chapter to describe the primary pyrolysis reactions in producing primary char and primary volatiles, as shown in Fig. 3.1(a). All reaction rate coefficients were described by the Arrhenius function, and the detailed kinetic parameters are listed in Table 3.1.

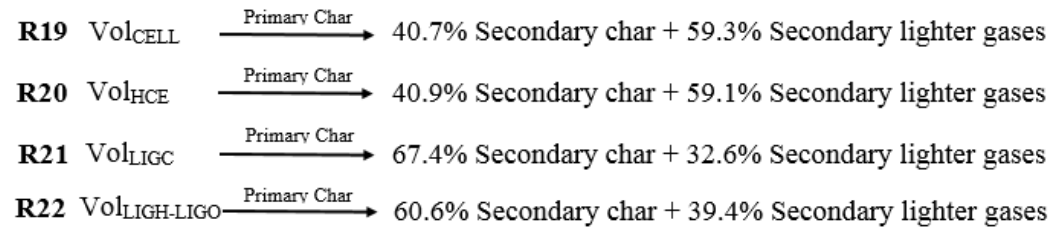
The reaction rate equation is expressed as $r = k\rho$, where $\rho[k/m^3]$ is the density of the reactant. $k[1/s]$ is the kinetic constant as calculated by $k = Ae^{\left(\frac{-E_a}{RT}\right)}$ (Arrhenius function), where $A[1/s]$ is the pre-exponential factor, $E_a[J/mol]$ is the activation energy, $R[J/(mol \cdot K)]$ is the gas constant and $T[K]$ is the temperature.

In Fig. 3.1(a), the percentages represent the weight fractions of various gaseous (at the pyrolysis condition, all the condensable and non-condensable volatiles are in gas phase) and solid products. The gas and solid species in Fig. 3.1(a) are separately grouped, as can be seen in Table 3.2. In Fig. 3.1(a), the original scheme of Ranzi *et al.*[68] was interpreted by lumping the gaseous products from cellulose as Vol_{CELL}, the gaseous products from hemicellulose as Vol_{HCE}, the gaseous products from carbon-rich lignin as Vol_{LIGC}, the gaseous products from hydrogen/oxygen-rich

lignin as Vol_{LIGH-LIGO}, and the gaseous products from the successive conversion of some primary char (Char_B, Char_C and Char_D, as shown in Table 3.2) as Vol_{Char}. Volatiles from different biomass components were separately lumped in order to define the secondary charry reactions resulting from the heterogeneous conversion of different volatiles from different biomass components, as described in the following section.



(a)



(b)

Fig. 3.1 Pyrolysis scheme of (a) primary pyrolysis reactions, (b) secondary charring reactions, (values in weight percentage) adapted from

Ranzi et al.[68]

Table 3.1 Pyrolysis kinetics of biomass for the multiple reactions adapted from Ranzi et al.[68]

Reaction number	Kinetic constant [1/s] (Activation energy in J/mol)	ΔH [kJ/kg]
R1	$8 \times 10^{13} \exp(-192500/RT)$	0 ^a
R2	$1 \times 10^9 \exp(-125600/RT)$	620 ^a
R3	$4 \times T \exp(-41900/RT)$	364 ^a
R4	$8 \times 10^7 \exp(-133900/RT)$	-1913 ^a
R5	$1 \times 10^{10} \exp(-129800/RT)$	100 ^a
R6	$3 \times 10^9 \exp(-113000/RT)$	-92 ^a
R7	$3 \times T \exp(-46000/RT)$	588 ^a
R8	$1 \times 10^{10} \exp(-138100/RT)$	212 ^a
R9	$4 \times 10^{15} \exp(-203000/RT)$	-490 ^a
R10	$2 \times 10^{13} \exp(-157000/RT)$	100 ^a
R11	$1 \times 10^9 \exp(-106700/RT)$	446 ^a
R12	$5 \times 10^6 \exp(-131900/RT)$	-503 ^a
R13	$1 \times 10^{13} \exp(-207200/RT)$	-120 ^a
R14	$8 \times 10^1 \times T \exp(-50200/RT)$	686 ^a
R15	$1.2 \times 10^9 \exp(-125600/RT)$	-470 ^a
R16	$1 \times 10^5 \exp(-100500/RT)$	-1814 ^a
R17	$1 \times 10^{13} \exp(-209300/RT)$	-2000 ^a
R18	$5 \times 10^{11} \exp(-272100/RT)$	6778 ^a
R19 ^b	$\theta \times 1.24 \times 10^7 \exp(-92400/RT)$	-42 ^c
R20 ^b	$\theta \times 1.24 \times 10^7 \exp(-92400/RT)$	-42 ^c
R21 ^b	$\theta \times 1.24 \times 10^7 \exp(-92400/RT)$	-42 ^c
R22 ^b	$\theta \times 1.24 \times 10^7 \exp(-92400/RT)$	-42 ^c

^a From the work of Ranzi et al.[71]

^b Through calibration with the experimental data of Pattanotai et al..[55] θ is a parameter, as defined in our previous work,[67] indicating that the reaction rate for the heterogeneous conversion of volatiles is proportional to the weight fraction ($\theta = \rho_{\text{primary char}} / (\rho_{\text{solid reactant}} + \rho_{\text{solid product}})$) of the primary char in the total solid species as shown in Table 3.2.

^c From the work of Park et al.[110]

Table 3.2 The list of gas and solid species in the reaction kinetics adapted from Ranzi et al.[68]

Abbreviation	The corresponding term in Ranzi et al. [68]	Name
Solid species		
<i>Solid reactant</i>		
CELL	CELL	Cellulose
HCE	HCE	Hemicellulose
LIGC	LIG-C	Carbon-rich lignin
LIGH	LIG-H	Hydrogen-rich lignin
LIGO	LIG-O	Oxygen-rich lignin
<i>Primary solid product</i>		
CELLA	CELLA	Activated cellulose
HCE1	HCE1	Activated hemicellulose 1
HCE2	HCE2	Activated hemicellulose 2
LIGCC	LIG _{CC}	Carbon-rich lignin 2
LIG	LIG	Lignin
LIGOH	LIG _{OH}	OH-rich lignin
Char _A	Char	Primary Char
Char _B	[CO ₂]	Primary Char
Char _C	[CO]	Primary Char
Char _D	[COH ₂]	Primary Char
<i>Secondary solid product</i>		
Secondary char	--	Secondary char
Gas species		
<i>Reactive volatiles</i>		
Vol _{CELL}	--	Primary reactive volatiles from cellulose
Vol _{HCE}	--	Primary reactive volatiles from hemicellulose
Vol _{LIGC}	--	Primary reactive volatiles from carbon-rich lignin
Vol _{LIGH-LIGO}	--	Primary reactive volatiles from hydrogen-rich lignin and oxygen-rich lignin
<i>Unreactive volatiles</i>		
Vol _{Char}	--	Primary unreactive volatiles from Char _B , Char _C , and Char _D
<i>Inert gas</i>		
N ₂	--	Nitrogen
<i>Secondary gas product</i>		
Secondary lighter gases	--	Secondary lighter gas

2.1.2 Secondary charring reactions kinetics

Kinetics on the secondary charring reactions due to the heterogeneous conversion of primary volatiles within centimeter-sized or larger biomass particles are very scarce in literature, which can be due to the difficulty of real-time measurement of the heterogeneous reaction parameters of primary volatiles consisting of various compounds including non-condensable gases, carbonyls and alcohols, phenolics, sugars, heterocyclic compounds and water vapor.[9]

For simplicity, the complex secondary charring reactions of individual compounds (e.g. non-condensable gases, carbonyls and alcohols, phenolics, sugars, heterocyclic compounds and water vapor[9]) in the primary volatiles were not explored. Instead, the lumped conversion of the primary volatiles (Vol_{CELL} , Vol_{HCE} , Vol_{LIGC} , and $Vol_{LIGH-LIGO}$ as shown in the above Section 2.1.1) from the corresponding biomass components were modeled. Fig. 3.1(b) shows the secondary charring reactions of each group of primary volatiles. In Fig. 3.1(b), the composition of the secondary products (the weight ratio of secondary char to secondary lighter gases) were obtained from Anca-Couce *et al.*[72, 73] The scheme of secondary charring reactions in Fig. 3.1(b) indicates that the primary volatiles from lignin have higher tendency to form secondary char than the primary volatiles from cellulose and hemicellulose, which was also addressed in the experiments of Boroson *et al.*[89] In Fig. 3.1(b), the amount of secondary char in the secondary products ranged from 40.7 wt.% to 67.4 wt.%. And this range covered the experimental value of Pattanotai *et al.*,[55] who experimentally determined that about 54 wt.%, of the tarry vapors (a heavy fraction of primary volatiles) were converted into secondary char (and 46 wt.% of tarry vapors to secondary lighter gases) during biomass pyrolysis.

To the author's knowledge, no data can be found in the literature about the kinetics of the secondary charring reactions resulting from individual components of the primary volatiles. Therefore, a single reaction kinetic constant was applied to all the secondary charring reactions, which should be considered as providing a mean conversion rate for all the primary volatiles. The procedure to obtain the kinetic parameters for the secondary charring reactions was based on the pyrolysis of the wood cylinder in the experimental work of Pattanotai *et al.*[55] The wood cylinder had a diameter of 8 mm and a length of 9 mm. An activation energy (in the Arrhenius

equation) of 92.4 kJ/mol, which was usually applied in predicting the heterogeneous conversion of volatiles within a centimeter-sized biomass particle,[67, 81, 144] was applied to describe the formation rate of the secondary products. The pre-exponential factor in the Arrhenius equation for describing the formation rate of the secondary products, as shown in *Reaction 19* to *Reaction 22* in Table 3.1, was determined after calibrating with the experimental values from Pattanotai *et al.*[55] with respect to the amount of secondary char formed within this particle.

2.2 Coupled physical-chemical model

The 3D CPM coupling the physical and chemical phenomena describes the mass balance of reactants and products, the heat transfer within the particle and the outflow of the gas phase (including inert gas N₂, primary volatiles and secondary lighter gases) in the porous particle. This model considered the anisotropic characteristics of the 3D particle, which means that the transport processes (mass, heat and momentum transfer) across the grain direction (in the *radial* direction of the cylindrical particle in the following text) of the biomass particle were different from those parallel to the grain direction (in the *axial* direction of the cylindrical particle in the following text).[109, 111] In the present model, it was assumed that no shrinkage (particle size) or distortion (particle shape) occurs during the pyrolysis of the biomass particle. The detailed description of the 3D CPM can be found in Chapter 2. Only the governing equations, the initial conditions and the boundary conditions are described here.

2.2.1 Governing equations

The mass balance for the solid species is:

$$\frac{\partial \rho_i}{\partial t} = S_i \quad (1)$$

Where ρ_i (kg/m^3) is the density of the solid species i (Table 3.2); t (s) is time; S_i ($kg/(m^3 \cdot s)$) is the net formation rate of the i th solid component resulting from the reaction kinetics described.

The mass balance for the total gas is:

$$\frac{\partial \varepsilon \rho_g}{\partial t} + \nabla \cdot (\rho_g u_g) = \sum S_g \quad (2)$$

Where ε is the particle's porosity; ρ_g (kg/m^3) is the density of the gas phase including the inert gas N_2 , the primary volatiles, and the secondary lighter gases, as shown in Table 3.2; u_g (m/s) is the velocity of the gas phase within the porous particle; $\sum S_g$ ($kg/(m^3 \cdot s)$) is the net formation of the all gas species resulting from the reaction kinetics.

The species transport equation for primary volatiles and secondary lighter gases within the porous particle is:

$$\frac{\partial \varepsilon \rho_j}{\partial t} + \nabla \cdot (\rho_j u_g) = \nabla \cdot (D_{eff,j} \nabla \rho_j) + S_j \quad (3)$$

Where ρ_j is the density of the gas species j (Table 3.2); $D_{eff,j}$ (m^2/s) is the effective diffusivity of gas species j in particle pores; S_j is the net formation of the gas species j from the reaction kinetics.

The momentum transfer of the gas phase in the porous particle was described using the Darcy Law:

$$u_g = - \frac{B_{eff,direction}}{\mu} \nabla P \quad (4)$$

Where $B_{eff,direction}$, ($direction = across, parallel$) (m^2) is the effective permeability (defined by the internal resistance of the particle to the bulk flow of the gas phase) across and parallel to the grain direction of the 3D particle; μ ($kg/(m \cdot s)$) is the dynamic viscosity of the gas phase; P (Pa) is the pressure.

The energy conservation equation is:

$$\left(\sum c_i \rho_i + \varepsilon c_g \rho_g \right) \frac{\partial T}{\partial t} + (c_g \rho_g u_g) \cdot \nabla T = \nabla \cdot (\lambda_{eff,direction} \nabla T) + Q \quad (5)$$

Where c_i ($J/(kg \cdot K)$) is the heat capacity for the i_{th} solid species; c_g is the heat capacity of the gas phase; $\lambda_{eff,direction}$, ($direction = across, parallel$) ($W/(m \cdot K)$) is the effective thermal conductivity across and parallel to the grain direction of the 3D particle; Q (W/m^3) is the heat source term. Details of the model parameters are listed in Table 3.3.

Table 3.3 Material properties for the model

Property	Value	Unit	Source
ε	$1 - \frac{\rho_{solid\ reactant} + \rho_{solid\ product}}{\rho_{solid\ reactant,0}} (1 - \varepsilon_0)$	-	Shi et al.[67]
$B_{eff,direction}$	$\frac{(\rho B)_{solid\ reactant,direction} + (\rho B)_{solid\ product,direction}}{\rho_{solid\ reactant} + \rho_{solid\ product}}$	-	Shi et al.[67]
$\lambda_{eff,direction}$	$\frac{(\rho \lambda)_{solid\ reactant,direction} + (\rho \lambda)_{solid\ product,direction}}{\rho_{solid\ reactant} + \rho_{solid\ product}} + \varepsilon \lambda_{gas\ phase} + \frac{13.5 \sigma T^3 d_{eff}}{e}$	-	Shi et al.[67]
d_{eff}	$\frac{(\rho d)_{solid\ reactant} + (\rho d)_{solid\ product}}{\rho_{solid\ reactant} + \rho_{solid\ product}}$	-	Shi et al.[67]
$c_{solid\ reactant}$	$1500 + 1.0T$	$J/(kg \cdot K)$	Gronli and Melaaen[148]
$c_{solid\ product}$	$420 + 2.09T + 6.85 \times 10^{-4} T^2$	$J/(kg \cdot K)$	Gronli and Melaaen[148]
$c_{gas\ phase}$	$-100 + 4.4T - 1.57 \times 10^{-3} T^2$	$J/(kg \cdot K)$	Gronli and Melaaen[148]
$d_{solid\ reactant}$	4×10^{-5}	M	Di Blasi[93]
$d_{solid\ product}$	4×10^{-4}	M	Di Blasi[93]
$B_{solid\ reactant}$	1×10^{-11} (parallel to grain), 1×10^{-14} (across grain)	m^2	Di Blasi[93]
$B_{solid\ product}$	5×10^{-11} (parallel to grain), 5×10^{-12} (across grain)	m^2	Di Blasi[93]

$D_{eff,j}$	1×10^{-5}	m^2/s	Shi et al.[67]
e	0.95	-	Bates and Ghoniem[83]
$h_{convective}$	5	$W/(m^2 \cdot K)$	Gronli and Melaaen[148]
MW_{vol}	0.076	kg/mol	Park et al.[110]
R_{cons}	8.314	$J/(mol \cdot K)$	
$\lambda_{solid\ reactant\ cross}$	$(\frac{\rho_{solid\ reactant,0}}{\rho_{water}})(0.1941 + 0.114064 \cdot Moisture + 0.01864)$	$W/(m \cdot K)$	Shi et al.[67]
$\lambda_{solid\ reactant\ para}$	$2.8 \cdot \lambda_{solid\ reactant\ cross}$	$W/(m \cdot K)$	Shi et al.[67]
$\lambda_{solid\ product}$	0.105 (parallel to grain), 0.071 (across grain)	$W/(m \cdot K)$	Di Blasi[93]
$\lambda_{gas\ phase}$	0.0258	$W/(m \cdot K)$	Gronli and Melaaen[148]
σ	5.67×10^{-8}	$W/(m^2 \cdot K^4)$	Gronli and Melaaen[148]
ε_0	0.4	-	Park et al.[110]
μ	3×10^{-5}	$kg/(m \cdot s)$	Di Blasi[93]
	398 (Pattanotai)	kg/m^3	Pattanotai et al.[55, 136]
$\rho_{solid\ reactant,0}$	650 (Koufopoulos)	kg/m^3	Koufopoulos et al.[82, 184]

2.2.2 Initial and boundary conditions

Initially, the biomass feedstock has a density of ρ_0 , and the initial density of the individual component was $\rho_{i,0} = w_{i,0}\rho_0$ (i =cellulose, hemicellulose, carbon-rich lignin, oxygen-rich lignin and hydrogen-rich lignin). Initially, the gas phase only contains inert gas (N_2), and it has an initial density of $\rho_{g,0} = \rho_{inert,0}$. The biomass particle has an initial temperature T_0 and is exposed to the ambient pressure (absolute pressure of $P_0 = 0.1MPa$). The initial velocity of the gas phase is $u_{g,0} = 0\ m/s$.

The biomass particle was assumed to be surrounded by inert gas (the concentration of volatiles outside the particle was assumed to be negligible[67]) with constant pressure. The particle was considered to be heated by convective and radiative heat flux. At the particle surface, the boundary conditions were defined by:

$$P(t, r = r_p) = P_0 \quad (6)$$

$$\rho_g(t, r = r_p) = \frac{P_0 MW_{inert}}{R_{cons} T_s} \quad (7)$$

$$-\mathbf{n} \cdot (-\lambda_{eff} \nabla T) = h_{convective}(T_{reactor} - T_s) + \sigma e(T_{reactor}^4 - T_s^4) \quad (8)$$

where $h_{convective}$ ($W/(m^2 \cdot K)$) is the convective heat transfer coefficient at the particle surface, $T_{reactor}$ is the reactor (operating) temperature and T_s is the temperature at the particle surface.

2.3 Model implementation

The finite element based solver COMSOL Multiphysics® 5.2 was applied to solve the set of equations. The three-dimensional spherical (for spherical biomass particle)/cylindrical (for cylindrical biomass particle) geometry of the biomass particle was drawn in COMSOL Multiphysics®. Free tetrahedral grids were used for discretization. Mesh-independency has been checked and the mesh details are listed in Table 3.4.

Table 3.4 Mesh details for simulating the pyrolysis of biomass particle

	For validation against Pattanotai et al.[55, 136]					For validation against Koufopoulos et al.[82, 184]
Cylinder dimensions, diameter × length	8mm × 2mm	8mm × 5mm	8mm × 9mm	8mm × 15mm	8mm × 40mm	20mm × 100mm
Number of domain elements	76479	194666	247289	475516	269994	530769
Number of boundary elements	5410	7732	8500	13016	10764	16364
Number of edge elements	212	256	276	368	424	528
Minimum element size, m	1.20×10 ⁻⁵	1.20×10 ⁻⁵	1.35×10 ⁻⁵	3.00×10 ⁻⁵	3.60×10 ⁻⁵	1.00×10 ⁻⁴
Maximum element size, m	2.80×10 ⁻⁴	2.80×10 ⁻⁴	3.15×10 ⁻⁴	3.00×10 ⁻⁴	5.00×10 ⁻⁴	1.00×10 ⁻³
Maximum element growth rate	1.35	1.35	1.35	1.30	1.40	1.35

2.4 Model validation

2.4.1 Comparison with Pattanotai et al.[55, 136]

Pattanotai *et al.*[55] experimentally conducted the pyrolysis of dry Japanese cypress sawdust (fine particles with size < 1 mm) and the pyrolysis of a dry wood cylinder (also from Japanese cypress) with a diameter of 8 mm and a length of 9 mm from an initial temperature of $T_0 = 383$ K to a final temperature of $T_0 = 873$ K at a heating rate of 30 K/min. Other physical properties of the cypress sawdust and cylinder are listed in Table 3.3. Pattanotai *et al.*,[55] found that the difference in char yield between the sawdust and the wood cylinder was a result of the secondary charring reactions within the wood cylinder (the secondary charring reactions in a sawdust particle were considered negligible).[55] Their experimental findings with respect to the secondary charring reactions were used in the calibration procedure in determining the kinetic parameters for the secondary charring reactions, as described in [Section 2.1.2](#). The pyrolysis of sawdust was modeled with the primary pyrolysis kinetics ([Section 2.1.1](#)). The predicted evolution of residual solids mass during the pyrolysis of sawdust was compared with the experimental data. The pyrolysis of the wood cylinder was simulated with the coupled physical-chemical model considering both the primary pyrolysis kinetics and the secondary charring reaction kinetics. In the experiments, Pattanotai *et al.* also measured the temperature evolution at various radial positions of the wood cylinder and they observed very limited intraparticle temperature gradients. The predicted temperature evolutions at the center and surface of the wood cylinder were validated against their experimental data.

Another experimental work of Pattanotai *et al.*[136] studied the pyrolysis of dry cylinders (also from Japanese cypress). Three cylindrical particles with the same

diameter of 8 mm and different lengths of 2, 5, and 9 mm were examined in their experiments at a heating rate of 60 K/min from an initial temperature of $T_0 = 383\text{ K}$ to a final temperature of $T_f = 1173\text{ K}$ with holding time of 5 min. The cylindrical particles were simulated with the coupled physical-chemical model taking into account both the primary pyrolysis kinetics and the intraparticle secondary charring reaction kinetics. The secondary char yield of the cylindrical particles were predicted and compared with the experimental data.

Pattanotai et al.[55, 136] conducted experiments with Japanese cypress, which is a type of softwood. This type of softwood was composed of 44 wt.% in cellulose, 26 wt.% in hemicellulose, 17.5 wt.% in carbon-rich lignin, 9.5 wt.% in hydrogen-rich lignin and 3 wt.% in oxygen-rich lignin, which were calculated using atomic balances[68] according to the experimental data with respect to the elemental composition of the Japanese cypress consisting of 51.5 wt.% in C, 6.2 wt.% in H and 42.2 wt.% in O[55, 136].

2.4.2 Comparison with Koufopoulos et al.[82, 184]

Koufopoulos *et al.*[82, 184] studied the pyrolysis of dry sawdust (beech wood with diameters in the range of 0.30~0.85 mm) and a dry biomass cylinder (beech wood with a diameter of 2 cm and a length of 10 cm). The physical properties of the beech wood sawdust and cylinder are listed in Table 3.3. Initially, both sawdust and cylinder were at $T_0 = 293\text{ K}$. They performed isothermal pyrolysis at 773 K and obtained evolutions of residual solids mass for both sawdust and cylindrical particles. The primary pyrolysis kinetics were applied to simulate the pyrolysis of the sawdust. For the cylindrical particle, the coupled physical-chemical model was applied taking into account both the primary pyrolysis kinetics and the intraparticle secondary charring reactions kinetics.

Beech wood is a type of hardwood, and Koufopoulos *et al.*[82, 184] provided the detailed composition (cellulose, hemicellulose, lignin, extractives and ash) for this hardwood. The extractives and ash in the composition of beech wood in their experiments were neglected in the simulation. The experimental weight fractions of the three main components (cellulose, hemicellulose and lignin) were normalized (dry-based, ash-free and extractives-free) in the simulation, and the initial composition of beech wood was 54 wt.% in cellulose, 14 wt.% in hemicellulose, 32 wt.% in lignin. The 32 wt.% of lignin in beech wood consists of 8.7 wt.% of carbon-rich lignin, 10.3 wt.% of hydrogen-rich lignin and 13.0 wt.% of oxygen-rich lignin, according to the representative composition for the lignin in hardwood as described in the work of Anca-Couce and Obernberger.[72]

2.5 Non-dimensional numbers

In literature various pyrolysis regimes (pure kinetic regime, thermally thin regime, thermal wave regime and thermally thick regime[9, 65]) for the pyrolysis of a single biomass particle have been defined. The definition of pyrolysis regime was usually based on the analysis of two dimensionless numbers that describe the main controlling factors: the thermal Biot number (Bi) and the pyrolysis number (Py and Py').[185]

$$Bi = \frac{h_{external}L}{\lambda} \quad (9)$$

$$\text{Internal pyrolysis number } \frac{1}{Py} = \frac{\dot{r}\rho_p c_p L^2}{\lambda} \quad (10)$$

$$\text{External pyrolysis number } \frac{1}{Py'} = \frac{\dot{r}\rho_p c_p L}{h_{external}} \quad (11)$$

Where $h_{external}$ ($W/(m^2 \cdot K)$) is the external heat transfer coefficient considering convective and radiative external heat transfer, and it is calculated by

$$h_{external} = h_{convective} + \sigma e_{surface} (T_{reactor} + T_s)(T_{reactor}^2 + T_s^2) \quad (12)$$

λ ($W/(m \cdot K)$) is the thermal conductivity of the particle, L (m) is the characteristic length, \dot{r} ($kg/(m^3 \cdot s)$) is the pyrolysis reaction rate, ρ_p (kg/m^3) is the density of the particle, and c_p ($J/(kg \cdot K)$) is the heat capacity of the particle.

For the Biot number, a value of 1 represents that the heat transfer resistance inside of and at the surface of the biomass particle are equally important. When $Bi < 1$, the internal heat transfer is rapid compared to the external heat transfer to the particle, and the internal heat transfer is no longer a rate limiting factor. How fast the particle reaches the reactor temperature will depend on the external heat transfer. Under these conditions, the rate-controlling process during the pyrolysis of a biomass particle can be identified by calculating the relative rates of the external heat transfer to the particle and the pyrolysis reaction kinetics with the external pyrolysis number Py' . In contrast, when $Bi > 1$, the internal heat transfer is slow compared to the external heat transfer. The key question will be the relative rates of the internal heat transfer and the pyrolysis reaction kinetics. Therefore, the internal pyrolysis number Py , which defines the relative rates of the internal heat transfer and the pyrolysis reaction kinetics, is applied to identify the rate-controlling process in between the pyrolysis reaction and the internal heat transfer.

Previous works[9, 65] usually analyzed the above dimensionless numbers at the assumption of steady conditions, while the pyrolysis of a single particle is practically unsteady. Unsteady conditions refer to the fact that the above dimensionless numbers will change with the time during the pyrolysis of the biomass particle, since

all the parameters (except the characteristic length of L) in Eq. 9 to Eq. 12 are dynamically changing with time. The evolutions of the above dimensionless numbers during the pyrolysis of the particle were calculated with the present physical-chemical model in [Section 2.2](#).

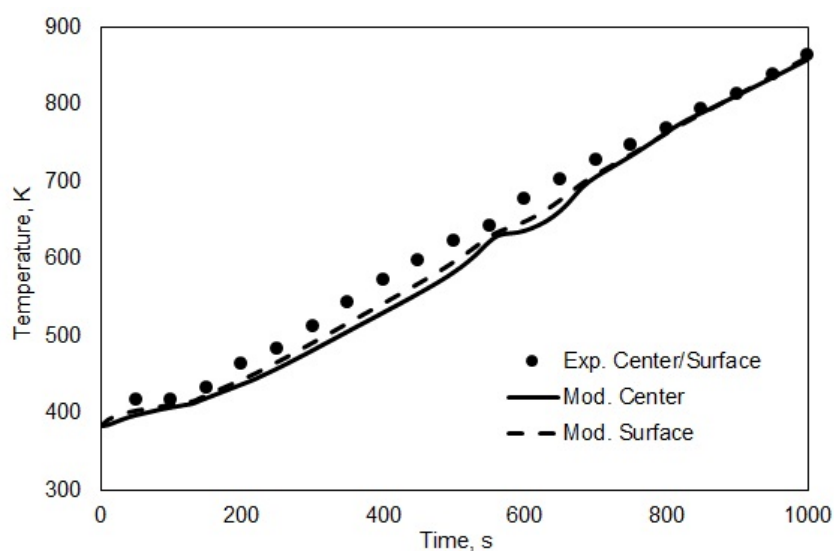
3. Results and discussion

3.1 Model validation against experiments of Pattanotai et al.[55, 136]

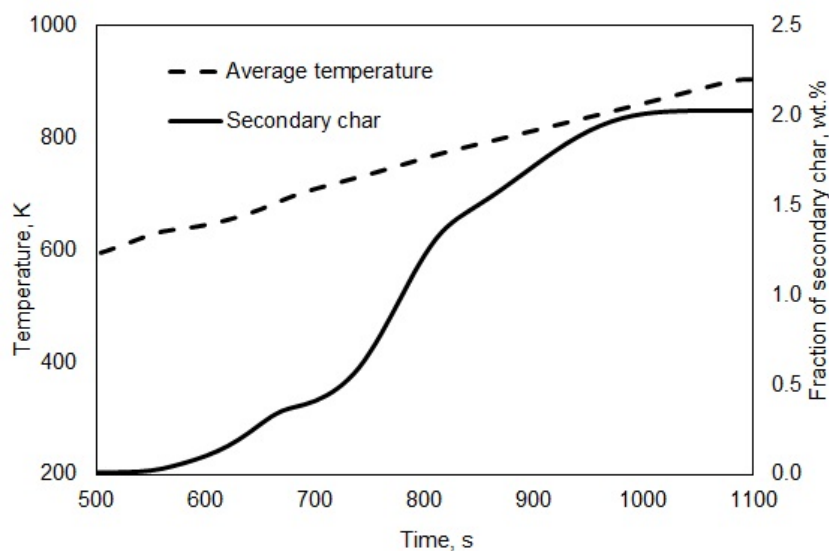
The intraparticle/internal temperature evolution characterizes the intraparticle heat transfer. The temperature evolutions at the center and surface of the wood cylinder (with a diameter of 8 mm and a length of 9 mm at a heating rate of 30 K/min from Pattanotai *et al.*[55]) were predicted and compared with the experimental data, as shown in Fig. 3.2(a). Fig. 3.2(a) shows that the predicted temperature evolutions were in good agreement with the experimental data considering the complex physical and chemical phenomena within the cylindrical particle during its pyrolysis. It was predicted that the intraparticle temperature gradients (with a maximum temperature difference between the surface and the center of around 10 K) were very small, which was also addressed in the experiment. The small intraparticle temperature gradients indicated that the heat transfer inside the wood cylinder was rapid as compared to the extraparticle/external heat transfer to the particle. The good agreement between the simulation results and the experimental data with respect to the intraparticle temperature profile indicates that the present model can be applied to predict the heat transfer process of the biomass particle during its pyrolysis.

Fig. 3.2(b) shows the evolutions of the predicted average particle temperature and of the predicted production of secondary char. As seen from Fig. 3.2(b), it was predicted that the secondary charring reactions mainly progress between 640 K and

800 K. This range was in reasonable agreement with the experimental observation of Pattanotai *et al.*[55], who concluded that the intraparticle heterogeneous conversion of primary volatiles mainly progressed between 670 K and 770 K. The comparison of the secondary charring reactions between the present model and the experiments indicates that the present model can be applied to study the intraparticle secondary charring reactions. In the following sections, further validations of the present model were conducted.



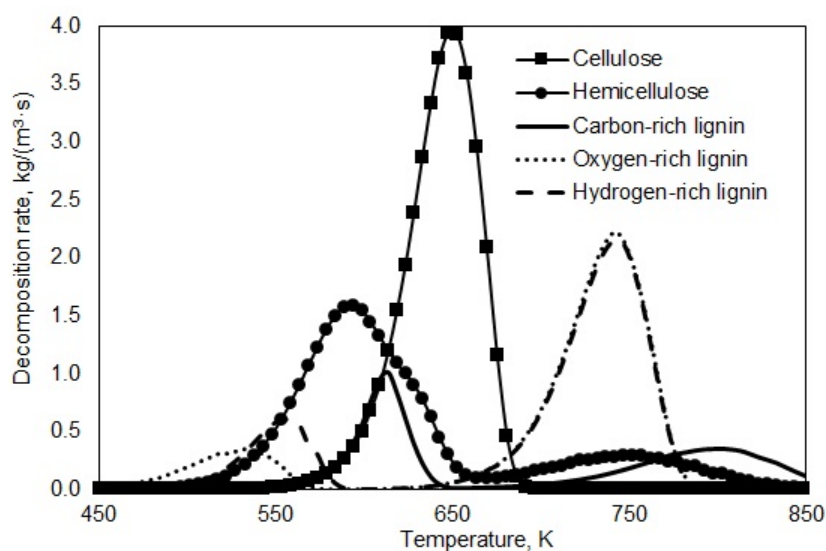
(a)



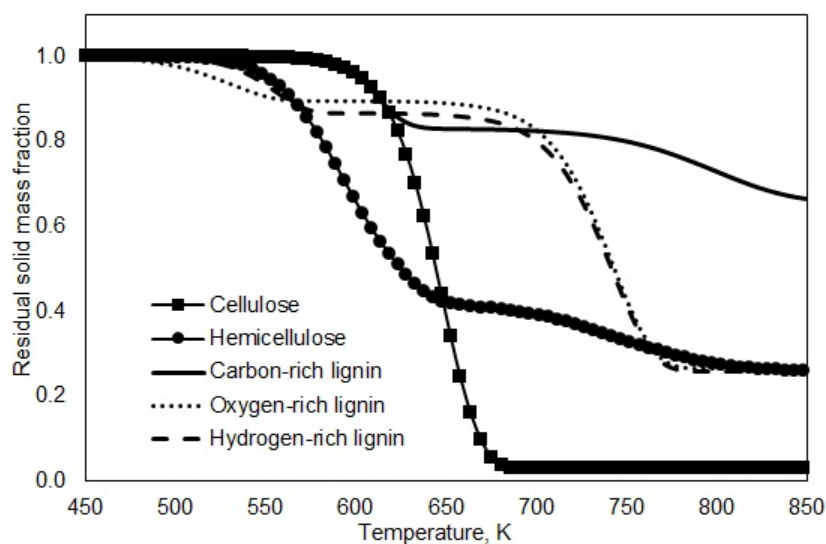
(b)

Fig. 3.2 Evolutions of temperature and of intraparticle secondary char production (a) comparison of the temperature at the center and surface of the cylindrical particle between model and experiment from Pattanotai et al. [55]; (b) the predicted evolutions of average particle temperature and the predicted production of secondary char (weight percentage based on the initial mass of biomass).

The pyrolysis of individual biomass components with the primary pyrolysis kinetics at a heating rate of 30 K/min was simulated to evaluate the results of the primary pyrolysis kinetics.



(a)



(b)

Fig. 3.3 Simulated pyrolysis behavior of individual biomass components, (a) decomposition rate, (b) residual solids mass fraction, at a heating rate of 30 K/min.

Fig. 3.3 shows the decomposition rates and the residual solid weight fractions of individual biomass components. The simulation results showed that the main decomposition stage of hemicellulose occurred at a temperature range from 500 K to 650 K, and the temperature corresponding to maximum decomposition rate was 590 K. These simulation results were in agreement with the experimental observations from Quan *et al.*, [63] who found that the weight loss of hemicellulose mainly happens

at 480 - 640 K and the maximum decomposition rate occurs at 590 K. In the simulation, there was about 26 wt.% of solid residuals left upon the termination of the hemicellulose decomposition at 850 K. The predicted yield of residual solids for hemicellulose decomposition was in the range of the experimental results, which ranged from about 15 wt.% [63] to about 40 wt.%. [62] In the simulation, the main decomposition stage of cellulose occurred at a higher but narrower temperature range from 570 K to 680 K with maximum decomposition rate at 645 K. These simulation results were consistent with the experimental results of Yang *et al.*, [57] who observed that the decomposition of cellulose mainly occurs at 590 – 670 K with a maximum decomposition rate at 630 K. The predicted yield of residual solids for cellulose decomposition was 3.0 wt.%, which was also close to the experimental range of 3.3-11.3 wt.% depending on the crystallinity of the cellulose. [58-61] The predicted decomposition of various lignin components occurred slowly over a broad temperature range from 450 K to over 850 K, which was in good agreement with the experimental results (from around 400 K to over 900 K). [57] In the predictions, yields of residual solids from the decomposition of various lignin components ranged from 26 wt.% to 67 wt.%, which also covered the experimental observations (45.7 wt.%, [57]). Fig. 3.3 (b) indicates that the commonly reported higher yield of residual solids for the decomposition of lignin in the literature [57, 63] can be mainly due to the presence of the carbon-rich component in lignin.

The residual solids mass evolution of the sawdust with the biomass composition (Section 2.4.1) from Pattanotai *et al.* [55] was also predicted. The simulation result was compared with the experimental data from Pattanotai *et al.*, [55] as shown in Fig. 3.4. Fig. 3.4 shows that the primary pyrolysis kinetics can reasonably predict the evolution of the residual solids mass for the sawdust. The above comparison

between the simulation results and the experimental results indicates that the primary pyrolysis kinetics of individual biomass components were reliable in predicting the primary pyrolysis of biomass.

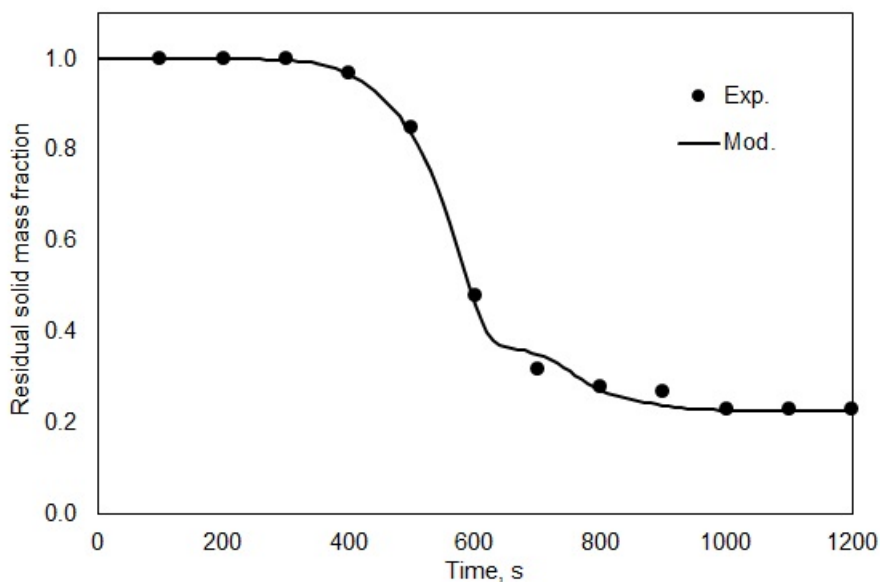


Fig. 3.4 Comparison of the residual solids evolution for biomass sawdust between the model predictions and the experimental data from Pattanotai *et al.* [55]

Table 3.5 shows the comparison of the primary and the secondary char yields predicted by the present model, and by the model (Chapter 2) using a general kinetic scheme [67], and the experimental data from Pattanotai *et al.* [55, 136]. Table 3.5 shows that the modeling results with the present model were in good accordance with the experimental results. Table 3.5 also indicates that the present model was more accurate in predicting the intraparticle secondary charring reactions than the model using general kinetics, in which the biomass was simply regarded as a single reactant species (see Chapter 2). [67] As can be seen from Table 3.5, it was predicted that the secondary char yield increased with the increase of the particle size (length of the cylinder), since larger particle size can provide longer retention

time for volatiles to be heterogeneously converted into secondary char.[9, 51, 65, 67, 79, 171-175].

Table 3.5 Comparison between the model prediction and the experimental data from Pattanotai et al.[55, 136] Results expressed as weight percentage relative to dry feedstock weight.

Terms	Primary char	Secondary char yield from cylinders		
	(experiment [55])	(experiment [136])		
Cylinder dimensions, $d \times L$	Sawdust	8mm \times 2mm	8mm \times 5mm	8mm \times 9mm
Experiment, wt. %	24.5	0.6 \pm 0.6	1.5 \pm 0.5	2.0 \pm 0.5
Present simulation results, wt. %	24.2	0.8	1.8	2.5
Model in Chapter 2	25.0	1.0	2.7	3.7

3.2 Model validation against experiments of Koufopoulos et al.[82, 184]

The evolution of the residual solids mass for beech sawdust and a centimeter-sized beech cylinder were predicted and the predicted results were compared with the experimental data, as shown in Fig. 3.5. This figure shows that the simulation results were in good agreement with the experimental data, indicating that the present model was also reliable in predicting both the primary pyrolysis and the secondary charring reactions during the pyrolysis of hardwood (beech wood). Upon the termination of the pyrolysis, the yields of the primary char, the secondary char and the total char (sum of the primary and secondary char) of the beech cylinder were predicted as 20.7 wt.%, 7.4 wt.% and 28.1 wt.%, respectively. The total char (only primary char) yield of the beech sawdust upon the termination of the pyrolysis was predicted as 18.2 wt.%. These results show that the total char yield of the beech cylinder was higher than that of the beech sawdust at the same isothermal pyrolysis temperature of 773K. The higher total char yield of the beech cylinder compared to

that of the beech sawdust can be explained by (1) the higher heat transfer resistance inside the beech cylinder (resulting into higher primary char yield of the beech cylinder than that of the beech sawdust), and (2) the formation of secondary char in the beech cylinder. Upon termination of the pyrolysis of the beech cylinder, the secondary char accounted for 26 wt.% of the total char, which indicates that the secondary char represents an important fraction of the total char.

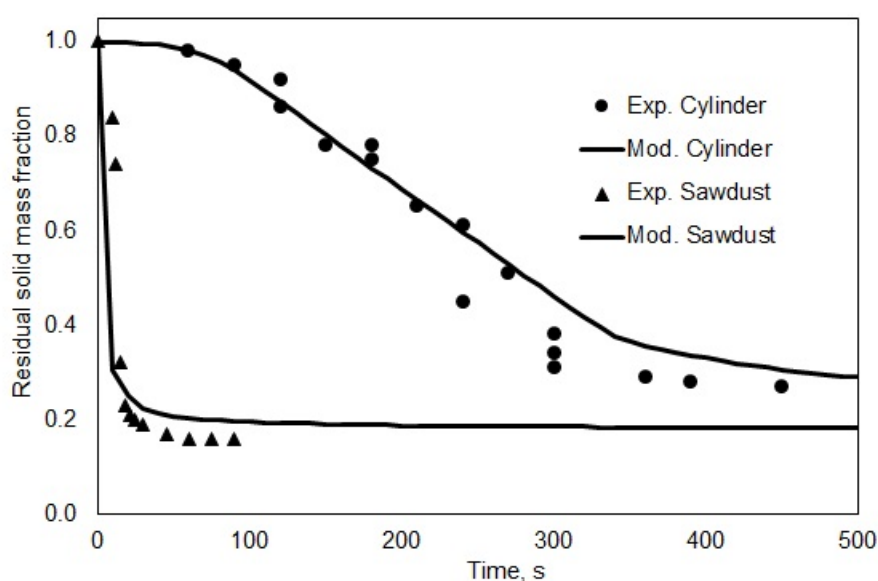


Fig. 3.5 Comparison of the residual solids mass evolution from the isothermal pyrolysis of sawdust and of a cylindrical particle at 773 K between the model predictions and the experimental data from Koufopoulos *et al.* [82, 184]

3.3 Effects of particle size at the thermally thin pyrolysis regime

Effects of particle size on the intraparticle secondary charring reactions were further studied by simulating the pyrolysis of wood cylinders with different lengths (2 mm, 5 mm, 9 mm, 15 mm, and 40 mm) and with the same diameter (8 mm) and at the same heating rate (30 K/min) as used in Pattanotai *et al.* [55]. First, the pyrolysis regime was characterized based on the analysis of the dimensionless numbers. The evolutions of the dimensionless numbers were calculated with the coupled physical-

chemical model for the cylinder with a length of 9 mm (conclusions were the same for cylinders with other lengths), as shown in Fig. 3.6.

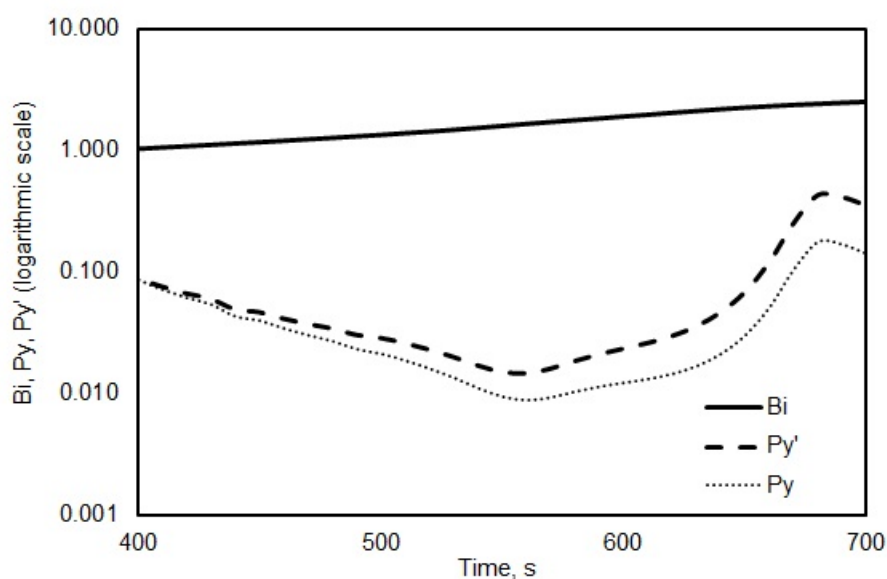


Fig. 3.6 Evolutions of the thermal Biot number and the pyrolysis numbers. (For the wood cylinder with a diameter of 8 mm and a length of 9 mm at a heating rate of 30 K/min)

The characteristic length for this cylinder was 4 mm (radius of the cylinder). As shown in Fig. 3.4, the (primary) pyrolysis of the Japanese cypress from Pattanotai *et al.*[55] mainly occurred at the time from 400 to 700 s. At this time range, Fig. 3.6 shows that the Biot number was small (around 1 or smaller). A small Biot number (around 1 or smaller) indicates that the internal heat transfer was rapid as compared to external heat transfer and that the temperature gradients inside the particle were not significant, which had also been addressed in Fig. 3.2(a). At a small Biot number, the key question would be the relative rates of the external heat transfer to the particle and the pyrolysis reactions, as characterized by the external pyrolysis number (Py'). Fig. 3.6 shows that the external pyrolysis numbers were lower than 1, indicating that the pyrolysis reactions were fast compared to the external heat transfer. [185] The above analysis indicated that the external heat transfer to the

particle controlled the overall pyrolysis of the wood cylinder, which, according to the definition in the literature,[9] was in the thermally thin regime (with low Bi and low Py').

Fig. 3.7 shows the production of the secondary char during the pyrolysis of these wood cylinders. It was predicted that longer cylinders produced higher amounts of secondary char upon the termination of pyrolysis (and hence higher amounts of total char since the primary char yields for all cylinders upon their termination of pyrolysis were the same, namely 22.6 wt.%), which is due to the increased retention time of primary volatiles inside the particle since they are mainly diffusing/flowing out of the particle along the direction parallel to the grain of the cylinder.[55, 136] Model results showed that the length of the cylinder significantly influenced the secondary charring reactions. Upon the termination of the pyrolysis, the secondary char accounted for a higher fraction in the total char as the length of the cylinder increased.

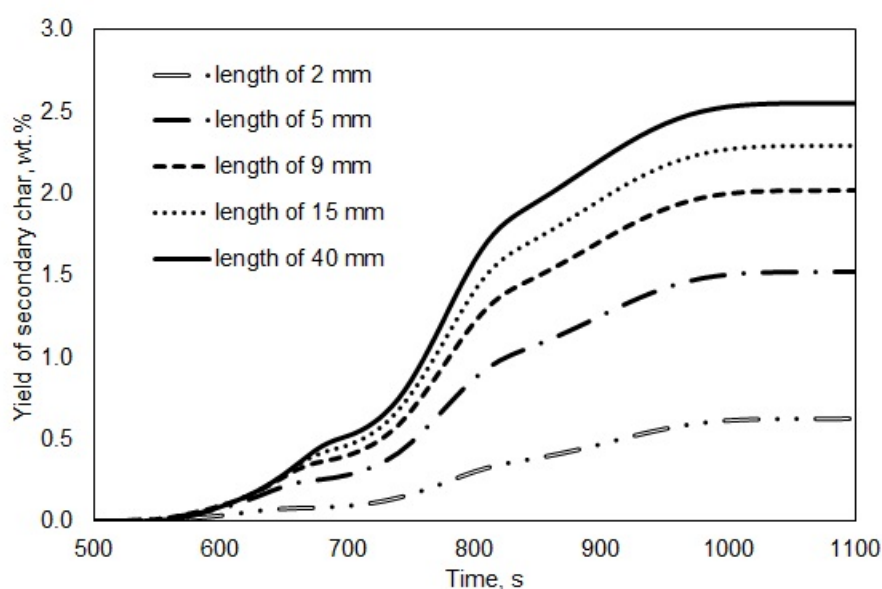


Fig. 3.7 The simulated production of secondary char (weight percentage based on the initial mass of biomass) for various wood cylinders at the thermally thin regime.

It is considered, in the present work, that the intraparticle secondary charring reactions are relevant when the amount of secondary char is higher than 5.0 wt.% of the amount of total char upon the termination of the pyrolysis. When the cylinder was longer than 5 mm, the predicted weight percentage of the secondary char in the total char was higher than 6.3 wt.% upon termination of the pyrolysis. Therefore, it is regarded in the present work that for the pyrolysis of wood cylinders with a diameter of 8 mm and at a heating rate of 30 K/min (at the thermally thin regime), the intraparticle secondary charring reactions start to be relevant when the length of the wood cylinder was longer than 5 mm (corresponding to a characteristic length of 2.5 mm). For the pyrolysis of cylinders shorter than 5 mm, the intraparticle secondary charring reactions were very limited, and the mass loss evolution of these short cylinders can thus be predicted only considering the external heat transfer and the primary pyrolysis kinetics without the need to solve the intraparticle transport phenomena[9]. However, when cylinders were longer than 5 mm, the intraparticle secondary charring reactions start to be relevant and the intraparticle transport phenomena should be calculated in order to quantify the intraparticle secondary charring reactions.

4. Conclusions

In this chapter, the pyrolysis of a single biomass particle with a comprehensive particle model, including a comprehensive kinetic scheme considering biomass composition, was studied. The intraparticle secondary charring reactions due were modelled. The model results were in good agreement with the experimental data from two independent research groups, indicating that the present model can be applied to study the pyrolysis of the biomass particle and the intraparticle secondary charring reactions. Results show that the secondary char yield can account for a

substantial amount of the total char yield and that the intraparticle secondary charring reactions are increasingly important for larger biomass particles. In addition, the intraparticle secondary charring reactions were quantified for the pyrolysis of *cylindrical* biomass particles at the thermally thin regime, where external heat transfer to the particle controls the pyrolysis of the particle. At thermally thin regime, a critical length, being 5 mm (corresponding to a characteristic length of 2.5 mm) for which the intraparticle secondary charring reactions start to be relevant was determined. This obtained value is valid for the pyrolysis of cylindrical biomass particles with a diameter of 8 mm at a heating rate of 30 K/min.

CHAPTER 4

Space-time integral method for simplifying the modeling of pyrolysis of a biomass particle

In previous chapters (Chapter 2 and Chapter 3), biomass pyrolysis at particle scale was studied with three-dimensional comprehensive particle models (3D CPMs), in which mathematical equations for the detailed transport phenomena and pyrolysis reactions were solved. Since the 3D CPM is computationally expensive (i.e. time consuming), the 3D CPM will be further simplified (resulting into a model named simplified particle model, or SPM) in this chapter for saving computational time by only considering the dominant intraparticle physical and chemical phenomena. The application of the SPM will be discussed by modeling the torrefaction (a subpart of slow pyrolysis) of a single biomass particle.

This chapter was published in a modified form as:

Xiaogang Shi, Frederik Ronsse, Jan G. Pieters. Space-time integral method for simplifying the modeling of torrefaction of a centimeter-sized biomass particle. Journal of Analytical and Applied Pyrolysis, 2017, Accepted for publication.

1. Introduction

As described in Chapter 1, slow pyrolysis covers both carbonization (or conventional slow pyrolysis) and torrefaction. Carbonization refers to the conventional slow pyrolysis of biomass aiming to produce a highly carbonaceous, charcoal-like material at temperatures higher than 650 K. In contrast, torrefaction is a thermal pretreatment method at a milder temperature of 470~570 K for the purpose of upgrading biomass, which results into a solid product with lower moisture content, higher energy density, and improved grindability compared to the raw biomass. In a sense, torrefaction can be considered as a mild and partial slow pyrolysis process. In previous chapters (Chapter 2 and Chapter 3), carbonization has been generally focused on. In the following chapters, torrefaction will be focused on, as one of the aims of this thesis is to study the torrefaction of biomass in the screw reactor. Torrefaction at the particle scale will be dealt with in this chapter. **The methodology** for studying biomass torrefaction in this chapter (and in the following chapters) may be extended to the study of carbonization by coupling carbonization kinetics and transport phenomena.

It was reported that the solid end product (char) of biomass torrefaction has a higher gravimetric energy density while at the same time it is more uniform, stable (doesn't rot), hydrophobic and has improved grindability compared to the original biomass feedstock, which makes the char from biomass torrefaction a promising energy substitute for solid fossil fuels (i.e. coal).[41, 83, 186] A substantial amount of experimental and numerical studies have been conducted on biomass torrefaction.[17, 72, 83, 145, 166, 186-194] Detailed kinetic schemes have been developed.[72] Torrefaction technology usually treats biomass with large particle sizes of around 1 cm or larger,[193, 195-197] and after torrefaction, these biomass

particles can be easily grinded for further applications including combustion or co-combustion with coal, gasification, etc.[187, 195, 198-203] Temperature gradients tend to develop within these large-sized biomass particles during torrefaction.[83, 145] In fact, as Peng et al.[204] indicated, the overall reaction rate during torrefaction is still influenced by the particle size even for particles smaller than 1 mm. The non-uniform distribution of temperature coupled to the thermochemical reaction kinetics across the biomass particle renders the torrefaction process difficult to be experimentally studied on the individual particle level. Therefore, researchers have developed computational models to study the physical and chemical processes during the torrefaction of a single biomass particle.[65, 67, 71, 81-83, 91, 93, 94, 102, 103, 105, 106, 108-110, 145, 146, 148, 181, 185, 205-215] Granados et al.[216] compared the torrefaction behavior of large and small biomass particles with two-dimensional particle models. Basu et al. [145] developed a one-dimensional particle model for the torrefaction of a centimeter-sized biomass particle, and their model considered the primary and secondary torrefaction reaction kinetics, drying, diffusive, convective and radiative heat transfer and particle shrinking. Bates and Ghoniem [83] developed a one-dimensional particle model by coupling heat and mass transfer, chemical reaction kinetics and drying for the torrefaction of a centimeter-sized biomass particle. These comprehensive particle models (CPMs) usually solved intraparticle transport (heat, mass and momentum) equations with partial differential equations (PDE) coupled with chemical reaction kinetics, which were capable to describe the spatial and temporal torrefaction characteristics including density of virgin/reacted biomass and solid/gas phase products, intraparticle temperature distribution, etc. These CPMs can allow to have an in-depth understanding of the physical and chemical processes during torrefaction of a single biomass particle.

However, it would require large computational resources and programming efforts to integrate these CPMs in models to simulate industrial-scale torrefaction reactors (i.e. screw reactor[87, 88]) containing large amounts of particles. Practically, the design of industrial torrefaction reactors usually depends on some major physical and chemical characteristics at the particle scale, such as the average particle temperature, biomass mass loss rate, heating time of the biomass particle to reach the designed operating temperature, product yields, etc.[113] To obtain these physical and chemical characteristics at the particle scale with optimized computational efficiency, it is important to reduce the complexity of the computational models (e.g. CPM) while maintaining a desired level of model accuracy.

Some works have been dedicated to search for a less complex model (simplified particle model, or SPM) predicting the physical-chemical processes during the pyrolysis of a single biomass particle.[115-121] These SPMs mainly follow one of two extremes: uniform conversion model (UCM) or unreacted-shrinking-core model (USCM).[65, 113, 114] In UCM, the pyrolysis process is assumed to happen homogeneously across the whole biomass particle. In USCM, the pyrolysis of a biomass particle is considered to occur at an infinitely thin surface, which is a moving reaction front separating the biomass particle into two layers with one layer of virgin biomass and another layer of char.[115-122] The application of UCM and USCM is strictly dependent on the rate-controlling process during the pyrolysis of a biomass particle. The UCM is applicable when the pyrolysis of a biomass particle can be assumed to be purely kinetically controlled, while the USCM is appropriate when the pyrolysis of a biomass particle can be assumed to be controlled by the internal heat transfer. However, neither the UCM nor the USCM is applicable in predicting the torrefaction of a centimeter-sized biomass particle, since the internal heat transfer

and the torrefaction reaction can play comparable roles in affecting the particle's torrefaction.[83, 145]

The purpose of this chapter is to develop a simplified particle model (SPM) that is applicable for modeling the torrefaction of a centimeter-sized biomass particle. Non-dimensional numbers are applied to briefly analyze the possible rate-controlling processes that can be assumed in developing the SPM. These assumptions are further validated by comparison of the model predicted data against the 3D CPM which is adapted from Chapter 2 and Chapter 3 and which is experimentally validated. Then, the space-time integral method is applied to derive the SPM. The accuracy of the SPM is then studied by comparing to the experimental data and to the CPM when experimental data are not available. Finally, the applicability of the SPM is discussed.

2. Methods

2.1 Analysis of non-dimensional numbers

The analysis of non-dimensional numbers (e.g. Biot number, pyrolysis number) has been usually applied to identify the rate-controlling processes that can be assumed in developing simplified particle models (SPMs) for the thermochemical conversion of biomass particles.[57] The analysis of non-dimensional numbers (details in **Appendix A**) indicates that both the internal heat transfer resistance and the chemical reactions need to be accounted for in the SPM for biomass torrefaction. It should be mentioned that the non-dimensional numbers only provide limited information about the intraparticle physical and chemical phenomena. Therefore, the CPM, in which detailed transport phenomena and torrefaction reactions can be predicted, was further applied to aid the development of the SPM.

2.2 Torrefaction kinetics

The kinetic scheme as shown in Fig. 4.1 was applied to describe the torrefaction reactions of biomass. This kinetic scheme was originally proposed by Di Blasi and Lanzetta,[217] and was later applied by other authors to describe the mass loss of various types of biomass up to 573 K [83, 218, 219]. In this kinetic scheme, the torrefaction process involves five lumped components, with biomass first decomposing into volatile 1 and an intermediate solid product. The solid intermediate then undergoes subsequent reaction into char and volatile 2. Each reaction rate in the torrefaction kinetics was described with a first order Arrhenius function. The drying process during biomass torrefaction was modeled as a first order reaction [83]. The kinetic rate parameters for torrefaction and for drying are listed in Table 4.1.

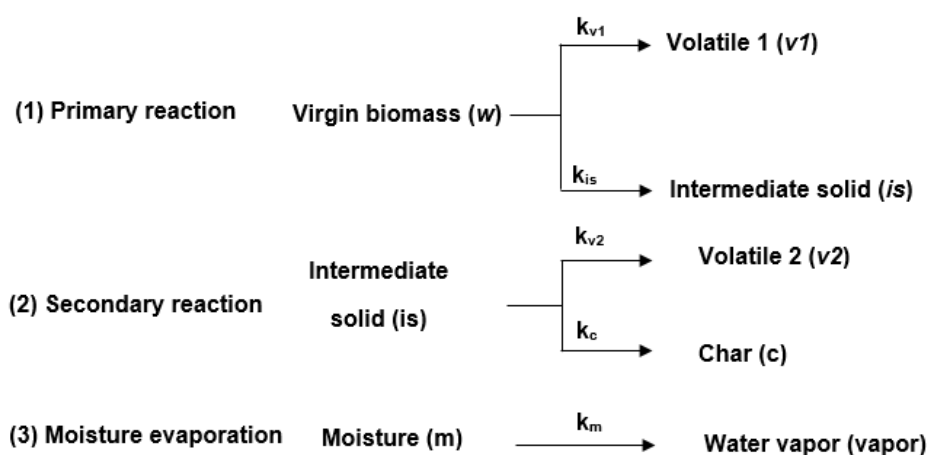


Fig. 4.1 Reaction kinetic scheme for the torrefaction and the drying process.

Table 4.1 Kinetic parameters for the torrefaction reaction and for the drying process.

Reaction	Reaction rate	Reference
k_{v1} [1/s]	$3.23 \times 10^7 \exp(-114,214/R_{\text{cons}}T)$	[219]
k_{is} [1/s]	$2.48 \times 10^4 \exp(-75,976/R_{\text{cons}}T)$	[219]
k_{v2} [1/s]	$1.59 \times 10^{10} \exp(-151,711/R_{\text{cons}}T)$	[219]
k_c [1/s]	$1.1 \times 10^{10} \exp(-151,711/R_{\text{cons}}T)$	[219]
k_m [1/s]	$4.5 \times 10^3 \exp(-45,000/R_{\text{cons}}T)$	[219]

2.3 Particle model

2.3.1 Comprehensive particle model (CPM)

Detailed characteristics for the torrefaction of a centimeter-sized biomass particle can be obtained from the CPM, which, in this chapter, is a modification of the CPMs in Chapter 2 and Chapter 3. The modification consisted of including appropriate torrefaction and drying kinetics as described in Section 2.2. The modification was made since the kinetics in previous chapters were not applicable to torrefaction (details are discussed in the **Appendix B**).

After it is validated against experimental data, the CPM will be applied to assess the importance of several physical and chemical phenomena and to validate the assumptions and simplifications that were made for developing the SPM for the torrefaction of a centimeter-sized biomass particle. In addition, the CPM will also be applied to provide a parameter, the *torrefaction temperature* ($T_{\text{torrefaction}}$), for use in developing the SPM. The *torrefaction temperature* is a parameter characterizing the temperature at which the torrefaction reactions are assumed to occur in the SPM. The *torrefaction temperature* is determined with the CPM by averaging the decomposition-rate-weighted temperature over the entire particle volume and over the entire torrefaction process[117], as calculated by the following equation:

$$T_{\text{torrefaction}} = \frac{1}{(1-\eta_{\text{residual}})\rho_{w0}} \int_0^{t_e} \left[\frac{1}{V} \int_0^V T(r, z, t) \frac{-\partial(\rho_w + \rho_{\text{is}} + \rho_{\text{char}})}{\partial t} dV \right] dt \quad (1)$$

where the term $(1-\eta_{\text{residual}})\rho_{w0}$ (kg/m^3) denotes the total density loss of the biomass particle over the entire torrefaction process. η_{residual} is the solid yield at the end of the torrefaction process, ρ_{w0} (kg/m^3) is the initial particle density, t_e (s) is the termination time of the torrefaction process, and V (m^3) is the particle volume. $T(r, z, t)$ (K) is the temperature at time t within the three-dimensional particle, r (m) is the radial position and z (m) is the axial position (for cylindrical particle). The term of $\frac{-\partial(\rho_w + \rho_{\text{is}} + \rho_{\text{char}})}{\partial t}$ ($\text{kg}/(\text{m}^3 \cdot \text{s})$) is the mass loss rate of the residual solid. ρ_w , ρ_{is} , ρ_{char} are the instantaneous densities of biomass, intermediate solid product and char.

2.3.2 Simplified particle model (SPM)

The SPM was developed for a dry centimeter-sized cylindrical biomass particle by taking into account its main pyrolysis characteristics including intraparticle heat transfer and torrefaction reactions. In the simplified model, it is assumed that the reaction heats are zero and that only conductive heat transfer occurs inside the particle, and that volatiles formed during torrefaction leave the particle instantly. These assumptions will be validated with the CPM (in Section 3.2). The conductive heat transfer is further assumed to occur one-dimensionally in the radial direction for the cylindrical biomass particle since the cylindrical particle has a large aspect ratio of 6.0.[220] The shrinkage of the particle size in the radial direction is neglected, as the shrinkage has only a minor influence on the torrefaction of a biomass particle.[67]

Based on the detailed results from the CPM, the present work decoupled the intraparticle heat transfer and torrefaction reactions in developing the SPM for the dry centimeter-sized cylindrical biomass particle. In the SPM, the particle is assumed to

first experience internal heating (particle heating-up, no reaction) until the instantaneous volume-averaged particle temperature predicted by the SPM reaches the torrefaction temperature ($T_{\text{torrefaction}}$), as defined in Eq. (1), and then the torrefaction reactions are assumed to be initiated at this temperature until the reaction is terminated at the end.

The SPM was developed with the space-time integral method[107, 113], and a one-dimensional finite control volume, as shown in Fig. 4.2, in the radial direction of the cylindrical particle was applied to describe the movement of the thermal front (at the position of $r = r_{\text{wave}}(t)$, as shown in Fig. 4.2) from particle surface towards center. Since heat was transferred from the surface to the center, to define $r=0$ at the particle surface is more convenient to deduce the heat transfer equations.

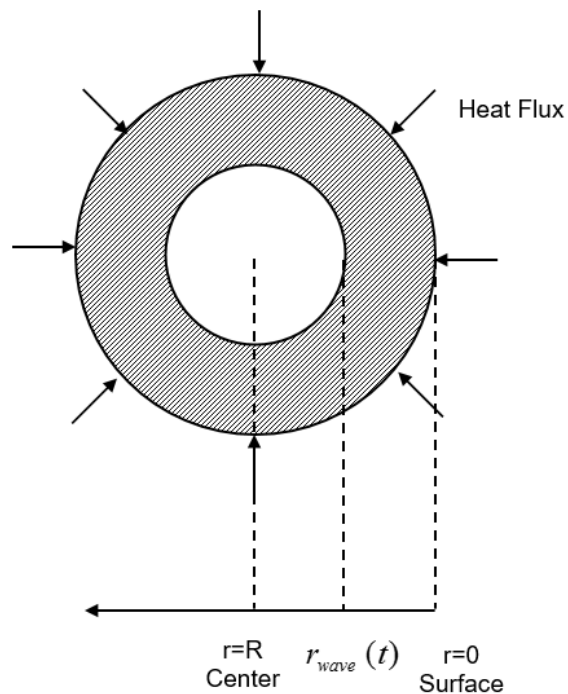


Fig. 4.2 The control volume for simplifying the torrefaction process of a cylindrical biomass particle.

As the particle heats up, the instantaneous volume-averaged particle temperature is calculated. If the instantaneous volume-averaged particle temperature has reached $T_{\text{torrefaction}}$ before the thermal front reaches the particle center, the particle is assumed to only experience the first heating stage as described below. Otherwise, the particle is assumed to experience the subsequent second heating stage after its first heating stage until the instantaneous volume-averaged particle temperature reaches $T_{\text{torrefaction}}$. With the space-time integral method, the intraparticle heat transfer can be described with a set of linearized equations, which are presented in the following

(1) First heating stage

The energy conservation on the finite control volume (Fig. 4.2, a thermal wave with a thickness of $r_{\text{wave}}(t)$ at time t (s)) is stated as,

$$\dot{E}_{in} - \dot{E}_{out} = \dot{E} \quad (2)$$

Where \dot{E}_{in} (W/m) is the energy added at the particle surface ($r=0$),

$$\dot{E}_{in} = -\lambda \cdot 2\pi(R-0) \cdot \frac{dT(r=0,t)}{dr} = 2\pi Rq(t) \quad (3)$$

Where λ (W/(m·K)) is the thermal conductivity of the biomass, R (m) is the radius of the particle, $q(t)$ (W/m²) is the net heat flux at the surface of the particle at time t ; $T(r=0,t)$ (K) is the temperature at the surface of the particle at time t .

The energy flow out of the finite volume is 0 ($\dot{E}_{out} = 0$) at $r = r_{\text{wave}}(t)$, and \dot{E} is the rate of change of energy inside the finite control volume,

$$\dot{E} = \rho_{w0} C_w \frac{d}{dt} \int_0^{r_{wave}(t)} [T(r,t) - T(r = r_{wave}(t), t)] d[\pi R^2 - \pi(R-r)^2] \quad (4)$$

Where ρ_{w0} (kg/m³) is the density of the biomass, C_w (J/(kg·K)) is the heat capacity of the biomass, $T(r = r_{wave}(t), t)$ is the temperature at $r = r_{wave}(t)$ at time t .

From the above, the following equation is obtained,

$$\frac{d}{dt} \int_0^{r_{wave}(t)} [T(r,t) - T(r = r_{wave}(t), t)] (R-r) dr = \frac{R}{\rho_{w0} C_w} q(t) \quad (5)$$

It was assumed that a quadratic distribution of temperature is developed inside the finite control volume at time t .

$$T(r, t) = Ar^2 + Br + C \quad (6)$$

and the constants of A, B and C can be obtained with the following boundary conditions,

$$\begin{aligned} \frac{dT(r = r_{wave}(t), t)}{dr} &= 0 \\ -\lambda \frac{dT(r = 0, t)}{dr} &= q(t) \end{aligned} \quad (7)$$

$$T(r = r_{wave}(t), t) = T_0$$

With the above boundary conditions, the temperature distribution at time t is expressed as,

$$T(r, t) = \frac{q(t)}{2\lambda r_{wave}(t)} r^2 - \frac{q(t)}{\lambda} r + T_0 + \frac{q(t)}{2\lambda} r_{wave}(t) \quad (8)$$

With the assumed temperature distribution inside the control volume, the following equation can be obtained,

$$d\left[\frac{q(t)}{24\lambda}(4Rr_{wave}(t)^2 - r_{wave}(t)^3)\right] = \frac{R}{\rho_{w0}C_w} q(t)dt \quad (9)$$

The initial conditions are (at time of $t = 0_s$),

$$\begin{aligned} T(r, t=0) &= T_0 \\ q(t=0) &= q_0 = h_{convective}(T_{reactor} - T_0) + \sigma e(T_{reactor}^4 - T_0^4) \\ r_{wave}(t=0) &= 0 \end{aligned} \quad (10)$$

Where $h_{convective}$ (W/(m²·K)) is the convective heat transfer coefficient, $T_{reactor}$ is the reactor (or operating) temperature, and σ and e are Stefan-Boltzmann constant and emissivity, respectively.

By integrating Eq. (9) from time of 0 to time of t , the following equation describing the relationship between the thickness of the thermal wave ($r_{wave}(t)$) and the time t is obtained,

$$t = \frac{4Rr_{wave}(t)^2 - r_{wave}(t)^3}{12R \frac{\lambda}{\rho_{w0}C_w} \left(1 + \frac{q_0}{q(t)}\right)} \quad (11)$$

The temperature at the surface of the particle at time t is,

$$T(r=0, t) = T_0 + \frac{q(t)}{2\lambda} r_{wave}(t) \quad (12)$$

The heat flux at the particle surface at time t is,

$$q(t) = h_{convective}(T_{reactor} - T(r=0, t)) + \sigma e(T_{reactor}^4 - T(r=0, t)^4) \quad (13)$$

And the instantaneous volume-averaged temperature of the particle at time t can be obtained,

$$T_m(t) = \frac{-q(t)}{12\lambda R^2} r_{wave}(t)^3 + \frac{q(t)}{3\lambda R} r_{wave}(t)^2 + T_0 \quad (14)$$

The time for the thermal front to reach the center of the particle ($r_{wave}(t) = R$) is,

$$t_R = \frac{R^2}{4 \frac{\lambda}{\rho_w C_w} \left(1 + \frac{q_0}{q(t=t_R)}\right)} \quad (15)$$

And the instantaneous volume-averaged temperature of the particle at time $t = t_R$ is,

$$T_m(t=t_R) = T_0 + \frac{q(t=t_R)}{4\lambda} R \quad (16)$$

The above instantaneous volume-averaged particle temperature is calculated to check whether it has reached $T_{torrefaction}$. If the instantaneous volume-averaged particle temperature is still lower than $T_{torrefaction}$, the second heating stage was calculated according to the procedure presented in the following section.

(2) Second heating stage

The initial condition for the surface temperature for the second stage of heating, starting at $t = t_R$ is,

$$T_2(r=0, t=t_R) = T_0 + \frac{q(t=t_R)}{2\lambda} R \quad (17)$$

Where $q(t=t_R)$ can be calculated in the first heating stage.

And the initial temperature distribution inside the particle for the second heating stage is,

$$T_2(r, t = t_R) = (T_0 + \frac{q(t = t_R)}{2\lambda} R) + \frac{q(t = t_R)}{2\lambda R} r^2 - \frac{q(t = t_R)}{\lambda} r \quad (18)$$

The boundary conditions at time $t(t > t_R)$ are,

$$\begin{aligned} \frac{dT_2(r = R, t)}{dr} &= 0 \\ -\lambda \frac{dT_2(r = 0, t)}{dr} &= q_2(t) \end{aligned} \quad (19)$$

$$T_2(r = 0, t) = T_s(t)$$

Where $q_2(t)$ is the net heat flux at the surface of the particle at time $t(t > t_R)$,

$$q_2(t) = h_{\text{convective}}(T_{\text{reactor}} - T_s(t)) + \sigma e(T_{\text{reactor}}^4 - T_s(t)^4) \quad (20)$$

And initially, $q_2(t)$ is expressed as $q_2(t = t_R) = q(t = t_R)$, which can be calculated in the first heating stage. $T_s(t)$ is the surface temperature at time $t(t > t_R)$ and its initial value is $T_s(t = t_R) = T_2(r = 0, t = t_R) = T_0 + \frac{q(t = t_R)}{2\lambda} R$, as described in Eq. (17).

With the above boundary condition, the temperature distribution within the particle is,

$$T_2(r, t) = T_s(t) - \frac{q_2(t)}{\lambda} r + \frac{q_2(t)}{2\lambda R} r^2 \quad (21)$$

With the energy conservation, the following equation can be obtained,

$$d\left[\frac{T_s(t)-T_0}{2}R^2 + \frac{q(t=t_R)-q_2(t)}{8\lambda}R^3\right] = \frac{R}{\rho_{w0}C_w}q_2(t)dt \quad (22)$$

Integrating the above equation from $t = t_R$ to t , the following equation describing the temperature at the particle surface is obtained,

$$T_s(t) = T_0 + \frac{q(t=t_R)+q_2(t)}{4\lambda}R + \frac{q(t=t_R)+q_2(t)}{\rho_{w0}C_wR}(t-t_R) \quad (23)$$

And the instantaneous volume-averaged particle temperature at time t can be obtained as

$$T_{m2}(t) = T_s(t) - \frac{q_2(t)}{4\lambda}R \quad (24)$$

In the second heating stage, when the instantaneous volume-averaged particle temperature is heated up to $T_{\text{torrefaction}}$, the torrefaction reactions were assumed to be triggered at this $T_{\text{torrefaction}}$ until the torrefaction reactions were terminated.

With the SPM, the time evolution of heat transfer (e.g. intraparticle temperature distribution) during the torrefaction of a biomass particle can be predicted with a group of linearized equations, which indicates that the model complexity can be significantly reduced compared to the set of partial differential equations (PDEs) in the CPM. From the above equations, it can be seen that the time evolution of heat transfer can be calculated with variables including the operating conditions (reactor temperature), the physical properties of the biomass particle (initial density, size, heat capacity, and thermal conductivity) and some model parameters (external convective heat transfer coefficient, Stefan-Boltzmann constant and emissivity).

2.4 Model validation and accuracy

2.4.1 Validation and accuracy of the CPM

To validate the CPM (with the specific torrefaction kinetics rather than the pyrolysis kinetics used in Chapters 2 and 3), the experimental data from Basu et al.[145] and from Van der Stelt[221] were used.

In the experimental work of Basu et al.[145] the torrefaction of a cylindrical biomass particle with a diameter of 2.54 cm and a length of 15.24 cm was studied. The ratio of length-to-diameter was 6. The particle had a moisture content of $\theta=6.4$ wt.% and a density of 500 kg/m^3 . They obtained evolutions of the residual solid mass and the temperature at the particle center at two reactor (or operating) temperatures of 513 K and 553 K.

The experimental work of Van der Stelt[221] dealt with the torrefaction process of a cylindrical biomass particle with a diameter of 2.8 cm and a length of 10cm. The particle had a moisture content of approximately $\theta=6$ wt.% and a density of 700 kg/m^3 . [83] The particle was initially at ambient temperature, and then it was heated with a heating rate of about 10 K/min to the final operating/reactor temperatures of 508 K and 553 K, respectively.

For each validation, the accuracy of the CPM was determined by calculating the mean deviation (*MD*) between the modeling results from the CPM and the experimental data.

$$MD = \frac{1}{n} \sum_{i=1}^n |X_{\text{exp}}(t_i) - X_{\text{mod}}(t_i)| \quad (25)$$

2.4.2 Validation and accuracy of the SPM

The validation of the SPM was conducted by comparing the time evolutions of the residual solid mass fraction predicted from the SPM with those from the

experimental work of Basu et al.[145], as described in Section 2.4.1, for the cylindrical biomass particle (feedstock dry basis) at two reactor temperatures of 513 K and 553 K. The *MD* value was also calculated to characterize the quantitative difference between the SPM and the experimental data.

The accuracy of the SPM was further assessed by comparing the time evolutions of the volume-averaged particle temperature, the temperature at the particle surface, and the temperature distribution inside the particle predicted by the SPM with those from the CPM for the dry cylindrical particle with the same size as in the experiments of Basu et al.[145].

The accuracy of the SPM was also studied for the particle with the same size as in the work of Van der Stelt[221] (feedstock dry basis). The predicted temperature at the particle surface and the predicted temperature distribution inside the particle using the SPM were compared to those from the CPM developed for the particle with the same size as in the work of Van der Stelt.[221].

3. Results and discussion

3.1 Validation of the comprehensive particle model (CPM)

3.1.1 Validation of the CPM against experimental results from Basu et al.[145]

Fig. 4.3 shows the comparison between the predicted time evolution of the residual solid mass fraction, using the CPM, and the experimental data from the work of Basu et al.[145] In Fig. 4.3, the mean deviations (*MD*) between experiment and model are 1.7 *wt.%* and 4.3 *wt.%* (feedstock wet basis) at reactor temperatures of 513 K and 553 K, respectively.

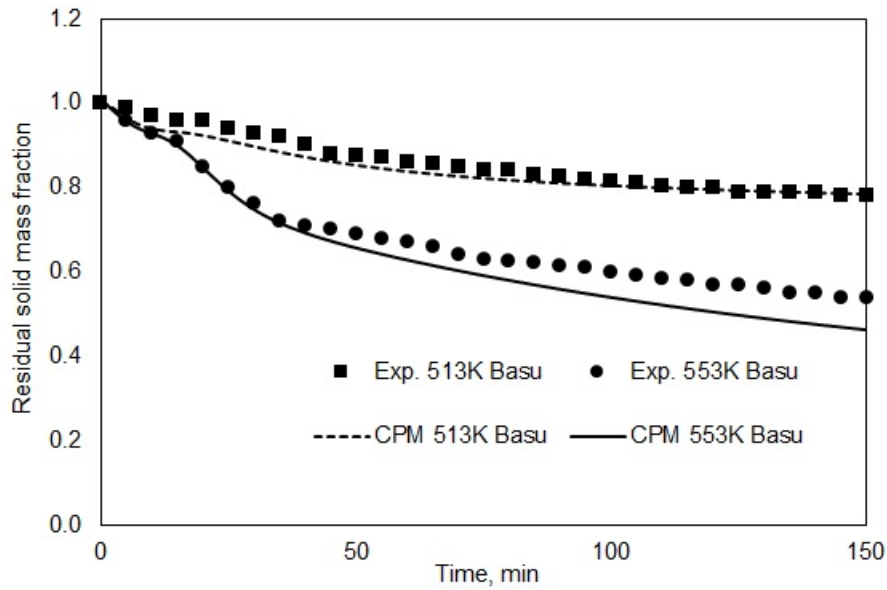


Fig. 4.3 Comparison of residual solid mass fraction evolution between the CPM and the experiment of Basu et al.[145] at two reactor temperatures of 513K and 553K.

Fig. 4.4 compares the predicted time evolution of the temperature at the particle center with the experimental data. In Fig. 4.4, the *MD* between experiment and model are 10 K and 14 K at reactor temperatures of 513 K and 553 K, respectively.

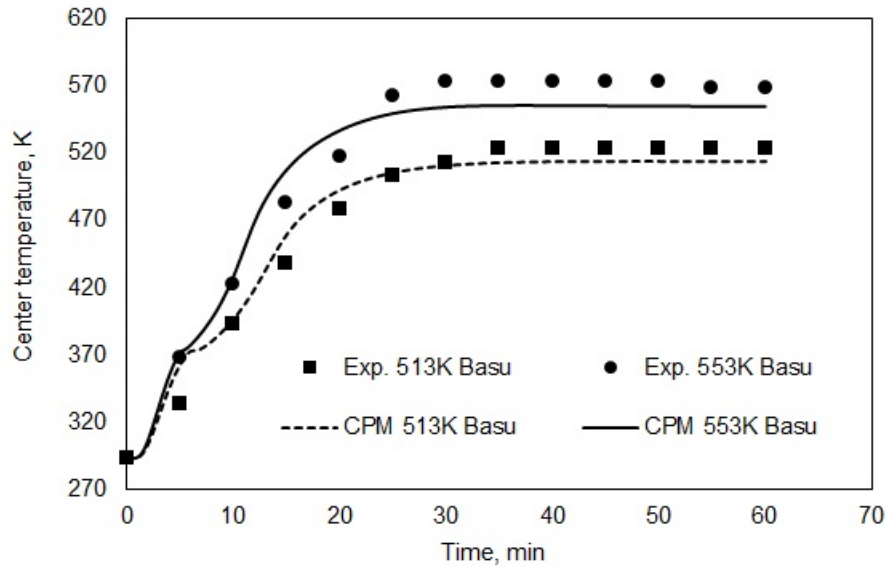


Fig. 4.4 Comparison of temperature at the particle center between the CPM and the experiment of Basu et al.[145] at two reactor temperatures of 513 K and 553 K.

Fig. 4.3 and Fig. 4.4 indicate that the CPM can reasonably predict the evolutions of the residual solid mass fraction and the temperature at the particle center, despite some quantitative differences being present.

3.1.2 Validation of the CPM against experimental results from Van der Stelt[221]

Fig. 4.5 shows the comparison of the time evolution of the particle center-temperature and the particle surface-temperature between the simulation results from the CPM and the experimental data from Van der Stelt.[221]

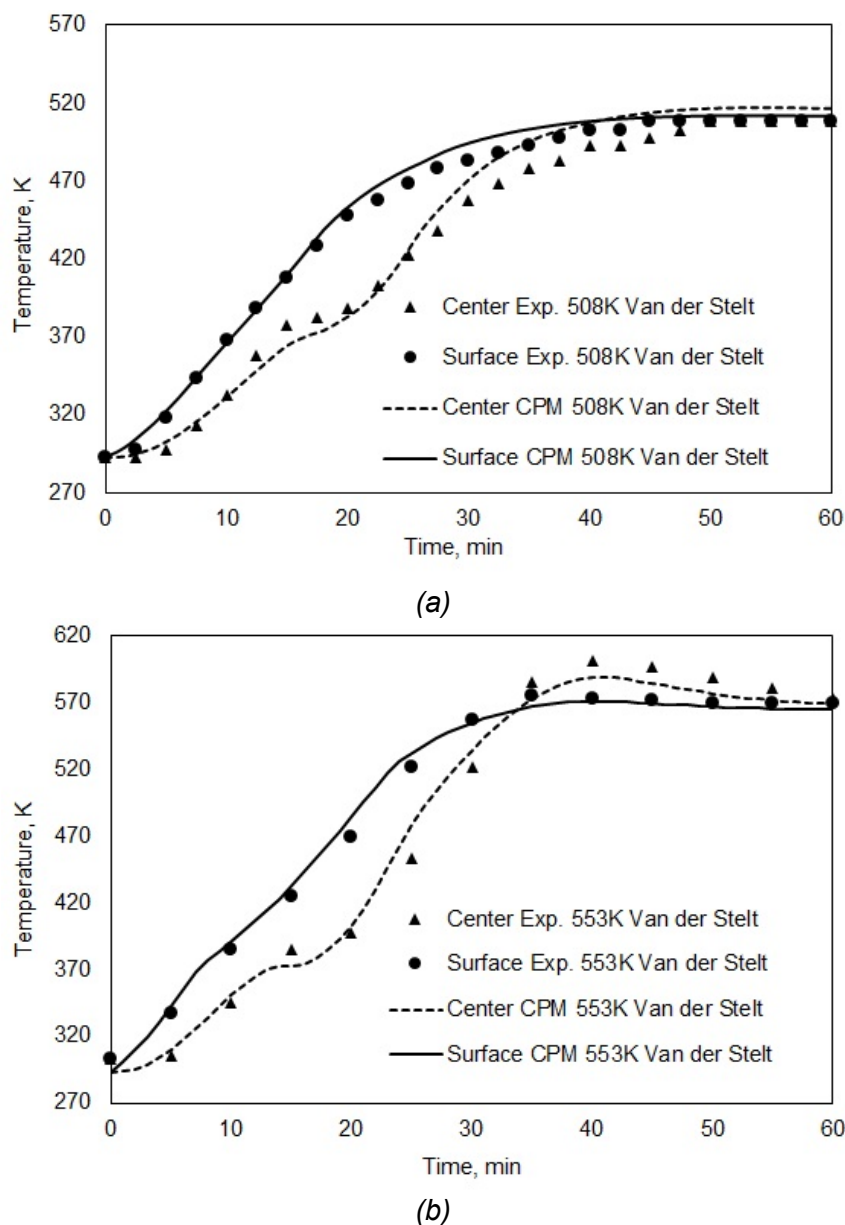


Fig. 4.5 Comparison of temperature at the particle center and surface between the CPM and the experiment of Van der Stelt[221] at the reactor temperature of (a) 508 K and (b) 553 K.

Fig. 4.5 (a) shows the comparison at the reactor temperature of 508 K. The center-temperature shows a plateau at around 15 minutes. Moisture evaporation occurs at around 100 °C. At this stage, the heat absorbed by the particle is mainly used to evaporate the moisture in the particle. Therefore, at this evaporation stage, temperature at the particle center will show a plateau. The *MD* between the model and the experiment is 7 K for the center-temperature and also 7 K for the surface-temperature. Fig. 4.5(b) shows the comparison at a reactor temperature of 553 K.

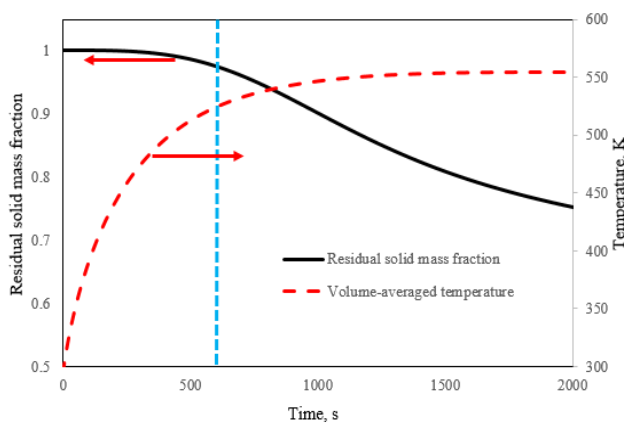
This figure shows a temperature-peak, which overshoots the reactor temperature, at the center of the particle, which has also been reported in many experimental and modeling works for centimeter-sized or larger biomass particles.[71, 81, 83] Fig. 4.5(b) shows that the predicted peak temperature at the center of the particle is in good agreement with the experiment. The *MD* between the model and the experiment is 11 K for the center-temperature and 6 K for the surface-temperature. It should be mentioned that a slight temperature-peak is also present in Fig. 4.4 at a reactor temperature of 553 K for the work of Basu et al.[145], which is less obvious than the one in Fig. 4.5(b), and this difference can be due to the larger size (diameter) of the biomass particle in the work of Van der Stelt.[221] Bates and Ghoniem[83] also reported that larger particles tend to exhibit stronger exothermicity during torrefaction, which leads to a more obvious temperature-peak at the center of a larger particle.

From the above validations, it can be concluded that the CPM was accurate to predict the intraparticle heat transfer and the torrefaction process of a centimeter-sized biomass particle. CPM-generated data, being more extensive than available experimental data in literature, was then used to develop the simplified particle model (SPM), by validating the assumptions made in the simplified particle model (SPM) and by assessing the accuracy and the computational efficiency of the SPM.

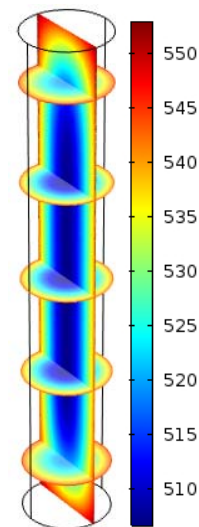
3.2 Validation of the assumptions of the simplified particle model (SPM)

The CPM was used to study the validity of the assumptions made in developing the SPM. The detailed torrefaction characteristics on a dry cylindrical particle with the same size as in the work of Basu et al.[145] (and the conclusions are similar for the particle with the same size as in the work of Van der Stelt.[221]) were first analyzed with the CPM. Fig. 4.6 shows the torrefaction behavior predicted by the CPM for the dry cylindrical biomass particle at the reactor temperature of 553 K. Fig. 4.6(a) shows

the time evolutions of the residual solid mass fraction and of the volume-averaged particle temperature. Fig. 4.6(b-f) shows the instantaneous torrefaction behavior at several planes in radial and axial directions of the 3D particle at the simulated time of 600 s. Fig. 4.6(b) shows that the temperature at the center of the particle is about 40K lower than that near the particle surface, indicating that heat transfer resistance inside the particle is not negligible during the torrefaction of a centimeter-sized biomass particle. Therefore, it is necessary for the SPM to account for the intraparticle heat transfer resistance that builds the intraparticle temperature gradient. Due to the temperature difference between particle center and surface, the mass loss rate of the residual solid is higher near the particle surface and lower near the particle center, as shown in Fig. 4.6(f), which leads to a lower concentration for the reactant (virgin biomass) and higher concentrations for the solid product (intermediate solid product and char) near the particle surface (Fig. 4.6(c-e)).



(a) Simulation of the temperature and solid mass profiles



(b) Temperature, K

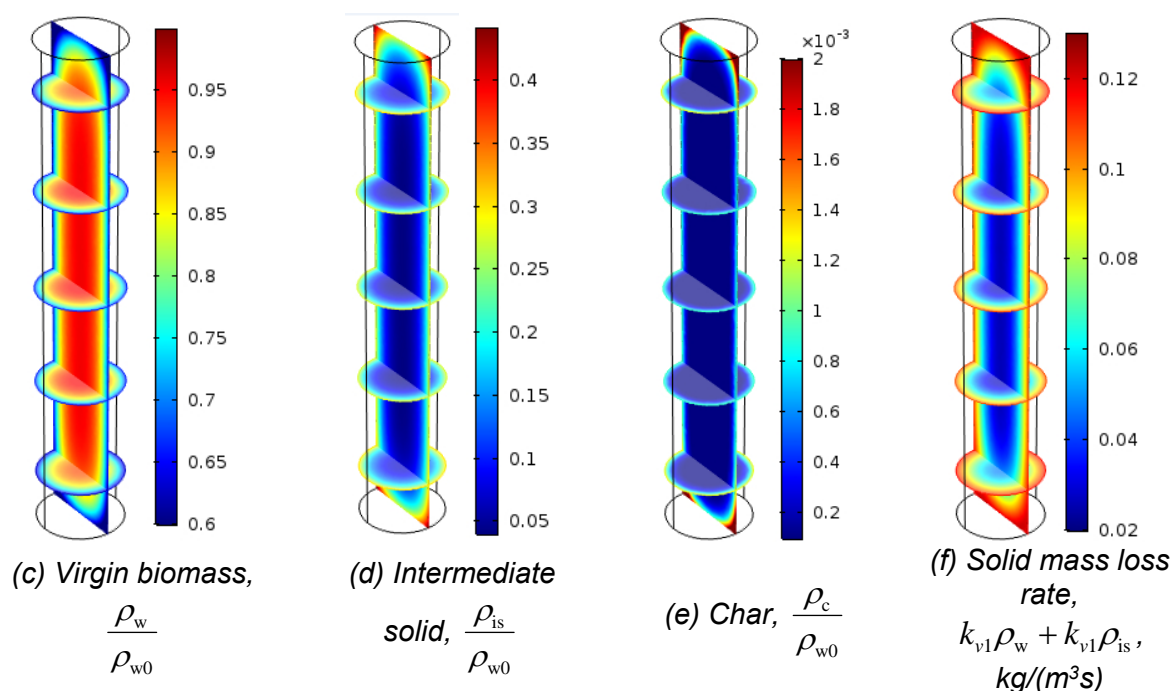
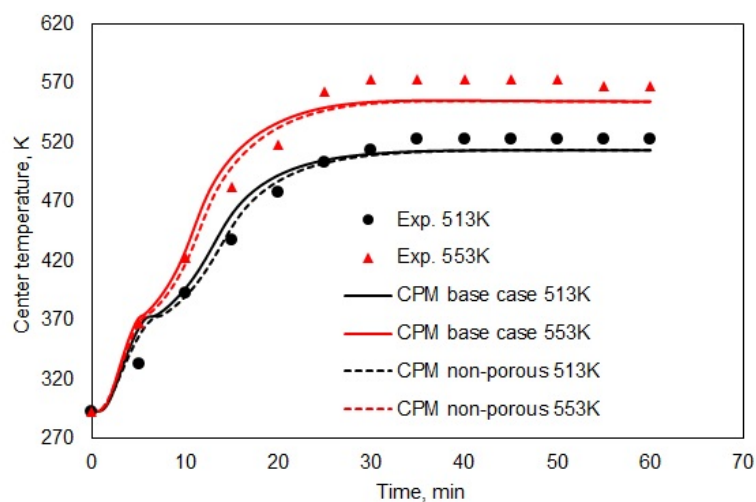


Fig. 4.6 Instantaneous torrefaction behavior predicted from the CPM for a dry cylindrical biomass particle at the time of 600s at a reactor temperature of 553K.

At the reactor temperature of 553 K, as shown in Fig. 4.6, the $T_{\text{torrefaction}}$ in Eq. (1) was calculated as 548 K. The solid mass that is lost before the instantaneous volume-averaged particle temperature reaches 548 K is about 20% of the total loss of the solid mass. At another reactor temperature of 513 K (not shown in the figures), the $T_{\text{torrefaction}}$ was calculated as 510 K, and the solid mass that was lost before the instantaneous volume-averaged particle temperature reached 510 K was about 16% of the total loss of the solid mass. These numerical results from the CPM show that a majority of the solid mass still remains inside the particle before the instantaneous volume-averaged particle temperature reaches $T_{\text{torrefaction}}$. These numerical results indicate that it is reasonable to assume that the particle experiences heating until the instantaneous volume-averaged particle temperature reaches $T_{\text{torrefaction}}$ at which the torrefaction reactions are triggered until their termination, an assumption which was made in the SPM for the torrefaction of a centimeter-sized particle.

The necessity of the assumption of including the intraparticle convective and radiative heat transfer, and the intraparticle convective mass transfer was examined by comparing the results predicted by the CPM in the base case to those by the CPM in which these assumptions were omitted. For the biomass particle from the experiment of Basu et al. [145] at two reactor temperatures of 513 K and 553 K, the evolutions of the temperature at the particle center and of the residual solid mass fraction from these two models were compared with those from the experiment, as shown in Fig. 4.7. This figure shows that the modeling results from both models are in reasonable agreement with the experimental data. Consequently, intraparticle convective and radiative heat transfer as well as the intraparticle convective mass transfer only have minor influence on the modeling results and can thus be assumed to be negligible in order to develop the SPM.



(a)

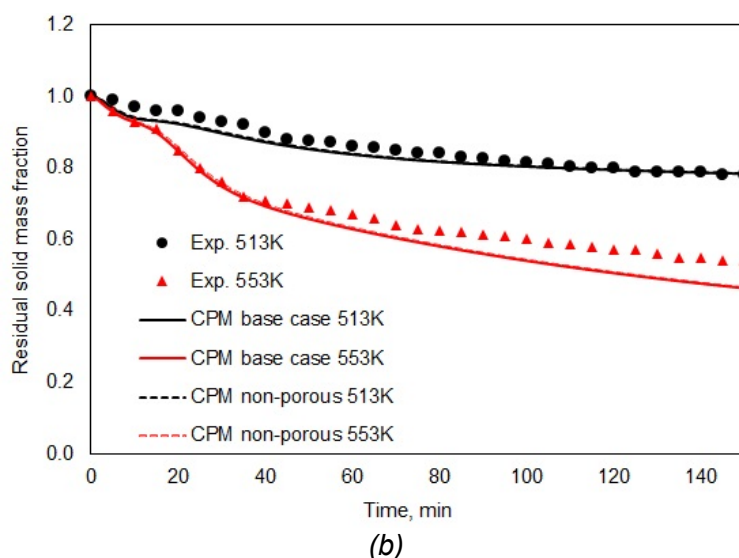
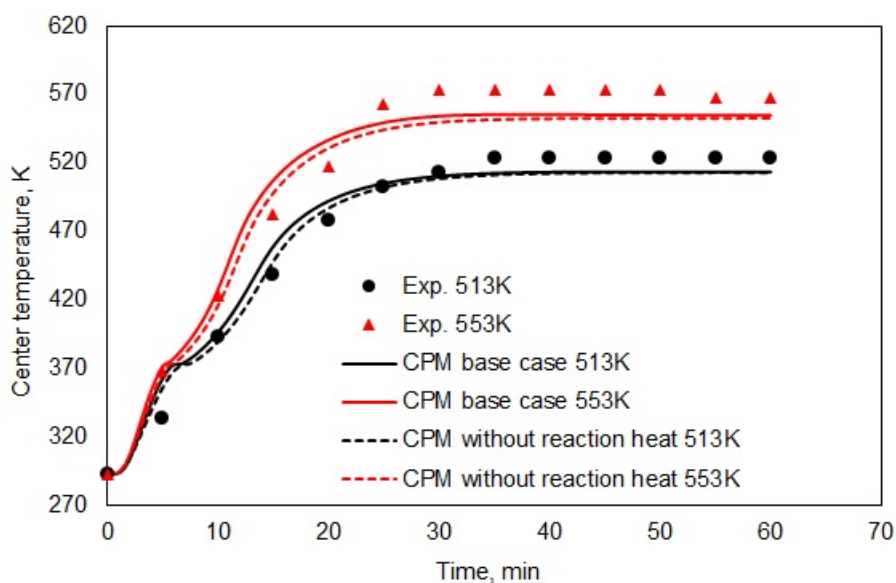
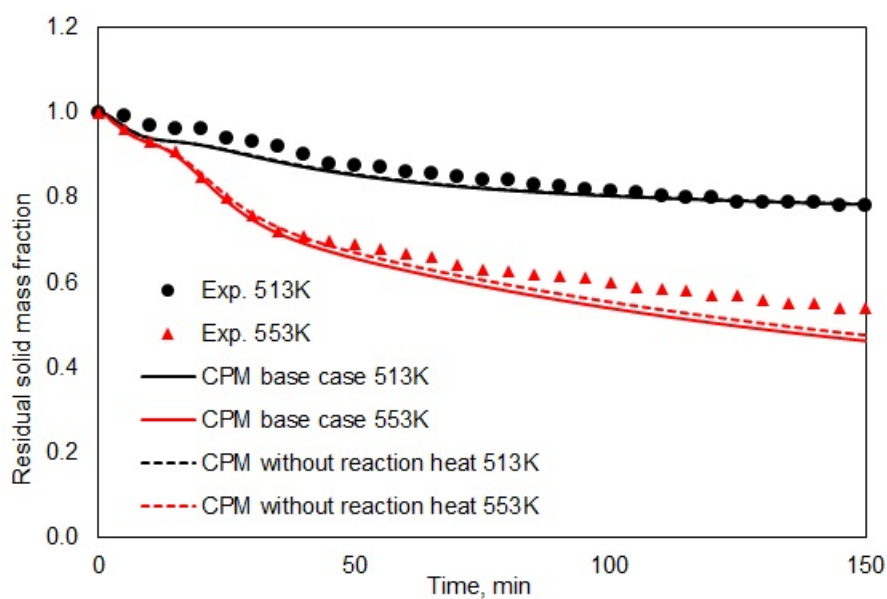


Fig. 4.7 Comparison of (a) temperature at particle center and (b) residual solid mass fraction between the experiment of Basu et al.[145] and the two models (the CPM in the base case and the CPM neglecting the porous structure) at reactor temperatures of 513 K and 553 K.

Torrefaction can be either endothermic or exothermic depending on type of the biomass, particle size and operating conditions.[9, 110, 162, 163, 222] Therefore, the necessity of the heats of the torrefaction reactions in the CPM was examined by comparing the results from the CPM in the base case to those from the CPM in which the heats of reaction were assumed to be zero. For the biomass particle from Basu et al. [145] at two reactor temperatures of 513K and 553K, Fig. 4.8 compares the evolutions of the temperature at the particle center and of the residual solid mass fraction resulting from these two models and those from the experiment. Fig. 4.8 shows that the modeling results from both these models were in good agreement with the experiments and that the heats of the torrefaction reaction only had minor influence on the modeling results. Therefore, the heat of reaction was assumed to be negligible in developing the SPM.



(a)



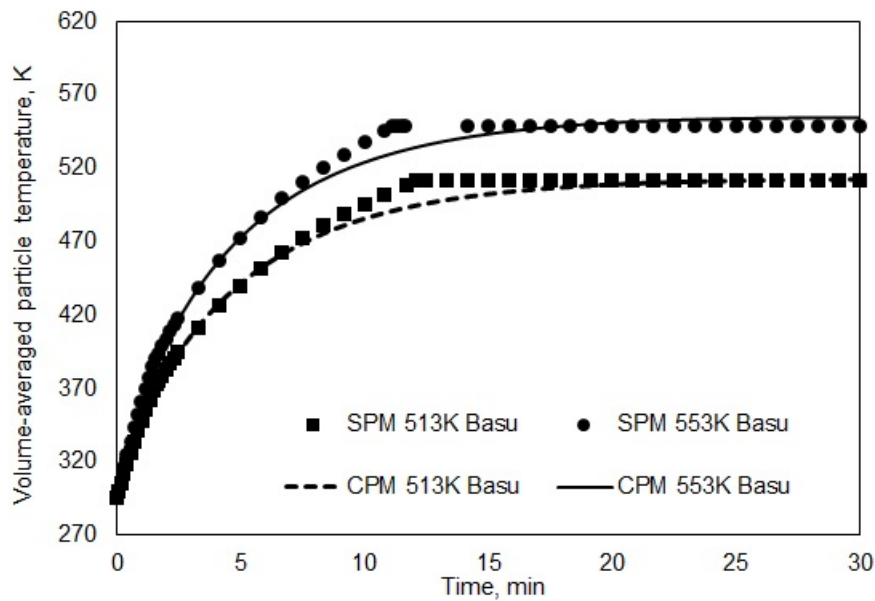
(b)

Fig. 4.8 Comparison of (a) temperature at particle center and (b) residual solid mass fraction between the experiment of Basu et al.[145] and the two models (the CPM in the base case and the CPM with zero reaction heat) at two reactor temperatures of 513K and 553K,.

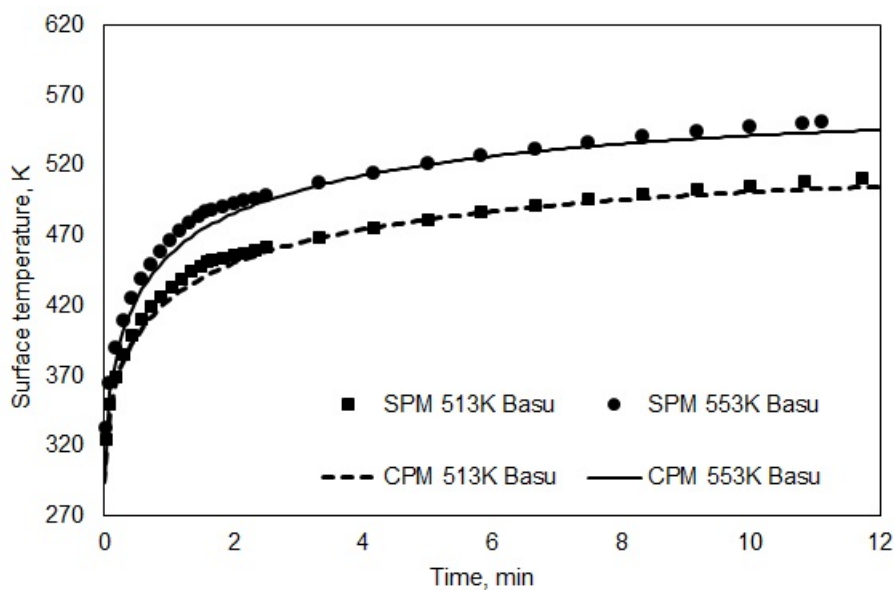
3.3 Accuracy of the simplified particle model (SPM)

3.3.1 Comparison to the experimental data of Basu et al.[145] and to the CPM

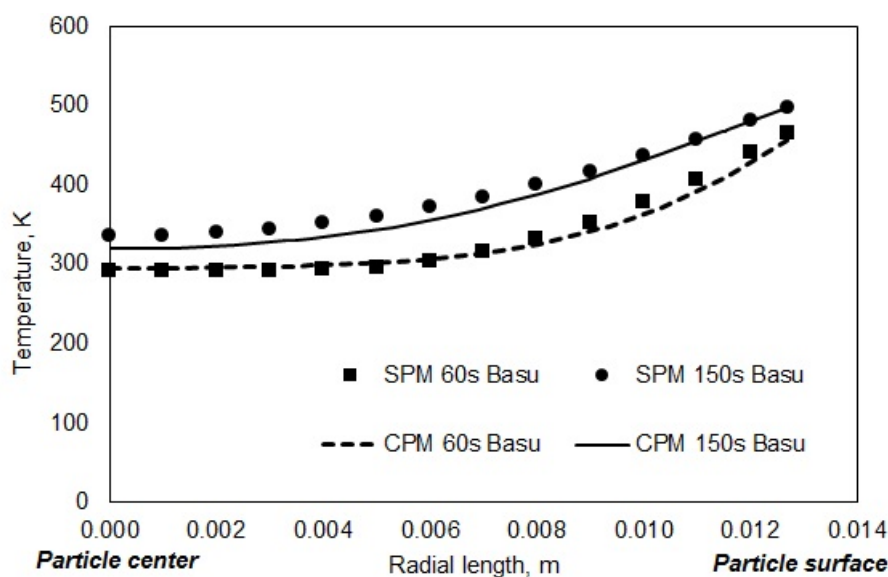
As discussed above, $T_{\text{torrefaction}}$ calculated from the CPM was 510 K and 548 K at the reactor temperature of 513 K and 553 K, respectively, for the work of Basu et al.[145]. Fig. 4.9 shows the comparison of the volume-averaged particle temperature (Fig. 4.9(a)), the temperature at the particle surface (Fig. 4.9(b)) and the temperature distribution inside the particle (Fig. 4.9(c)) predicted with the SPM and with the CPM.



(a)



(b)



(c)

Fig. 4.9 Comparison of (a) the volume-averaged particle temperature, (b) the temperature at the particle surface and (c) the temperature distribution inside the particle between the SPM and the CPM for the process conditions in the work of Basu et al.[145].

Fig. 4.9(a) shows that the instantaneous volume-averaged particle temperature predicted by the simplified model was overall in good agreement with the CPM. The instantaneous volume-averaged particle temperature from the simplified model was slightly higher than that from the CPM after about 8.5 minutes, and then it was calculated to be constant in the SPM when it reached the value of $T_{\text{torrefaction}}$, under which the present work assumed that the torrefaction reactions are triggered.

Fig. 4.9(b) shows that the predicted surface-temperature from the SPM increases fast at the beginning (0~2 minutes), and then approaches the reactor temperature, which is in good agreement with the results from the CPM. The fast increase of surface-temperature is due to the large temperature difference between the particle surface and the reactor at the beginning.

With the SPM, it was calculated that the time, t_R in Eq. (15), for the thermal front to reach the center of the particle is 93 s at the reactor temperature of 553 K and 96 s at the reactor temperature of 513 K. Fig. 4.9(c) shows the predicted intraparticle temperature distribution for the case at the reactor temperature of 553 K (with similar conclusions for the case at the reactor temperature of 513 K) at two different times: one at 60 s before the thermal front reaches the particle center, and another at 150 s after the thermal front has reached the particle center. As can be seen from Fig. 4.9(c), at 60 s, the SPM predicted that the temperature near the particle center is still at its initial value of 293 K while the temperature near the particle surface is elevated. At the time of 150 s, the temperature at any position has been increased to higher values than the initial 293 K. Fig. 4.9(c) shows that the results from the SPM are in good agreement with those from the CPM. Fig. 4.9(c) also indicates that it is appropriate to assume a quadratic distribution for the intraparticle temperature profile in Eq. (6), Eq. (8) and Eq. (21), in developing the SPM.

Fig. 4.10 compares the evolutions of residual solid mass fraction (feedstock dry basis) between the SPM and the experimental data for the work of Basu et al.[145]. This figure shows that the predicted residual solid mass fraction is constant before the instantaneous volume-averaged particle temperature reaches the value of $T_{\text{torrefaction}}$. Once the value of $T_{\text{torrefaction}}$ is reached, the torrefaction reactions are assumed to be triggered and the predicted residual solid mass decreases with time at this torrefaction temperature. At the reactor temperature of 513 K and 553 K, the *MD* values evaluating the difference between the SPM and the experiment were 2.0 wt.% and 3.0 wt.% (feedstock dry basis), respectively, indicating that the modeling results from the SPM were in good agreement with the experiment.

Overall, Fig. 4.9 and Fig. 4.10 show that the present SPM is capable to predict both the heat transfer and the torrefaction reactions for the torrefaction of a centimeter-sized biomass particle. While it took more than one hour for the three-dimensional CPM (with our Windows computer with Intel® Core™ i7 CPU, 2.93 GHz and 8 processors) to calculate the torrefaction process of a centimeter-sized biomass particle, the prediction results with the SPM, which solves intraparticle heat transfer with a group of linearized equations, was instantly (<1s) obtained. Therefore, the SPM is computationally cheaper compared to the CPM.

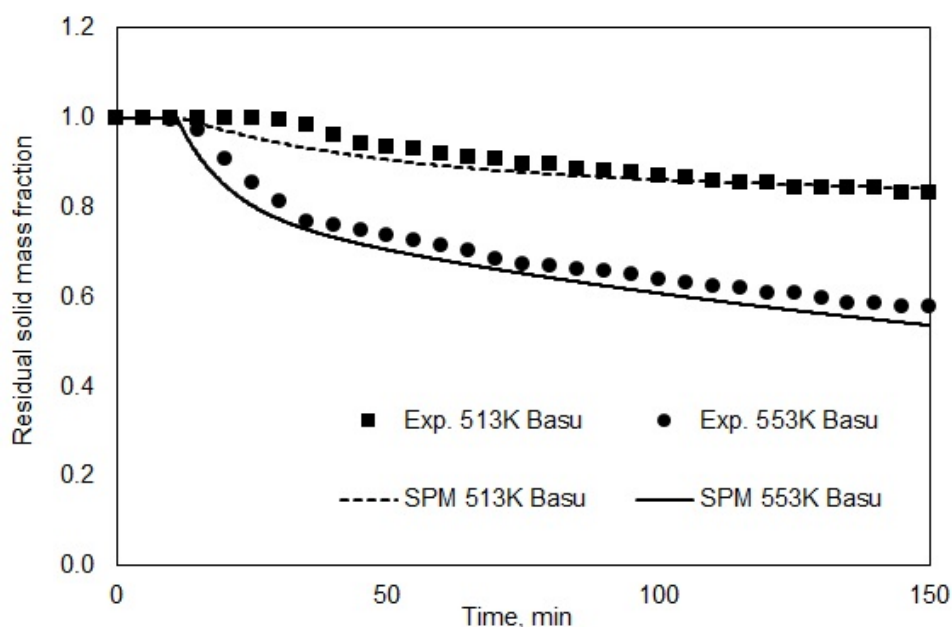
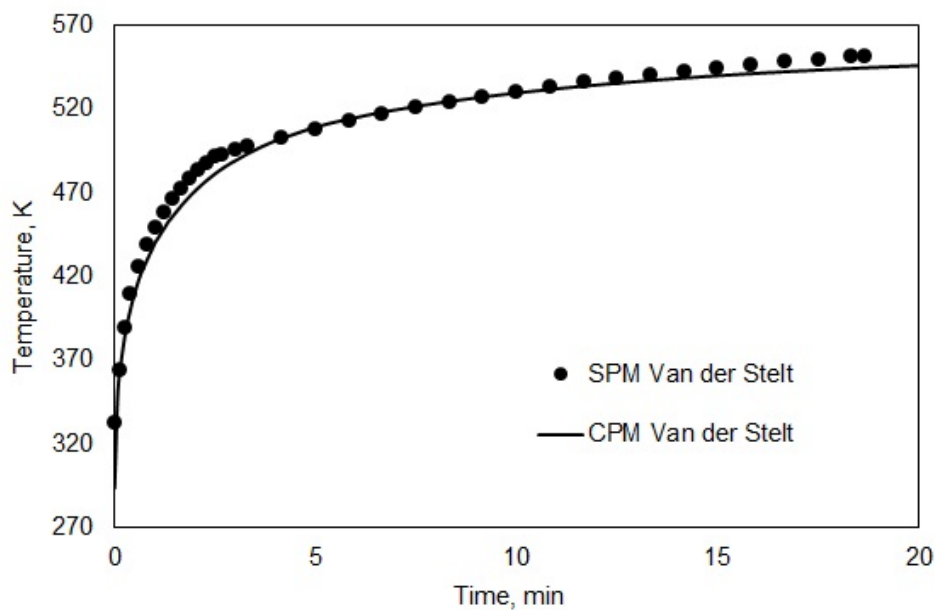


Fig. 4.10 Comparison of residual solid mass fraction evolution between the SPM and the experiment (dry-based) of Basu et al.[145] at two reactor temperatures of 513K and 553K.

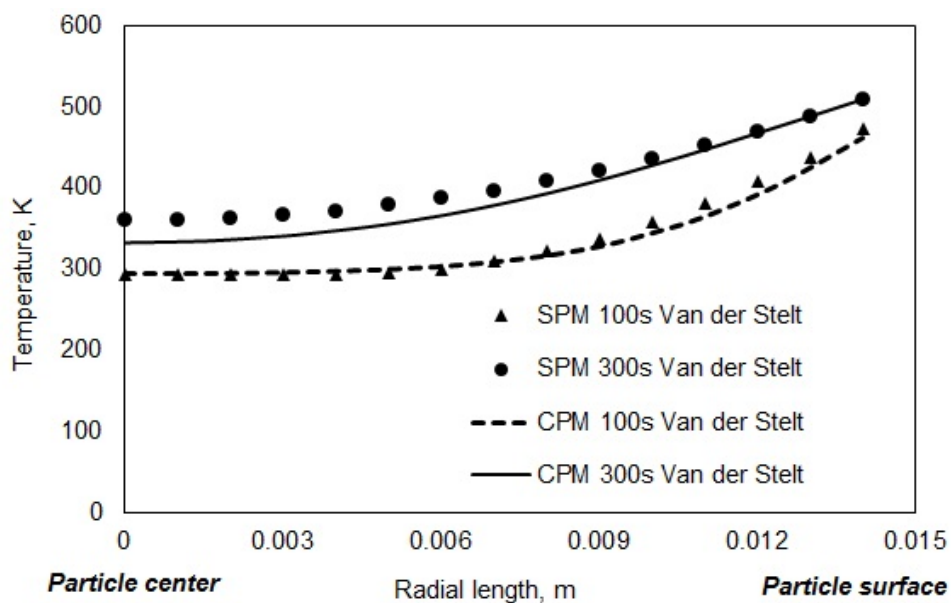
3.3.2 Comparison to the CPM using torrefaction conditions applied by Van der Stelt [221]

The accuracy of the SPM was assessed by comparing the temperature evolution at the particle surface (Fig. 4.11(a)) and the temperature distribution inside the particle (Fig. 4.11(b)) predicted by the SPM to those from the CPM using the process

conditions as applied by Van der Stelt[221] (reactor temperature of 553 K). Fig. 4.11(a) shows that the predicted evolution of the surface temperature from the SPM is in good agreement with that from the CPM (which was validated for the conditions as applied by Van der Stelt in Section 3.1.2). In the SPM, it was calculated that the time for the thermal front to reach the center of the particle was 150 s at the reactor temperature of 553 K. Fig. 4.11(b) shows the intraparticle temperature profiles at two different times: one at 100 s before the thermal front reached the particle center, and another at 300 s after the thermal front has reached the particle center. This figure shows that the predicted intraparticle temperature profiles from the SPM and CPM were in good agreement.



(a)



(b)

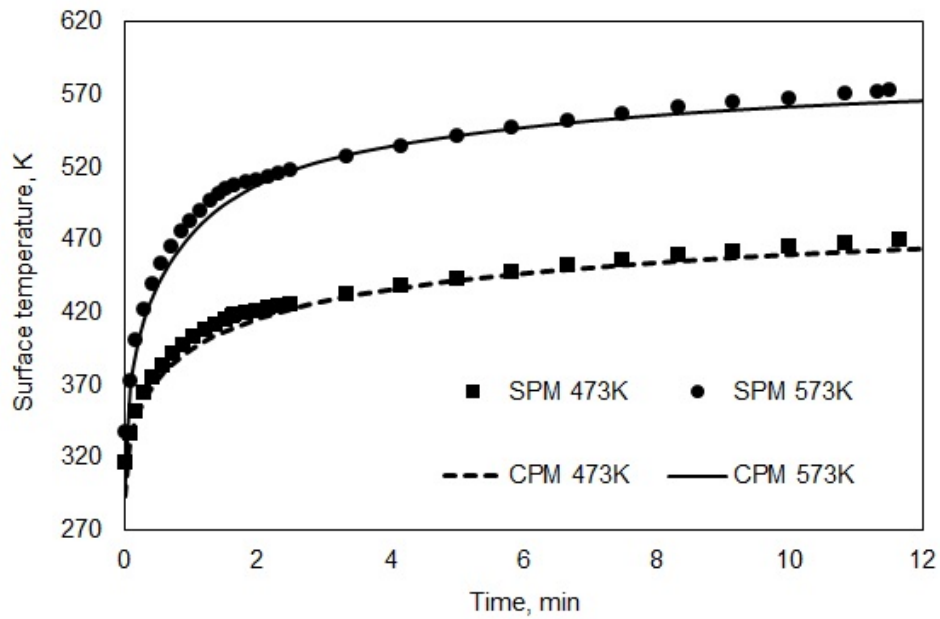
Fig. 4.11 Comparison of (a) temperature evolution at the particle surface and (b) intraparticle temperature distribution between the SPM and the CPM for the process conditions applied by Van der Stelt [77] at the reactor temperature of 553 K.

3.4 Applicability of the SPM

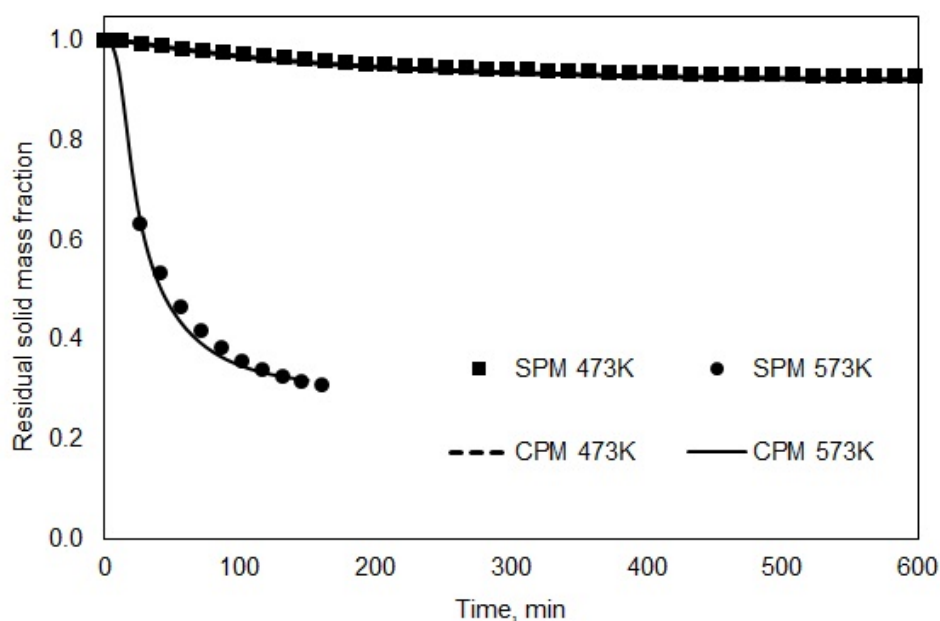
As discussed above, the SPM can predict comparable results to the CPM for biomass particles with different densities and sizes. In the following, the applicability of the SPM was further examined with respect to the operating conditions (reactor temperature covering the torrefaction range of 473-573 K), and the physical properties of the biomass particle (initial moisture content of $\theta = 0.1 \sim 10$ wt.%, varying particle size at constant aspect ratio of 6.0, and varying particle aspect ratio at constant particle diameter of 2.54 cm). The applicability study was performed by comparing the results of the SPM with those of the CPM that itself had been experimentally validated in Section 3.1. The base case was for a dry cylindrical particle with a diameter of 2.54 cm, a length of 15.24 cm and an aspect ratio of 6.0 (similar to the work of Basu et al. [16]).

3.4.1 Reactor temperature

Biomass torrefaction is usually operated at a temperature ranging from 473 to 573 K. Fig. 4.12 compares the predicted evolution of particle surface temperature and residual solid mass fraction between the SPM and the CPM at a reactor temperature of 473 K and 573 K.



(a)



(b)

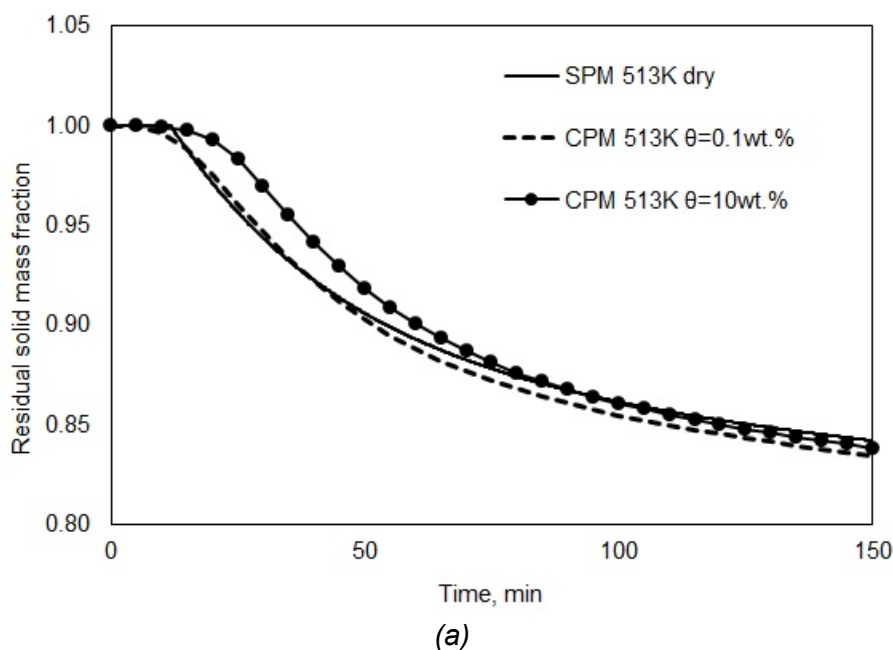
Fig. 4.12 Comparison of (a) temperature evolution at the particle surface and (b) residual solid mass fraction evolution predicted by the SPM and the CPM at two reactor temperatures of 473K and 573K.

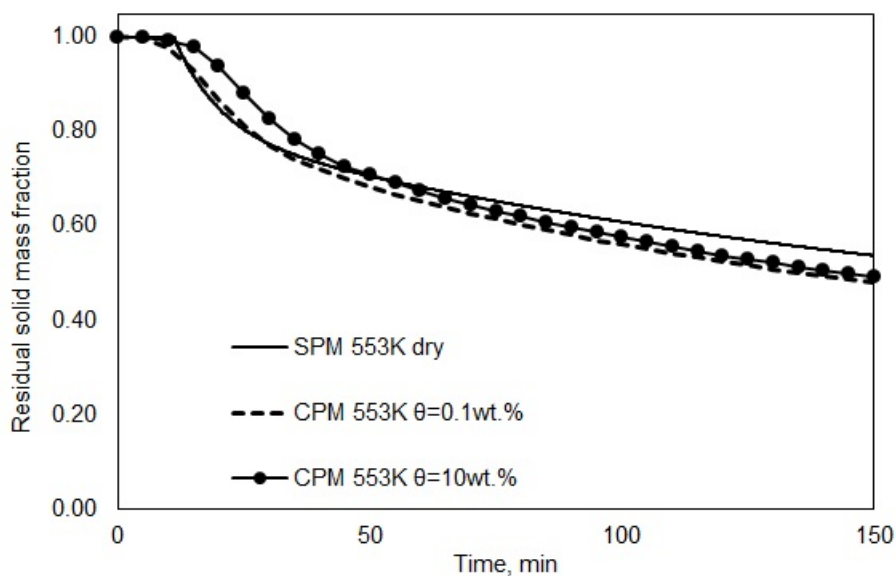
Fig. 4.12(a) shows that both the SPM and the CPM predict a faster temperature increase at the particle surface at a higher reactor temperature. The higher reactor temperature also resulted in higher solid mass loss rate and lower yield of solid product (char) upon termination of the torrefaction process, as shown in Fig. 4.12(b). Fig. 4.12 shows that the prediction results from the SPM agreed well with those from the CPM at both reactor temperatures, indicating that the SPM can predict comparable results to the CPM over the whole temperature range (473-573 K) for biomass torrefaction. The applicability of the SPM was not examined beyond this temperature range, as the torrefaction kinetics applied in the present model were developed for this temperature range [74] and may not be appropriate to be extrapolated to a lower or a higher reactor temperature.

3.4.2 Moisture content (θ)

As the SPM was developed for a dry biomass particle, we assessed the validity of the model for particles with a specific initial moisture content by comparing the mass loss evolution of a dry particle predicted by the SPM with the mass loss evolution of the dry biomass fraction predicted by the CPM in wet particles with moisture contents of $\theta = 0.1$ wt.% and $\theta = 10$ wt.%, respectively.

The simulation results in Fig. 4.13 show that, at the beginning of the process (at 10~70 minutes), the results from the SPM agree better with the results from the CPM with a moisture content of $\theta = 0.1$ wt.%. The mass loss of the dry biomass fraction in the wet particle, as predicted by the CPM, occurred later at the higher initial moisture content of $\theta = 10$ wt.%, which is due to water evaporation initially taking place. Upon termination of the torrefaction reaction (at about 150 minutes), the predicted yield of the solid product (char) from the SPM is similar to that from the CPM, indicating that the initial moisture content has limited influence on the final predicted yield of the solid product (on feedstock dry basis).





(b)

Fig. 4.13 Comparison of solid mass evolution between the SPM and the CPM at different initial moisture contents at the reactor temperature of (a) 513K and (b) 553K.

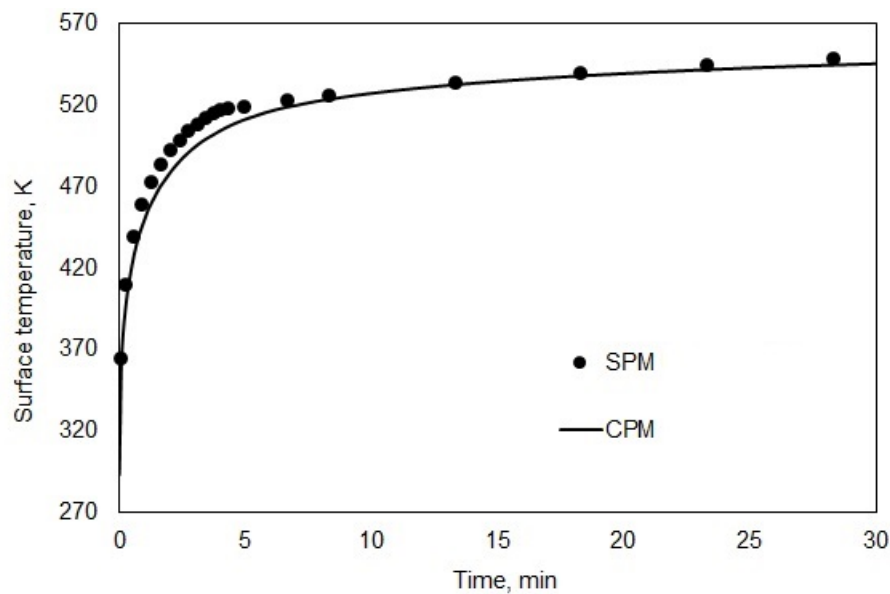
These results also indicate that the SPM can still be reasonably valid in predicting the yield of the solid product (on feedstock dry basis) for a wet biomass particle, despite some quantitative differences are present with respect to the solid mass loss rate at the initial stage of the torrefaction process. The applicability of the SPM was not performed for moisture contents higher than 10 wt.%, since naturally dried biomass particles usually contain a moisture content less than 10 wt.%. [16,60,77]

3.4.3 Particle size at constant aspect ratio

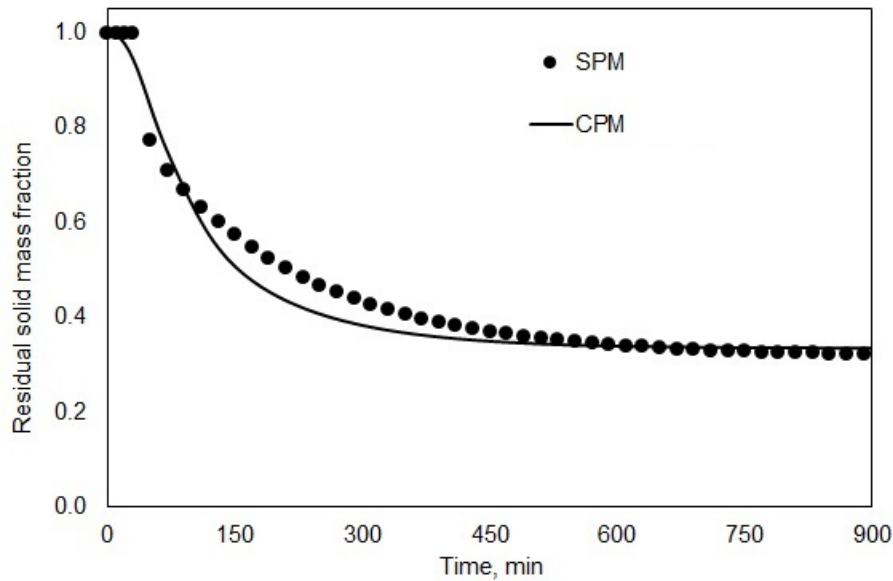
For the cylindrical biomass particle with an aspect ratio of 6.0, the intraparticle heat conduction can be assumed to occur one-dimensionally in the radial direction, and the diameter of the cylindrical particle is one of the factors affecting the intraparticle heat transfer. As temperature gradients are less important in cylindrical particles with smaller diameters, the applicability of the SPM was only performed for

a larger cylindrical particle with a diameter of 5.08 cm and a length of 30.48 cm (aspect ratio = 6.0), which is twice as large as the particle in the base case.

Fig. 4.14 compares the model predicted evolutions of the temperature at the particle surface (Fig. 4.14(a)) and the residual solid mass fraction (Fig. 4.14(b)) between the SPM and the CPM at a reactor temperature of 553 K. These figures indicate that the SPM can still predict comparable results to the CPM when the particle size is doubled at a constant aspect ratio of 6.0. The applicability of the SPM was not performed for even larger biomass particles, as the current reported torrefaction reactors (e.g. screw reactor [60]) do not treat such large biomass particles.



(a)



(b)

Fig. 4.14 Comparison of (a) the model predicted temperature evolution at the particle surface and (b) the residual solid mass fraction evolution between the SPM and the CPM for a particle with $d = 5.08$ cm at a reactor temperature of 553 K.

3.4.4 Particle aspect ratio at constant diameter

The SPM was developed with the assumption that the heat transfer occurs one-dimensionally in the radial direction of the cylindrical particle. At a constant diameter (2.54 cm), the heat transfer in the axial direction becomes increasingly important with the decrease of the particle length (and hence the decrease of the aspect ratio). Consequently, the one-dimensional heat transfer assumption in the SPM will be less valid. The effect of varying the aspect ratio was studied by comparing the evolution of the residual solid mass fraction predicted from the SPM with those from the CPM at ratios of 0.5, 1.0 and 3.0 (at constant particle diameter of 2.54 cm) and at a reactor temperature of 553 K.

Fig. 4.15. shows that the prediction results from the SPM deviate more from the CPM with a decreasing aspect ratio. The SPM is reasonably valid for an aspect ratio

of 3.0; for lower values, the difference between the SPM and the CPM cannot be neglected.

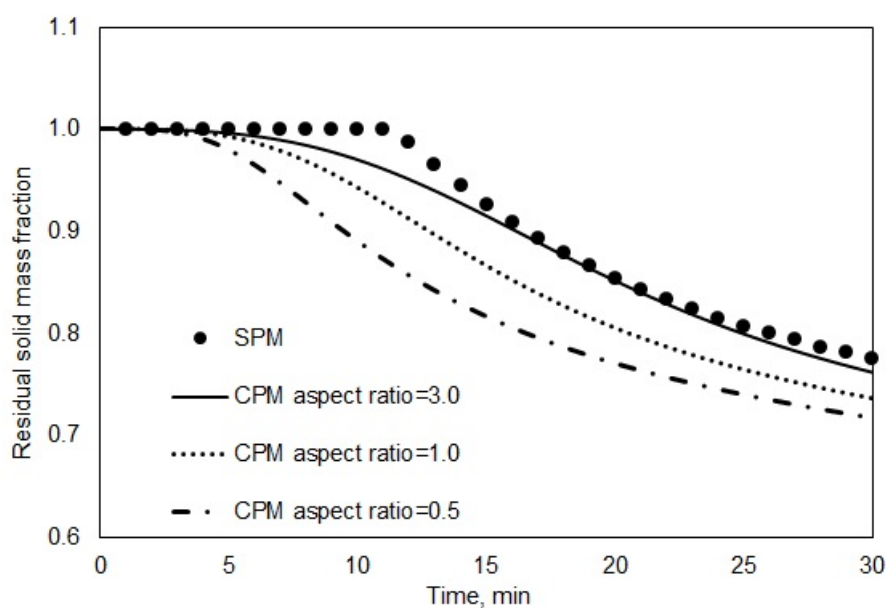


Fig. 4.15 Comparison of the evolutions of the residual solid mass fraction predicted from the SPM with those from the CPM with various aspect ratios at a constant particle diameter of 2.54 cm at a reactor temperature of 553 K.

4. Conclusions

In this chapter, a method has been proposed to develop a simplified particle model (SPM) for the torrefaction of a centimeter-sized biomass particle. The method contains steps of (1) validation of the model assumptions in developing the SPM with the CPM that itself was experimentally validated, (2) derivation of the SPM based on the space-time integral method, (3) assessment of the accuracy of the SPM by comparing either to the experimental data or to the CPM when experimental data were not available, and (4) study of the applicability of the SPM with respect to the operating conditions (reactor temperature), and the physical properties of the biomass particle (initial moisture content, particle size, and particle shape).

Results show that it was reasonable to neglect the intraparticle convective and radiative heat transfer, the intraparticle convective mass transfer and the reaction heat in developing the SPM. The SPM was reasonably accurate to predict the time evolution of the residual solid mass fraction (mean deviation of lower than 3.0 *wt.%* between the SPM and the experiment, feedstock dry basis). Results also showed that the SPM was applicable for predicting the torrefaction of centimeter-sized biomass particles with an aspect ratio larger than 3 with moisture content up to 10 *wt.%* at a temperature range of 473-573 K. In addition, the SPM can predict comparable results (e.g. intraparticle temperature profile and residual solid mass fraction) to the CPM but runs over 100 times faster than the CPM.

CHAPTER 5

3D Eulerian-Eulerian simulations of solids flow dynamics and back-mixing in a screw reactor

In previous chapters (Chapter 2 to 4), the modeling of the physical and chemical phenomena for biomass pyrolysis at the particle scale was studied. In the following two chapters (Chapter 5 and Chapter 6), the modeling of the physical and chemical phenomena for biomass pyrolysis at the reactor (i.e. screw reactor) scale will be discussed. Specifically, in Chapter 5, the physical phenomena (solids flow dynamics and solids back-mixing) occurring at the reactor scale will be studied with three-dimensional (3D) computational fluid dynamics (CFD) simulations based on the Eulerian-Eulerian method, while in Chapter 6, pyrolysis reaction kinetics will be further incorporated into the CFD model to study biomass pyrolysis at the reactor scale.

This chapter was redrafted after:

Xiaogang Shi, Frederik Ronsse, Jelle Roegiers, Jan G. Pieters. 3D Eulerian-Eulerian simulations of solids flow dynamics and back-mixing in a screw reactor. To be submitted to Fuel Processing Technology.

1. Introduction

Rotating screw systems are widely applied to transport granular materials in industries like chemical, agricultural, food, etc.[86, 223] Much research has been focused on the overall volumetric throughput and power requirements of screw systems.[87] Recently, the rotating screw system as a novel reactor (and hence called screw reactor, or auger reactor) has found potential applications in thermochemical processing of biomass, for instance in fast and slow pyrolysis (the latter including both torrefaction and carbonization).[88, 129, 224-229] The reaction extent and the product (being non-condensable gases, condensable vapors (or oil) and char) distribution of biomass pyrolysis are highly dependent on the flow dynamics and the residence time of biomass particles in a reactor.[65, 228, 230] Therefore, in-depth understanding of the particle flow dynamics and particle residence time in the screw reactor is necessary to target reactor conditions that favor the production of desired products (e.g. desired products of oil for fast pyrolysis, and char for carbonization).

Biomass particles can pass through the screw reactor at the mechanical action of the rotating screw. In addition, carrier gas is usually injected from the reactor inlet to remove the pyrolysis products in the gas phase out of the screw reactor.[87, 88, 129] The reactor wall (screw shell) is usually used to provide heat for the biomass pyrolysis process, and sometimes, an additional heating medium, such as hot sand, is fed along with the biomass particles to enhance heat transfer among solids, gases, and the reactor wall.[88] As a result, complex interactions exist among phases, and between the solid phase and the physical structure of the screw reactor. Due to these complex interactions, the experimental method has difficulty in capturing the transient behavior of the particle flow dynamics, the particle RTD and the degree of solids

back-mixing in the screw reactor.[86-88, 129, 223, 231] In contrast, the CFD approach can describe, by means of modeling, the complicated transient profiles of the multiphase fluid dynamics in a multiphase reactor (e.g. screw reactor) by solving the related conservation laws and equations,[128, 232-234] and can help in-depth understanding of the complex solids flow dynamics in the screw reactor.

Both Lagrangian models and Eulerian multi-fluid models have been applied to study the multiphase flow inside the screw reactor.[124, 125, 129, 235-238] In the Lagrangian approach, like the Discrete Element Method (DEM), the motion of particles is described by Newton's laws of motion. Detailed information on the forces acting on each individual particle and the information on the particle's dynamic trajectory, which is currently extremely difficult, if not impossible, to obtain with experimental measurements may be calculated by DEM.[126] However, current DEM models are normally limited to relatively small numbers of particles due to computational limitations,[127] which makes it difficult to simulate a full-scale screw reactor containing millions or more of particles. The Eulerian multi-fluid model, on the other hand, treats gas and solid phases as interpenetrating continua and consequently is able to handle multiphase systems containing large numbers of particles at a relatively large scale.[128] Some researchers have tried to study the multiphase flow in a screw reactor based on the Eulerian-Eulerian model. Aramideh et al.[129] simulated biomass pyrolysis in a screw reactor based on an Eulerian-Eulerian model, and they analyzed the solids distributions inside the reactor. However, still little is known about the detailed solids flow dynamics in the axial (forward transportation) and the radial directions of the reactor. The overall distribution of solids residence time, as well as the solids back-mixing behavior remain largely unknown.

The purpose of this chapter is to study the solids flow dynamics and to discuss the possible effects of the solids flow dynamics on the solids back-mixing behavior inside a screw reactor based on 3D simulation with the Eulerian-Eulerian model. The model is validated against experimental results from Nachenius et al.[87] The solids RTD is obtained using the virtual tracing method. The reasons for solids back-mixing are analyzed based on the predicted solids flow dynamics. The effect of operating conditions (e.g. screw speed) on the degree of solids back-mixing is further discussed.

2. Model development

The Eulerian-Eulerian two-fluid approach, which is widely used to model dense gas-solid systems,[239-241] was applied to simulate the gas-solid flow in the screw reactor. The detailed governing equations and their constitutive equations are shown in the following.

2.1 Governing equations

Mass conservation for the two phases was described as,[239]

$$\frac{\partial}{\partial t}(\varepsilon_g \rho_g) + \nabla \cdot (\varepsilon_g \rho_g \mathbf{u}_g) = 0 \quad (1)$$

$$\frac{\partial}{\partial t}(\varepsilon_s \rho_s) + \nabla \cdot (\varepsilon_s \rho_s \mathbf{u}_s) = 0 \quad (2)$$

where ε_g and ε_s represent the volume fractions of the gas phase and the solid phase, respectively. ρ_g and ρ_s are the density (kg/m^3) of the gas phase and the solid phase, respectively. \mathbf{u}_g (m/s) and \mathbf{u}_s are the velocity of the gas phase and the solid phase, respectively. Each computational cell is occupied by the two inter-penetrating

phases in the Eulerian-Eulerian model, and their overall volume fraction in the computational cell equals unity:[239]

$$\varepsilon_g + \varepsilon_s = 1 \quad (3)$$

Momentum conservation is derived by balancing the momentum accumulation for each phase with the convective momentum flux and other forces related to gravity, drag force, stress tensor and pressure. The mathematical expressions of the momentum conservation for the two phases are:[239]

$$\frac{\partial}{\partial t}(\varepsilon_g \rho_g \mathbf{u}_g) + \nabla \cdot (\varepsilon_g \rho_g \mathbf{u}_g \mathbf{u}_g) = -\varepsilon_g \nabla p + \nabla \cdot \bar{\bar{\tau}}_g + \varepsilon_g \rho_g \mathbf{g} + \beta (\mathbf{u}_s - \mathbf{u}_g) \quad (4)$$

$$\frac{\partial}{\partial t}(\varepsilon_s \rho_s \mathbf{u}_s) + \nabla \cdot (\varepsilon_s \rho_s \mathbf{u}_s \mathbf{u}_s) = -\varepsilon_s \nabla p - \nabla p_s + \nabla \cdot \bar{\bar{\tau}}_s + \varepsilon_s \rho_s \mathbf{g} + \beta (\mathbf{u}_g - \mathbf{u}_s) \quad (5)$$

Where p (Pa) is the pressure shared by the gas phase and the solid phase. p_s (Pa) is the solids pressure. $\bar{\bar{\tau}}_g$ (Pa) and $\bar{\bar{\tau}}_s$ represent the stress tensors of the gas phase and the solid phase, respectively. The symbol \mathbf{g} (m/s²) stands for the gravitational constant while β (kg/(m³·s)) represents the interphase momentum exchange coefficient.

The conservation of fluctuating kinetic energy for the solid phase is based on the kinetic theory of granular flow:[239]

$$\frac{3}{2} \left[\frac{\partial}{\partial t} (\rho_s \varepsilon_s \Theta_s) + \nabla \cdot (\rho_s \varepsilon_s \mathbf{u}_s \Theta_s) \right] = \left(-\rho_s \bar{\bar{I}} + \bar{\bar{\tau}}_s \right) : \nabla \mathbf{u}_s + \nabla \cdot (k_{\Theta_s} \nabla \Theta_s) - \gamma_{\Theta_s} + \phi_{gs} \quad (6)$$

where θ_s (m^2/s^2) is the granular temperature, k_{θ_s} ($kg/(m \cdot s)$) is the diffusion coefficient of the fluctuating kinetic energy, γ_{θ_s} ($kg/(m^3 \cdot s)$) is the collisional dissipation of the fluctuating kinetic energy, and ϕ_{gs} is the fluctuating energy exchange between phases.

The species transport equation for tracer particles was used for calculating the solids residence time distribution:[242]

$$\frac{\partial}{\partial t}(\varepsilon_s \rho_s Y_{\text{tracer}}) + \nabla \cdot (\varepsilon_s \rho_s \mathbf{u}_s Y_{\text{tracer}}) = \nabla \cdot (\varepsilon_s \rho_s D_s \nabla Y_{\text{tr}}) \quad (7)$$

Where Y_{tracer} is the mass concentration of the tracer particle in the solid phase.

2.2 Constitutive equations

Constitutive equations are used to close the governing equations in order to facilitate the solving process. The following summarizes the required constitutive equations.

The stress tensor for the gas phase is[242]

$$\bar{\bar{\tau}}_g = \varepsilon_g \mu_g (\nabla \mathbf{u}_g + \nabla \mathbf{u}_g^T) + \varepsilon_g \left(\lambda_g - \frac{2}{3} \mu_g \right) \nabla \cdot \mathbf{u}_g \bar{\mathbf{I}} \quad (8)$$

The stress tensor for the solid phase is[242]

$$\bar{\bar{\tau}}_s = \varepsilon_s \mu_s (\nabla \mathbf{u}_s + \nabla \mathbf{u}_s^T) + \varepsilon_s \left(\lambda_s - \frac{2}{3} \mu_s \right) \nabla \cdot \mathbf{u}_s \bar{\mathbf{I}} \quad (9)$$

Where μ_g (Pa·s) and μ_s are the shear viscosities of the gas phase and the solid phase, respectively. λ_g (Pa·s) and λ_s are the bulk viscosities for the gas phase and the solid phase, respectively. $\bar{\mathbf{I}}$ is the unit tensor.

In a screw system, particles tend to be conveyed in a state of dense packing, and the frictional stress between particles is an important factor influencing the flow of the solid phase.[243] It is assumed that the frictional stress starts to be relevant when the solids volume fraction exceeds a critical value (friction packing limit) of $\varepsilon_{s,max,friction} = 0.28$, which is slightly smaller than the maximum packing limit ($\varepsilon_{s,max} = 0.30$). The maximum packing limit was determined by the ratio of the bulk density (165.4 kg/m³) to the tapped density of pine wood (551 kg/m³), being the material used in the experiments of Nachenius et al.[87] against which the model predicted results are compared in this chapter.

The solids pressure is composed of a kinetic term ($p_{s,kinetic}$), a second term due to particle collisions ($p_{s,collision}$), and a third term due to friction ($p_{s,friction}$):[242]

$$p_s = p_{s,kinetic} + p_{s,collision} + p_{s,friction} \quad (10)$$

$$p_{s,kinetic} = \varepsilon_s \rho_s \Theta \quad (11)$$

$$p_{s,collision} = 2\varepsilon_s^2 \rho_s \Theta_s (1 + e_{ss}) g_{0,ss} \quad (12)$$

Where e_{ss} is the particle-particle restitution coefficient, and $g_{0,ss}$ is the radial distribution function, which modifies the probability of particle collisions when the solid phase becomes dense,[244]

$$g_{0,ss} = \left[1 - \left(\frac{\varepsilon_s}{\varepsilon_{s,max}} \right)^{\frac{1}{3}} \right]^{-1} \quad (13)$$

The derivation of the frictional pressure ($p_{s,friction}$) is mainly semi-empirical, and the model from the work of Ding and Gidaspow[239] was applied to calculate $p_{s,friction}$. The frictional pressure starts to be relevant when the solids volume fraction exceeds the friction packing limit, before which the solids pressure is mainly contributed by the kinetic term and the collisional term. When the solids volume fraction is higher than the friction packing limit (0.28) but lower than its maximum packing limit (0.30), the particle collisions are less important, and therefore the solids pressure is mainly contributed by the kinetic term and the frictional term.

The shear viscosity of the solid phase is expressed below[242]

$$\mu_s = \mu_{s,kinetic} + \mu_{s,collision} + \mu_{s,friction} \quad (14)$$

Where $\mu_{s,kinetic}$, [239] $\mu_{s,collision}$, [239] and $\mu_{s,friction}$ [242] represent the kinetic viscosity, the collisional viscosity and the frictional viscosity of the solid phase, respectively.

$$\mu_{s,kinetic} = \frac{10d_s\rho_s\sqrt{\Theta_s\pi}}{96\varepsilon_s(1+e_{ss})g_{0,ss}} \left[1 + \frac{4}{5}g_{0,ss}\varepsilon_s(1+e_{ss}) \right]^2 \quad (15)$$

$$\mu_{s,collision} = \frac{4}{5}\varepsilon_s\rho_s d_s g_{0,ss} (1+e_{ss}) \sqrt{\frac{\Theta_s}{\pi}} \quad (16)$$

$$\mu_{s,friction} = \frac{p_s \sin \varphi}{2\sqrt{l_{2D}}} \quad (17)$$

where d_s (m) is the diameter of the particle, φ is the angle of internal friction (45°), and I_D is the second invariant of the stress deviatoric tensor.

Similarly, the shear viscosity of the solid phase is mainly contributed by the frictional viscosity and by the kinetic viscosity when the solids volume fraction is between the friction packing limit and the maximum packing limit. Otherwise, the shear viscosity of the solid phase is mainly contributed by the kinetic viscosity and by the collisional viscosity.

The bulk viscosity for the solid phase represents the resistance of particles due to expansion and compression, and it is expressed as:[245]

$$\lambda_s = \frac{4}{3} \varepsilon_s \rho_s d_s g_{0,ss} (1 + e_{ss}) \sqrt{\frac{\Theta_s}{\pi}} \quad (18)$$

The diffusion coefficient of the solids fluctuating kinetic energy is,[239]

$$k_{\Theta_s} = \frac{150 \rho_s d_s \sqrt{\Theta_s \pi}}{384 (1 + e_{ss}) g_{0,ss}} \left[1 + \frac{6}{5} \varepsilon_s g_{0,ss} (1 + e_{ss}) \right]^2 + 2 \rho_s \varepsilon_s^2 d_s (1 + e_{ss}) g_{0,ss} \sqrt{\frac{\Theta_s}{\pi}} \quad (19)$$

The collisional dissipation of solids fluctuating kinetic energy is,[245]

$$\gamma_{\Theta_s} = \frac{12 (1 - e_{ss}^2) g_{0,ss}}{d_s \sqrt{\pi}} \rho_s \varepsilon_s^2 \Theta_s^{3/2} \quad (20)$$

The exchange of fluctuating energy between phases is,[239]

$$\phi_{gs} = -3\beta\Theta_s \quad (21)$$

The interphase drag model developed by Gidaspow[239] was adopted. This drag model is suitable for dense gas-solid systems, and it is expressed as below,

$$\beta = \begin{cases} \frac{3}{4} C_d \frac{\varepsilon_s \varepsilon_g \rho_g |\mathbf{u}_g - \mathbf{u}_s|}{d_s} \varepsilon_g^{-2.65} & \varepsilon_g > 0.8 \\ 150 \frac{\varepsilon_s (1 - \varepsilon_g) \mu_g}{\varepsilon_g d_s^2} + 1.75 \frac{\rho_g \varepsilon_s |\mathbf{u}_g - \mathbf{u}_s|}{d_s} & \varepsilon_g \leq 0.8 \end{cases} \quad (22)$$

Where C_d is the drag coefficient defined as,

$$C_d = \begin{cases} \frac{24}{\text{Re}_s} (1 + 0.15 \text{Re}_s^{0.687}) & (\text{Re}_s \leq 1000) \\ 0.44 & (\text{Re}_s > 1000) \end{cases} \quad (23)$$

Where Re_s is the relative Reynolds number expressed as,[239]

$$\text{Re}_s = \frac{\varepsilon_g \rho_g d_s |\mathbf{u}_g - \mathbf{u}_s|}{\mu_g} \quad (24)$$

2.3 Residence time distribution model

The RTD curve can give an indication on the flow behavior of a fluid phase and can characterize the intensity of the mixing process in the reactor. In ideal plug-flow, all fluid elements leave the reactor with the same residence time, and the RTD curve is a vertical line after the injection time. In contrast, in ideal mixing-flow, the fluid is completely mixed inside the reactor and its RTD curve at the outlet would increase abruptly in an instantaneous rise at the injection time and then decay exponentially with time thereafter.[246]

The numerical virtual tracing method,[247, 248] which is similar to the experimental tracing method,[231] was applied to derive the solids RTD. The virtual tracer, which has the same physical properties as the solid phase in the simulation, was introduced in the modelled reactor geometry from the inlet after steady-state flow

had been achieved. At the outlet, the tracer concentration was monitored. The solids RTD function, $E(t)$, is calculated as,

$$E(t) = \frac{Y_n(t)}{\int_0^{\infty} Y_n(t)dt} \quad (25)$$

The cumulative solids RTD function, $F(t)$, is,

$$F(t) = \int_0^t E(t)dt \quad (26)$$

The mean solids residence time is calculated from the CFD simulation by,

$$t_{m,CFD} = \int_0^{\infty} tE(t)dt \quad (27)$$

The $E(t)$ and $F(t)$ function can also be described using a dimensionless time variable (θ),

$$\theta = \frac{t}{t_{m,CFD}} \quad (28)$$

$$E(\theta) = t_{m,CFD}E(t) \quad (29)$$

$$F(\theta) = \int_0^{\theta} E(\theta)d\theta \quad (30)$$

The variance characterizing the width of solids RTD is,

$$\sigma^2 = \int_0^{\infty} (t - t_{m,CFD})^2 E(t)dt \quad (31)$$

And the dimensionless variance characterizing the degree of solids back-mixing is,

$$\sigma_{\theta}^2 = \frac{\sigma^2}{t_{m,CFD}^2} \quad (32)$$

2.4 Theoretical mean solids residence time

For screw systems, the mean solids residence time can be theoretically determined from the length of the screw, the screw rotating frequency and the pitch.[86, 87, 231] Ideally, the forward movement of a particle per complete rotation of the screw is equal to the pitch. The theoretical calculation is based on the assumption that all particles spend the same amount of time inside the screw system (ideal plug flow), and potential axial solids back-mixing is neglected. Considering that the thickness of the flight (the helical blade) cannot be ignored, the theoretically ideal mean solids residence time can be determined by,

$$t_{m,theoretical} = \frac{L_{screw}}{\nu \times (L_{pitch} + L_{flight})} \quad (33)$$

Where, as shown in Fig. 5.1, L_{screw} (m) is the length of the screw, L_{pitch} is the length of the pitch, L_{flight} is the thickness of the flight and ν is the screw rotating frequency (Hz).

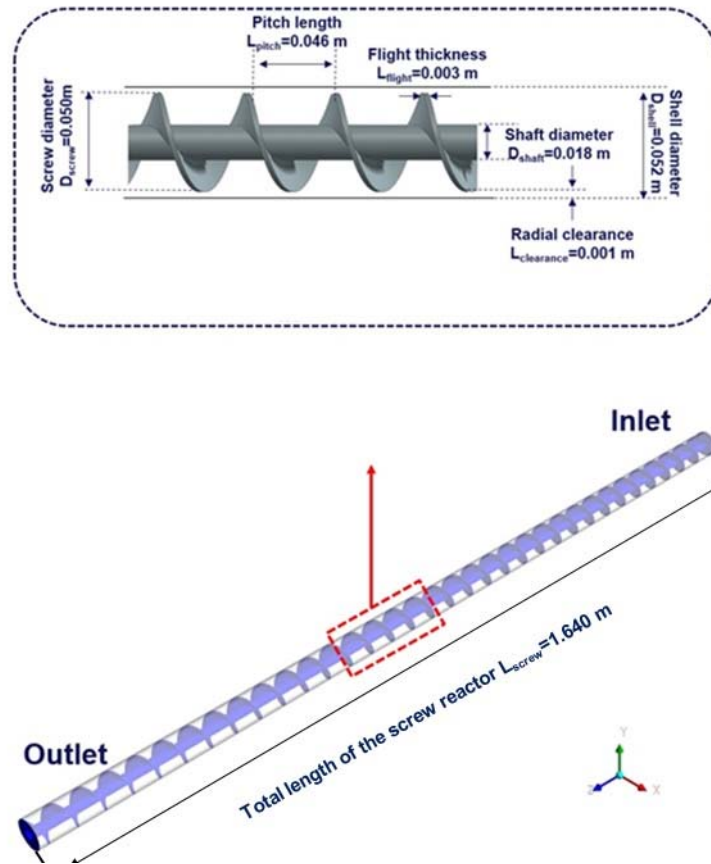


Fig. 5.1 Geometry of the screw reactor in the CFD simulation

3. Simulation set-up

3.1 Simulation system

The model was based on the experimental apparatus in the work of Nachenius et al.[87] The screw reactor is composed of a shell, flight (helical blade), and shaft, and the total length of the screw reactor from the inlet to the outlet was 1.640 m. The 3D geometry of the reactor and its detailed dimensions are shown in Fig. 5.1. Nachenius et al.[87] performed cold flow experiments, and their experimental data were used to validate the model in this study. The gas used was air (air was used in this model only for cold flow, and inert gas, N_2 , would be used in real thermochemical process involving biomass). Particles were pine wood with an average size of 2 mm, as the material used in the experiments of Nachenius et al.[87] The physical

properties of gas and solids, and other simulation parameters are listed in Table 5.1. The operating conditions, including the screw rotating frequency, the inlet gas and solids mass flow rate, for three distinct simulation cases were set similar to the experiments of Nachenius et al.[87] and are listed in Table 5.2. The inlet solids/gas mass flow rates were almost identical for all three simulation cases.

Table 5.1 *Physical properties of the gas phase and the solid particles and other simulation parameters used.*

Parameter	Values
Particle diameter	0.002 m
Particle density	551 kg/m ³
Gas density	1.225 kg/m ³
Gas dynamic viscosity	1.7×10 ⁻⁵ kg/(m·s)
Maximum solids packing limit	0.30
Solids friction packing limit	0.28
Particle–particle restitution coefficient	0.90
Angle of internal friction	45°
Time step	0.001 s

Table 5.2 *Operating conditions for various cases*

Case number	Screw rotating frequency, Hz	Inlet solids mass flow rate, g/s	Inlet gas mass flow rate, g/s
1	0.243	0.62	2.72×10 ⁻³
2	0.364	0.61	2.72×10 ⁻³
3	0.486	0.61	2.72×10 ⁻³

The unstructured mesh with different mesh resolutions was constructed for the 3D geometry of the screw reactor, and a grid independency study was performed as described in Section 4.1. The commercial CFD package of ANSYS Fluent 16.2 was

used to solve the governing and constitutive equations in Section 2. A time step of 0.001s was used. The moving mesh method was applied to simulate the rotating screw.

3.2 Boundary and initial conditions

The mass flow rates of the gas phase and of the solid phase at the inlet were set according to Table 5.2. Atmospheric pressure was assumed at the outlet for both gas and solid phases. At the wall (shell, shaft and flight), no-slip boundary conditions were assumed for the gas and the solid phases. Initially, no solids were present inside the reactor. The initial velocities of the gas and solid phases were set at zero.

4. Results and discussion

4.1 Grid independency study

To assess whether the simulation results were mesh-independent, a grid independency analysis was performed using three different mesh resolutions (coarse mesh, medium mesh and fine mesh, as shown in Table 5.3).

Table 5.3 Simulation results with respect to the mean solids residence time, the dimensionless variance of the solids RTD and the total solid mass inside the reactor at steady-state at three different mesh resolutions (Case 3)

Mesh resolutions	Number of cells	Mean solids residence time ($t_{m,CFD}$), s	Dimensionless variance (σ_{θ}^2)	Total solid mass at steady state, g
Fine mesh	306120	84.5	0.0019	49.3
Medium mesh	248352	84.6	0.0019	49.4
Coarse mesh	156627	84.2	0.0018	49.1

Fig. 5.2 shows the predicted solids RTD function $E(t)$ and the cumulative function $F(t)$ at different mesh resolutions at a screw rotating frequency of 0.486 Hz

(Case 3). This figure shows that the predicted solids RTD function $E(t)$ and the cumulative function $F(t)$ using the medium mesh were close to those using the fine mesh, while the results using the coarse mesh deviated, to some extent, from the results using the medium mesh and the fine mesh. Table 5.3 shows the predicted mean solids residence time, the dimensionless variance of the solids RTD and the total solid mass inside the reactor at steady-state at different mesh resolutions. This table shows that the simulation results using the medium mesh, compared to the one using the coarse mesh, were closer to those using the fine mesh. These simulation results in Fig. 5.2 and in Table 5.3 indicate that the medium mesh size was already sufficiently fine for providing mesh independent results. Therefore, the medium mesh was applied throughout the rest of this chapter.

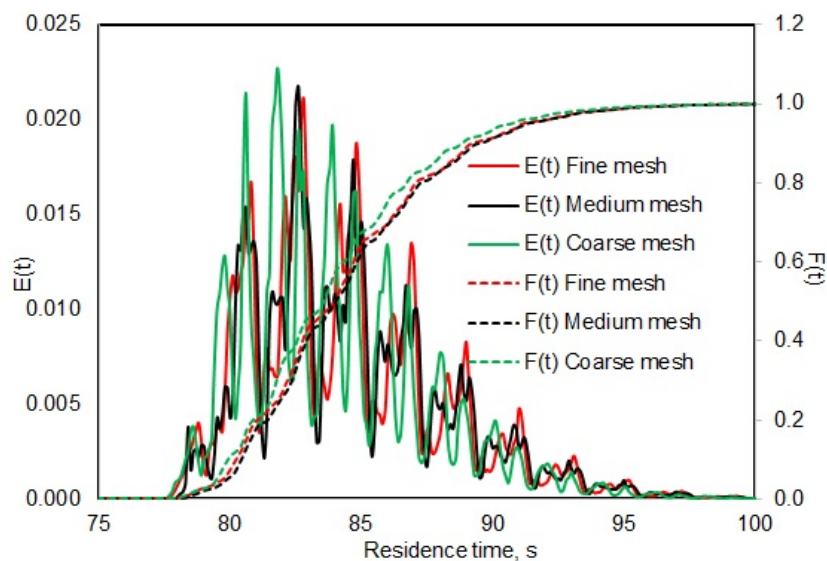


Fig. 5.2 Simulation results with respect to the solids RTD function of $E(t)$ and the cumulative function of $F(t)$ at different mesh resolutions (Case 3)

4.2 Particle flow dynamics

Fig. 5.3 shows a front view of the model predicted, steady-state spatial distribution of solids volume fraction in a short section of the reactor for Case 1 and Case 3 that were operated at different screw rotating speeds. This figure shows that

more solids are present in the reactor when the screw rotating speed is lower (Case 1). This figure also shows that in both cases solids tend to cluster towards the bottom of the reactor, which is the result of gravity. While solids were mainly present in the lower part of the reactor between the bottom shell and the shaft in both cases, some solids were present, as shown by the slightly blue color for Case 3, above the shaft at the front face of the flight. The presence of solids above the shaft indicates that the solids can be lifted up by the rotating screw, which is due to the frictional force between the solid phase and the rotating screw. In contrast, much less particles can be found above the shaft in Case 1, which is lower in rotating speed and hence smaller in frictional interaction between the solid phase and the rotating screw compared to Case 3. This trend of more particles appearing above the shaft at a higher rotating speed was also demonstrated in the DEM simulation of a screw reactor in the work of Owen and Cleary.[124]

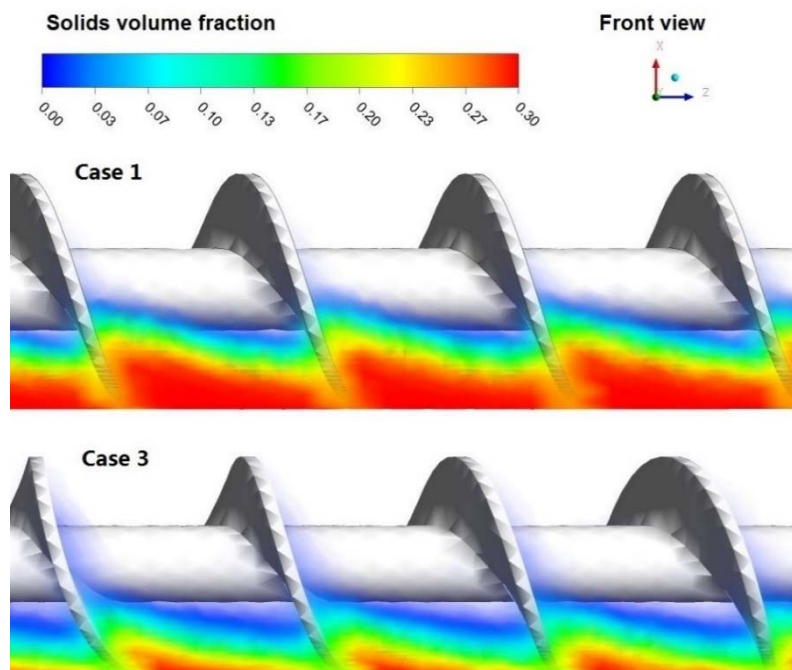


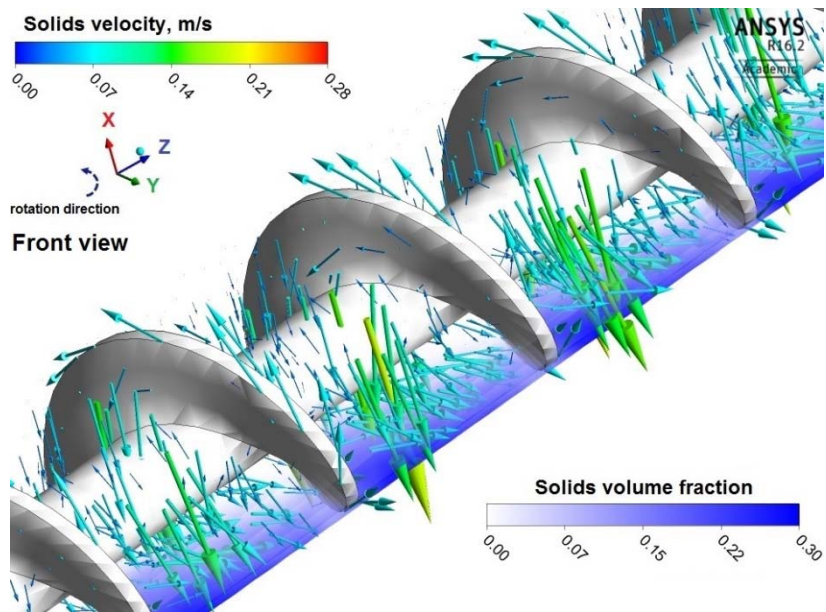
Fig. 5.3 Spatial distribution of solids volume fraction in a short section of the reactor

(Case 1 and Case 3)

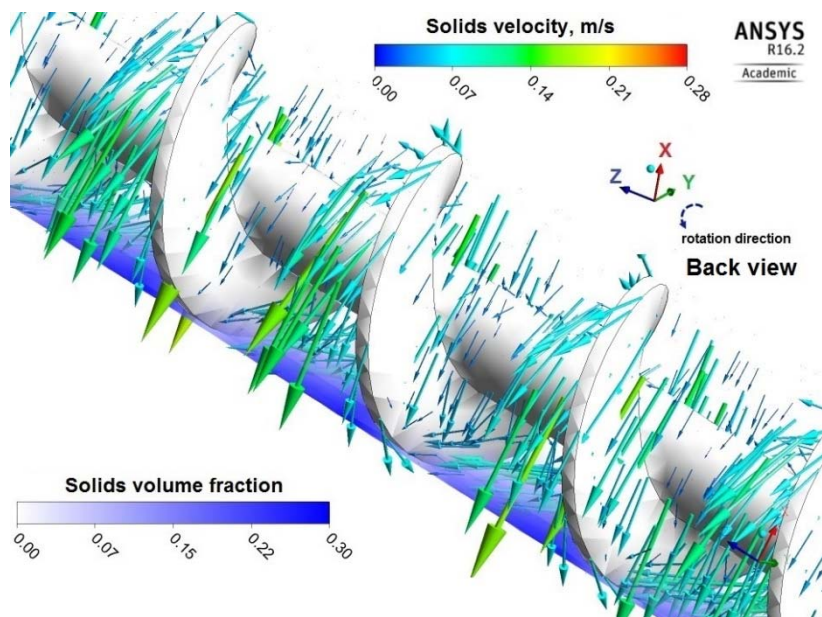
Fig. 5.3. also shows that in both cases the spatial distribution of the solids volume fraction in each pitch (also in other pitches of the reactor that were not shown in this picture) is similar, which is, in each pitch, the height of the surface of the solids phase slightly decreasing along the forward transportation direction. Reasons for the elevated height of the surface of the solid phase at the front of the flight can be explained by the fact that (1) solids at the front of the flight can experience forward pushing from the rotating screw, which can gather a portion of particles at the front of the flight, and by the fact that (2) solids near the front of the flight can be lifted up due to the friction between the solid phase and the rotating screw.

In addition, Fig. 5.3 shows that the solids volume fraction in the bottom clearance underneath the screw (the space with a size of 1 mm as shown in Fig. 5.1 between the flight and the bottom shell) is lower (about 0.10 in Case 3 compared to 0.25 in Case 1) at a higher screw rotating speed, indicating that less solids can flow through the bottom clearance, which can be explained by the fact that the solids can be carried/transported more efficiently by the screw at a higher screw rotating speed.[243] It should be mentioned that the Eulerian-Eulerian two-fluid model, in which the solid phase was assumed to be continuous, predicted the solids flow at the bottom clearance underneath the screw, while in reality the particles may be too large to pass through the bottom clearance underneath the screw, since most of the biomass particles in the experiments of Nachenius et al.[87] were larger than the size of this clearance.

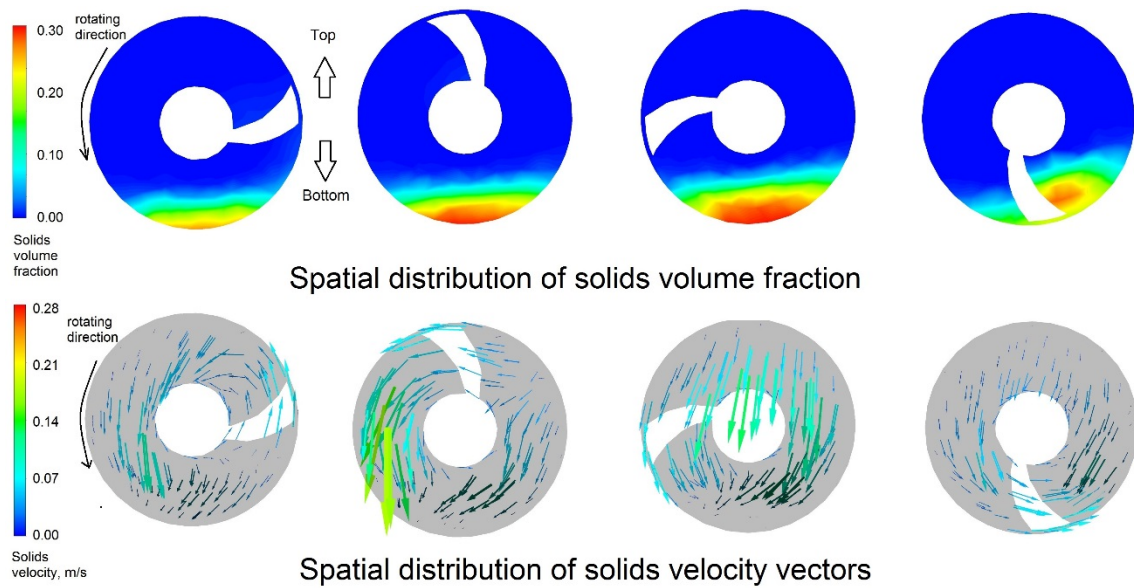
Fig. 5.4 shows the volume fraction and velocity vectors of the solids phase in selected parts of the screw reactor for Case 3 at a flow time of 80 s. From this figure, it can be seen that the solid phase experiences both rotational flow (radially) and forward transportation flow (axially).



(a)



(b)



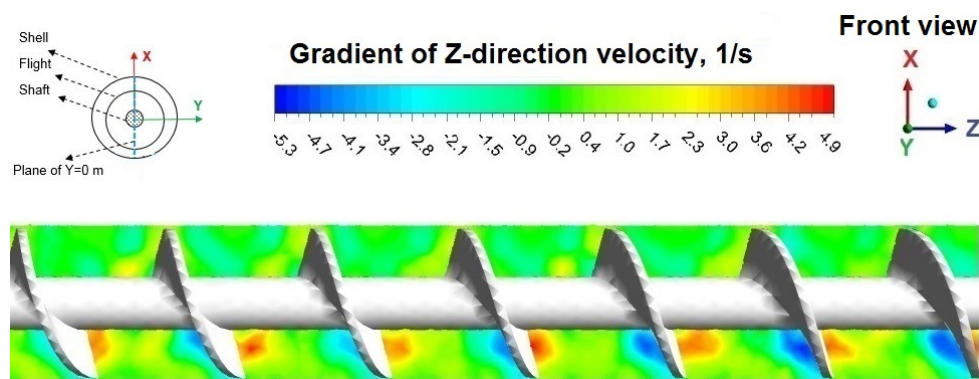
(c)

Fig. 5.4 Volume fraction and velocity vectors of the solid phase, (a) 3D front view in four pitches, (b) 3D back view in four pitches and (c) at various radial cross-sections in one pitch for Case 3

The rotational flow of the solid phase is due to the frictional interaction between the solid phase and the rotating screw, as indicated by the velocity vectors at the surface of the flight in Fig. 5.4(a) and Fig. 5.4(b). The frictional interaction between the solid phase and the rotating screw was also demonstrated in this simulation particularly when the rotating screw was predicted to contact with the solid phase at the bottom part of the reactor, where most particles are accumulating, as shown by the cross-sectional view in Fig. 5.4(c). Particles being lifted by the rotating screw can be classified among two groups. One group of the lifted particles do not acquire enough kinetic energy to be propelled over the shaft and will fall/slide down due to gravity,[223] as can be seen at the front side of the reactor in Fig. 5.4 (a) and also can be seen in the cross-sectional view in Fig. 5.4(c). Another group of the lifted particles are flung over the shaft, and they will fall down toward the succeeding pitch

with a rather high velocity magnitude, which is the combined result of friction (between the solid phase and the rotating screw) and gravity, at the back side of the reactor as shown in Fig. 5.4 (b) and in Fig. 5.4(c). Solids back-mixing occurs when this portion of particles being flung over the shaft falls down toward the succeeding pitch, which was also demonstrated in the experiments of Waje et al.[223, 231] For cases at lower screw rotating speeds (Case 1 and Case 2, not shown in Fig. 5.4), the amount of lifted particles being flung over the shaft is smaller compared to that for Case 3, which is due to the smaller frictional interaction between the solid phase and the rotating screw at lower screw rotating speeds. Considering the lower height for the surface of the solid phase (and lower filling degree and less total solid mass inside the reactor at steady-state, which is discussed later in Section 4.3) at a higher rotating speed (Case 3), as shown in Fig. 5.3, the simulation results indicated that a higher portion of particles can be flung over the shaft at a higher rotating speed. Fig. 5.4(a) and Fig. 5.4(b) also show that, at the reactor bottom, where most particles are accumulating, particles mainly experience forward transportation flow due to the mechanical push of the flight.

Fig. 5.5 (a) (front view) shows the spatial distribution of the gradients of solids forward transportation velocity (or Z-direction velocity) at the plane of $Y=0$ m for Case 3 (conclusions are similar for Case 1 and Case 2).



(a)

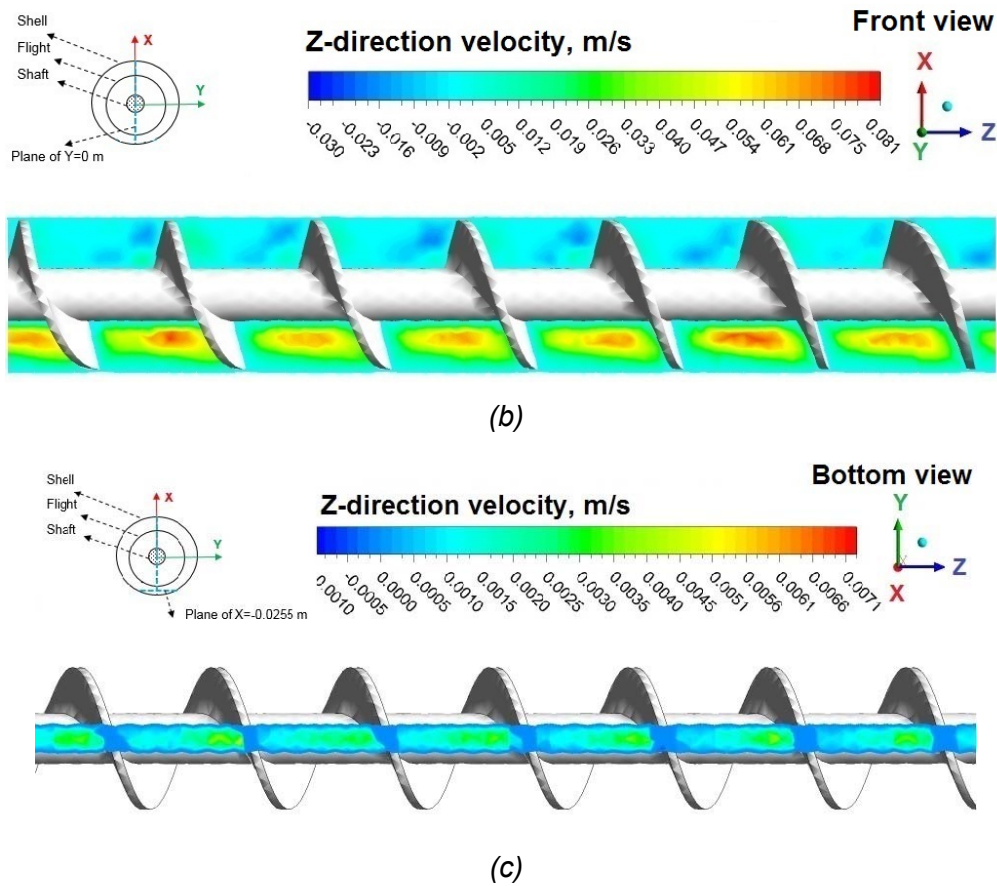


Fig. 5.5 Spatial distributions (for Case 3) of, (a) gradient of solids transportation velocity at plane of $Y=0$ m (front view), (b) solids transportation velocity at plane of $Y=0$ m (front view), and (c) solids transportation velocity at plane of $X=-0.0255$ m (bottom view).

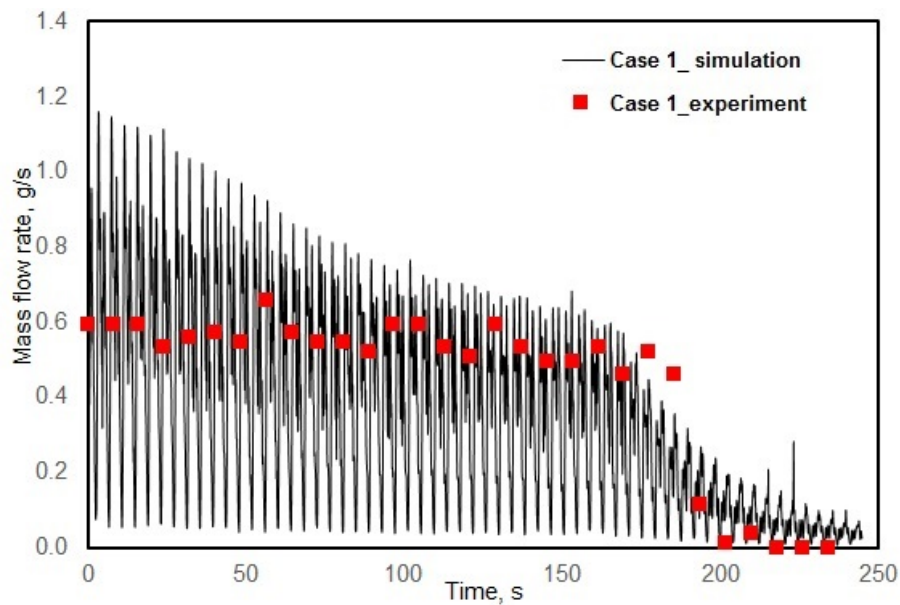
Fig. 5.5 (a) shows that, at the bottom part (between the shaft and the bottom shell, where most particles are gathering) of each pitch, the solids forward transportation velocity increases at the front of the flight, which is due to the mechanical push by the rotating screw. At the backside of the flight, negative gradients are present, indicating that the solids forward transportation velocity decreases, which is due to the friction between the solid phase and the bottom shell. As a result, the corresponding spatial distribution of the solids forward transportation velocity at this plane of $Y=0$ m in Fig. 5.5 (b) (front view) shows that, at the bottom part of each pitch, the solids forward transportation velocity is higher away from the physical structure of the screw reactor. Fig. 5.5 (b) also indicates that the solid

forward transportation velocity near the bottom shell is about one order of magnitude lower than that near the center of the bottom of each pitch. The spatial distribution of the solids forward transportation velocity at the bottom plane of $X = -0.0255$ m (in the middle of the clearance between the flight and the shell) in Fig. 5.5 (c) (bottom view) further shows that the solids forward transportation velocity right under the flight is even lower, which can result into solids back-leakage, and this phenomenon is an important reason of solids back-mixing, as reported by Waje et al.[231] The experiments of Nachenius et al.[87] did not provide any information on the extent to which biomass particles can flow through the clearance between the flight and the shell. It should be mentioned that, while the Eulerian-Eulerian two-fluid model with the continuous assumption for the solid phase predicted the solids back-leakage at the clearance, in their experiments,[87] only very few particles (3 wt.%) had a diameter smaller than the size of the clearance (i.e. 1 mm), indicating that the solids back-leakage at the clearance was likely to occur to a smaller extent in their experiments.

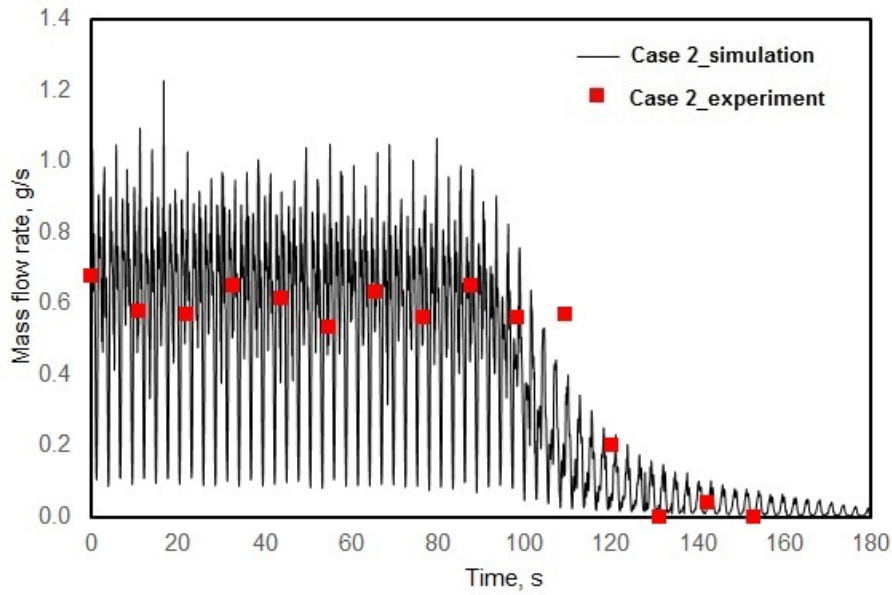
4.3 Model validation

In their original experiment, Nachenius et al.[87] introduced a negative step change (stopping the inlet flow of biomass particles) for the system after the system had reached steady-state flow conditions. They monitored the solids mass flow rate at the outlet from the time they stopped the inlet flow of biomass particles until all particles had flowed out of the reactor. In the simulation, a similar negative step change was performed after steady-state flow conditions had been reached for the three simulation cases. The solids mass flow rate was monitored from the time that the inlet flow of the solid phase was set to zero. Fig. 5.6 shows the simulation and the experimental results for the solids mass flow rate at the outlet of the reactor for the

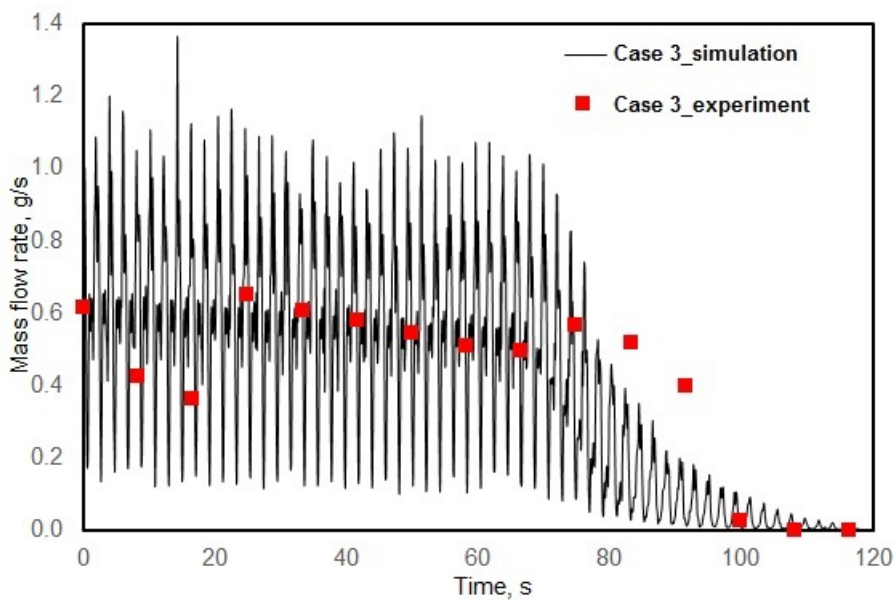
three cases. As can be seen from this figure, the predicted solids mass outflow rates fluctuated around an average of 0.6 g/s (as shown in Table 5.2) before they finally dropped to zero, which is in good agreement with the experimental results. In the simulation, the time (around 170 s in Case 1, 100 s in Case 2 and 75 s in Case 3), at which the solids mass flow rate at the outlet started to drop, decreased with the increase of the screw rotating frequency (from Case 1 to Case 3), which is the result of the more rapid pushing of the screw at higher rotating frequencies. These simulation results agree well with the experimental results (around 177 s in Case 1, 105 s in Case 2 and 75 s in Case 3).



(a)



(b)



(c)

Fig. 5.6 Comparison of the solids mass flow rate at the outlet for (a) Case 1, (b) Case 2, and (c) Case 3 between the simulations and the experiments.

Fig. 5.6 also indicates that the tapering off (from around an average of 0.6 g/s to finally 0 g/s) of the solids mass flow rate was predicted to take a longer time in the simulations than in the experiments. This difference between the simulation and the

experiment can be explained by the fact that the model predicted solids back-leakage to take place as the continuous solid phase (in the Eulerian model) would flow through the clearance between the flight and the shell, while in the experiments of Nachenius et al.,[87] wood particles were used with a certain particle size distribution (97 wt.% of wood particles in their experiments are larger than the size of the clearance, i.e. 1 mm) and the solids back-leakage at the clearance was likely to occur to a smaller extent in the experiments. Fig. 5.6 also shows that the predicted solids outflow had a periodic pattern. This periodic pattern of the solids outflow is a result of the non-uniform distribution of the solid phase in each pitch, as shown by the decreased height for the surface of the solids phase along the Z-direction in each pitch (Fig. 5.3). Nachenius et al.[87] in their experiment also observed that the solids left the reactor in periodic pulses. As the original experimental set-up was not transparent, the authors were not able to provide information regarding the flow behavior of the biomass particles inside the reactor. Their observations of the periodic pulse of the solids outflow indicates that the solids were not uniformly distributed inside the experimental screw reactor, which further demonstrates the reasonability of the simulation results with respect to the non-uniform distribution of the solid phase inside the screw.

Table 5.4 shows the comparison of the total solids mass and the filling degree (or solid hold-up defined as the bulk volume fraction of solids inside the screw reactor) inside the reactor at steady state between the simulation and the experimental results. The predicted solids mass (86.1 g to 49.4 g from Case 1 to Case 3) and filling degree (0.18 to 0.10 from Case 1 to Case 3) decreased with the increase of the screw rotating frequency (0.243 Hz to 0.486 Hz from Case 1 to Case 3). Similar trends have been frequently reported in previous experimental works.[87,

231] From this table, it can be seen that the deviations between the simulation and the experiment were less than 5 g on average for the solids mass, and less than 0.01 on average for the filling degree inside the reactor at steady state for Case 2 and Case 3, indicating that the simulation results were in good agreement with these experimental cases. Large differences between the simulation and the experiment for Case 1 were present with respect to the solids mass and filling degree, which may be due to the continuous treatment for the solid phase in the Eulerian model and due to some possible systematic errors in the experiments, which are, however, difficult to quantify.

Table 5.4 Solid mass and filling degree inside the screw reactor at steady-state

Case	Solid mass, g			Filling degree		
	Experiment	Simulation	Deviation	Experiment	Simulation	Deviation
Case 1	109.9 ± 2.5	86.1	23.8	0.20± 0.00	0.18	0.02
Case 2	69.5 ± 5.0	65.2	4.3	0.12 ± 0.01	0.13	0.01
Case 3	51.4 ± 0.7	49.4	2.7	0.09± 0.00	0.10	0.01

Overall, the above comparisons between the simulation and experimental results indicate that the model was capable of predicting the solids flow behavior inside the screw reactor, despite some quantitative differences.

4.4 Mean solids residence time

Fig. 5.7 compares the mean solids residence time from the prediction, the experimental value and the theoretical value (assuming ideal plug flow). This figure shows that the predicted mean solids residence time is in good agreement with the experiment (mean deviation of 11.4 s), while the theoretical calculation underestimates the solids residence time. Waje et al.[86, 231] also reported that the theoretical mean solids residence time was lower than the experimental value. The

mean theoretical solids residence time was calculated with the assumption that particles are pushed forward by the rotation of the screw and that particles are in ideal plug flow, which does not take into account the axial solids back-mixing. In contrast, the Eulerian-Eulerian simulation, despite some quantitative differences from the experimental results as discussed in Section 4.3, can predict the solids flow dynamics in the reactor in a more detailed way, and thus the back-mixing behavior of the solid phase can be accounted for. Fig. 5.7 also shows that the mean solids residence time decreases with the increase of the screw rotating frequency, which is due to the more rapid forward pushing of the rotating screw at higher screw rotating frequencies.

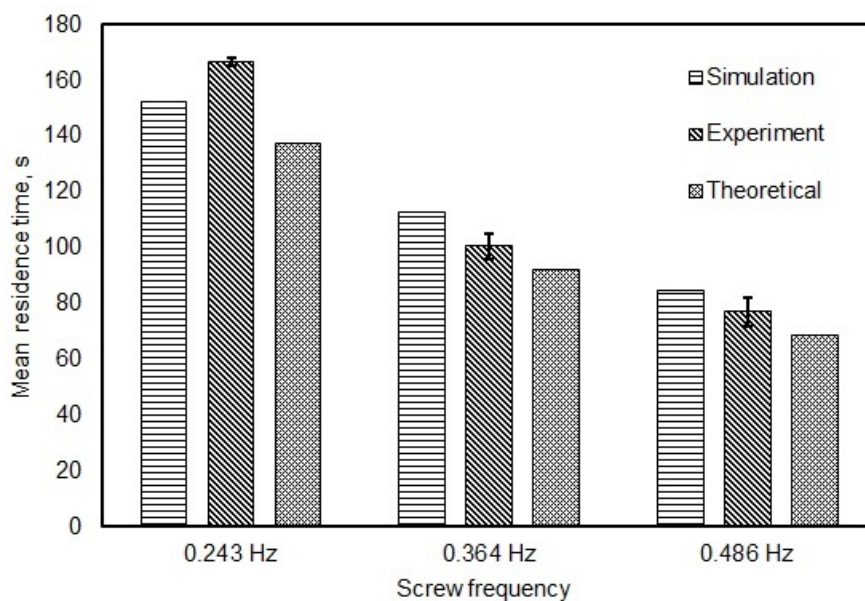
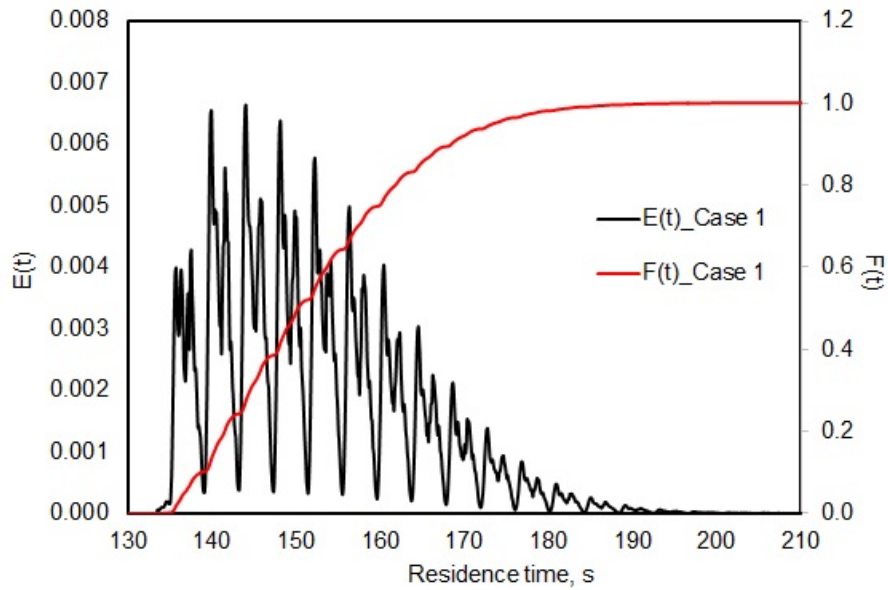


Fig. 5.7 Comparison of mean solids residence time among the simulation, the experimental value and the theoretical value

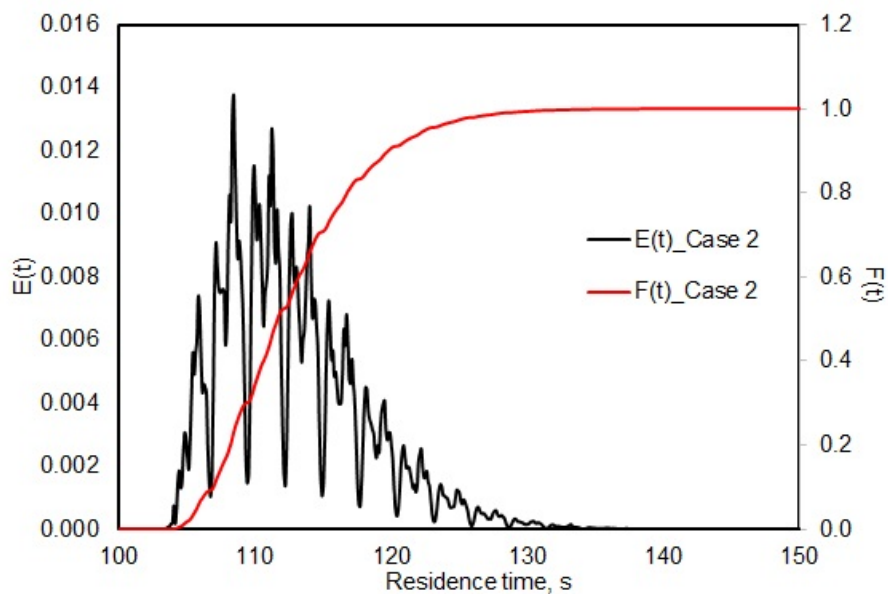
4.5 Solids residence time distribution and axial back-mixing

Fig. 5.8 shows the curves of the model predicted solids RTD $E(t)$ and the curves of the corresponding cumulative function $F(t)$. The results were averaged on a sampling time interval of 0.1 s. It can be seen that the RTD curves fluctuate,

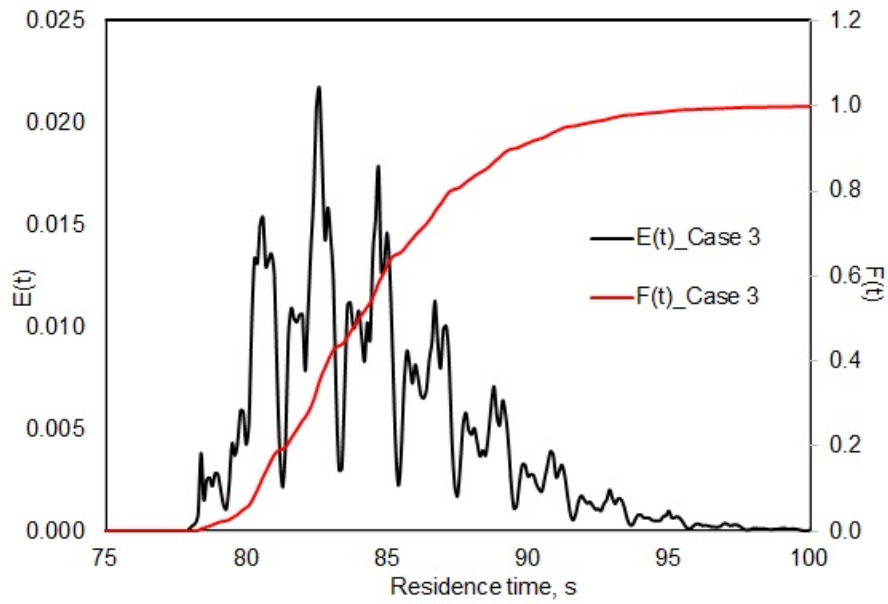
indicating that the outflow of the solid phase is in periodic pulse and that the solid phase is not uniformly distributed inside (in each pitch, as shown in Fig. 5.3) the reactor, as discussed above. Fig. 5.8 also shows that all solids RTD curves exhibit tails, indicating back-mixing of the solid phase along the forward transportation direction of the reactor.



(a)



(b)



(c)

Fig. 5.8 Model-predicted solids RTD functions, $E(t)$, and their cumulative functions, $F(t)$, for (a) Case 1, (b) Case 2, and (c) Case 3

Fig. 5.9 shows the dimensionless cumulative function, $F(\theta)$, of the solids residence time. It can be seen that all the $F(\theta)$ curves in these three cases deviate from the plug flow curve, indicating the existence of solids back-mixing in the forward transportation direction of the reactor. The $F(\theta)$ curve deviates more from the plug flow curve with the decrease of the screw rotating frequency, which means that the degree of solids back-mixing is stronger at lower screw rotating frequency. Tsai and Lin[243] also experimentally reported that the degree of particle back-mixing increased by decreasing the screw rotating speeds.

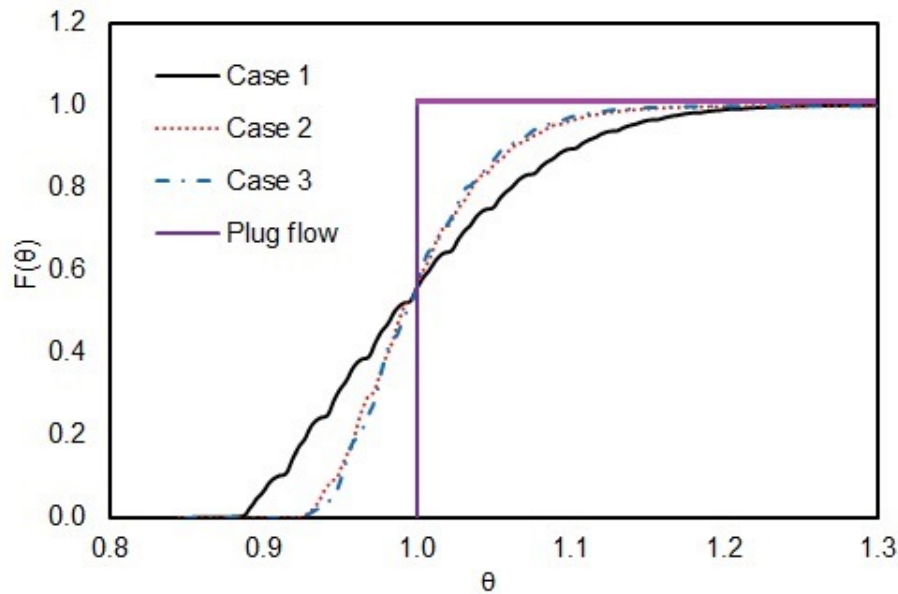


Fig. 5.9 Model-predicted dimensionless cumulative functions, $F(\theta)$, of solids RTD for three cases

To quantitatively characterize the back-mixing behavior of the solids inside the screw reactor, the variance (σ^2) and the dimensionless variance (σ_{θ^2}) of the solids RTD were calculated, as listed in Table 5.5.

Table 5.5 Model-predicted variance and dimensionless variance of solid RTD

Case number	Variance (σ^2 , s^2)	Dimensionless variance (σ_{θ^2})
Case 1	132.4	0.0057
Case 2	28.0	0.0022
Case 3	13.6	0.0019

This table shows that the variance decreases with the increase of the screw rotating frequency, indicating a narrower RTD curve at a higher screw rotating frequency. Narrower solids RTD curve is beneficial for more uniform treatments of particles, for instance in thermal conversion processes carried out in a screw reactor.[88] Table 5.5 also shows decreased dimensionless variance with the increase of the screw rotating frequency, which indicates that the solids back-mixing

in the forward transportation direction of the screw reactor is reduced at higher rotating speeds, which was also experimentally reported by Tsai and Lin.[243] As analyzed in Section 4.2, back-mixing refers to the mixing between particles at different locations along the forward transportation direction or z-direction. Back-mixing occurred in two different ways. The first way is solids back-leakage, which is defined as particles near the bottom shell tending to leak behind the main solids stream and underneath the screw, since the solids forward transportation velocity in close proximity of the bottom shell is lower than that in the bulk of the solids. The second way is solids back-flow, which is defined as particles being flung over the shaft and falling down toward the succeeding pitch. As discussed in Section 4.2, a higher portion of solids tend to be flung over the shaft due to the lift of the rotating screw at a higher screw rotating speed, resulting into more intense solids back-mixing. However, higher screw rotating speeds can also lead to less solids back-leakage, as inferred from the lower solids concentration at the clearance at higher screw rotating speeds (Fig. 5.3). The overall decreased degree of solids back-mixing (as characterized by the decreased dimensionless variance of the solids RTD) at higher screw rotating speeds means that the effect of the decreased solids back-leakage (resulting into less extent of solids back-mixing) can counteract the effect of the increased flow of solids being flung over the shaft (resulting into greater extent of solids back-mixing). The simulation results indicated that the solids back-leakage at the clearance plays a more important role than the flow of solids being flung over the shaft in affecting the solids back-mixing in the screw reactor.

It should be mentioned that the predicted curves with respect to the functions of $E(t)$, $F(t)$ and $F(\theta)$ were not validated against the experiment, since the experimental work of Nachenius et al.[87] did not provide such kind of information. Therefore, the

conclusions with respect to the solids back-mixing, which were calculated from these functions, are rather theoretical. However, these simulation results can be helpful in assessing the role of solids back-leakage at the clearance in affecting the solids back-mixing in the screw reactor, considering that more particles that are sufficiently fine to flow through the clearance are expected to be produced due to particle attrition during the thermal treatment (e.g. torrefaction[88]) of biomass in the screw reactor. Besides, the real biomass particles in the screw reactor are typically non-spherical or rather flat,[87] and these kind of shaped particles (e.g. chopped grassy or straw material) may easily fit in the clearance between screw and shell. In addition, during the torrefaction or pyrolysis in the screw reactor, biomass particles will become gradually fragile when a portion of hemicellulose in the biomass composition is gradually removed and the cell walls in biomass are gradually destroyed.[17] This fragility due to torrefaction or pyrolysis treatment can intensify the production of sufficiently fine particles (with sizes smaller than the size of the clearance) through abrasion and fragmentation, though not mentioned by Nachenius et al.,[87, 88] which can intensify the extent of solids back-leakage (solids back-mixing) and hence can be detrimental to the product uniformity.

5. Conclusions

In this chapter, a 3D CFD model for the screw reactor in processing biomass particles was developed using the Eulerian-Eulerian method. The solids flow dynamics and the solids RTD were predicted and were compared with experimental results. The simulation results with respect to the solids mass flow at the outlet, the total solids mass and filling degree at steady-state inside the reactor, and the mean solids residence time were compared with the experimental data (mean deviation of about 0.01 for the filling degree and of 11.4 s for the mean solids residence time

between the simulation and the experiment). The solids' rotational flow due to the lift of the rotating screw and the solids' forward transportation flow due to the forward-push of the screw were demonstrated in the simulation. The simulation results show that the solids back-mixing in the forward transportation direction is mainly contributed by the back-flow of solids being flung over the shaft and falling down toward the succeeding pitch, and by the back-leakage of solids with low forward transportation velocity at the clearance between the flight and the bottom shell. With the increase of the screw rotating speed, the degree of solids back-mixing can be intensified by the increased flow of solids being flung over the shaft. However, it can be reduced by the decreased solids back-leakage through the clearance. Simulation results show that the overall degree of solids back-mixing decreases with the increase of the screw rotating speed, indicating that the solids back-leakage at the clearance plays a more important role than the flow of solids being flung over the shaft in affecting the solids back-mixing in the screw reactor. These simulation results are helpful for the operation of screw reactors considering that the thermal treatment (e.g. torrefaction) of typically non-spherical biomass particles can potentially produce sufficiently fine particles that can experience back-leakage (back-mixing) at the clearance.

CHAPTER 6

Numerical study of biomass slow pyrolysis for char production in a screw reactor

In the previous chapter (Chapter 5), a CFD model was developed for studying the particle flow dynamics in a lab-scale screw reactor. In this chapter, pyrolysis reaction kinetics will be further incorporated into the CFD model to study biomass slow pyrolysis in this screw reactor. It should be mentioned that, the particle models in Chapter 2, Chapter 3 and Chapter 4 were conducted for centimeter-sized biomass particles, in which intraparticle transport phenomena were relevant. The CFD model at the reactor scale in Chapter 5 and Chapter 6 will be developed for a lab-scale screw reactor, in which pine wood particles with an average size of around 2 mm are processed. Intraparticle transport phenomena for such a small size of pine wood particles are not relevant under slow pyrolysis conditions, therefore will not be considered in the present simulation. In this chapter, simulation results with respect to temperature profiles in the reactor, products yields, and elemental composition of the char will be validated against experimental data. The energy density and energy yield of the char will be studied with the model.

This chapter was redrafted after:

Xiaogang Shi, Frederik Ronsse, Robert Nachenius, Jan G. Pieters. Numerical study of biomass pyrolysis for char production in a screw reactor using a comprehensive kinetic scheme. To be submitted to Fuel Processing Technology.

1. Introduction

Char production through biomass pyrolysis can be conducted in various reactors, and the screw reactor is one of the reactors that can continuously produce char through biomass pyrolysis.[5, 35, 88, 225, 249] Screw reactors are usually composed of a stationary shell and a rotating screw.[87] The rotating screw can provide mechanical force to transport the biomass through the reactor. Usually, the screw reactor is heated, either electrically (lab and small scale) or by using combusted pyrolysis gases and vapors (larger scale), to provide heat for driving the pyrolysis of biomass.[5, 88] Screw reactors have a number of advantages for producing char through biomass pyrolysis. For instance, the flow of biomass particles inside the screw reactor can be flexibly adjusted by manipulating the rotational speed (or frequency) of the rotating screw. In addition, the mechanical force from the rotating screw makes the screw reactor advantageous when processing biomass feedstocks with various particle shapes, sizes and morphological characteristics (from fine sawdust, to lumpy, sticky and fibrous biomass particles).[5] Researchers have shown that the energy density of the char produced in the screw reactor may be comparable to that of coal.[88]

The yield and the quality of the char in a screw reactor are highly dependent on the transport phenomena and chemical reactions occurring at multiscale (particle to reactor scale) and in multiphase (char, condensable and non-condensable volatiles). Although experimental investigations have been performed to study the flow dynamics and pyrolysis reactions of biomass in the screw reactor,[87, 88] the complex physical and chemical phenomena occurring inside the screw reactor, which are essential for reactor design and scale-up, are largely beyond the capabilities of typical experimental set-ups to reveal. With the rapid development of computational

sciences, CFD has evolved as a useful tool to study the coupled transport phenomena and chemical reactions in multiphase reactors (e.g. screw reactor) by solving the related conservation laws and equations (mass, momentum and energy).[128, 232-234, 250, 251] Plenty of modeling works based on CFD simulations have been reported for biomass pyrolysis in fluidized bed reactors.[249-255] In contrast, only a limited amount of works based on CFD simulations have been reported in the literature for biomass pyrolysis in screw reactors. Aramideh et al.[129] performed CFD simulations for biomass pyrolysis in a screw reactor, and they predicted the effects of operating conditions (operating temperature, feed rate of biomass feedstocks, etc.) on the yields of char, condensable volatiles and non-condensable gas. While CFD simulations on particle flow dynamics and product yields from biomass pyrolysis in the screw reactor have been reported,[129] the elemental composition (C, H and O), the quality (e.g. energy density) as well as the energy yield (characterizing the energy loss of the biomass during pyrolysis) of the char from biomass pyrolysis in screw reactors are seldomly reported based on CFD simulations.

The purpose of this chapter is to demonstrate the development of a working CFD model to predict the elemental composition, the energy density and the energy yield of the char from the pyrolysis of biomass in a screw reactor. In the previous chapter (Chapter 5), a (cold flow) CFD model based on the Eulerian-Eulerian approach has been developed and validated against available experiments, and the flow dynamics, residence time distribution (RTD) and back-mixing behavior of biomass particles inside the screw reactor have been obtained with the CFD model. In the present chapter, a comprehensive pyrolysis reaction scheme based on the biomass compositions (cellulose, hemicellulose and lignin) with detailed elemental

information is further incorporated into this CFD model. The axial temperature distribution in the screw reactor and the mass yields of the pyrolysis products are predicted and compared against available experimental data to address the model accuracy. The elemental composition of the char is predicted, and the predicted elemental composition is then used to calculate the energy density and the energy yield of the char, and these simulation results are also compared with available experimental results.

2. Model development

2.1 Eulerian-Eulerian model

Based on the previous work in Chapter 5, a CFD model based on the Eulerian-Eulerian approach was applied to simulate the flow dynamics and heat transfer in the screw reactor. Governing equations for mass, momentum and energy conservation of the gas and solid phases are summarized in Table 6.1,

Table 6.1 Governing equations for mass, momentum and energy conservations**Gas phase**

Continuity equation:

$$\frac{\partial}{\partial t}(\varepsilon_g \rho_g) + \nabla \cdot (\varepsilon_g \rho_g \mathbf{u}_g) = R_g$$

Momentum equation:

$$\frac{\partial}{\partial t}(\varepsilon_g \rho_g \mathbf{u}_g) + \nabla \cdot (\varepsilon_g \rho_g \mathbf{u}_g \mathbf{u}_g) = -\varepsilon_g \nabla p + \nabla \cdot \bar{\bar{\tau}}_g + \varepsilon_g \rho_g \mathbf{g} + \beta(\mathbf{u}_s - \mathbf{u}_g) + \varphi_{gs}$$

Energy equation:

$$\frac{\partial}{\partial t}(\varepsilon_g \rho_g C_{pg} T_g) + \nabla \cdot (\varepsilon_g \rho_g C_{pg} T_g \mathbf{u}_g) = \nabla \cdot \mathbf{q}_g + h_{gs}(T_s - T_g) - \Delta H_g + h_{wall}(T_{wall} - T_g)$$

Conductive heat flux:

$$\mathbf{q}_g = \varepsilon_g \lambda_g \nabla T_g$$

Species equation:

$$\frac{\partial}{\partial t}(\varepsilon_g \rho_g Y_{gk}) + \nabla \cdot (\varepsilon_g \rho_g Y_{gk} \mathbf{u}_g) = \nabla \cdot (\varepsilon_g \rho_g D_{gk} \nabla Y_{gk}) + R_{gk}$$

Solid phase

Continuity equation:

$$\frac{\partial}{\partial t}(\varepsilon_s \rho_s) + \nabla \cdot (\varepsilon_s \rho_s \mathbf{u}_s) = R_s$$

Momentum equation:

$$\frac{\partial}{\partial t}(\varepsilon_s \rho_s \mathbf{u}_s) + \nabla \cdot (\varepsilon_s \rho_s \mathbf{u}_s \mathbf{u}_s) = -\varepsilon_s \nabla p - \nabla p_s + \nabla \cdot \bar{\bar{\tau}}_s + \varepsilon_s \rho_s \mathbf{g} + \beta(\mathbf{u}_g - \mathbf{u}_s) + \varphi_{sg}$$

Energy equation:

$$\frac{\partial}{\partial t}(\varepsilon_s \rho_s C_{ps} T_s) + \nabla \cdot (\varepsilon_s \rho_s C_{ps} T_s \mathbf{u}_s) = \nabla \cdot \mathbf{q}_s + h_{gs}(T_g - T_s) - \Delta H_s + h_{wall}(T_{wall} - T_s)$$

Conductive heat flux:

$$\mathbf{q}_s = \varepsilon_s \lambda_s \nabla T_s$$

Species equation:

$$\frac{\partial}{\partial t}(\varepsilon_s \rho_s Y_{sk}) + \nabla \cdot (\varepsilon_s \rho_s Y_{sk} \mathbf{u}_s) = R_{sk}$$

2.2 Reaction kinetics

A comprehensive multi-component, multi-step kinetic scheme, as shown in Table 6.2, which was modified (hence named modified kinetic scheme) from the work of Ranzi *et al.* [68] was incorporated into the CFD model to describe the biomass pyrolysis reactions in the screw reactor. Modifications were made to the original

kinetic scheme of Ranzi *et al.*[68] considering that this original kinetic scheme of Ranzi *et al.*[68] was not balanced in mass (or elements). The following modifications were made in the present modified kinetic scheme compared to the original one from Ranzi *et al.*[68]

For the modified kinetic scheme in the present work, the elements were balanced by adding 0.3 G[COH₂] to reaction R6 in the original kinetic scheme of Ranzi *et al.*,[68] by subtracting 0.8 [COH₂] from reaction R8 in the original kinetic scheme, by changing 1.0 G[CO] to 0.5 [CO] for reaction R13 in the original kinetic scheme, and by changing 0.2 C₃H₆O₂ to 0.2 C₃H₆O for reaction R15 in the original kinetic scheme, as shown in Table 6.2. All pyrolysis reactions (R1 to R18) in Table 6.2 were assumed to be first order. In addition, the evaporation of moisture in wet biomass feedstock was included in this modified kinetic scheme, and the evaporation of moisture was also assumed to be a first order reaction, as shown in reaction R19 in Table 6.2.

Table 6.2 Reaction kinetics (Modified from Ranzi *et al.* [68])

Reaction number	Reaction	Kinetic constant [1/s] (Activation energy in J/mol)	ΔH [kJ/kg]
R1	CELL→CELLA	$8 \times 10^{13} \exp(-192000/RT)$	0 ^a
R2	CELLA→0.95HAA+0.25GLYOX+0.2CH ₃ CHO+0.2C ₃ H ₆ O+0.25HMFU+0.2CO ₂ +0.15CO+0.1CH ₄ +0.9H ₂ O+0.65Char	$1 \times 10^{10} \exp(-126000/RT)$	620 ^a
R3	CELLA→LVG	$4 \times T \exp(-41800/RT)$	364 ^a
R4	CELL→5H ₂ O+6Char	$8 \times 10^7 \exp(-134000/RT)$	-1913 ^a
R5	HCE→0.4HCE1+0.6HCE2	$1 \times 10^{10} \exp(-130000/RT)$	100 ^a
R6*	HCE1→2.5 H ₂ +0.125H ₂ O+CO+ CO ₂ +0.5CH ₂ O+0.25CH ₃ OH+0.125ETOH+2Char+ 0.3G[COH₂]	$3 \times 10^9 \exp(-113000/RT)$	-92 ^a
R7	HCE1→XYL	$3 \times T \exp(-46000/RT)$	588 ^a
R8*	HCE2→1.5H ₂ +0.125H ₂ O+0.2CO ₂ +0.7CH ₂ O+0.25CH ₃ OH+0.125ETOH+0.8 G[CO ₂]+2Char	$1 \times 10^{10} \exp(-138000/RT)$	212 ^a
R9	LIGC→0.35LIGCC+0.1pCOUMARYL+0.08PHE NOL+1.49H ₂ +H ₂ O +1.32G[COH ₂]+7.05Char	$4 \times 10^{15} \exp(-203000/RT)$	-490 ^a
R10	LIGH→LIGOH+C ₃ H ₆ O	$2 \times 10^{13} \exp(-157000/RT)$	100 ^a
R11	LIGO→LIGOH+ CO ₂	$1 \times 10^9 \exp(-107000/RT)$	446 ^a
R12	LIGCC→0.3pCOUMARYL+0.2PHENOL+0.35 C ₃ H ₄ O ₂ +1.2 H ₂ +0.7H ₂ O+0.25CH ₄ +0.25C ₂ H ₄ +1.3G[COH ₂]+0.5G[CO]+7.5Char	$5 \times 10^6 \exp(-132000/RT)$	-503 ^a
R13*	LIGOH→LIG+0.5H ₂ +H ₂ O+CH ₃ OH+ 0.5G[CO] +1.5G[COH ₂]+5Char	$1 \times 10^{13} \exp(-207000/RT)$	-120 ^a
R14	LIG→FE2MACR	$8 \times 10^1 \times T \exp(-50000/RT)$	686 ^a
R15*	LIG→0.7 H ₂ +H ₂ O+0.2CH ₂ O+0.5CO+0.4 CH ₃ OH+0.2 CH ₃ CHO + 0.2 C₃H₆O +0.4 CH ₄ +0.5C ₂ H ₄ +G[CO] +0.5G[COH ₂]+6Char	$1.2 \times 10^9 \exp(-126000/RT)$	-470 ^a
R16	G[CO ₂]→CO ₂	$1 \times 10^5 \exp(-100000/RT)$	-1814 ^a
R17	G[CO]→CO	$1 \times 10^{13} \exp(-209000/RT)$	-2000 ^a
R18	G[COH ₂]→CO+H ₂	$5 \times 10^{11} \exp(-272000/RT)$	6778 ^a
R19	H ₂ O (water in biomass)→ H ₂ O (vapor)	$4.5 \times 10^3 \exp(-45000/RT)^a$	2257 ^b

* Modifications were made to the original kinetic scheme of Ranzi et al. [68]

^a Prins, et. al. [219]

^b Michael Jones[256]

In the present modified kinetic scheme, the biomass was described as a mixture of pseudo-components (cellulose, hemicellulose, carbon-rich lignin, oxygen-rich lignin and hydrogen-rich lignin). It was assumed that there were no interactions among these pseudo-components, and therefore the overall progression of biomass pyrolysis was considered to be the sum of the individual contributions of the biomass pseudo-component pyrolysis reactions. The composition of the biomass feedstock

and its pyrolysis products are listed in Table 6.3. In the present Eulerian-Eulerian based CFD model, the components in Table 6.3 were grouped into two phases: the solid phase and the gas phase. The solid phase refers to the solid mixture of the reactant (wet biomass feedstock) and the solid product, as shown in Table 6.3. The gas phase refers to all volatile products, including the condensable volatiles (named liquid product), non-condensable volatiles (named gas product) and the inert gas (nitrogen). Condensable volatiles refer to the volatile components in Table 6.3 that can be condensed into liquid phase at room temperature, while non-condensable volatiles refer to the components in Table 6.3 that are still in gas phase at room temperature. At pyrolysis conditions (temperature of 598 K or higher, as will be described later), all these condensable and non-condensable volatiles are in the gas phase.

Table 6.3 *The list of gas and solid species (Modified from Ranzi et al. [68])*

Abbreviation	Molecular name	Atomic composition
Solid phase		
<i>Solid reactant</i>		
CELL	Cellulose	$C_6H_{10}O_5$
HCE	Hemicellulose	$C_5H_8O_4$
LIG-C	Carbon-rich lignin	$C_{15}H_{14}O_4$
LIG-H	Hydrogen-rich lignin	$C_{22}H_{28}O_9$
LIG-O	Oxygen-rich lignin	$C_{20}H_{22}O_{10}$
H ₂ O	Water inside the wet biomass feedstock	
<i>Solid product</i>		
CELLA	Activated cellulose	$C_6H_{10}O_5$
HCE1	Activated hemicellulose 1	$C_5H_8O_4$
HCE2	Activated hemicellulose 2	$C_5H_8O_4$
LIGCC	Carbon-rich lignin 2	$C_{15}H_{14}O_4$
LIG	Lignin	$C_{11}H_{12}O_4$
LIGOH	OH-rich lignin	$C_{19}H_{22}O_8$
G[CO ₂]	Trapped CO ₂	CO ₂
G[CO]	Trapped CO	CO
G[COH ₂]	Trapped COH ₂	CH ₂ O
Char	Char	C
Gas phase		
<i>Condensable volatiles (liquid product)</i>		
HAA	Hydroxyacetaldehyde	$C_2H_4O_2$
GLYOX	Glyoxal	$C_2H_2O_2$
C ₃ H ₆ O	Acetone	C_3H_6O
C ₃ H ₄ O ₂	Propanedial	$C_3H_4O_2$
HMFU	5-Hydroxymethylfurfural	$C_6H_6O_3$
LVG	Levogluconan	$C_6H_{10}O_5$
XYL	Xylose monomer	$C_5H_8O_4$
pCOUMARYL	Paracoumaryl alcohol	$C_9H_{10}O_2$
PHENOL	Phenol	C_6H_6O
FE2MACR	Sinapaldehyde	$C_{11}H_{12}O_4$
CH ₂ O	Formaldehyde	CH ₂ O
CH ₃ OH	Methanol	CH ₄ O
CH ₃ CHO	Acetaldehyde	C_2H_4O
ETOH	Ethanol	C_2H_6O
H ₂ O	Water vapor	H ₂ O
<i>Non-condensable volatiles (gas product)</i>		
H ₂	Hydrogen	H ₂
CO	Carbon monoxide	CO
CO ₂	Carbon dioxide	CO ₂
CH ₄	Methane	CH ₄
C ₂ H ₄	Ethylene	C_2H_4
<i>Inert gas</i>		
	N ₂	N ₂

One benefit of the modified kinetic scheme is that it includes the elemental information (C, H and O) for all components, as shown in Table 6.3, which allows to predict the elemental composition and hence the energy density and the energy yield of the char, as will be discussed later. Despite that the secondary conversion of the

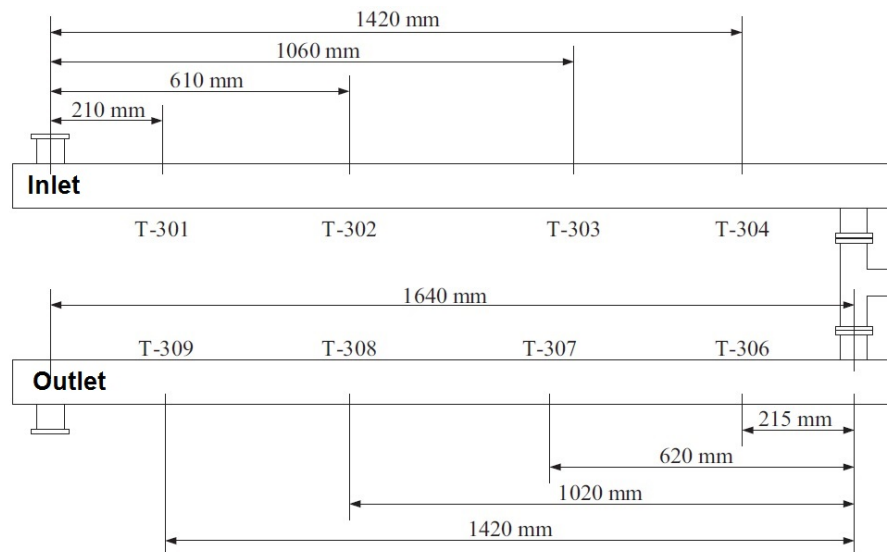
condensable volatiles into additional char and additional gas during biomass pyrolysis have long been known,[9] the detailed secondary reaction kinetics for *individual components* (hydroxyacetaldehyde, glyoxal, etc.) in the condensable volatiles in Table 6.3 are still not available.[9] Therefore, in the present modified kinetic scheme, the secondary conversion of *individual components* in the condensable volatiles was not considered, a limitation of the present modified kinetic scheme. In previous chapters (Chapter 2 and Chapter 3), secondary reaction kinetics for the condensable volatiles were explored. However, the condensable volatiles were treated as a single lumped component in these two chapters without distinguishing among the secondary conversion of *individual components* in the condensable volatiles.

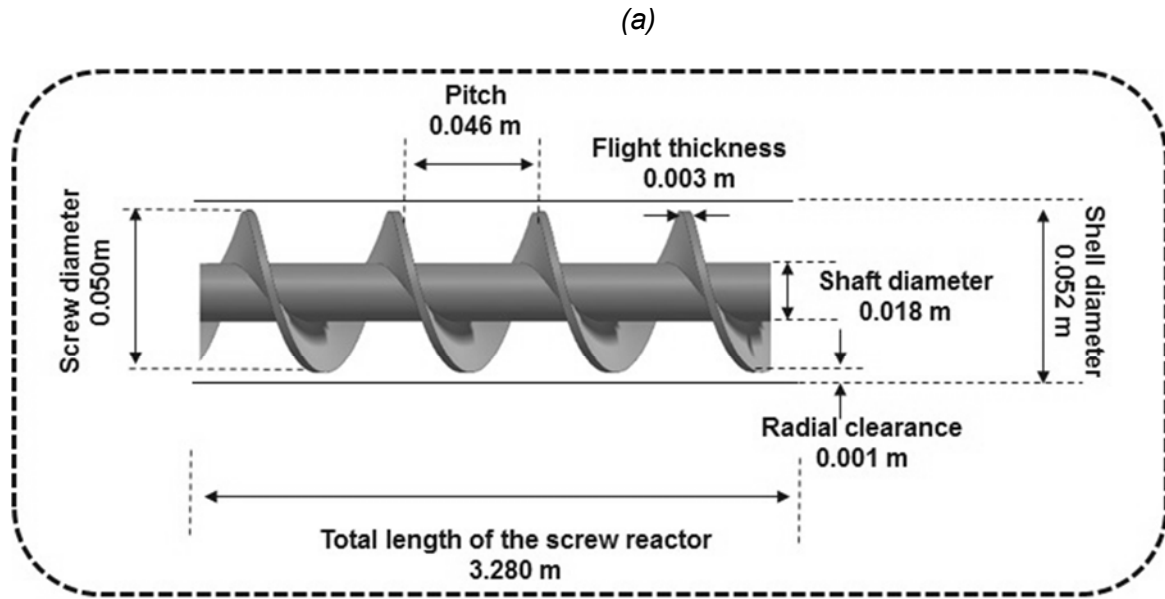
2.3 Modeled reactor geometry

As the model-predicted simulation results are validated against the experimental results from Nachenius et al.[88] in which pine wood particles were torrefied (at temperatures ranging from 598 K to 648 K) in a screw reactor, identical reactor geometry and process conditions were applied in the CFD model. The schematic geometry of the reactor and its detailed dimensions are shown in Fig. 6.1. The screw reactor is composed of a stationary shell and a rotating screw. In the experiments of Nachenius et al.[88], due to practical requirements of reducing the installation size, the screw reactor was split into two equal sections, which were operated in series, as shown in Fig. 6.1(a). The two equal sections were combined into a single reactor in the simulation. In this figure, T301-T309 indicate the position of the thermocouples which were fixed to the surface of the screw and which measured the local temperature of the solids in the experiments. Similarly, in the simulation, the

temperature of the solids at these positions was also computed for comparison with the experimental results.

The physical properties of gas and particles in the simulation, and other simulation parameters are listed in Table 6.4. According to the experiments of Nachenius et al.[88], the screw rotating frequency was 0.292 Hz, and the operating temperature was 598 K, 623 K and 648 K for three different cases. In the CFD model, the medium mesh size from Chapter 5, in which the grid independency had been examined, was applied in this chapter. The commercial CFD package ANSYS Fluent 16.2 was applied to solve the governing equations in Table 6.1. A time step of 0.002s was used, and the moving mesh method was used to model the rotation of the screw.





(b)

Fig. 6.1 Geometry of the screw reactor, (a) the actual geometry in the experiment of Nachenius et al.[88] with the locations of the screw-mounted thermocouples indicated and (b) the detailed geometry of the screw with dimensions

Table 6.4 Physical properties of gas and particles and other simulation parameters

Parameter	Values	Source
Particle diameter	0.002 m	Nachenius et al.[88]
Density of biomass feedstock	551 kg/m ³	Nachenius et al.[88]
Density of water	998.2 kg/m ³	ANSYS Fluent[257]
Density of char	2333 kg/m ³	Xiong et al.[258]
Specific heat of biomass feedstock	(1500+T/[K]) J/(kg·K)	Gronli and Melaaen[148]
Specific heat of water	4182 J/(kg·K)	ANSYS Fluent[257]
Specific heat of char	1100 J/(kg·K)	Xiong et al.[258]
Thermal conductivity of biomass feedstock	0.3 W/(m·K)	Koufopoulos et al.[82]
Thermal conductivity of water	0.6 W/(m·K)	ANSYS Fluent[257]
Thermal conductivity of char	0.1 W/(m·K)	Xiong et al.[258]
Gas density	Equation of state for ideal gas	ANSYS Fluent[257]
Gas viscosity	1.72×10 ⁻⁵ kg/(m·s)	ANSYS Fluent[257]
Gas specific heat	(601+2.262T/[K]) J/(kg·K)	Bates and Ghoniem[259]
Gas thermal conductivity	0.02577 W/(m·K)	Xiong et al.[258]
Gas mass diffusivity	10 ⁻⁵ m ² /s	Shi et al.[67]
Maximum solids packing limit	0.30	Chapter 5
Solids friction packing limit	0.28	Chapter 5
Particle-particle restitution	0.90	Chapter 5
Angle of internal friction	45°	Chapter 5
Time step	0.002 s	

2.4 Boundary and initial conditions

According to the experiments of Nachenius et al.[88] at the inlet, the mass flow rate of the inert gas was set to 2.72×10⁻⁶ kg/s, the temperature was set to 300 K and the inert gas was pure nitrogen. For the solid phase at the inlet, the mass flow rate

was 6.89×10^{-4} kg/s, the temperature was set to 300 K, and the initial solid phase consisted of pine wood with a composition of 50.3 wt.% in cellulose, 29.7 wt.% in hemicellulose, 10.5 wt.% in carbon-rich lignin, 6.5 wt.% in hydrogen-rich lignin and 3.0 wt.% in oxygen-rich lignin (these values were feedstock dry-based and were calculated using atomic balances[68] according to the elemental composition of the pine wood, consisting of 48.8 wt.% in C, 6.1 wt.% in H and 45.1 wt.% in O, as reported in the experiments of Nachenius et al.[88]) and of 11.9 wt.% (feedstock wet-based) in moisture.[88] At the outlet, atmospheric pressure was assumed for both gas phase and solid phase. At the wall (shell, shaft and flight), no-slip boundary conditions were assumed for the gas and the solid phases. The temperature at the shell was set as the operating temperature (598 K, 623 K and 648 K in three different cases). Initially, no solids were present inside the reactor, and the initial gas velocity and solid velocity were both set to zero.

2.5 Modeling energy density and energy yield of the char

(1) Energy density

With the predicted elemental composition (C, H and O) of the char, the energy density (characterized by the higher heating value, or HHV, MJ/kg) of the char was calculated with the correlation from Sheng and Azevedo,[74]

$$HHV = -1.3675 + 0.3137 \times C_{model} + 0.7009 \times H_{model} + 0.0318 \times O_{model} \quad (1)$$

Where C_{model} , H_{model} and O_{model} represent the predicted mass fractions (wt.%) of C, H, and O in the char on dry basis.

The correlation of Tillman[260], which only considered the contribution of C to the HHV, was also used for comparison,

$$HHV = 0.4373 \times C_{model} - 1.6701 \quad (2)$$

It should be mentioned that other researchers have proposed many other HHV correlations (see the review of Sheng and Azevedo[74]) based on the elemental composition of the material. In this chapter, the HHV correlations from Sheng and Azevedo[74] and from Tillman[260] were adopted to demonstrate the potential difference of the HHV value calculated from different correlations. In the present model, the HHV of the biomass feedstock (dry basis) was also calculated with either Eq. (1) or Eq. (2) based on the known elemental composition of the biomass feedstock (48.8 wt.% in C, 6.1 wt.% in H and 45.1 wt.% in O, as described in Section 2.4). In their experiments, Nachenius et al.[88] measured the HHV of the biomass feedstock (dry basis) and the HHV of the char (dry basis) with bomb calorimetry.

A parameter, named enhancement factor (EF), was introduced to characterize the HHV ratio between the char and the biomass feedstock,[17, 261, 262] and was calculated as,

$$EF = \frac{HHV_{solid\ charry\ product}}{HHV_{feedstock}} \quad (3)$$

In Eq. (3), $HHV_{solid\ charry\ product}$ is the calculated (or experimental) HHV of the char, and $HHV_{feedstock}$ is the calculated (or experimental) HHV of biomass feedstock, the latter is either directly determined by bomb calorimetry or calculated using known elemental composition.

(2) Energy yield

The energy yield η_{energy} , defined as the fraction of the energy contained within the biomass feedstock that is recovered in the char, was calculated by,

$$\eta_{energy} = Y_{solid\ charry\ product} EF \quad (4)$$

Where $Y_{solid\ charry\ product}$ is the calculated (or experimental) mass yield of the char (feedstock dry basis), and EF is the calculated (or experimental) enhancement factor, as calculated by Eq. (3).

2.6 Model accuracy

During model validation, the accuracy of the simulation results (temperature, product mass yields, elemental composition, energy density and energy yield of the char) were characterized by the mean deviation (MD) between the simulation and the experimental results

$$MD = \frac{1}{n} \sum_{i=1}^n |X_{experiment,i} - X_{model,i}| \quad (5)$$

Where n is the number and X is the value of the variable.

2.7 Processing of experimental data

The experimental data from Nachenius et al.[88] with respect to the sum of the mass yields of solid, gas and liquid products were not 100 wt.% (not mass balanced), which may be due to condensation of the condensable volatiles (named liquid product) at the wall of the screw reactor and at the condenser (for condensing and quantifying the liquid product) inlet piping in their experiments.[88] The potential condensation of volatiles outside the condenser indicated that their measured mass yield for the liquid product may be lower than actually produced. Therefore, the

experimental data with respect to the mass yields of the char and gas product were directly read from the publication of Nachenius et al.,[88] while the mass yield of the liquid product was assumed by closing the mass balance (i.e. the sum of all products should yield 100 wt.%) for comparing against the present simulation results.

3. Results and discussion

3.1 Temperature distribution

Fig. 6.2 shows the temperature distributions of the solid phase along the axial direction of the screw reactor for the simulations and the experiment[88] at the operating temperature of 598 K. The simulation results indicate that biomass was first heated from ambient temperature when it was introduced into the reactor at the reactor inlet, and then its temperature approached the operating temperature after a distance of about 2 m from the inlet, which shows the same trend as the experimental results. While the predicted solids temperature gradually increased to the operating temperature along the axial position of the reactor, in the experiments a temperature drop between the axial position of 1.42 m and 1.86 m was observed. This temperature drop in the experiments, as clarified by Nachenius et al.,[88] was due to the heat loss in the (thermally non-insulated) connection between the two identical screw reactor sections (Fig. 6.1(a)).

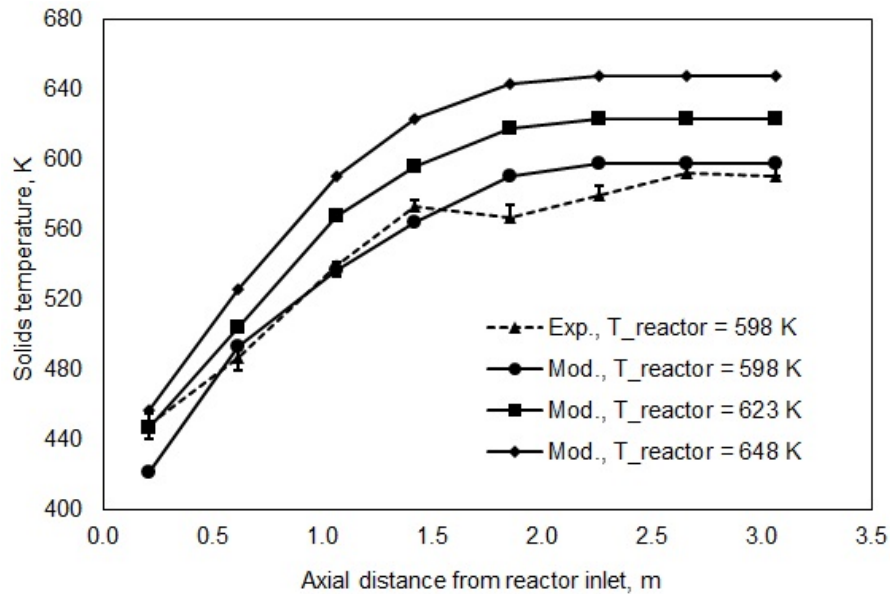


Fig. 6.2 Comparison of the solids temperature inside the reactor between the simulation and the experimental results of Nachenius et al.[88] at an operating temperatures of 598 K. For the reactor temperatures of 623 K and 648 K, no experimental data were available.

The MD between the simulation and the experimental results was 12.6 K, indicating that the model was capable of predicting the temperature distribution inside the reactor with an acceptable error margin. Fig. 6.2 also shows the predicted temperature distributions of the solid phase at higher operating temperatures. The experimental data[88] with respect to the temperature distribution of the solids was not available at operating temperatures of 623 K and 648 K. At a higher operating temperature, solids temperature was predicted to be higher at each axial position, which was expected as the biomass can be heated faster at a higher operating temperature than that at a lower operating temperature.

3.2 Product mass yields

Fig. 6.3 shows the mass yields (feedstock dry basis) of the char, the gas product (non-condensable volatiles, as shown in Table 6.3) and the liquid product

(condensable volatiles, as shown in Table 6.3) for the simulations and the experiments at operating temperatures of 598 K, 623 K and 648 K.

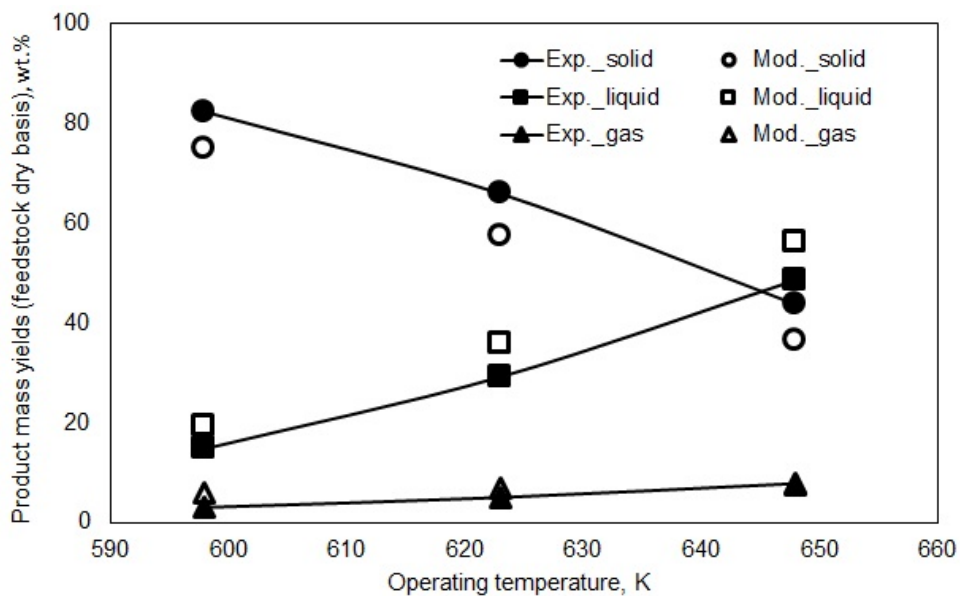


Fig. 6.3 Comparison of the product mass yields (feedstock dry basis) between the simulation and the experimental results of Nachenius et al.[88] at different operating temperatures.

As can be seen from this figure, with the increase in the operating temperature, the predicted mass yield of the char decreased while the mass yields of the gas and liquid products increased, and these trends were also demonstrated by Nachenius et al.[88] The predicted mass yield of the char was systematically lower and that of the liquid product was systematically higher compared to the experimental results. Several reasons, as listed in the following, may explain these differences between the simulation and the experimental data.

The first reason is that the secondary conversion of the condensable volatiles (ultimately accounted for as liquid product, as shown in Table 6.3) into secondary char was not considered in the present modified kinetic scheme, since the detailed reaction kinetics of *individual components* (hydroxyacetaldehyde, glyoxal, etc.) in the

condensable volatiles in Table 6.3 are still not available. Some researchers have proposed lumped kinetic models for describing the secondary conversion of the condensable volatiles by assuming these condensable volatiles to be represented as a single component with a single elemental (i.e. C, H, O) composition.[67, 94] This approach does not require information about the individual volatile components (hydroxyacetaldehyde, glyoxal, etc.) and does not consider the elemental composition of these individual condensable volatiles. As the comprehensive kinetic scheme used in this study requires to be balanced in each individual element (C, H, O), the approach of lumping all volatile species for a single secondary char-forming reaction is thus not compatible.

Another reason is the potential systemic errors in the experiment. As described above, a temperature drop at the middle of the reactor was observed in the experiment. Such a temperature drop can have an influence, however difficult to quantify, on the experimentally measured product yields.

Overall, MDs between the simulation and the experimental results at these three different operating temperatures were 7.7 wt.%, 6.2 wt.% and 1.7 wt.% for the mass yields of the char, the liquid product, and the gas product, respectively, indicating that the model can predict the product yields at different operating conditions, despite some quantitative differences being present.

3.3 Elemental composition of char

Fig. 6.4 shows the experimental and the simulation results for the elemental composition (C, H, and O, dry basis) of the char at different operating temperatures. At all operating temperatures, the char was predicted to have a higher content of C and lower contents of O and H compared to the biomass feedstock (the latter being

48.8 wt.% in C, 6.1 wt.% in H and 45.1 wt.% in O, dry basis), indicating that C was predicted to be concentrated into the char, while O and H were predicted to be devolatilized into the volatile products (gas and liquid), and similar trends have been frequently reported by experimental studies.[5, 17, 88]

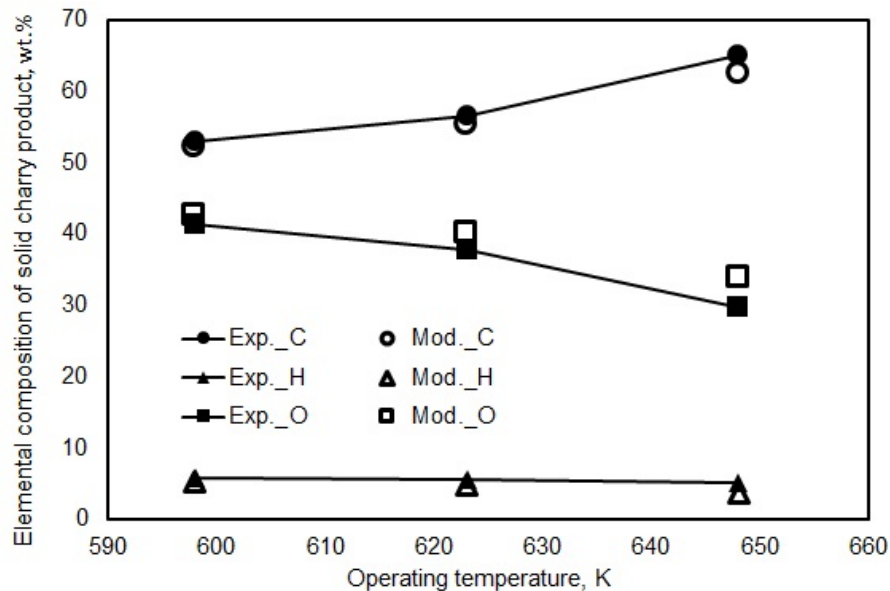


Fig. 6.4 Comparison between the simulation and the experimental results of Nachenius et al.[88] with respect to the elemental composition of the char at different operating temperatures.

This figure shows that, with the increase in the operating temperature, the predicted mass fraction of C increased, while those of O and H decreased in char, which follows similar trends as the experimental observations of Nachenius et al.[88]. This trend of higher content of C in char at higher operating temperatures has also been frequently demonstrated in other experimental studies.[5, 17, 263]. Quantitatively, MDs between the simulation results and the experimental data were 1.6 wt.%, 0.9 wt.% and 2.5 wt.% for the mass fraction of C, H and O, respectively, in the char. The above comparison between the simulation results and the experimental data indicates that the present model was capable of predicting the elemental

composition of the char at different operating conditions (i.e. different operating temperatures). The capability of the model in predicting the elemental composition allows to predict the energy density (HHV) and the energy yield of the char with appropriate correlations (i.e. HHV correlation as a function of elemental composition, as shown in Eq. (1) and Eq. (2)) from literature, as will be discussed in detail in Section 3.4.

3.4 Energy density and energy yield of char

While Nachenius et al.[88] directly measured the energy densities (i.e. HHVs) of the biomass feedstock and the char with bomb calorimetry in their experiments, in the present simulation, the HHV of the char was calculated based on the above predicted elemental composition by correlations from the literature (for comparison within the model-predicted results, the HHV of the biomass feedstock in the experiment was also calculated in a similar way based on its elemental composition). In the literature, various correlations have been proposed to calculate the HHV based on the materials' elemental composition, as reviewed by Sheng and Azevedo.[74] The HHV correlations in Eq. (1) and Eq. (2) are two typical correlations from the literature.

Fig. 6.5 shows the HHV of the char and of the biomass feedstock (dry basis) for the simulation and the experiment. As can be seen from this figure, the HHVs of the char at all operating temperatures were predicted to be higher than the HHV of the feedstock (dry basis). Experimental studies have also reported that the char obtained from biomass pyrolysis has a higher energy density than its parent biomass.[5, 17, 264]

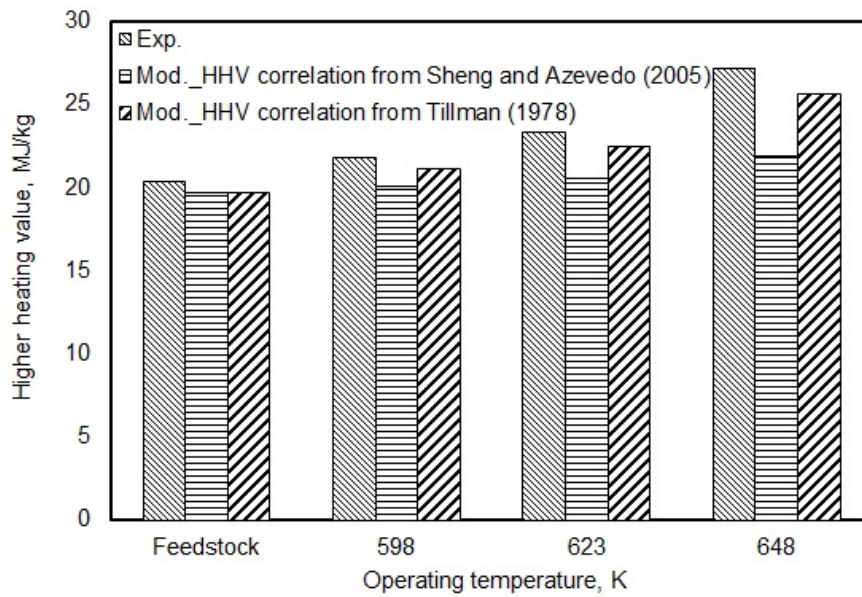


Fig. 6.5 Comparison between the simulation and the experimental results of Nachenius et al.[88] with respect to the energy density (higher heating value, HHV) of the char and of the biomass feedstock (dry basis) at different operating temperatures.

As shown in this figure, with the HHV correlation from both Sheng and Azevedo[74] in Eq. (1) and Tillman[260] in Eq. (2), the HHV of the char was predicted to increase with the increase in the operating temperature. The predicted trend of higher HHV of the char at higher operating temperatures was also demonstrated by experimental works in the literature.[5, 17, 88, 264] Quantitatively, the MD was 3.3 MJ/kg between the simulation results, when predicting the HHV of the char with the HHV correlation of Sheng and Azevedo[74], and the experimental data. For comparison, the HHV correlation of Tillman[260] resulted into a MD of 1.0 MJ/kg for the HHV of the char between the simulation and the experiment. It can be seen from this comparison that the selection of the HHV correlation from the literature influences the deviation of the simulation from the experiment with respect to the HHV of the char. Overall, the present model was capable of predicting the HHV of the char at different operating conditions (i.e. different operating temperatures) based on the predicted elemental composition of the char.

The predicted enhancement factor (EF), as defined in Eq. (3), was calculated to be 1.02, 1.05 and 1.11 when using the HHV correlation of Sheng and Azevedo[74], and was calculated to be 1.07, 1.14 and 1.30 when using the HHV correlation of Tillman[260], at the operating temperature of 598 K, 623 K and 648 K, respectively. In comparison, the experimental EF at these three operating temperatures was 1.07, 1.14 and 1.33, respectively. It can be seen that the HHV correlation of Tillman[260] would result into a slightly lower predicted EF than the experimental EF only at the operating temperature of 648 K, while the HHV correlation of Sheng and Azevedo[74] would lead to much lower predicted EFs than the experimental EF at all operating temperatures.

The predicted energy yields (feedstock dry basis) of the char were obtained with Eq. (4) for different operating temperatures, and were compared to the experimental data, as shown in Fig. 6.6. As can be seen from this figure, the predicted energy yield of the char decreased with the increase of the operating temperature, and similar trends were also experimentally reported.[17, 88, 264]

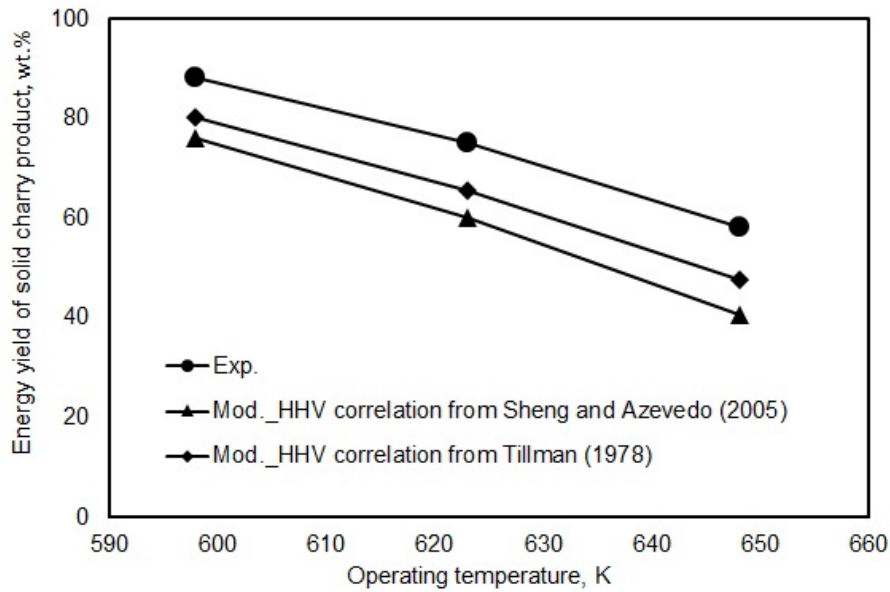


Fig. 6.6 Comparison between the simulation and the experimental results of Nachenius et al.[88] with respect to the energy yield (feedstock dry basis) of the char at different operating temperatures.

This figure also shows that the simulation results were lower than the experimental data with respect to the energy yield of the char at all three operating temperatures. As can be seen from Eq. (4), both the EF and the yield of the char can influence the energy yield. Therefore, the lower simulation results compared to the experimental data with respect to the energy yield of the char can be explained by the following two reasons:

The first reason is that, the predicted EF, which was calculated to be lower using either HHV correlations (Eq. (1) or Eq. (2)) as discussed above, can partly contribute to the lower predicted energy yield of the char compared to the experimental data. The HHV correlation of Tillman,[260] compared to that of Sheng and Azevedo,[74] resulted into predicted EF that was better comparable to the experimental EF. As a result. the HHV correlation of Tillman,[260] compared to that of Sheng and

Azevedo,[74] resulted in a lower MD (9.4 wt.% versus 14.9 wt.%) between the simulation and the experiment with respect to the energy yield of the char.

Another reason is that the yield of the char was predicted to be lower than the experiment, as discussed in Section 3.2, which also contributes to the lower energy yield of the char in the simulation compared to that in the experiment.

Overall, the above results showed that, with the increase of the operating temperature, the energy density of the char can be improved, however at the loss of the mass yield and the energy yield of the char, which indicates that a compromise should be made between the energy density and the mass/energy yield of the char in selecting appropriate operating conditions for char production through biomass pyrolysis.

3.5 The relevance of including secondary reactions in the model

As discussed above, not including the secondary conversion of the condensable volatiles into additional char in the model was partly responsible for the higher predicted mass yield of the liquid product and the lower predicted mass yield (and hence lower predicted energy yield, as discussed in Section 3.4) of the char compared to the experimental results. However, the detailed kinetic parameters for the secondary conversion of *individual components* in condensable volatiles, as listed in Table 6.3, are still not available. To demonstrate the potential of including secondary conversion of the condensable volatiles into the modeled reaction kinetics, a simplified CFD model was developed. The CFD model adopted a simple kinetic reaction scheme, where components were lumped into virgin biomass, char, gas and condensable volatiles, and which can account for the secondary reaction kinetics of the condensable volatiles. A shorter screw reactor with a length of 0.49 m (other

dimensional parameters, including shell diameter, shaft diameter, etc., were similar to those in Section 2.3) was simulated. A shorter screw reactor was simulated since (1) general conclusions with respect to the secondary conversion of condensable volatiles, as described later, for a shorter screw reactor would be similar to those for a longer screw reactor (e.g. the one in Section 2.3), and (2) a shorter simulated screw reactor (indicating less computational grids) can save computational time. An isothermal condition at an operating temperature of 648 K was assumed in the simulation. Details about the development of the CFD model are described in **Appendix C**.

Two cases, with (Case 1) and without (base case, Case 2) including the secondary reaction kinetics of the condensable volatiles were simulated for comparison. Fig. 6.7 shows the predicted normalized product mass yields ($\frac{Y_{i,Case 1}}{Y_{i,Case 2}}, i = char, condensable volatiles, gas$) when the secondary reaction kinetics of the condensable volatiles were accounted for. This figure indicates that, compared to the base case (Case 2) where the secondary reaction kinetics of the condensable volatiles were not included, the case (Case 1) including the secondary reaction kinetics of the condensable volatiles predicted a lower mass yield of condensable volatiles and higher mass yields of solid (char) and gas, which was due to the secondary conversion of condensable volatiles into additional char and additional gas. It was predicted that the secondary conversion of condensable volatiles tended to produce more gas and less char, which was due to the fact that the formation rate of gas was 2.6 times the formation rate of char in the secondary conversion of condensable volatiles, as shown in the kinetic parameters in Table C1 in **Appendix C**.

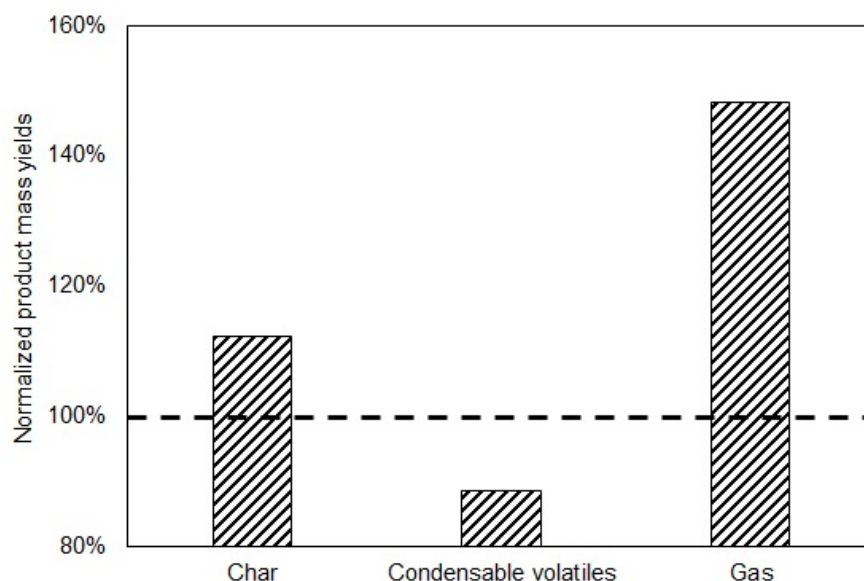


Fig. 6.7 Predicted product mass yields (feedstock dry basis), which were normalized by the product mass yields in the base simulation case only considering the primary pyrolysis of virgin biomass, for the simulation case including both the primary reaction kinetics of the virgin biomass and the secondary reaction kinetics of the lumped condensable volatiles.

It should be mentioned that the simulation in this section was a preliminary analysis on the secondary conversion of the condensable volatiles inside the simulated screw reactor. From the above simulation results, it can be inferred that the consideration of the secondary reaction kinetics of *individual components* in condensable volatiles, as listed the comprehensive kinetic scheme in Table 6.3, with additional production of secondary char, can be expected to improve the accuracy of the CFD model (Section 2) in predicting the mass yields for products (char, gas and condensable volatiles) and in predicting the energy yield for the char. However, this can only be done on the condition that the detailed secondary reaction kinetics of *individual components* in condensable volatiles in Table 6.3 are well established.

4. Conclusions

In this chapter, biomass pyrolysis in a lab-scale screw reactor using CFD

simulations based on the Eulerian-Eulerian method was studied. A multi-component, multi-step kinetic model with detailed elemental information (C, H and O) was incorporated into the CFD model to predict the pyrolysis reactions. The model was validated against the experimental data with respect to the axial temperature distribution inside the reactor, the product (char, liquid product and gas product) mass yields, and the elemental composition of the char. Results showed that the model can well predict the temperature distribution along the axial direction of the screw reactor, despite some quantitative differences being present (with a MD of 12.6 K between the simulation and experiment at the operating temperature of 598 K). The predicted product yields were in reasonable agreement with the experimental data (with MDs of 7.7 wt.%, 6.2 wt.% and 1.7 wt.% for the mass yields of the char, the liquid product, and the gas product, respectively) at different operating temperatures. The elemental composition (C, H and O) of the char was predicted and was compared with the experimental data (with MDs of 1.6 wt.%, 0.9 wt.% and 2.5 wt.% for the mass fractions of C, H and O, respectively). Based on the simulation results with respect to the elemental composition of the char, the energy density (HHV, depending on the literature source for the HHV correlation as a function of the elemental composition), the enhancement factor (EF) of the HHV, and the energy yield of the char were subsequently predicted and were compared against the experimental results. The use of HHV correlation of Tillman[260] resulted into a MD of 1.0 MJ/kg for the HHV and a MD of 9.4 wt.% for the energy yield. This HHV correlation of Tillman[260] resulted into predicted EF of increasing from 1.07 to 1.30 compared with experimental EF of increasing from 1.07 to 1.33 when the operating temperature increased from 598 K to 648 K. Results also showed that the simulation case including the secondary reaction kinetics of the condensable volatiles predicted

a lower mass yield for the condensable volatiles and higher mass yields for the char and the gas compared to the simulation case that did not account for the secondary reaction kinetics of the condensable volatiles.

MAIN CONCLUSIONS AND FUTURE PERSPECTIVES

(1) Main conclusions

Biomass resources can be processed to generate renewable energy and chemical products through various thermochemical technologies. Pyrolysis is one of the promising thermochemical technologies to convert biomass into gas, liquid/tar/oil and char. Char produced from biomass pyrolysis (particularly slow pyrolysis) can be used either as a solid fuel or as a carbon-rich material for further applications in improving soil health, preparing functional carbon materials, making contaminant adsorbents, etc.. Char production from biomass pyrolysis involves multiscale (e.g. atomic and molecular scale, particle scale, reactor scale, etc.) and multiphase (virgin biomass and its char in the solid phase and its volatile products in the gas phase) phenomena. Many factors, including biomass type, physical properties of the biomass particles and operating conditions in the pyrolysis reactor, can influence the char production during biomass pyrolysis in terms of yield and physicochemical properties of the resulting char. Computational modeling is therefore a potential tool for studying the complex physical and chemical phenomena occurring at the multiscale for char production. In this thesis, the multiscale modeling of the slow pyrolysis of biomass in producing char was performed. The physical and chemical phenomena at both the particle scale and the reactor scale were addressed.

To study the physical and chemical phenomena at the particle scale, three-dimensional comprehensive particle models (3D CPMs) were developed by coupling the transport phenomena and either a general pyrolysis kinetic scheme (treating biomass as a whole, without accounting for the composition) or a comprehensive pyrolysis kinetic scheme (treating biomass as a mixture of its components including

cellulose, hemicellulose, and lignin). For saving computational time, the 3D CPM was further simplified based on the space-time integral method, resulting into a simplified particle model (SPM) that was then applied to study the slow pyrolysis of a biomass particle (i.e. at torrefaction conditions). With these particle models, the effects of operating conditions (e.g. temperature, heating rate, etc.) and physical properties of biomass particles (size, shape, etc.) on the char production were explored.

For analyzing the physical and chemical phenomena at the reactor scale, the CFD-based reactor model using the Eulerian-Eulerian method was developed for a lab-scale pyrolysis reactor (screw reactor). With the CFD model, the flow dynamics and back-mixing of biomass particles inside the screw reactor were studied. The mass yield of char and its qualities (i.e. elemental composition and energy density) under different operating conditions were analyzed.

The operation and optimization of biomass slow pyrolysis in producing char are highly dependent on the in-depth understanding of the related physical and chemical phenomena. The particle and reactor models developed in this thesis can provide multiscale views on understanding these physical and chemical phenomena. The multiscale modeling was achieved by simultaneously solving the conservation equations for heat, mass and momentum and equations for pyrolysis reaction kinetics at both particle scale (particle models) and reactor scale (reactor models). Results from the multiscale modeling have been validated against available experimental results. From the study in this thesis, it can be seen that the multiscale modeling can provide detailed information, which are difficult to experimentally determine, on the intraparticle phenomena (e.g. intraparticle secondary charry reactions, intraparticle temperature distribution, etc.) and on the phenomena occurring in the reactor (e.g. flow and mixing behaviors of biomass particles in the

screw reactor, mass yield of pyrolysis products, elemental composition and energy density of char, etc.). This information is helpful in guiding the design, operation and optimization of biomass slow pyrolysis reactors in producing char.

It should be mentioned that the present models have their limitations. In the present particle model, a homogeneous porous distribution across the whole biomass particle was assumed, while in real biomass, the porosity is not uniformly distributed inside the particle. Large pores formed from vessels along the grain of biomass will serve as conduits for vapors and gases, while flow of vapors and gases across the grain will be through smaller pores and cracks formed in and in-between cell walls. The physical porous structure of an actual biomass particle indicates that there will be a preferential flow of vapors and gases along the grain of biomass particle during biomass pyrolysis. To achieve the ability of the particle model in accounting for the preferential flow of vapors and gases along the sample grain, it had been assumed in the particle model that the permeability (defined by the internal resistance of the particle to the bulk outflow of the vapors and gases) along the grain was higher than that across the grain. Since the outflow velocity of the gas mixture was proportional to the permeability, it was possible to predict the preferential volatiles flow along the sample grain with such treatment in the particle model. However, the permeability is actually a function of material properties. Such kind of treatment in the model was only reasonable when revealing the preferential flow of vapors and gases (and hence their secondary conversions) along the grain of biomass. The most reasonable treatment in the model would be that the detailed porous structure across the whole biomass particle is incorporated into the particle model once such kind of porous structure has been experimentally obtained. However, new problems would again emerge if the detailed porous structure is

implemented into the particle model as the actual deformation of the porous structure during biomass pyrolysis would be extremely difficult to predict with the model (i.e. extremely detailed grids with a large number of cells would be required in the simulation resulting in huge demands in computational capacity). Maybe the present treatment (i.e. homogeneous porous assumption but different physical properties along and across the grain of biomass) is currently a reasonable choice to both achieve model accuracy within an acceptable computational time.

The methodology of the model in the present work is helpful for guiding future modeling studies. The possible applications of the methodology in the present work are discussed in the following three aspects: feedstock type, thermochemical conversion and reactor type. (1) Feedstock type: while the present work mainly focused on woody biomass, the pyrolysis of other biomass types (non-woody biomasses), including biomass wastes, microalgae, herbaceous biomass, etc., can also be tackled with the methodology in the present work. By adopting a comprehensive chemical reaction kinetic scheme considering the woody biomass' main components (cellulose, hemicellulose and lignin), it was shown that in the present work the pyrolysis of different woody biomasses (i.e. softwood and hardwood) can be handled. The methodology indicates that if the chemical composition (e.g. protein, lipid, carbohydrate and mineral content) and their corresponding pyrolysis reaction kinetics are known for these non-woody biomass constituents, it is possible by adopting the methodology in the present work to simulate the pyrolysis of these non-woody biomasses. (2) Thermochemical conversion. In addition, if the reaction kinetics of thermochemical conversion processes other than pyrolysis are known (e.g. gasification and combustion), the present methodology is still expected to be feasible to tackle these thermochemical conversion processes of biomass. (3) Reactor type.

At the reactor scale modeling, the present work focused on the screw reactor. The Eulerian-Eulerian method coupling pyrolysis reaction kinetics in the reactor scale modeling can also be extended to other types of reactors in which multiphase reaction flows are present. For example, the fluidized bed reactors are widely applied for biomass pyrolysis as well as for other thermochemical conversions. In fluidized bed reactors, the dominant phenomena are the complex interactions with respect to gas-solids, solids-solids and solids-walls, which are fully coupled with heat and mass transfer and chemical reactions. Such kind of complex physical and chemical phenomena occurring in fluidized bed reactors for biomass thermochemical conversion can also be tackled with the present Eulerian-Eulerian method coupling chemical reaction kinetics. Therefore, the methodology in the present work can be extended for wider applications in biomass thermochemical conversion processes.

(2) Future perspectives

Based on this work, it can be concluded that the multiscale modeling is capable of revealing the physical and chemical phenomena during biomass pyrolysis in producing char at both the particle scale and the reactor scale. Despite that some key phenomena (e.g. intraparticle secondary char production, solids flow and back-mixing and biomass pyrolysis inside the screw reactor) have been investigated in this work aiming to produce char from biomass pyrolysis, this work needs to be further improved in future research by addressing, but not limited to, the following aspects:

- At the particle scale, the detailed three-dimensional intraparticle microstructure (e.g. pores) should be included into the particle model to better describe the intraparticle volatiles outflow and hence the secondary char production from the conversion of the volatiles. The detailed intraparticle microstructure can be first obtained by, e.g., image analysis

or microtomography in the experiments and then can be implemented into the particle model for particle scale modeling. Such more detailed particle models should allow the prediction of more advanced physicochemical properties (i.e. BET-surface area) whose control is essential in certain applications, like in preparing functional carbon materials.

- Simplified models for biomass particles with other geometries (e.g. cubic and spherical geometry, and finally any other abnormal geometries) have to be developed by applying the approach of developing the simplified model for a cylindrical biomass particle in this thesis.
- It is still required to get a consensus on what exactly occurs in the chemical pyrolysis reactions (e.g. the secondary conversion of condensable pyrolysis volatiles, including levoglucosan, hydroxyacetaldehyde, glyoxal, etc., into secondary char), and to get accurate kinetic rate parameters for further applications in particle and reactor models. Experiments should be first performed to study the detailed chemical reactions occurring in biomass pyrolysis, and kinetic parameters should then be derived based on these experimental results. These kinetic parameters can then be applied in particle and reactor models.
- At the reactor scale, the particle size distribution (PSD) should be considered, which may substantially increase the computational load but is necessary considering that the PSD may influence the char production during biomass pyrolysis.
- The multiscale modeling approach developed in this thesis can be further applied to study various factors (e.g. reactor geometries) that can

influence char production in slow pyrolysis reactors. This information would be useful for designing, controlling and optimizing char production in slow pyrolysis reactors.

- Work is still needed for developing a combined particle-reactor model for the industrial slow pyrolysis reactors which handle centimeter-sized or larger biomass particles where intraparticle phenomena are relevant. Such kind of a combined particle-reactor model can be achieved by implementing the (simplified) particle model into the CFD-based (Eulerian-Eulerian or Eulerian- Lagrangian methods) reactor models. This combined particle-reactor model should be validated against the experiment that itself should be first performed in the future. Applicability of this combined particle-reactor model should be examined under various operating conditions and for various types of biomass.

APPENDIX A

Analysis of non-dimensional numbers

Torrefaction of a biomass particle involves three main physical/chemical processes: external (convective and radiative) heat transfer to the particle, (conductive) heat transfer within the particle, and the torrefaction reactions. Three non-dimensional numbers proposed by Pyle and Zaror[185] were applied to characterize the relative importance of the above-mentioned three processes:

$$\text{Biot number:} \quad Bi = \frac{h_{ext} R}{\lambda} \quad (\text{A-1})$$

$$\text{Internal pyrolysis number:} \quad \frac{1}{Py} = \frac{k \rho_{w0} C_w R^2}{\lambda} \quad (\text{A-2})$$

$$\text{External pyrolysis number:} \quad \frac{1}{Py'} = \frac{k \rho_{w0} C_w R}{h_{ext}} \quad (\text{A-3})$$

where R (m) is the characteristic length, λ (W/(m·K)) is the thermal conductivity of the biomass. The overall solid mass loss rate during biomass torrefaction, k (1/s), was adopted from the work of Peng et al.[265] ($k = 2.9 \times 10^8 \exp(-130,690 / R_{cons} T)$). It should be mentioned that Peng et al.[265] obtained this value with the assumption that the biomass is converted into volatiles and char in one step, which is a simple and convenient method in calculating the overall solid mass loss rate constant during biomass torrefaction. However, the mass loss kinetic from the work of Peng et al.[265] provides very limited compositional information with respect to the torrefaction products, and a more complex multi-step torrefaction kinetics from Prins et al.[219] was applied in developing the models (CPM and SPM) in this work.

ρ_{w0} (kg/m³) is the biomass density, c_w (J/(kg·K)) is the heat capacity of the biomass and h_{ext} (W/(m²·K)) is the external heat transfer coefficient. The external heat transfer coefficient (h_{ext}), including both convection and radiation, was calculated by

$$h_{ext} = h_{convective} + \sigma e (T^2 + T_s^2)(T + T_s) \quad (A-4a)$$

The external heat transfer coefficient is variable since the surface temperature T_s (K) is practically a function of time. However, the external heat transfer coefficient can be evaluated at steady conditions by assuming, for simplicity, that the torrefaction/reactor temperature T and the surface temperature T_s are coincident. The external heat transfer coefficient can then be evaluated by the expression[65]:

$$h_{ext} = h_{convective} + 4\sigma e T^3 \quad (A-4b)$$

where $h_{convective}$ is the external convective heat transfer coefficient, σ is the Stefan-Boltzmann constant and e is the emissivity.

For the Biot number, a value of 1 represents that the heat transfer resistance inside of and at the surface of the biomass particle are equally important. When $Bi < 1$, the internal heat transfer is rapid compared to the external heat transfer to the particle, and the internal heat transfer is no longer a rate limiting factor. How fast the particle reaches the torrefaction/reactor temperature will depend on the external heat transfer. Under these conditions, the rate-controlling process during the torrefaction of a biomass particle can be identified by calculating the relative rates of the external heat transfer to the particle and the torrefaction reaction kinetics with the external

pyrolysis number Py' . [185] In contrast, when $Bi > 1$, the internal heat transfer is slow compared to the external heat transfer. The key question will be the relative rates of the internal heat transfer and the torrefaction reaction kinetics. Therefore, the internal pyrolysis number Py , which defines the relative rates of the internal heat transfer and the torrefaction reaction kinetics, is applied to identify the rate-controlling process in between the torrefaction reaction and the internal heat transfer. [185]

For a typical biomass particle with a density of 500 kg/m^3 , a thermal conductivity of $0.15 \text{ W/(m}\cdot\text{K)}$ and a heat capacity of $2000 \text{ J/(kg}\cdot\text{K)}$, the three non-dimensional numbers at two typical torrefaction/reactor temperatures of 473 K and 573 K for various characteristic lengths were calculated, as shown in Fig. A1. It was calculated that the torrefaction of a biomass particle with a characteristic length at millimeter scale (or smaller) is characterized by a low Biot number ($Bi < 1$) and a high external pyrolysis number ($Py' > 100$), which indicates that the torrefaction of this small biomass particle (with a characteristic length of 3.5 mm at the reactor temperature of 473 K , and a characteristic length of 2.5 mm at the reactor temperature of 573 K) tends to be kinetically controlled. And this characteristic length is the dimension up to which the kinetic model can be valid. However, for particles at the centimeter scale, the torrefaction process has a moderate Biot number ($Bi \sim 3$) and a moderate internal pyrolysis number ($Py \sim 10$), which indicates that the internal heat transfer and the torrefaction reactions play comparable roles in affecting the torrefaction of a centimeter-sized biomass particle (with a characteristic length of 10.5 mm at the reactor temperature of 473 K , and a characteristic length of 7.5 mm at the reactor temperature of 573 K). And at this condition, the combined model of heat transfer

and reaction kinetics are necessary to predict the torrefaction of this (or larger) biomass particle.

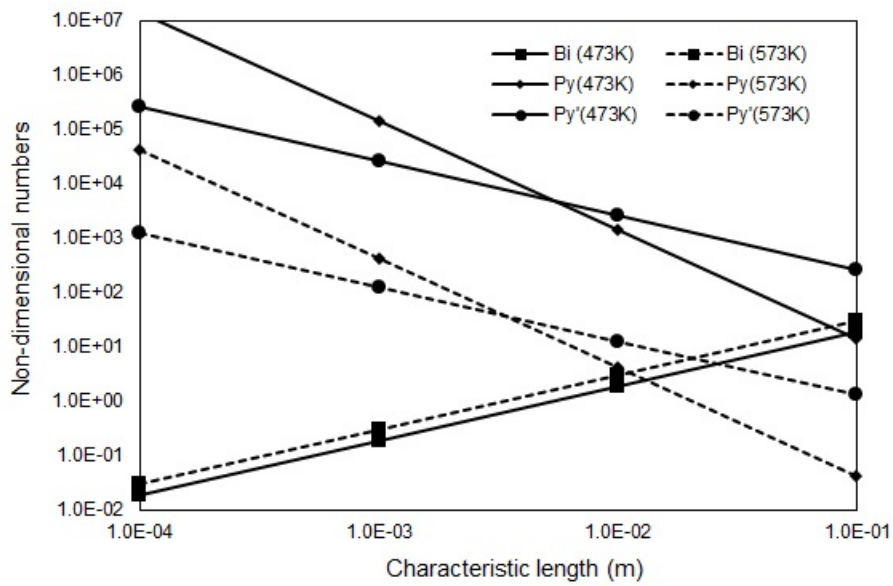


Fig. A1 Analysis of non-dimensional numbers (in logarithmic scale)

APPENDIX B

Selection of appropriate torrefaction kinetics

Fig. B1 shows the kinetic scheme in Chapter 2. It should be mentioned that the kinetic parameters describing the biomass conversion into tar, gas and primary char, which dominate the residual solid mass loss rate, in this kinetic scheme were originally proposed by Blasi and Branca.[152] They obtained this group of kinetic parameters at heating rates of 1000 K/min and final reactor temperatures in the range of 573–708 K, which is largely different from the torrefaction conditions (at heating rates in the range of 10-15 K/min and to reactor temperatures in the range of 473-573 K).

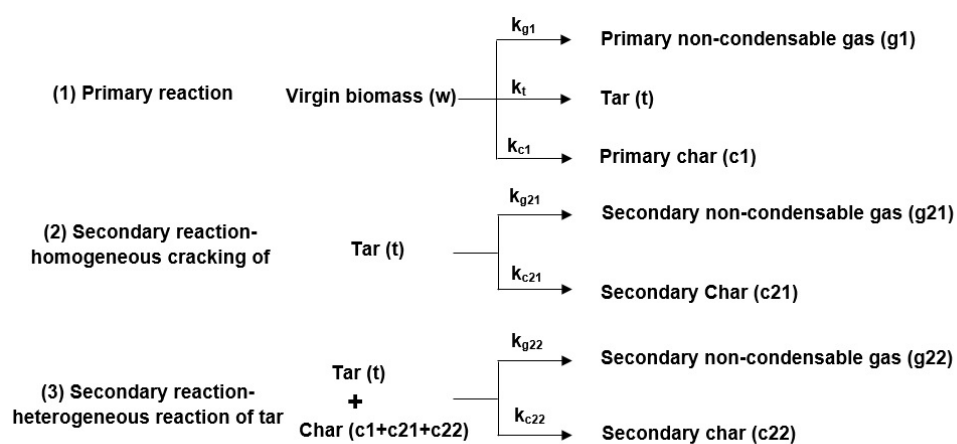


Fig. B1 The kinetic scheme in Chapter 2

Fig. B2 compares the predicted evolution of the residual solid mass fraction using the kinetics in Fig. B1 and the torrefaction kinetics used in Chapter 4. Compared to the experimental data of Basu et al.,[145] this figure shows that the pyrolysis kinetics in Fig. B1 significantly underestimate the residual solid mass loss

rate. In contrast, the prediction results with the torrefaction kinetics in Chapter 4, which is originally proposed for biomass torrefaction, are in good agreement with the experimental data. Therefore, the CPM in Chapter 4 was adapted with the torrefaction kinetic model in this chapter.

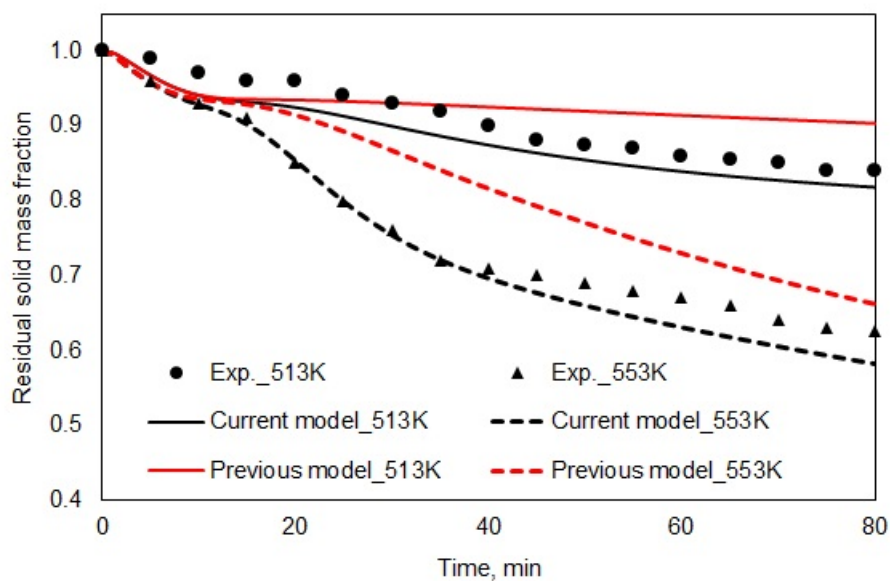


Fig. B2 Comparison of the evolutions of residual solid mass fraction with the kinetic scheme in Chapter 2 and with the torrefaction kinetic model in the Chapter 4.

APPENDIX C

The potential of including the secondary conversion of the condensable volatiles (lumped into a single component) into the modeled kinetic scheme was analyzed with a simplified CFD model. A shorter screw reactor with a length of 0.49 m was simulated. Conclusions for a longer screw reactor would be similar. An isothermal condition at a temperature of 648 K was assumed. The screw rotating frequency was the same as that in the main context.

At the inlet, solid mass flow rate (dry basis) was set to be 6.07×10^{-4} kg/s, which was equal to the mass flow rate of the dry biomass in the main context according to Eq. (C1)

$$\text{Dry solid mass flow rate} = \text{Wet solid mass flow rate} \times (1 - \text{Moisture}) \quad (\text{C1})$$

Where $\text{Wet solid mass flow rate} = 6.89 \times 10^{-4}$ kg/s, and $\text{Moisture} = 11.9$ wt. %, as described in the main context.

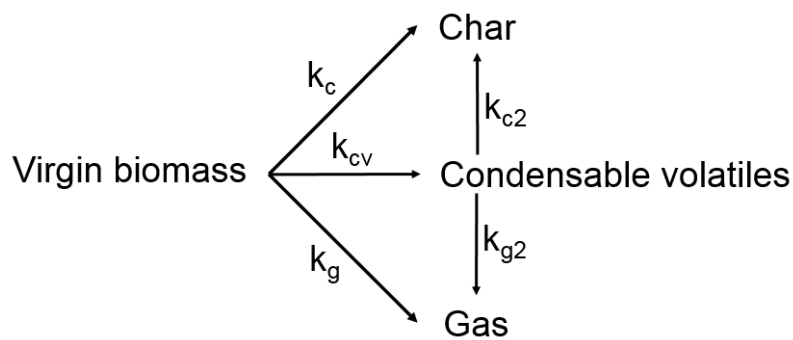
Similarly, at the inlet, the gas mass flow rate was set to be 8.47×10^{-5} kg/s, which was determined from Eq. (C2) and Eq. (C3),

$$\text{Gas mass flow rate} = N_2 \text{ mass flow rate} + \text{Moisture flow rate} \quad (\text{C2})$$

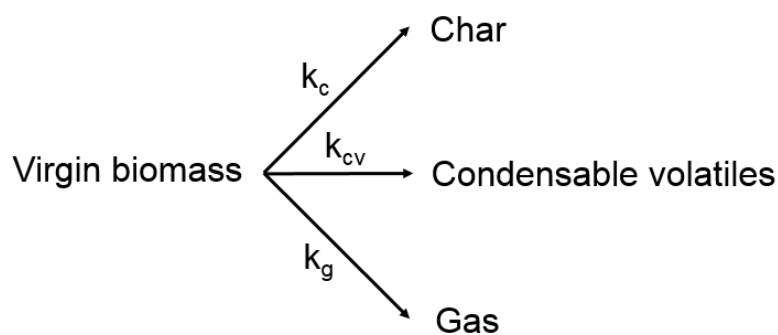
$$\text{Moisture flow rate} = \text{Wet solid mass flow rate} \times \text{Moisture} \quad (\text{C3})$$

Where $N_2 \text{ mass flow rate} = 2.72 \times 10^{-6}$ kg/s, as described in the main context.

Two simulation cases were performed. In Case 1, both the primary pyrolysis reaction kinetics of virgin biomass and the secondary reaction kinetics of the condensable volatiles were included into the CFD model, while in Case 2, only the primary pyrolysis reaction kinetics of virgin biomass were included into the CFD model. The reaction scheme for Case 1 is shown in Fig. C1(a), and for Case 2 in Fig. C1(b). In the reaction schemes in Fig. C1, the virgin biomass was regarded as a single component and products were lumped into char, condensable volatiles and gas. The kinetic parameters are shown in Table C1.



(a)



(b)

Figure C1 A simple kinetic scheme (a) with secondary reactions in Case 1 and (b) without secondary reactions in Case 2

Table C1 Kinetic parameters for primary and secondary reactions

Parameters	Expression	Reference
Primary reaction		
k_c	$3.27 \times 10^6 \exp(-111700/RT)$	Blasi and Branca[152]
k_{cv}	$1.08 \times 10^{10} \exp(-148000/RT)$	Blasi and Branca[152]
k_g	$4.38 \times 10^9 \exp(-152700/RT)$	Blasi and Branca[152]
Secondary reaction		
k_{c2}	$1.00 \times 10^6 \exp(-108000/RT)$	CD Blasi[94]
k_{g2}	$2.60 \times 10^6 \exp(-108000/RT)$	CD Blasi[94]

REFERENCE

1. IEA, International energy agency statistics, 2002.
2. Asif, M. and T. Muneer, *Energy supply, its demand and security issues for developed and emerging economies*. Renewable & Sustainable Energy Reviews, 2007. **11**(7): p. 1388-1413.
3. <http://www.theverge.com/2016/12/20/14021722/china-smog-red-alert-beijing-pollution>. 2016.
4. Armaroli, N. and V. Balzani, *The future of energy supply: Challenges and opportunities*. Angewandte Chemie-International Edition, 2007. **46**(1-2): p. 52-66.
5. Frederik, R., N. Robert W., and P. Wolter, *Carbonization of Biomass, Recent Advances in Thermo-Chemical Conversion of Biomass*. 2015: p. 293-324.
6. Routa, J., S. Kellomaki, and H. Strandman, *Effects of Forest Management on Total Biomass Production and CO₂ Emissions from use of Energy Biomass of Norway Spruce and Scots Pine*. Bioenergy Research, 2012. **5**(3): p. 733-747.
7. Vassilev, S.V., et al., *An overview of the chemical composition of biomass*. Fuel, 2010. **89**(5): p. 913-933.
8. Haberl, H., et al., *Bioenergy: how much can we expect for 2050?* Environmental Research Letters, 2013. **8**: p. 031004. doi:10.1088/1748-9326/8/3/031004.
9. Anca-Couce, A., *Reaction mechanisms and multi-scale modelling of lignocellulosic biomass pyrolysis*. Progress in Energy and Combustion Science, 2016: p. 41-79.
10. McKendry, P., *Energy production from biomass (part 1): overview of biomass*. Bioresource Technology, 2002. **83**(1): p. 37-46.
11. Sathitsuksanoh, N., A. George, and Y.H.P. Zhang, *New lignocellulose pretreatments using cellulose solvents: a review*. Journal of Chemical Technology and Biotechnology, 2013. **88**(2): p. 169-180.
12. Chaturvedi, V. and P. Verma, *An overview of key pretreatment processes employed for bioconversion of lignocellulosic biomass into biofuels and value added products*. 3 Biotech, 2013. **3**(5): p. 415-431.
13. Khan, A.A., et al., *Biomass combustion in fluidized bed boilers: Potential problems and remedies*. Fuel Processing Technology, 2009. **90**(1): p. 21-50.
14. Demirbas, A., *Potential applications of renewable energy sources, biomass combustion problems in boiler power systems and combustion related environmental issues*. Progress in Energy and Combustion Science, 2005. **31**(2): p. 171-192.

15. Bridgwater, A.V., *Review of fast pyrolysis of biomass and product upgrading*. Biomass & Bioenergy, 2012. **38**: p. 68-94.
16. Mohan, D., C.U. Pittman, and P.H. Steele, *Pyrolysis of wood/biomass for bio-oil: A critical review*. Energy & Fuels, 2006. **20**(3): p. 848-889.
17. Chen, W.H., J.H. Peng, and X.T.T. Bi, *A state-of-the-art review of biomass torrefaction, densification and applications*. Renewable & Sustainable Energy Reviews, 2015. **44**: p. 847-866.
18. Carlson, T.R., et al., *Aromatic Production from Catalytic Fast Pyrolysis of Biomass-Derived Feedstocks*. Topics in Catalysis, 2009. **52**(3): p. 241-252.
19. Li, X.T., et al., *Biomass gasification in a circulating fluidized bed*. Biomass & Bioenergy, 2004. **26**(2): p. 171-193.
20. Devi, L., K.J. Ptasinski, and F.J.J.G. Janssen, *A review of the primary measures for tar elimination in biomass gasification processes*. Biomass & Bioenergy, 2003. **24**(2): p. 125-140.
21. Funke, A. and F. Ziegler, *Hydrothermal carbonization of biomass: A summary and discussion of chemical mechanisms for process engineering*. Biofuels Bioproducts & Biorefining-Biofpr, 2010. **4**(2): p. 160-177.
22. Burguete, P., et al., *Fuel and chemicals from wet lignocellulosic biomass waste streams by hydrothermal carbonization*. Green Chemistry, 2016. **18**(4): p. 1051-1060.
23. Toor, S.S., L. Rosendahl, and A. Rudolf, *Hydrothermal liquefaction of biomass: A review of subcritical water technologies*. Energy, 2011. **36**(5): p. 2328-2342.
24. Elliott, D.C., et al., *Hydrothermal liquefaction of biomass: Developments from batch to continuous process*. Bioresource Technology, 2015. **178**: p. 147-156.
25. Yoshida, T., Y. Oshima, and Y. Matsumura, *Gasification of biomass model compounds and real biomass in supercritical water*. Biomass & Bioenergy, 2004. **26**(1): p. 71-78.
26. Zhang, Q., et al., *Review of biomass pyrolysis oil properties and upgrading research*. Energy Conversion and Management, 2007. **48**(1): p. 87-92.
27. HarpreetSinghKambo and AnimeshDutta, *A comparative review of biochar and hydrochar in terms of production, physico-chemical properties and applications*. Renewable and Sustainable Energy Reviews, 2015. **45**.
28. Antal, M.J., et al., *Attainment of the theoretical yield of carbon from biomass*. Industrial & Engineering Chemistry Research, 2000. **39**(11): p. 4024-4031.
29. Ondfej, M., R. Frederik, and D. Dane, *Biochar production and feedstock*. Biochar in European Soils and Agriculture: Science and Practice, 2016.

30. Gonzalez, J.F., et al., *Pyrolysis of various biomass residues and char utilization for the production of activated carbons*. Journal of Analytical and Applied Pyrolysis, 2009. **85**(1-2): p. 134-141.
31. Lehmann, J., *A handful of carbon*. Nature, 2007. **447**(7141): p. 143-144.
32. Bridgwater, A.V. and G.V.C. Peacocke, *Fast pyrolysis processes for biomass*. Renewable & Sustainable Energy Reviews, 2000. **4**(1): p. 1-73.
33. Qian, K.Z., et al., *Recent advances in utilization of biochar*. Renewable & Sustainable Energy Reviews, 2015. **42**: p. 1055-1064.
34. Ronsse, F., et al., *Production and characterization of slow pyrolysis biochar: influence of feedstock type and pyrolysis conditions*. Global Change Biology Bioenergy, 2013. **5**(2): p. 104-115.
35. Masek, O., et al., *Influence of production conditions on the yield and environmental stability of biochar*. Fuel, 2013. **103**: p. 151-155.
36. Crombie, K. and O. Masek, *Pyrolysis biochar systems, balance between bioenergy and carbon sequestration*. Global Change Biology Bioenergy, 2015. **7**(2): p. 349-361.
37. Masek, O., et al., *Microwave and slow pyrolysis biochar-Comparison of physical and functional properties*. Journal of Analytical and Applied Pyrolysis, 2013. **100**: p. 41-48.
38. Liu, W.J., H. Jiang, and H.Q. Yu, *Development of Biochar-Based Functional Materials: Toward a Sustainable Platform Carbon Material*. Chemical Reviews, 2015. **115**(22): p. 12251-12285.
39. Kastanaki, E. and D. Vamvuka, *A comparative reactivity and kinetic study on the combustion of coal-biomass char blends*. Fuel, 2006. **85**(9): p. 1186-1193.
40. Yilun Li, et al., *Biochar as a renewable source for high-performance CO₂ sorbent*. Carbon, 2016. **In Press**.
41. van der Stelt, M.J.C., et al., *Biomass upgrading by torrefaction for the production of biofuels: A review*. Biomass & Bioenergy, 2011. **35**(9): p. 3748-3762.
42. Williams, P.T. and S. Besler, *The influence of temperature and heating rate on the pyrolysis of biomass*. Renewable Energy, 1996. **7**(3): p. 233-250.
43. FAO, Food and Agriculture Organization of the United Nations, *FAOSTAT – ForesSTAT wood charcoal production*. faostat.fao.org, 2013. **10.03.13**.
44. Manya, J.J., *Pyrolysis for Biochar Purposes: A Review to Establish Current Knowledge Gaps and Research Needs*. Environmental Science & Technology, 2012. **46**(15): p. 7939-7954.
45. Yoshida, T. and M.J. Antal, *Sewage Sludge Carbonization for Terra Preta Applications*. Energy & Fuels, 2009. **23**: p. 5454-5459.

46. Huggins, T., et al., *Biochar as a sustainable electrode material for electricity production in microbial fuel cells*. *Bioresource Technology*, 2014. **157**: p. 114-119.
47. Kacprzak, A., et al., *The effect of fuel type on the performance of a direct Carbon fuel cell with molten alkaline electrolyte*. *Journal of Power Sources*, 2014. **255**: p. 179-186.
48. Titirici, M.M., et al., *Black perspectives for a green future: hydrothermal carbons for environment protection and energy storage*. *Energy & Environmental Science*, 2012. **5**(5): p. 6796-6822.
49. Shen, Y.F., *Chars as carbonaceous adsorbents/catalysts for tar elimination during biomass pyrolysis or gasification*. *Renewable & Sustainable Energy Reviews*, 2015. **43**: p. 281-295.
50. Schimmelpfennig, S. and B. Glaser, *One Step Forward toward Characterization: Some Important Material Properties to Distinguish Biochars*. *Journal of Environmental Quality*, 2012. **41**(4): p. 1001-1013.
51. Di Blasi, C., *Combustion and gasification rates of lignocellulosic chars*. *Progress in Energy and Combustion Science*, 2009. **35**(2): p. 121-140.
52. Meyer, S., B. Glaser, and P. Quicker, *Technical, Economical, and Climate-Related Aspects of Biochar Production Technologies: A Literature Review*. *Environmental Science & Technology*, 2011. **45**(22): p. 9473-9483.
53. Kruse, A., A. Funke, and M.M. Titirici, *Hydrothermal conversion of biomass to fuels and energetic materials*. *Current Opinion in Chemical Biology*, 2013. **17**(3): p. 515-521.
54. Boroson, M.L., et al., *Product Yields and Kinetics from the Vapor-Phase Cracking of Wood Pyrolysis Tars*. *AIChE Journal*, 1989. **35**(1): p. 120-128.
55. Pattanotai, T., H. Watanabe, and K. Okazaki, *Experimental investigation of intraparticle secondary reactions of tar during wood pyrolysis*. *Fuel*, 2013. **104**: p. 468-475.
56. Vassilev, S.V., et al., *An overview of the organic and inorganic phase composition of biomass*. *Fuel*, 2012. **94**(1): p. 1-33.
57. Yang, H.P., et al., *Characteristics of hemicellulose, cellulose and lignin pyrolysis*. *Fuel*, 2007. **86**(12-13): p. 1781-1788.
58. Wang, S.R., et al., *A study on the mechanism research on cellulose pyrolysis under catalysis of metallic salts*. *Korean Journal of Chemical Engineering*, 2007. **24**(2): p. 336-340.
59. Gronli, M., M.J. Antal, and G. Varhegyi, *A round-robin study of cellulose pyrolysis kinetics by thermogravimetry*. *Industrial & Engineering Chemistry Research*, 1999. **38**(6): p. 2238-2244.
60. Kim, U.J., S.H. Eom, and M. Wada, *Thermal decomposition of native cellulose: Influence on crystallite size*. *Polymer Degradation and Stability*, 2010. **95**(5): p. 778-781.

61. Zhang, J.X., et al., *The dependence of pyrolysis behavior on the crystal state of cellulose*. Carbohydrate Polymers, 2010. **79**(1): p. 164-169.
62. Wang, S., et al., *Structural Characterization and Pyrolysis Behavior of Cellulose and Hemicellulose Isolated from Softwood Pinus armandii Franch.* Energy & Fuels, 2016: p. In Press.
63. Quan, C., N. Gao, and Q. Song, *Pyrolysis of biomass components in a TGA and a fixed-bed reactor: Thermochemical behaviors, kinetics, and product characterization*. Journal of Analytical and Applied Pyrolysis, 2016: p. In Press.
64. Papari, S. and K. Hawboldt, *A review on the pyrolysis of woody biomass to bio-oil: Focus on kinetic models*. Renewable & Sustainable Energy Reviews, 2015. **52**: p. 1580-1595.
65. Di Blasi, C., *Modeling chemical and physical processes of wood and biomass pyrolysis*. Progress in Energy and Combustion Science, 2008. **34**(1): p. 47-90.
66. Sharma, A., V. Pareek, and D.K. Zhang, *Biomass pyrolysis—A review of modelling, process parameters and catalytic studies*. Renewable and Sustainable Energy Reviews, 2015. **50**: p. 1081-1096.
67. Shi, X., F. Ronsse, and J.G. Pieters, *Finite element modeling of intraparticle heterogeneous tar conversion during pyrolysis of woody biomass particles*. Fuel Processing Technology, 2016. **148**: p. 302-316.
68. Ranzi, E., et al., *Chemical Kinetics of Biomass Pyrolysis*. Energy & Fuels, 2008. **22**(6): p. 4292-4300.
69. Debiagi, P.E.A., et al., *Detailed kinetic mechanism of gas-phase reactions of volatiles released from biomass pyrolysis*. Biomass and Bioenergy, 2016. **93**: p. 60-71.
70. Calonaci, M., et al., *Comprehensive Kinetic Modeling Study of Bio-oil Formation from Fast Pyrolysis of Biomass*. Energy & Fuels, 2010. **24**: p. 5727-5734.
71. Corbetta, M., et al., *Pyrolysis of centimeter-scale woody biomass particles: kinetic modeling and experimental validation*. Energy & Fuels, 2014. **28**(6): p. 3884-3898.
72. Anca-Couce, A. and I. Obernberger, *Application of a detailed biomass pyrolysis kinetic scheme to hardwood and softwood torrefaction*. Fuel, 2016. **167**: p. 158-167.
73. Anca-Couce, A., et al., *Kinetic scheme of biomass pyrolysis considering secondary charring reactions*. Energy Conversion and Management, 2014. **87**: p. 687-696.
74. Sheng, C.D. and J.L.T. Azevedo, *Estimating the higher heating value of biomass fuels from basic analysis data*. Biomass & Bioenergy, 2005. **28**(5): p. 499-507.

75. Cai, J.M., W.X. Wu, and R.H. Liu, *An overview of distributed activation energy model and its application in the pyrolysis of lignocellulosic biomass*. *Renewable & Sustainable Energy Reviews*, 2014. **36**: p. 236-246.
76. Grant, D.M., et al., *Chemical-Model of Coal Devolatilization Using Percolation Lattice Statistics*. *Energy & Fuels*, 1989. **3**(2): p. 175-186.
77. Sheng, C.D. and J.L.T. Azevedo, *Modeling biomass devolatilization using the chemical percolation devolatilization model for the main components*. *Proceedings of the Combustion Institute*, 2002. **29**: p. 407-414.
78. Zobel, N. and A. Anca-Couce, *Influence of intraparticle secondary heterogeneous reactions on the reaction enthalpy of wood pyrolysis*. *Journal of Analytical and Applied Pyrolysis*, 2015. **116**: p. 281-286.
79. Antal, M.J. and G. Varhegyi, *Cellulose Pyrolysis Kinetics - the Current State Knowledge*. *Industrial & Engineering Chemistry Research*, 1995. **34**(3): p. 703-717.
80. Ahuja, P., S. Kumar, and P.C. Singh, *A model for primary and heterogeneous secondary reactions of wood pyrolysis*. *Chemical Engineering & Technology*, 1996. **19**(3): p. 272-282.
81. Sadhukhan, A.K., P. Gupta, and R.K. Saha, *Modelling of pyrolysis of large wood particles*. *Bioresource Technology*, 2009. **100**(12): p. 3134-3139.
82. Koufopoulos, C.A., et al., *Modeling of the Pyrolysis of Biomass Particles - Studies on Kinetics, Thermal and Heat-Transfer Effects*. *Canadian Journal of Chemical Engineering*, 1991. **69**(4): p. 907-915.
83. Richard B. Bates and A.F. Ghoniem, *Modeling kinetics-transport interactions during biomass torrefaction: The effects of temperature, particle size, and moisture content*. *Fuel*, 2014. **137**: p. 216-229.
84. Mašek, O., R. Frederik, and D. Dane, *Biochar production and feedstock*. *Biochar in European Soils and Agriculture: Science and Practice*, 2016.
85. Roberts, A.W., *The influence of granular vortex motion on the volumetric performance of enclosed screw conveyors*. *Powder Technology*, 1999. **104**(1): p. 56-67.
86. Waje, S.S., B.N. Thorat, and A.S. Mujumdar, *Screw conveyor dryer: Process and equipment design*. *Drying Technology*, 2007. **25**(1-3): p. 241-247.
87. Nachenius, R.W., et al., *Residence time distributions of coarse biomass particles in a screw conveyor reactor*. *Fuel Processing Technology*, 2015. **130**: p. 87-95.
88. Nachenius, R.W., et al., *Torrefaction of pine in a bench-scale screw conveyor reactor*. *Biomass & Bioenergy*, 2015. **79**: p. 96-104.
89. Boroson, M.L., et al., *Heterogeneous Cracking of Wood Pyrolysis Tars over Fresh Wood Char Surfaces*. *Energy & Fuels*, 1989. **3**(6): p. 735-740.
90. Antal, M.J. and M. Gronli, *The art, science, and technology of charcoal production*. *Industrial & Engineering Chemistry Research*, 2003. **42**(8): p. 1619-1640.

91. Lu, H., et al., *Effects of particle shape and size on devolatilization of biomass particle*. Fuel, 2010. **89**(5): p. 1156-1168.
92. Wiggins, G.M., P.N. Ciesielski, and C.S. Daw, *Low-Order Modeling of Internal Heat Transfer in Biomass Particle Pyrolysis*. Energy & Fuels, 2016. **30**(6): p. 4960-4969.
93. Di Blasi, C., *Physico-chemical processes occurring inside a degrading two-dimensional anisotropic porous medium*. International Journal of Heat and Mass Transfer, 1998. **41**(24): p. 4139-4150.
94. DiBlasi, C., *Heat, momentum and mass transport through a shrinking biomass particle exposed to thermal radiation*. Chemical Engineering Science, 1996. **51**(7): p. 1121-1132.
95. Akhtar, J. and N.S. Amin, *A review on operating parameters for optimum liquid oil yield in biomass pyrolysis*. Renewable & Sustainable Energy Reviews, 2012. **16**(7): p. 5101-5109.
96. Chen, G.X., Q.Z. Yu, and K. Sjoström, *Reactivity of char from pyrolysis of birch wood*. Journal of Analytical and Applied Pyrolysis, 1997. **40-1**: p. 491-499.
97. Mok, W.S.L. and M.J. Antal, *Effects of Pressure on Biomass Pyrolysis .2. Heats of Reaction of Cellulose Pyrolysis*. Thermochemica Acta, 1983. **68**(2-3): p. 165-186.
98. Williams, S., et al., *The fundamentals of biocarbon formation at elevated pressure: From 1851 to the 21st century*. Journal of Analytical and Applied Pyrolysis, 2015. **113**: p. 225-230.
99. Mok, W.S.L., et al., *Formation of Charcoal from Biomass in a Sealed Reactor*. Industrial & Engineering Chemistry Research, 1992. **31**(4): p. 1162-1166.
100. Ciesielski, P.N., et al., *Biomass Particle Models with Realistic Morphology and Resolved Microstructure for Simulations of Intraparticle Transport Phenomena*. Energy & Fuels, 2015. **29**(1): p. 242-254.
101. Yang, H., et al., *Simulation of the Evolution of Pressure in a Lignite Particle during Pyrolysis*. Energy & Fuels, 2014. **28**(5): p. 3511-3518.
102. Victor Pozzobon, S.S., Jean Jacques Bézian, Mouna El-Hafi, Yannick Le Maoult, Gilles Flamant, *Radiative pyrolysis of wet wood under intermediate heat flux: Experiments and modelling*. Fuel Processing Technology, 2014. **128**: p. 319-330.
103. Sharma, A., et al., *A phenomenological model of the mechanisms of lignocellulosic biomass pyrolysis processes*. Computers & Chemical Engineering, 2014. **60**: p. 231-241.
104. Paulsen, A.D., et al., *Fast Pyrolysis of Wood for Biofuels: Spatiotemporally Resolved Diffuse Reflectance In situ Spectroscopy of Particles*. Chemsuschem, 2014. **7**(3): p. 765-776.

105. Bennadji, H., et al., *Low-Temperature Pyrolysis of Woody Biomass in the Thermally Thick Regime*. Energy & Fuels, 2013. **27**(3): p. 1453-1459.
106. Lin, Y.H., et al., *Reaction-transport model for the pyrolysis of shrinking cellulose particles*. Chemical Engineering Science, 2012. **74**: p. 160-171.
107. Haseli, Y., J.A. van Oijen, and L.P.H. de Goey, *A Simplified Pyrolysis Model of a Biomass Particle Based on Infinitesimally Thin Reaction Front Approximation*. Energy & Fuels, 2012. **26**(6): p. 3230-3243.
108. Anca-Couce, A. and N. Zobel, *Numerical analysis of a biomass pyrolysis particle model: Solution method optimized for the coupling to reactor models*. Fuel, 2012. **97**: p. 80-88.
109. Sudhakar, D.R. and A.K. Kolar, *Transient Three-Dimensional Mathematical Model and Experimental Investigation of a Wet Devolatilizing Wood in a Hot Fluidized Bed*. Energy & Fuels, 2010. **24**: p. 4820-4832.
110. Park, W.C., A. Atreya, and H.R. Baum, *Experimental and theoretical investigation of heat and mass transfer processes during wood pyrolysis*. Combustion and Flame, 2010. **157**(3): p. 481-494.
111. Yuen, R.K.K., et al., *Modelling the pyrolysis of wet wood - I. Three-dimensional formulation and analysis*. International Journal of Heat and Mass Transfer, 2007. **50**(21-22): p. 4371-4386.
112. Chan, R. and B.B. Krieger, *Modeling of Physical and Chemical Processes during Pyrolysis of a Large Biomass Pellet with Experimental-Verification*. Abstracts of Papers of the American Chemical Society, 1983. **186**(Aug): p. 84-Fuel.
113. Haseli, Y., J.A. van Oijen, and L.P.H. de Goey, *Predicting the pyrolysis of single biomass particles based on a time and space integral method*. Journal of Analytical and Applied Pyrolysis, 2012. **96**: p. 126-138.
114. Gomez-Barea, A. and B. Leckner, *Modeling of biomass gasification in fluidized bed*. Progress in Energy and Combustion Science, 2010. **36**(4): p. 444-509.
115. Biswas, A.K. and K. Umeki, *Simplification of devolatilization models for thermally-thick particles: Differences between wood logs and pellets*. Chemical Engineering Journal, 2015. **274**: p. 181-191.
116. Wasan, S.R., et al., *Application of a simple enthalpy-based pyrolysis model in numerical simulations of pyrolysis of charring materials*. Fire and Materials, 2010. **34**(1): p. 39-54.
117. Park, W.C., A. Atreya, and H.R. Baum, *Determination of pyrolysis temperature for charring materials*. Proceedings of the Combustion Institute, 2009. **32**: p. 2471-2479.
118. Theuns, E., et al., *Critical evaluation of an integral model for the pyrolysis of charring materials*. Fire Safety Journal, 2005. **40**(2): p. 121-140.

119. Galgano, A. and C. Di Blasi, *Infinite- versus finite-rate kinetics in simplified models of wood pyrolysis*. Combustion Science and Technology, 2005. **177**(2): p. 279-303.
120. Chen, Y., M.A. Delichatsios, and V. Motevalli, *Material Pyrolysis Properties .1. An Integral Model for One-Dimensional Transient Pyrolysis of Charring and Non-Charring Materials*. Combustion Science and Technology, 1993. **88**(5-6): p. 309-328.
121. Theuns, E., J. Vierendeels, and P. Vandeveldel, *Validation of the integral model for the pyrolysis of charring materials with a moving grid*. Journal of Computational and Applied Mathematics, 2004. **168**(1-2): p. 471-479.
122. Galgano, A. and C. Di Blasi, *Modeling wood degradation by the unreacted-core-shrinking approximation*. Industrial & Engineering Chemistry Research, 2003. **42**(10): p. 2101-2111.
123. L. Orefice and J.G. Khinast, *DEM study of granular transport in partially filled horizontal screw conveyors*. Powder Technology, 2016. **305**: p. 347-356.
124. Owen, P.J. and P.W. Cleary, *Prediction of screw conveyor performance using the Discrete Element Method (DEM)*. Powder Technology, 2009. **193**(3): p. 274-288.
125. Hou, Q.F., K.J. Dong, and A.B. Yu, *DEM study of the flow of cohesive particles in a screw feeder*. Powder Technology, 2014. **256**: p. 529-539.
126. Zhu, H.P., et al., *Discrete particle simulation of particulate systems: A review of major applications and findings*. Chemical Engineering Science, 2008. **63**(23): p. 5728-5770.
127. Shi, X.G., et al., *Effects of the riser exit geometries on the hydrodynamics and solids back-mixing in CFB risers: 3D simulation using CPFD approach*. Powder Technology, 2015. **284**: p. 130-142.
128. Lan, X.Y., et al., *CFD modeling of gas-solid flow and cracking reaction in two-stage riser FCC reactors*. Chemical Engineering Science, 2009. **64**(17): p. 3847-3858.
129. Aramideh, S., et al., *Numerical simulation of biomass fast pyrolysis in an auger reactor*. Fuel, 2015. **156**: p. 234-242.
130. Huang, Y., et al., *Simultaneous Maximization of the Char Yield and Volatility of Oil from Biomass Pyrolysis*. Energy & Fuels, 2013. **27**(1): p. 247-254.
131. Ronsse, F., et al., *Secondary Reactions of Levoglucosan and Char in the Fast Pyrolysis of Cellulose*. Environmental Progress & Sustainable Energy, 2012. **31**(2): p. 256-260.
132. Morf, P., P. Hasler, and T. Nussbaumer, *Mechanisms and kinetics of homogeneous secondary reactions of tar from continuous pyrolysis of wood chips*. Fuel, 2002. **81**(7): p. 843-853.

133. Hoekstra, E., et al., *Heterogeneous and homogeneous reactions of pyrolysis vapors from pine wood*. AIChE Journal, 2012. **58**(9): p. 2830-2842.
134. Antal, M.J., *Effects of Reactor Severity on the Gas-Phase Pyrolysis of Cellulose-Derived and Kraft Lignin-Derived Volatile Matter*. Industrial & Engineering Chemistry Product Research and Development, 1983. **22**(2): p. 366-375.
135. Chan, W.C.R., M. Kelbon, and B. Kriegerbrockett, *Single-Particle Biomass Pyrolysis - Correlations of Reaction-Products with Process Conditions*. Industrial & Engineering Chemistry Research, 1988. **27**(12): p. 2261-2275.
136. Pattanotai, T., H. Watanabe, and K. Okazaki, *Gasification characteristic of large wood chars with anisotropic structure*. Fuel, 2014. **117**: p. 331-339.
137. Pattanotai, T., H. Watanabe, and K. Okazaki, *Effects of particle aspect ratio on pyrolysis and gasification of anisotropic wood cylinder*. Fuel, 2015. **150**(15).
138. Ciuta, S., et al., *Biomass energy behavior study during pyrolysis process by intraparticle gas sampling*. Journal of Analytical and Applied Pyrolysis, 2014. **108**: p. 316-322.
139. Babu, B.V. and A.S. Chaurasia, *Heat transfer and kinetics in the pyrolysis of shrinking biomass particle*. Chemical Engineering Science, 2004. **59**(10): p. 1999-2012.
140. Babu, B.V. and A.S. Chaurasia, *Dominant design variables in pyrolysis of biomass particles of different geometries in thermally thick regime*. Chemical Engineering Science, 2004. **59**(3): p. 611-622.
141. Babu, B.V. and A.S. Chaurasia, *Modeling, simulation and estimation of optimum parameters in pyrolysis of biomass*. Energy Conversion and Management, 2003. **44**(13): p. 2135-2158.
142. Babu, B.V. and A.S. Chaurasia, *Parametric study of thermal and thermodynamic properties on pyrolysis of biomass in thermally thick regime*. Energy Conversion and Management, 2004. **45**(1): p. 53-72.
143. Babu, B.V. and A.S. Chaurasia, *Pyrolysis of biomass: improved models for simultaneous kinetics and transport of heat, mass and momentum*. Energy Conversion and Management, 2004. **45**(9-10): p. 1297-1327.
144. Sadhukhan, A.K., P. Gupta, and R.K. Saha, *Modelling and experimental studies on pyrolysis of biomass particles*. Journal of Analytical and Applied Pyrolysis, 2008. **81**(2): p. 183-192.
145. Basu, P., et al., *An experimental and theoretical investigation on torrefaction of a large wet wood particle*. Bioresource Technology, 2014. **159**: p. 215-222.
146. Chan, W.C.R., M. Kelbon, and B.B. Krieger, *Modeling and Experimental-Verification of Physical and Chemical Processes during Pyrolysis of a Large Biomass Particle*. Fuel, 1985. **64**(11): p. 1505-1513.

147. Lee, C.K., R.F. Chaiken, and J.M. Singer, *Charring pyrolysis of wood in fires by laser simulation*. Symposium (International) on Combustion, 1977. **16**.
148. Gronli, M.G. and M.C. Melaaen, *Mathematical model for wood pyrolysis - Comparison of experimental measurements with model predictions*. Energy & Fuels, 2000. **14**(4): p. 791-800.
149. Yang, H., et al., *Estimation of Enthalpy of Bio-Oil Vapor and Heat Required for Pyrolysis of Biomass*. Energy & Fuels, 2013. **27**(5): p. 2675-2686.
150. MG, G., *A theoretical and experimental study of the thermal degradation of biomass*. PhD thesis, Norwegian University of Science and Technology, 1996.
151. Vanholme, B., et al., *Towards a carbon-negative sustainable bio-based economy*. Frontiers in Plant Science, 2013. **4**.
152. Di Blasi, C. and C. Branca, *Kinetics of primary product formation from wood pyrolysis*. Industrial & Engineering Chemistry Research, 2001. **40**(23): p. 5547-5556.
153. Liden, A.G., F. Berruti, and D.S. Scott, *A Kinetic-Model for the Production of Liquids from the Flash Pyrolysis of Biomass*. Chemical Engineering Communications, 1988. **65**: p. 207-221.
154. Diblasi, C., *Analysis of Convection and Secondary Reaction Effects within Porous Solid Fuels Undergoing Pyrolysis*. Combustion Science and Technology, 1993. **90**(5-6): p. 315-340.
155. Crombie, K. and O. Masek, *Investigating the potential for a self-sustaining slow pyrolysis system under varying operating conditions*. Bioresource Technology, 2014. **162**: p. 148-156.
156. Kloekhorst, A., J. Wildschut, and H.J. Heeres, *Catalytic hydrotreatment of pyrolytic lignins to give alkylphenolics and aromatics using a supported Ru catalyst*. Catalysis Science & Technology, 2014. **4**(8): p. 2367-2377.
157. Millington, R. and J. Quirk, *Permeability of porous solids*. Transactions of the Faraday Society 1961. **57**.
158. Poling, B., J. Prausnitz, and J. O'connell, *The properties of gases and liquids*. New York: McGraw-Hill, 2001.
159. Yildiz, G., et al., *Effect of biomass ash in catalytic fast pyrolysis of pine wood*. Applied Catalysis B-Environmental, 2015. **168**: p. 203-211.
160. William Simpson, A.T., *Physical properties and moisture relations of wood*. 1999.
161. Di Blasi, C., *Modeling intra- and extra-particle processes of wood fast pyrolysis*. AIChE Journal, 2002. **48**(10): p. 2386-2397.
162. Haseli, Y., J.A. van Oijen, and L.P.H. de Goey, *Modeling biomass particle pyrolysis with temperature-dependent heat of reactions*. Journal of Analytical and Applied Pyrolysis, 2011. **90**(2): p. 140-154.
163. Di Blasi, C., et al., *Experimental Analysis of Reaction Heat Effects during Beech Wood Pyrolysis*. Energy & Fuels, 2013. **27**(5): p. 2665-2674.

164. Scala, F., *Attrition during steam gasification of lignite char in a fluidized bed reactor*. Fuel Processing Technology, 2015. **In Press**.
165. Scala, F., R. Chirone, and P. Salatino, *Combustion and attrition of biomass chars in a fluidized bed*. Energy & Fuels, 2006. **20**(1): p. 91-102.
166. Li, T., et al., *Experimental and Modeling Study of the Effect of Torrefaction on the Rapid Devolatilization of Biomass*. Energy & Fuels, 2015. **29**(7): p. 4328-4338.
167. Stahl, M., et al., *Industrial processes for biomass drying and their effects on the quality properties of wood pellets*. Biomass & Bioenergy, 2004. **27**(6): p. 621-628.
168. Song, Y., et al., *Importance of the aromatic structures in volatiles to the in-situ destruction of nascent tar during the volatile-char interactions*. Fuel Processing Technology, 2015. **132**: p. 31-38.
169. Jinje Park, Yongwoon Lee, and C. Ryu, *Reduction of primary tar vapor from biomass by hot char particles in fixed bed gasification*. Biomass and Bioenergy, 2016. **90**: p. 114–121.
170. Dieguez-Alonso, A., et al., *Understanding the primary and secondary slow pyrolysis mechanisms of holocellulose, lignin and wood with laser-induced fluorescence*. Fuel, 2015. **153**: p. 102-109.
171. Milosavljevic, I., V. Oja, and E.M. Suuberg, *Thermal effects in cellulose pyrolysis: Relationship to char formation processes*. Industrial & Engineering Chemistry Research, 1996. **35**(3): p. 653-662.
172. Mok, W.S.L. and M.J. Antal, *Effects of Pressure on Biomass Pyrolysis .I. Cellulose Pyrolysis Products*. Thermochemica Acta, 1983. **68**(2-3): p. 155-164.
173. Volker, S. and T. Rieckmann, *Thermokinetic investigation of cellulose pyrolysis - impact of initial and final mass on kinetic results*. Journal of Analytical and Applied Pyrolysis, 2002. **62**(2): p. 165-177.
174. Shafizadeh, F., *Introduction to Pyrolysis of Biomass*. Journal of Analytical and Applied Pyrolysis, 1982. **3**(4): p. 283-305.
175. Varhegyi, G., et al., *TG, TG-MS, and FTIR characterization of high-yield biomass charcoals*. Energy & Fuels, 1998. **12**(5): p. 969-974.
176. Huang, Y., et al., *Interactions between Volatiles and Char during Pyrolysis of Biomass: Reactive Species Determining and Reaction over Functionalized Carbon Nanotubes*. Energy & Fuels, 2016: p. In Press.
177. Gao, J.S., et al., *Advanced model for turbulent gas-solid flow and reaction in FCC riser reactors*. AIChE Journal, 1999. **45**(5): p. 1095-1113.
178. Zhong, H.B., et al., *Multi-fluid model with variable particle density and diameter based on mass conservation at the particle scale*. Powder Technology, 2016. **294**: p. 43-54.
179. Zhong, H., et al., *Multi-fluid Modeling Biomass Fast Pyrolysis in the Fluidized Bed Reactor Including Particle Shrinkage Effects*. Energy & Fuels, 2016: p. In Press.

180. Bruchmuller, J., et al., *Modeling the thermochemical degradation of biomass inside a fast pyrolysis fluidized bed reactor*. *AIChE Journal*, 2012. **58**(10): p. 3030-3042.
181. Blondeau, J. and H. Jeanmart, *Biomass pyrolysis at high temperatures: Prediction of gaseous species yields from an anisotropic particle*. *Biomass & Bioenergy*, 2012. **41**: p. 107-121.
182. Vinu, R. and L.J. Broadbelt, *A mechanistic model of fast pyrolysis of glucose-based carbohydrates to predict bio-oil composition*. *Energy & Environmental Science*, 2012. **5**(12): p. 9808-9826.
183. Ranzi, E., et al., *Kinetic modeling of the thermal degradation and combustion of biomass*. *Chemical Engineering Science*, 2014. **110**(0): p. 2-12.
184. Koufopoulos, C.A., G. Maschio, and A. Lucchesi, *Kinetic Modeling of the Pyrolysis of Biomass and Biomass Components*. *Canadian Journal of Chemical Engineering*, 1989. **67**(1): p. 75-84.
185. Pyle, D.L. and C.A. Zaror, *Heat-Transfer and Kinetics in the Low-Temperature Pyrolysis of Solids*. *Chemical Engineering Science*, 1984. **39**(1): p. 147-158.
186. Chew, J.J. and V. Doshi, *Recent advances in biomass pretreatment - Torrefaction fundamentals and technology*. *Renewable & Sustainable Energy Reviews*, 2011. **15**(8): p. 4212-4222.
187. Bridgeman, T.G., et al., *Torrefaction of reed canary grass, wheat straw and willow to enhance solid fuel qualities and combustion properties*. *Fuel*, 2008. **87**(6): p. 844-856.
188. Chen, W.H., et al., *Thermal pretreatment of wood (Lauan) block by torrefaction and its influence on the properties of the biomass*. *Energy*, 2011. **36**(5): p. 3012-3021.
189. Saleh, S.B., et al., *Efficient Fuel Pretreatment: Simultaneous Torrefaction and Grinding of Biomass*. *Energy & Fuels*, 2013. **27**(12): p. 7531-7540.
190. Via, B.K., S. Adhikari, and S. Taylor, *Modeling for proximate analysis and heating value of torrefied biomass with vibration spectroscopy*. *Bioresource Technology*, 2013. **133**: p. 1-8.
191. Di Blasi, C., et al., *Role of Pretreatments in the Thermal Runaway of Hazelnut Shell Pyrolysis*. *Energy & Fuels*, 2015. **29**(4): p. 2514-2526.
192. Grigante, M. and D. Antolini, *Mass yield as guide parameter of the torrefaction process. An experimental study of the solid fuel properties referred to two types of biomass*. *Fuel*, 2015. **153**: p. 499-509.
193. Strandberg, M., et al., *Effects of temperature and residence time on continuous torrefaction of spruce wood*. *Fuel Processing Technology*, 2015. **134**: p. 387-398.

194. Gronnow, M.J., et al., *Torrefaction/biochar production by microwave and conventional slow pyrolysis - comparison of energy properties*. *Global Change Biology Bioenergy*, 2013. **5**(2): p. 144-152.
195. Couhert, C., S. Salvador, and J.M. Commandre, *Impact of torrefaction on syngas production from wood*. *Fuel*, 2009. **88**(11): p. 2286-2290.
196. Chen, W.H., et al., *Product characteristics from the torrefaction of oil palm fiber pellets in inert and oxidative atmospheres*. *Bioresource Technology*, 2016. **199**: p. 367-374.
197. Tapasvi, D., et al., *Torrefaction of Norwegian Birch and Spruce: An Experimental Study Using Macro-TGA*. *Energy & Fuels*, 2012. **26**(8): p. 5232-5240.
198. Chen, W.H., et al., *A comparison of gasification phenomena among raw biomass, torrefied biomass and coal in an entrained-flow reactor*. *Applied Energy*, 2013. **112**: p. 421-430.
199. Deng, J., et al., *Pretreatment of agricultural residues for co-gasification via torrefaction*. *Journal of Analytical and Applied Pyrolysis*, 2009. **86**(2): p. 331-337.
200. Prins, M.J., K.J. Ptasinski, and F.J.J.G. Janssen, *More efficient biomass gasification via torrefaction*. *Energy*, 2006. **31**(15): p. 3458-3470.
201. Gil, M.V., et al., *Grindability and combustion behavior of coal and torrefied biomass blends*. *Bioresource Technology*, 2015. **191**: p. 205-212.
202. Li, J., et al., *Co-firing based on biomass torrefaction in a pulverized coal boiler with aim of 100% fuel switching*. *Applied Energy*, 2012. **99**: p. 344-354.
203. Du, S.W., W.H. Chen, and J.A. Lucas, *Pretreatment of biomass by torrefaction and carbonization for coal blend used in pulverized coal injection*. *Bioresource Technology*, 2014. **161**: p. 333-339.
204. Peng, J.H., et al., *A Study of Particle Size Effect on Biomass Torrefaction and Densification*. *Energy & Fuels*, 2012. **26**(6): p. 3826-3839.
205. Kamil, K., et al., *Pyrolysis and gasification of a thermally thick wood particle – Effect of fragmentation*. *Fuel*, 2014. **132**: p. 125-134.
206. Haseli, Y., J.A. van Oijen, and L.P.H. de Goey, *Numerical study of the conversion time of single pyrolyzing biomass particles at high heating conditions*. *Chemical Engineering Journal*, 2011. **169**(1-3): p. 299-312.
207. Dufour, A., et al., *Modelling intra-particle phenomena of biomass pyrolysis*. *Chemical Engineering Research & Design*, 2011. **89**(10A): p. 2136-2146.
208. Turner, I., et al., *An experimental and theoretical investigation of the thermal treatment of wood (*Fagus sylvatica* L.) in the range 200-260 degrees C*. *International Journal of Heat and Mass Transfer*, 2010. **53**(4): p. 715-725.
209. Sadhukhan, A.K., P. Gupta, and R.K. Saha, *Modelling of combustion characteristics of high ash coal char particles at high pressure: Shrinking reactive core model*. *Fuel*, 2010. **89**(1): p. 162-169.

210. Sand, U., et al., *Numerical prediction of the transport and pyrolysis in the interior and surrounding of dry and wet wood log*. Applied Energy, 2008. **85**(12): p. 1208-1224.
211. Bharadwaj, A., L.L. Baxter, and A.L. Robinson, *Effects of intraparticle heat and mass transfer on biomass devolatilization: Experimental results and model predictions*. Energy & Fuels, 2004. **18**(4): p. 1021-1031.
212. Bryden, K.M. and M.J. Hagge, *Modeling the combined impact of moisture and char shrinkage on the pyrolysis of a biomass particle*. Fuel, 2003. **82**(13): p. 1633-1644.
213. Larfeldt, J., B. Leckner, and M.C. Melaaen, *Modelling and measurements of the pyrolysis of large wood particles*. Fuel, 2000. **79**(13): p. 1637-1643.
214. Janse, A.M.C., R.W.J. Westerhout, and W. Prins, *Modelling of flash pyrolysis of a single wood particle*. Chemical Engineering and Processing, 2000. **39**(3): p. 239-252.
215. Grønli, M.G., *A theoretical and experimental study of the thermal degradation of biomass*. Ph.D. thesis, The Norwegian University of Science and Technology, 1996.
216. Granados, D.A., F. Chejne, and P. Basu, *A two dimensional model for torrefaction of large biomass particles*. Journal of Analytical and Applied Pyrolysis, 2016. **120**: p. 1-14.
217. DiBlasi, C. and M. Lanzetta, *Intrinsic kinetics of isothermal xylan degradation in inert atmosphere*. Journal of Analytical and Applied Pyrolysis, 1997. **40-1**: p. 287-303.
218. Prins, M.J., *Thermodynamic analysis of biomass gasification and torrefaction*. PhD thesis, Eindhoven University of Technology, 2005.
219. Prins, M.J., K.J. Ptasinski, and F.J.J.G. Janssen, *Torrefaction of wood - Part 1. Weight loss kinetics*. Journal of Analytical and Applied Pyrolysis, 2006. **77**(1): p. 28-34.
220. Kersten, S.R.A., et al., *Biomass pyrolysis in a fluidized bed reactor. Part 1: Literature review and model simulations*. Industrial & Engineering Chemistry Research, 2005. **44**(23): p. 8773-8785.
221. MJC, V.d.S., *Chemistry and reaction kinetics of biowaste torrefaction*. PhD thesis, Eindhoven University of Technology, 2011.
222. Branca, C. and C.D. Blasi, *A summative model for the pyrolysis reaction heats of beech wood*. Thermochemica Acta, 2016. **638**: p. 10-16.
223. Waje, S.S., B.N. Thorat, and A.S. Mujumdar, *Hydrodynamic characteristics of a pilot-scale screw conveyor dryer*. Drying Technology, 2007. **25**(4-6): p. 609-616.
224. Ingram, L., et al., *Pyrolysis of wood and bark in an auger reactor: Physical properties and chemical analysis of the produced bio-oils*. Energy & Fuels, 2008. **22**(1): p. 614-625.

225. Brown, J.N. and R.C. Brown, *Process optimization of an auger pyrolyzer with heat carrier using response surface methodology*. Bioresource Technology, 2012. **103**(1): p. 405-414.
226. Liaw, S.S., et al., *Effect of pyrolysis temperature on the yield and properties of bio-oils obtained from the auger pyrolysis of Douglas Fir wood*. Journal of Analytical and Applied Pyrolysis, 2012. **93**: p. 52-62.
227. Liaw, S.S., et al., *Effect of pretreatment temperature on the yield and properties of bio-oils obtained from the auger pyrolysis of Douglas fir wood*. Fuel, 2013. **103**: p. 672-682.
228. Ronsse, F., R.W. Nachenius, and W. Prins, *Carbonization of Biomass, Recent Advances in Thermo-Chemical Conversion of Biomass*. 2015: p. 293-324.
229. Pfitzer, C., et al., *Fast Pyrolysis of Wheat Straw in the Bioliq Pilot Plant*. Energy & Fuels, 2016. **30**(10): p. 8047-8054.
230. Anca-Couce, A., *Reaction mechanisms and multi-scale modelling of lignocellulosic biomass pyrolysis*. Progress in Energy and Combustion Science, 2016. **53**: p. 41-79.
231. Waje, S.S., et al., *Study of residence time distribution in a pilot-scale screw conveyor dryer*. Drying Technology, 2007. **25**(1-3): p. 249-259.
232. Lu, H.L. and D. Gidaspow, *Hydrodynamic simulations of gas-solid flow in a riser*. Industrial & Engineering Chemistry Research, 2003. **42**(11): p. 2390-2398.
233. Yang, N., et al., *CFD simulation of concurrent-up gas-solid flow in circulating fluidized beds with structure-dependent drag coefficient*. Chemical Engineering Journal, 2003. **96**(1-3): p. 71-80.
234. Deen, N.C., et al., *Numerical Analysis of Solids Mixing in Pressurized Fluidized Beds*. Industrial & Engineering Chemistry Research, 2010. **49**(11): p. 5246-5253.
235. Shimizu, Y. and P.A. Cundall, *Three-dimensional DEM simulations of bulk handling by screw conveyors*. Journal of Engineering Mechanics-Asce, 2001. **127**(9): p. 864-872.
236. Moysey, P.A. and M.R. Thompson, *Modelling the solids inflow and solids conveying of single-screw extruders using the discrete element method*. Powder Technology, 2005. **153**(2): p. 95-107.
237. Cleary, P.W., *DEM modelling of particulate flow in a screw feeder*. Progress in Computational Fluid Dynamics, 2007. **7**(2-4): p. 128-138.
238. Fernandez, J.W., P.W. Cleary, and W. McBride, *Effect of screw design on hopper drawdown of spherical particles in a horizontal screw feeder*. Chemical Engineering Science, 2011. **66**(22): p. 5585-5601.
239. Ding, J. and D. Gidaspow, *A Bubbling Fluidization Model Using Kinetic-Theory of Granular Flow*. AIChE Journal, 1990. **36**(4): p. 523-538.

240. van Wachem, B.G.M., et al., *Comparative analysis of CFD models of dense gas-solid systems*. AIChE Journal, 2001. **47**(5): p. 1035-1051.
241. Gao, J.S., et al., *CFD simulation of gas solid flow in FCC strippers*. Chemical Engineering Science, 2008. **63**(7): p. 1827-1841.
242. *Help File*. ANSYS Fluent.
243. Tsai, W.R. and C.I. Lin, *On the Mixing of Granular-Materials in a Screw Feeder*. Powder Technology, 1994. **80**(2): p. 119-126.
244. Ogawa, S., A. Umemura, and N. Oshima, *On the Equations of Fully Fluidized Granular-Materials*. Zeitschrift Fur Angewandte Mathematik Und Physik, 1980. **31**(4): p. 483-493.
245. Lun, C.K.K., et al., *Kinetic Theories for Granular Flow - Inelastic Particles in Couette-Flow and Slightly Inelastic Particles in a General Flowfield*. Journal of Fluid Mechanics, 1984. **140**(Mar): p. 223-256.
246. Choi, B.S., et al., *Residence time distributions in a stirred tank: Comparison of CFD predictions with experiment*. Industrial & Engineering Chemistry Research, 2004. **43**(20): p. 6548-6556.
247. Liu, Y.J., et al., *CFD simulation of gas and solids mixing in FCC strippers*. AIChE Journal, 2012. **58**(4): p. 1119-1132.
248. Hua, L.N., J.W. Wang, and J.H. Li, *CFD simulation of solids residence time distribution in a CFB riser*. Chemical Engineering Science, 2014. **117**: p. 264-282.
249. Zhong, H.B., et al., *Multi-fluid Modeling Biomass Fast Pyrolysis in the Fluidized-Bed Reactor Including Particle Shrinkage Effects*. Energy & Fuels, 2016. **30**(8): p. 6440-6447.
250. Mellin, P., E. Kantarelis, and W.H. Yang, *Computational fluid dynamics modeling of biomass fast pyrolysis in a fluidized bed reactor, using a comprehensive chemistry scheme*. Fuel, 2014. **117**: p. 704-715.
251. Ranganathan, P. and S. Gu, *Computational fluid dynamics modelling of biomass fast pyrolysis in fluidised bed reactors, focusing different kinetic schemes*. Bioresource Technology, 2016. **213**: p. 333-341.
252. Papadakis, K., et al., *Application of CFD to model fast pyrolysis of biomass*. Fuel Processing Technology, 2009. **90**(4): p. 504-512.
253. Sharma, A., et al., *Multi-fluid reactive modeling of fluidized bed pyrolysis process*. Chemical Engineering Science, 2015. **123**: p. 311-321.
254. Xue, Q., T.J. Heindel, and R. Fox, *A CFD model for biomass fast pyrolysis in fluidized-bed reactors*. Chemical Engineering Science, 2011. **66**(11): p. 2440-2452.
255. Xiong, Q.G., et al., *Coupling DAEM and CFD for simulating biomass fast pyrolysis in fluidized beds*. Journal of Analytical and Applied Pyrolysis, 2016. **117**: p. 176-181.
256. Jones, M., *The Grass Crop: The Physiological basis of production*. 1988: p. 210.

257. ANSYS Fluent.
258. Xiong, Q.G., S.C. Kong, and A. Passalacqua, *Development of a generalized numerical framework for simulating biomass fast pyrolysis in fluidized-bed reactors*. Chemical Engineering Science, 2013. **99**: p. 305-313.
259. Bates, R.B. and A.F. Ghoniem, *Biomass torrefaction: Modeling of reaction thermochemistry*. Bioresource Technology, 2013. **134**: p. 331-340.
260. Tillman, D.A., *Wood as an energy resource*, Academic Press, New York 1978.
261. Chen, W.H., K.M. Lu, and C.M. Tsai, *An experimental analysis on property and structure variations of agricultural wastes undergoing torrefaction*. Applied Energy, 2012. **100**: p. 318-325.
262. Park, S.W., et al., *Torrefaction and low-temperature carbonization of woody biomass: Evaluation of fuel characteristics of the products*. Energy, 2012. **45**(1): p. 676-685.
263. Cordero, T., et al., *Predicting heating values of lignocellulosics and carbonaceous materials from proximate analysis*. Fuel, 2001. **80**(11): p. 1567-1571.
264. Prins, M.J., K.J. Ptasinski, and F.J.J.G. Janssen, *Torrefaction of wood - Part 2. Analysis of products*. Journal of Analytical and Applied Pyrolysis, 2006. **77**(1): p. 35-40.
265. Peng, J.H., et al., *Development of Torrefaction Kinetics for British Columbia Softwoods*. International Journal of Chemical Reactor Engineering, 2012. **10**.

Acknowledgements

I would like to take a few words to express my sincere gratitude to all those who gave me help and support during my doctoral study in Ghent University.

First of all, I would like to express my sincere gratitude to my academic promoters Prof. Jan Pieters and Prof. Frederik Ronsse for their continuous support during my doctoral research. They gave me freedom to carry out a research topic on the field that I wanted. They gave me constructive comments for performing my research work. Their academic experience and immense knowledge always guided me at all stages of my doctoral study.

The kind help from Prof. Jinsen Gao and Prof. Xingying Lan in China University of Petroleum (Beijing) are always acknowledged for my access to the computational resources in their group. My fellow colleagues from the Department of Biosystems Engineering, Ramadan, Dieter, Zuoyi, Lut, Dongdong, Mingsheng, Junfeng, Xinyu, Robert, Luis and others, you are the ones that make my doctoral life rememberable. And my gratitude also goes to Dr. Andrés Anca-Couce in Graz University of Technology, and he has given me constructive instructions to improve my research work.

I would like to give my gratitude to my family, and their supports are always the power that drives me forward.

Thanks for the financial support from China Scholarship Council (CSC) and from the Special Research Fund (BOF) in Ghent University.

Curriculum Vitae

Xiaogang Shi

Date of Birth: February 26, 1987

Citizenship: Chinese

Email: gang.xiao.shi@gmail.com

shixiaogang68@126.com

Education

- | | |
|--------------------------|--|
| September 2013- | PhD candidate in Applied Biological Sciences: Chemistry and Bioprocess Technology
Department of Biosystems Engineering
Faculty of Bioscience Engineering
Ghent University, Ghent, Belgium
Supervisor: Prof. dr. ir. Jan Pieters
Prof. dr. ir. Frederik Ronsse |
| September 2010-July 2013 | Master of Science (M.Sc.) in Chemical Engineering
Faculty of Chemical Engineering
China University of Petroleum (Beijing), Beijing, China
Supervisor: Prof. Xingying Lan
Prof. Jinsen Gao |
| September 2006-July 2010 | Bachelor of Science (B.Sc.) in Chemical Engineering
Faculty of Chemical Engineering
China University of Petroleum (East China), Qingdao, China
Supervisor: Prof. Chunyi Li |
| September 2007-July 2010 | Bachelor of Arts (B.A.) in English Language and Literature
Faculty of Arts
China University of Petroleum (East China), Qingdao, China |

Scientific publications

A1 (Articles in international journals with peer review, listed in ISI-Web of Science)

(1) **Xiaogang Shi**, Frederik Ronsse, Jan G. Pieters. Space-time integral method for simplifying the modeling of torrefaction of a centimeter-sized biomass particle. *Journal of Analytical and Applied Pyrolysis*, 2017, 124: 486-498 (Impact Factor=3.652, Q1 in the categories of Analytical Chemistry)

(2) **Xiaogang Shi**, Frederik Ronsse, Jan G. Pieters. Finite element modeling of intraparticle heterogeneous tar conversion during pyrolysis of woody biomass particles. *Fuel Processing Technology*, 2016, 148: 302-316. (Impact Factor=3.847, Q1 in the category of Chemical Engineering)

(3) **Xiaogang Shi**, Yingya Wu, Min Wang, Linying Lv, Jinsen Gao, Xingying Lan. Physicochemical Processes Occurring inside Clusters Consisting of FCC Catalyst Particles. *Chemical Engineering & Technology*, 2017, 40:847-853. (Impact Factor=2.385, Q2 in the category of Chemical Engineering)

(4) **Xiaogang Shi**, Yingya Wu, Xingying Lan, Feng Liu, Jinsen Gao. Effects of the riser exit geometries on the hydrodynamics and solids back-mixing in CFB risers: 3D simulation using CPFD approach. *Powder Technology*, 2015, 284:130-142. (Impact Factor=2.759, Q1 in the category of Chemical Engineering)

(5) **Xiaogang Shi**, Renjin Sun, Xingying Lan, Feng Liu, Yinghui Zhang, Jinsen Gao. CPFD simulation of solids residence time and back-mixing in CFB risers. *Powder Technology*, 2015, 271: 16 – 25. (Impact Factor=2.759, Q1 in the category of Chemical Engineering)

(6) **Xiaogang Shi**, Xingying Lan, Feng Liu, Yinghui Zhang, Jinsen Gao. Effect of particle size distribution on hydrodynamics and solids back-mixing in CFB risers using CPFD simulation. *Powder Technology*, 2014, 266: 135 – 143. (Impact Factor=2.759, Q1 in the category of Chemical Engineering)

(7) Xingying Lan, **Xiaogang Shi**, Yinghui Zhang, Yu Wang, Chunming Xu, and Jinsen Gao. Solids Back-mixing Behavior and Effect of the Mesoscale Structure in CFB Risers. *Industrial & Engineering Chemistry Research*, 2013, 52 (34): 11888 – 11896. (Impact Factor=2.567, Q2 in the category of Chemical Engineering)

A1 (Articles in international journals with peer review, listed in ISI-Web of Science) submitted and/or in progress

(1) **Xiaogang Shi**, Frederik Ronsse, Jelle Roegiers, Jan G. Pieters. 3D Eulerian-Eulerian simulations of solids flow dynamics and back-mixing in a screw reactor. To be submitted to *Fuel Processing Technology*. (Impact Factor=3.847, Q1 in the category of Chemical Engineering)

(2) **Xiaogang Shi**, Frederik Ronsse, Andrés Anca-Couce, Zuoyi Yan, Jan G. Pieters. Simulation of intraparticle secondary charring reactions during biomass pyrolysis by considering biomass composition. To be submitted to *Energy & Fuels*. (Impact Factor=2.835, Q1 in the category of Chemical Engineering)

(3) **Xiaogang Shi**, Frederik Ronsse, Robert Nachenius, Jan G. Pieters. Numerical study of biomass pyrolysis for char production in a screw reactor using a comprehensive kinetic scheme. To be submitted to *Fuel Processing Technology*. (Impact Factor=3.847, Q1 in the category of Chemical Engineering)

C1 (Articles published in proceedings of scientific conferences and/or symposia)

(1) **Xiaogang Shi**, Jelle Roegiers, Jan G. Pieters, Frederik Ronsse. 3D Eulerian-Eulerian simulations of particle flow dynamics and back-mixing in a screw reactor for biomass pyrolysis. Proceedings Venice 2016: 6th international symposium on energy from biomass and waste. 2016, Venice, Italy.

C3 (Active participation to symposia, conferences, or workshops with oral presentation)

(1) **Xiaogang Shi**, Frederik Ronsse, Jan G. Pieters. Finite element and space-time integral models for biomass torrefaction. 21st International symposium on analytical and applied pyrolysis. 2016: 218-218, Nancy, France.

(2) **Xiaogang Shi**, Frederik Ronsse, Jan G. Pieters. Intraparticle heat and mass transfer modeling on the thermal decomposition of dry biomass. AOG RENEW meeting-Energy from water and biomass. 2013, Ghent, Belgium.

(3) Xingying Lan, Yinghui Zhang, **Xiaogang Shi**, Jinsen Gao. Effect of meso-scale structure on solids mixing behavior in CFB risers. The 4th International Conference on Multi-scale Structures and Systems in Process Engineering. 2012, Beijing, China.

(4) **Xiaogang Shi**, Xingying Lan, Jinsen Gao. Oxy-combustion for FCC regeneration process. The 6th Sino-US Joint Conference of Chemical Engineering. 2011, Beijing, China.

Patent

Zhaoqian Zhang, Jinsen Gao, Xingying Lan, **Xiaogang Shi**, Yuehua Bai. Method and set-up for online sampling oil gas from the FCC stripper. Authorized on April 03, 2015. Patent number: CN 201510157888.

Award

(1) Candidate for China Scholarship Council (CSC)

(2) First class in Shandong Province, China, 2009. The third session of "Long Teng Cup" in Chemical Engineering Experimental Design for undergraduate student.

(3) National Scholarship (Top 1%), 2008